Project No. 11-3150

Optimized Compositional Design and Processing-Fabrication Paths for Larger Heats of Nanostructured Ferritic Alloys

Fuel Cycle Research and Development

G. Robert Odette
University of California, Santa Barbara

Frank Goldner, Federal POC
Stuart Maloy, Technical POC

NEUP Nuclear Energy University Programs
U.S. Department of Energy

US DOE NUCLEAR ENERGY UNIVERSITY PROGRAM

Optimized Compositional Design and Processing-Fabrication Paths for Larger Heats of Nanostructured Ferritic Alloys

Final Report

DOE NEUP Contract ID: 119430

Work Package: NU-11-CA-UCSB-0201-01

Project: 11-3150

October 1, 2011 to September 30, 2016

G. Robert Odette

University of California Santa Barbara

Submitted: January 29, 2017

This final report contains three sections and each section contains various numbers of chapters.

TABLE OF CONTENTS

LIST OF TABLES

LIST OF FIGURES

SECTION 2: REPORT ON CHARACTERIZATION OF FCRD NFA-1 PROCESSED COMPONENTS

LIST OF TABLES

LIST OF FIGURES

LIST OF TABLES

LIST OF FIGURES

SECTION 1: FINAL SUMMARY REPORT ON UCSB RESEARCH 14YWT ALLOYS FOR FISSION REACTOR APPLICATIONS

CHAPTER 1. CHARACTERIZATION OF THE FINAL PRECURSOR ALLOY TO A LARGER BEST PRACTICE HEAT OF 14YWT

1.1 OBJECTIVES

The objective of this work was to characterize the alloy 14YWT-PM2, which is an extruded and cross-rolled precursor alloy to a large heat of 14YWT being produced using an alternative processing path that incorporates Y during gas atomization process.

1.2 SUMMARY

We describe our characterization of a new, extruded and cross-rolled nanostructured ferritic alloy (NFA) designated 14YWT-PM2 (PM2). Atomized Fe14Cr powders containing Y, Ti, and W were milled for 40 h with FeO, extruded at 850°C, and cross-rolled at 1000°C. The consolidated alloy was characterized by transmission electron microscopy (TEM) and atom probe tomography (APT), as well as by various mechanical property tests. A summary of the TEM, APT and mechanical testing results are shown in Table 1. PM2 contains a high number density of$N = 8.4\pm2.6\times10^{23}\ m^{-3}$, small $\langle d \rangle = 1.75\pm0.35$ nm Y-Ti-O nanofeatures (NFs). The balance ofthe microstructure consists of: a) a fine, nearly unimodal size distribution of grains with approximately equiaxed cross sections, that are moderately extended in the extrusion direction, with an average effective diameter $d_g \approx 424$ nm; and, b) a high dislocation density of $\approx 1.2\times10^{15} m^{-2}$. Larger Ti oxi-nitride precipitate phases are also observed. The corresponding $\mu H = 401\pm15\ kg/mm^2$, is consistent with yield and ultimate strengths of 1125 and 1298 MPa, respectively. The cleavage fracture toughness of PM2 increases in the temperature regime from ≈ -200 to -100°C up to a ductile tearing upper shelf transition at ≈ 80 MPa√m. A limited number of strain rate jump creep tests also showed high strength, comparable to that of the strongest NFA, in spite of the formation of edge cracks and possible necking during loading.

In addition, milled powders annealed at 850ºC, 1000ºC and 1150ºC were characterized by small angle neutron scattering (SANS) and transmission electron microscopy (TEM). They also contained a high number density of NFs with increasing <d> and decreasing (N) and volume fraction (f) with increasing temperature.

1.3 BACKGROUND

Nanostructured ferritic alloys (NFAs) have applications in advanced fission and fusion reactors and are strengthened and made irradiation tolerant by a high number density of thermally stable Y-Ti-O nanofeatures (NFs). The conventional NFA processing path uses ball milling to mechanically alloy Y_2O_3 in the Fe-Cr matrix, which is expensive and often leads to heterogeneous distributions of NFs. To overcome these challenges an alternative processing path in which Y is included in the melt prior to gas atomization and rapid solidification was developed in collaboration with partner institutions including Oak Ridge National Lab, Los Alamos National Lab, ATI Powder Metals, UC Berkeley and South Dakota School of Mines.

Many small lab heats of NFA were prepared using this alternative processing method and analyzed in a program primarily funded by the DOE Office of Nuclear Energy [1]. The results of this extensive effort were used to identify the best processing practices. This preliminary work culminated in the final production of an extruded and hot, cross-rolled heat at ORNL known as14YWT-PM2 (PM2). The following report describes the characterization of this new material.

1.4 STATUS AND PROGRESS

ATI Powder Metals (Pittsburgh, PA) produced the 14YWT atomized powders in its Laboratory Gas Atomizer (LGA) with a 27 kg (nominal) capacity vacuum induction melting (VIM) furnace lined with an alumina crucible. The crucible tilts to pour the melted alloy into a refractory tundish with a ceramic nozzle at the bottom. The combined effects of gravity and aspiration pressure deliver the melt through the nozzle to the gas atomization die in a close-coupled mode consisting of coaxial, co-directional supersonic gas flow to disrupt the stream of molten metal. Atomization breaks the melt stream into spheroidal droplets that solidify rapidly in an Ar or He atmospheres while moving through a stainless steel cooling tower. The objective is to solute trap Y in solution. Unfortunately this did not occur and the powder cellular solidification microstructure contained phase separated Y, mostly in ≈100 nm $Fe_{17}Y_2$ boundary precipitates or Y-rich precipitates within the grains. In addition, the large batch of powders prepared for subsequent industrial milling in greater quantities by Zoz Corporation in Germany, had a low O content, which was previously found to be inadequate to form fine dispersions of Y-Ti-O NFs [2]. Therefore, attritor ball milling was required both to adequately mix the Y and to add O. The PM2 powder was Zoz CM08 attritor milled at ORNL for 40 h with FeO (-10 mesh, Alpha Aesar, Part #30513) to increase the O content to ≈ 0.135 wt.%. The milling used 5 mm hardened steel balls at a ball to powder mass ratio of 10:1. The milling speed alternated between 900 (2 minutes) and 450 rpm (9 minutes). Care was used to limit O and N contamination from the atmosphere by better chamber sealing and evacuating and backfilling with Ar several times. The powders were then canned and degassed at 400ºC, hot extruded at 850º, annealed for 1 h at 1000ºC and hot cross-rolled to a ≈ 50% thickness of 5 mm. Optical microscopy, SANS, APT and TEM was performed on the extruded and cross-rolled alloy. The volume of available consolidated PM2 was approximately 14 cm^3, allowing for limited mechanical property measurements, including μH, tensile, strain rate jump creep and fracture testing.

Limited SANS and TEM studies were performed on milled powders annealed at 850, 1000 and 1150ºC for 3 h. The baseline anneals involved a 15ºC/min ramp to temperature and cooling, but one condition was an isotherm anneal at 1150ºC.

1.4.1 Microstructural Characterization

The TEM micrographs in Figures 1.1a and b show a moderately elongated grain structure in the extrusion direction, with an effective grain diameter of 424 nm. The SEM back-scattered images in Figures 1.1c and d show a more isotropic grain structure in the plane normal to the extrusion direction. At these high magnifications PM2 appears to have a uni-modal grain size distribution in the areas probed. In contrast, previous work on alloys consolidated at 1150ºC showed a bimodal grain size distributions with the smallest grains a few hundred nm in diameter and a significant fraction of larger grains up to 10 μm in diameter.

Optical micrographs for chemically etched samples in Figure 1.2 show the grain structure at lower magnification in three directions. Note that the samples are difficult to etch due to the high Cr content and small grain size. Nevertheless, there appears to be a bimodal grain size distribution perpendicular to the extrusion and rolling direction as shown in Figure 1.2a. However, the large grain area fraction is small.

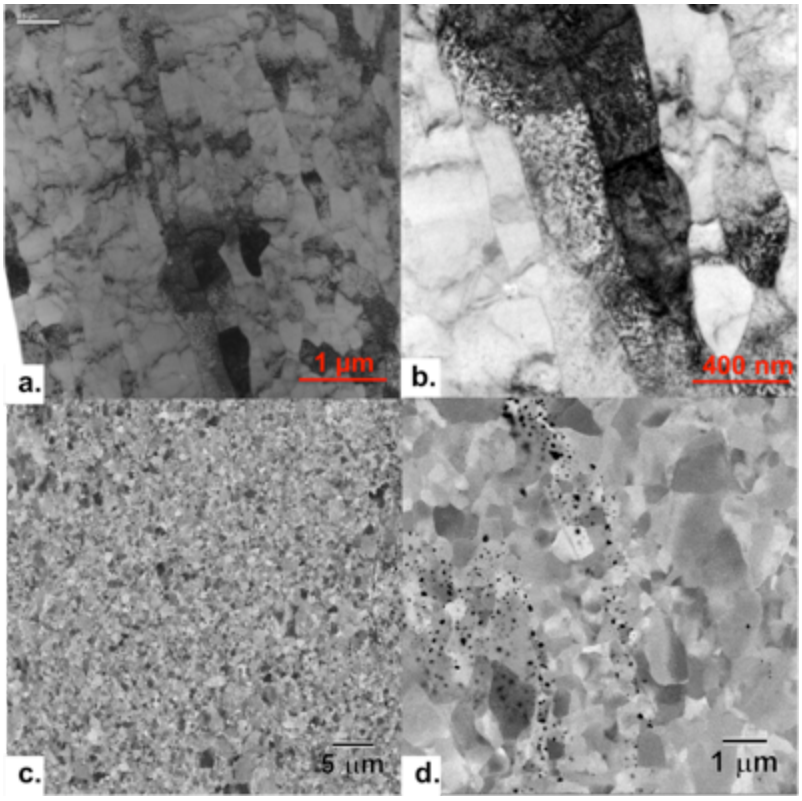

Figure 1 . 1. a-b) TEM micrographs perpendicular to extrusion direction showing elongated grain structure; c-d) SEM back-scattered imaging showing fine grain size; the black regions in these micrograph are Ti oxi-nitride phases.

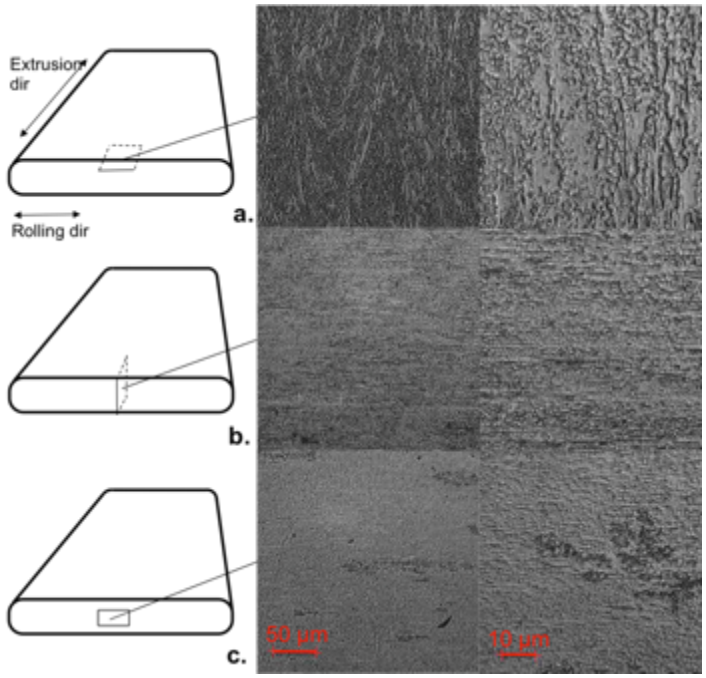

Figure 1.2. Etched PM2 alloy of surface a) perpendicular to the rolling direction; b) perpendicular to the extrusion direction; c) parallel to the extrusion direction.

Table 1.1. Summary of the PM2 characterization results.

NFs	
TEM <d>(nm)	1.4 2.1
Average <d> (nm)	1.75±0.35
TEM N (10^{23} m^{-3}) APT N (10^{23} m^{-3})	5.8 11.0
Average N (10^{23} m^{-3})	8.4±2.6
TEM f (%) APT	0.07 0.47
Average f	0.27±0.2
EDX	0.5 -1
APT	12/43/45
Other Microstructures	
Dislocation density (m^{-2})	1.2x$10^{15}$$m^{-2}$
Average grain size	424 nm
Mechanical Properties	
μH_2	401±15
Yield Stress, LX(MPa)	1125
Ultimate tensile stress, LX (MPa)	1298
Elongation to a load drop (%)	6
Total	11
Temperature ≈ half way between lower and upper shelf toughness (°C)	-170
LMP estimation of the stress at 750°C, for a	310/260

TEM also revealed a high density of dislocations. Figure 1.3 shows two-beam bright field image showing a dislocation density of 1.2x10^{15} m^{2}.

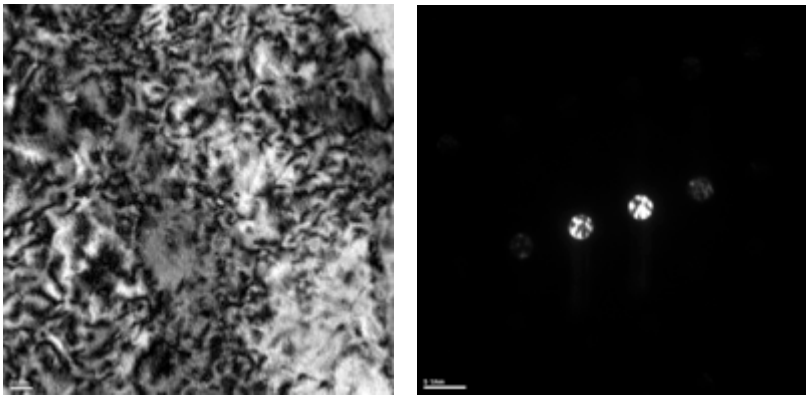

Figure 1.3. Two-beam bright field TEM image showing high density of dislocations.

The main focus of this research was on characterizing the Y-Ti-O NFs.TEM was first performed on the powder annealed at 1150ºC. Figure 1.4 shows a high N ≈ $2.1x10^{23}/m^3$ of <d> ≈ 2.8 nm NFs, with a volume fraction f ≈ 0.24. EDX showed a Y/Ti ratio of 0.74 for the NF.

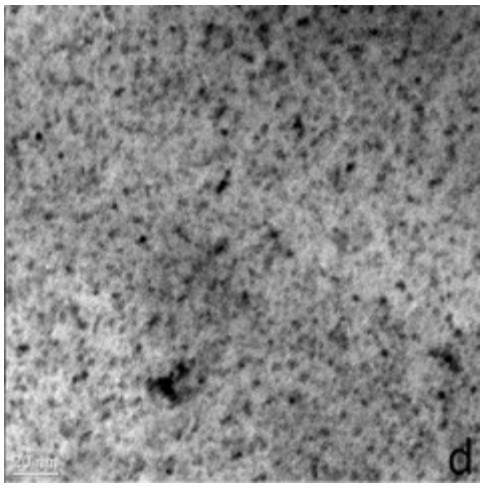

Figure 1.4. TEM on powder milled with FeO and annealed for 3 h at 1150ºC.

SANS was also performed on four powders milled with FeO for 40 h and annealed for 3 h at 850ºC, 1000ºC and 1150ºC. Three powders were ramped up to the hold temperature at 5ºC/min and cooled at the same rate to mimic the HIPing time-temperature history. A fourth powder was isothermally annealed at 1150ºC, which is closer to that experienced during extrusion; note the temperature was lower for PM2. Table 1.2 summarizes the SANS results. The <d> increased and the N and f decreased with increasing annealing temperature. The M/N ratio remained relatively constant. No significant difference was observed between the ramp anneal and isothermal anneal at 1150ºC. SANS has not yet been performed on the consolidated alloy.

Table 1.2. Summary of the SANS results on milled and annealed powders

T(°C)-cycle	<d>, (nm)	M/N	N ($10^{23}/m^3$)	f (%)
1150-ramp	2.8	1.2	7.1	0.8
1000-ramp	2.46	1.1	12.5	1.0
850-ramp	2.14	1.1	23.4	1.2
1150-isothermal	2.82	1.2	7.2	0.9

The consolidated PM2 alloy was also analyzed using TEM and APT. TEM measured <d> ≈ 1.4 nm and N ≈ $5.2x10^{23}$, indicating smaller and more numerous NF than in the annealed powders. This gives a volume fraction of 0.07%, which is lower than expected and measured by APT. In foil EDX showed the NF to typically have an estimated Y/Ti ratio less than 1. Figure 1.5 shows a fairly

uniform distribution and high number density of NF. Some larger precipitates were found to contain high levels of Ti and N.

An APT atom map with 2% Y-Ti-O iso-concentration surfaces, shown in Figure 1.6, has uniformly distributed NFs. Only one APT volume of PM2 was analyzed, with N ≈ $11.0 \times 10^{23}/m^3$ and <d> ≈ 2.1 nm. The size distributions of a previous 1150ºC HIP consolidated alloy, OW2, and PM2 are compared in Figure 1.7.

The bulk, matrix and NF compositions are shown in Table 1.3. The high nominal Fe content is believed to be an APT artifact due to trajectory aberrations that artificially place matrix inside the NF. The Y/Ti/O ratio is 12/43/45 giving a Y/Ti ratio of 0.29. The Y/Ti ratio in PM2 is similar to alloy MA957. In addition to Y, Ti, and O, PM2 also appears to contain a high Cr content in the NFs. The 1-D profiles in Figure 8a show a reduction in Fe but a slight increase in Cr through the NFs. The 1-D profiles of Y, Ti, and O in both the z and x-y directions show a Ti and O tail below the Y core with more symmetric concentration profiles in the x-y direction. The extra matrix atoms in the NF are known to be artifacts since the atom density in the precipitates increases to non-physical levels as shown in Figure 1.8b. This increase in density is caused by dimpling of the atom probe tip surface during evaporation when the NF atoms evaporate at lower electric fields than the matrix or when higher electric fields are induced above the NF [3]. The dimpling alters the electric field lines so that matrix atoms at the NF interface are projected inward and thus observed as part of the NF after data reconstruction.

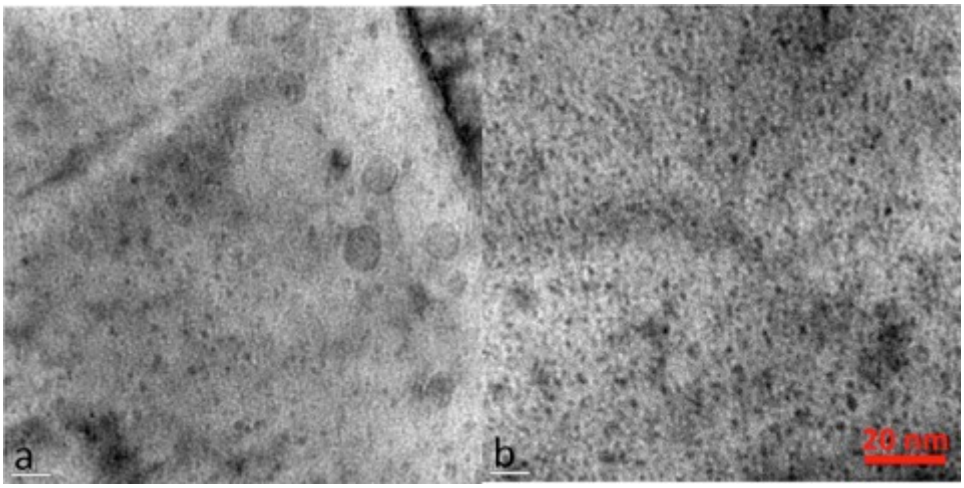

Figure 1.5. Bright field TEM images of extruded and cross-rolled PM2 alloy.

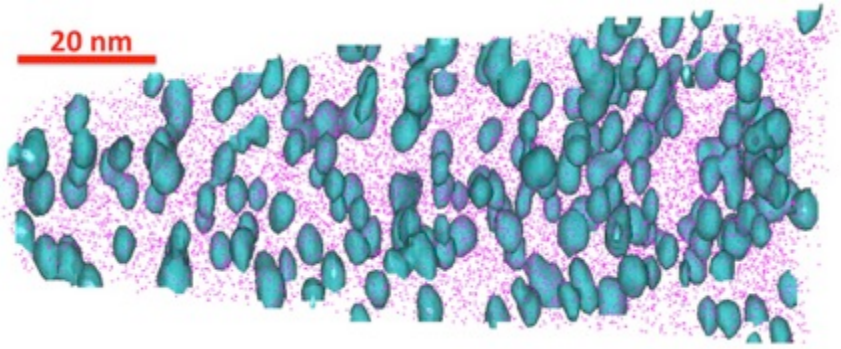

Figure 1.6. An APT reconstruction of a volume of PM2 analyzed by APT. The NFs are shown by Y-Ti-O iso-concentration surfaces (2.0 at.%).

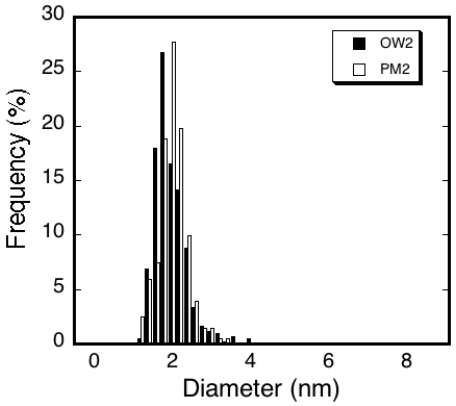

Figure 1.7. Comparison of the size distribution of NFs in OW2 and PM2.

Table 1.3. The average APT NF composition (at.%) in PM2.

	Fe	Cr	W	Ti	Y	O	C	Al	Si
Bulk	83.6	14.5	0.952	0.257	0.073	0.342	0.120	0.016	0.075
Matrix	84.2	14.4	0.961	0.059	0.016	0.134	0.108	0.009	0.073
Cluster	72.6	17.3	0.963	3.64	1.05	3.88	0.330	0.132	0.108
Y-Ti-O				42.5	12.3	45.3			

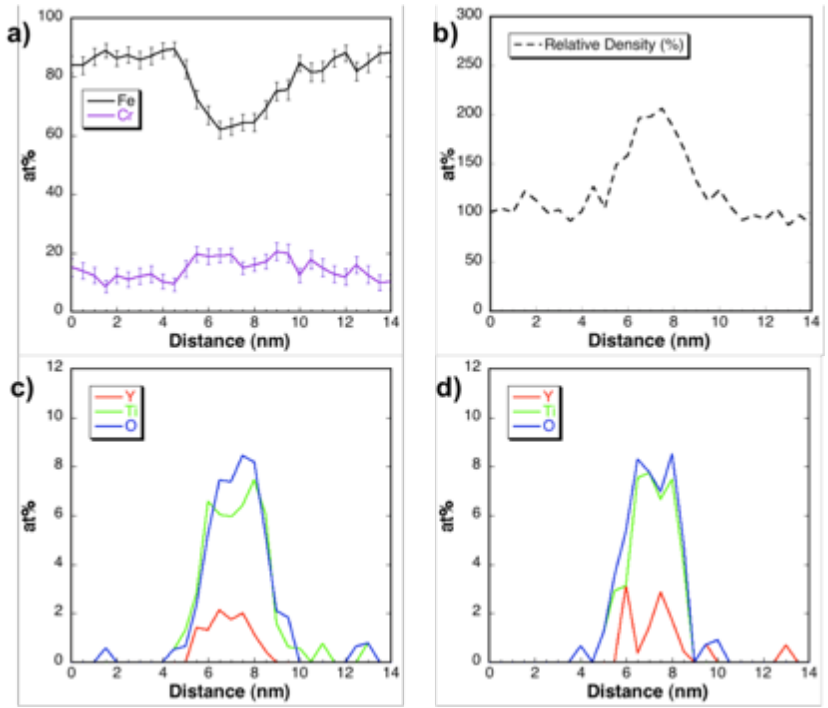

Figure 1.8. 1-D composition profiles of single NF in PM2 alloy showing a) Fe and Cr content and b) atom density relative to the matrix density in Z direction; c) Z and d) X-Y direction atomic Y, Ti, and O content.

1.4.2 Mechanical Testing

Due to time and material constraints only a limited number of scoping mechanical property tests could be performed. So the results reported here should be generally considered provisional. A hardness of ≈ 401±15 kg/mm^2 was measured on the PM2 surface perpendicular to the extrusion direction. Tensile and creep tests used SSJ2 tensile specimens (4×16×0.5mm) while fracture tests used small bend bars (3.33x3.33x18mm). The tensile and bend bar specimens were oriented as shown in Figure 1.9. Since there are two deformation orientations we use a modified nomenclature for the bend specimens where the crack propagation path and tensile axis are parallel to the extrusion (LE) or the cross-rolling (LX) directions, while the crack plane normal is transverse to these processing deformation directions.

A yield stress of 1125 MPa and ultimate tensile stress of 1298 MPa was observed in the LX orientation. Thus the ratio of the average of these two stresses with the microhardness value is almost exactly 3. The engineering flow stress has a near plateau between ≈ 1 and 6% strain, indicating limited strain hardening and significant pre-necking uniform elongation. The total elongation was ≈ 11%. An SEM micrograph of the tensile specimen's fracture surface is shown in Figure 1.10. The material has what appear to be delamination cracks on planes defined by the extrusion and rolling directions. Slightly lower strength was observed in the LE orientation with a yield stress of 1035 MPa and ultimate tensile stress of 1164 MPa, as summarized in Table 1.4.

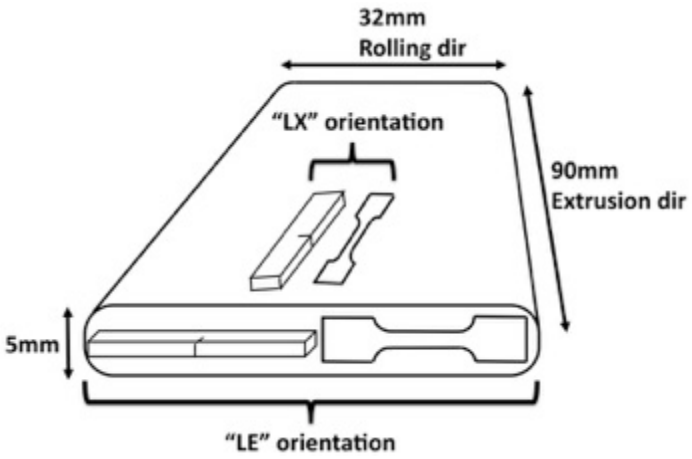

Figure 1.9. SSJ2 tensile and 1/3 bend bars produced from PM2 extruded and cross- rolled material (not to scale).

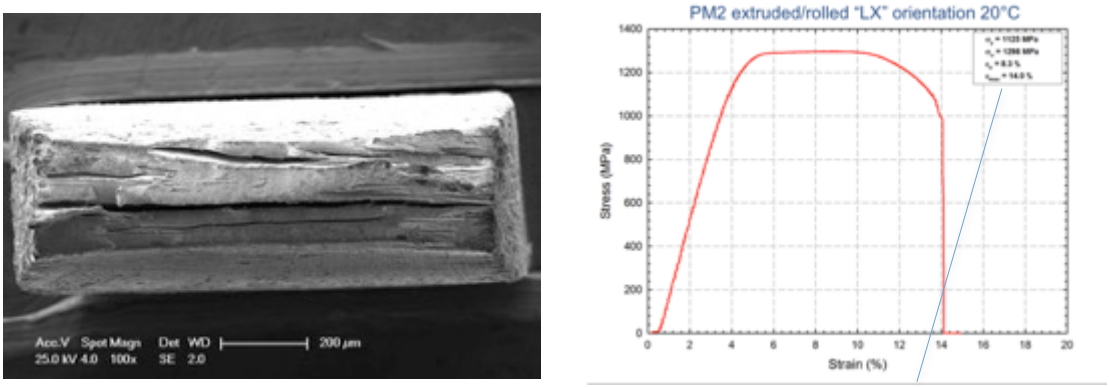

Figure 1.10. Tensile test fracture surface of PM2 (LX orientation) showing cracks along extrusion and rolling direction.

Table 1.4. Tensile test results.

T(°C)-cycle	LX	LE
σ_Y (MPa)	1125	1035
σ_U (MPa)	1298	1165

Four strain rate jump tests were performed; one in the LE orientation and three in the LX orientation. Stress increases were observed upon application of higher strain rates as expected. However, the stresses did not plateau, but rather slowly decreased with increasing strain. This is believed to be due to development of edge cracks that reduce the load bearing cross section, and possible onset of necking. Thus nominal stresses after the jumps are likely to be less than the actual values, but the results still provide a reasonable basis to estimate the comparative strength of PM2. Future testing will use larger, polished cylindrical specimens, but due to the limited material availability this was not possible for PM2. The strain rates are shown in the Larson-Miller type plot in Figure 12 as filled circles for both orientations. In spite of the fact that these are probably less than the actual stresses, the PM2 strength is higher than either the US and French heats of MA957 and close to that for the Japanese 12YWT that is considered to be one of the strongest NFA variants produced to date.

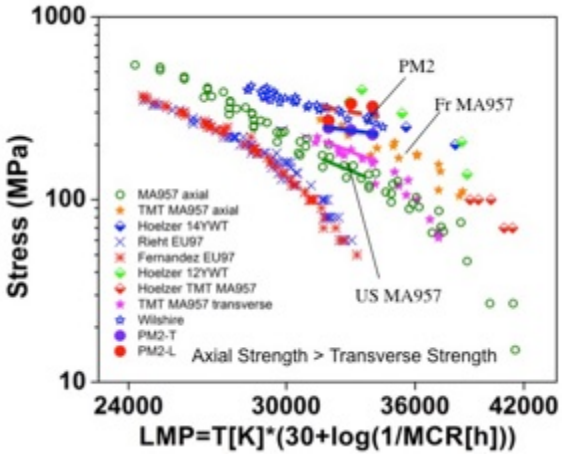

Figure 1.11. Larson-Miller plot comparing PM2 with other NFA alloys.

Three-point bend bar tests measure fracture toughness of PM2 from -200ºC up to 150ºC for PM2. The results are shown in Figure 1.12a along with this NFA HIP consolidated at 1150°C and designated OW4. In the latter case the cleavage transition to the upper shelf occurs between 0 and 150°C at ≈ 70 MPa√m (and even lower at 600°C). The high transition temperature is attributed to the large grains and bimodal grain size distribution in this NFA. In contrast the cleavage transition for both orientations of PM2 is much lower, between -200 and -100°C. However, the upper shelf ductile tearing toughness is still low in PM2 at ≈ 80 MPa√m.

The temperature at the mid-point between lower and upper shelf, assumed to be at ≈ 20 and 80 MPa√m, respectively, is ≈ -160°C. The much lower transition temperature in PM2 is attributed to its more uniformly fine grain structure. The low ductile tearing toughness is thought to be due to a high density of coarser scale Ti-oxides or oxi-nitrides that act as microvoid nucleation sites as illustrated to the micrograph in Figure 1.12b. Figure 1.12c shows the same type of delamination cracks that are also observed in the tensile test.

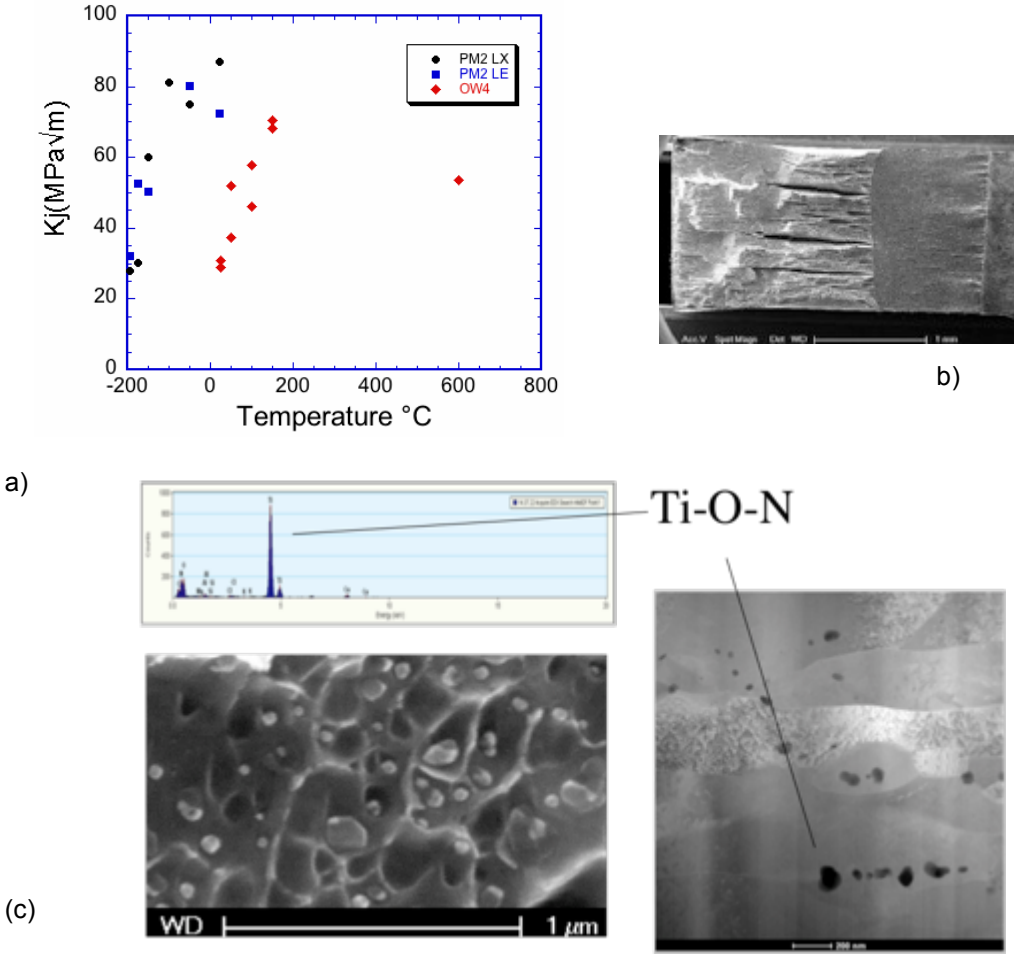

Figure 1.12. DBTT of OW4 and PM2 in LE and LX orientations; and b) high magnification fracture surface and TEM image showing large Ti-oxi-nitrides; c) low magnification fracture surface of PM2 LX bend bar showing delamination.

CHAPTER 2. CHARACTERIZATION OF A LARGER BEST PRACTICE HEAT OF 14YWT IN ANNEALED POWDER, HIP CONSOLIDATED AND EXTRUDED FORMS

2.1 OBJECTIVES

The objective is to characterize a set of 14YWT alloys made from a large heat of gas atomized and mechanically alloyed powder using an alternative processing method that incorporates Y during the gas atomization process.

2.2 SUMMARY

We describe the characterization of new 14YWT heats from gas atomized and mechanically alloyed powder using an alternative processing method that incorporates Y during the gas atomization process. Post mechanically alloying processes included annealing the powder at 850ºC and 1150ºC, HIP consolidation at 850ºC and 1150ºC, and consolidation by hot extrusion at 850ºC, annealing for 1 h at 1000ºC, and then cross-rolling to 50% thickness at 1000ºC; the latter has been dubbed FCRD-NFA1. In all cases a high number density of nm-sized features were observed using a combination of atom probe tomography, transmission electron microscopy, and small angle neutron scattering. The 850ºC lower temperature annealing and HIP consolidation resulted in smaller precipitates compared to the 1150ºC processing temperature. However, after annealing at 1200ºC for 48 h the precipitate size and number density were similar in the two cases. The FCRD-NFA1 had a microstructure and NF distribution similar to a previously reported alloy, PM2. However, the extruded samples also had a large number of large (>20 nm) Ti-rich precipitates. These larger precipitates may affect the mechanical properties, which are currently under investigation.

2.3 BACKGROUND

Nanostructured ferritic alloys (NFAs) have outstanding properties for applications in advanced fission and fusion reactors. NFAs are strengthened and made irradiation tolerant by a high number density of thermally stable Y-Ti-O nanofeatures (NFs). The conventional NFA processing path uses ball milling to mechanically alloy Y_2O_3 in the Fe-Cr matrix, which is an expensive process and often leads to heterogeneous distributions of NFs. To overcome these challenges an alternative processing path in which Y is included in the melt prior to gas atomization and rapid solidification was developed in collaboration with partner institutions including Oak Ridge National and Los Alamos National Laboratory, ATI Powder Metals, UC Berkeley and South Dakota School of Mines. Many small lab heats of NFA were prepared using this alternative processing method and analyzed in a program primarily funded by the DOE Office of Nuclear Energy [1]. The results of this extensive effort were used to identify the best processing practices. Chapter 1 detailed the production, characterization, and mechanical property testing of the final extruded and hot cross-rolled heat known as 14YWT- PM2 (PM2) for the small-batch studies. This chapter describes a larger heat of gas atomized and ball milled powder that was produced using the “best practices” knowledge gained by the smaller scale testing.

ATI Powder Metals Laboratory (Pittsburgh, PA) produced the 14YWT-atomized powders in its Laboratory Gas Atomizer (LGA) vacuum induction melting (VIM) furnace. Details of the atomization process are described in Chapter 1. After atomization the Y is phase separated

and requires ball milling. A total of 15 kg of nominal 14wt.%Cr-3wt.%W-0.35wt.%Ti-0.25wt.%Y iron alloy powder was ball milled by Zoz, GmbH (Wenden, Germany) with 52.5 g of FeO powder for 40 h in a CM100b attritor mill with a ball mass-to-charge ratio of 10:1 and ball size of 5 mm. The canister was evacuated and backfilled with Ar three times to remove any atmosphere contamination and milled in Ar at an overpressure of 100 mbar. The milling speed alternated between 256 (2 minutes) and 150 rpm (10 minutes). FeO was added to increase the O content to ≈ 0.08 wt.%.

This milled powder (V540) was analyzed in several conditions, including as annealed powder, after HIP consolidation and after hot extrusion. After outgassing at 400ºC under vacuum the powder was annealed at both 850 and 1150ºC for 3 h at 15ºC/min ramp and cooling rates. Atom probe tomography (APT) was performed on both conditions and TEM was performed on the 1150ºC-annealed powder. Two HIP consolidated alloys were produced from the outgassed samples using a pressure of 200 MPa for 3 h also at both 850 and 1150ºC. The HIP consolidated alloys were subsequently aged at 1200ºC for times of 48, 96, 144, and 228 h. Both small angle neutron scattering (SANS) and Vicker's micro-hardness (μH) measurements were performed on the as-HIPed and aged specimens. A final alloy designated FCRD-NFA1 was consolidated at ORNL. The powders were first canned and degassed at 400ºC then hot extruded at 850º. After extrusion the alloy was annealed for 1 h at 1000ºC and hot cross-rolled to a ≈ 50% thickness of ≈10 mm. A full microscopic analysis was performed on this alloy including SANS, μH, APT, and TEM. Mechanical testing including fracture, creep, and tensile testing is currently underway.

TEM was performed on FIB lift-out specimens using both FEI Titan 300 kV and FEI T20 200 kV instruments. Grain size measurements and NF size and number density measurements typically used bright field imaging. The NFs were manually counted and the size distribution and number density was measured using image J. The convergent beam techniques were used to measure the foil thickness. Atom probe tomography was performed using a LEAP3000X HR instrument. All samples were prepared using an FEI Helios FIB using the lift-out method outlined by Thompson [4]. Samples were primarily run in voltage mode, with one sample run in laser mode. All voltage mode samples were at temperatures between 35 and 55K, 1% evaporation rate, 20-25% voltage pulse, and 200 kHz pulse frequency. The normal green laser energy was ≈ 0.2 nJ, but a test on one sample was performed to assess the effects of very high laser energy of 0.7 nJ. All analysis was performed using the IVAS software. SANS was performed at the NIST Center for Neutron Research in Gaithersburg, MD on the NG-7 30m SANS beamline. A collimated neutron beam with 5±0.3 Å wavelength was scattered by 1 mm x10 mm x 10 mm samples in a 1.7±0.1 T horizontal magnetic field. The raw SANS data consists of an intensity map, $I(x,y) = I(q,\varphi)$, of the neutron counts on a two-dimensional ^3He detector. Here φ is the angle with respect to the magnetic field and q is the scattering vector, which is a function of the scattering half angle, θ, and the neutron wavelength, λ. The 64 cm x 64 cm detector with 0.5 cm X 0.5 cm pixel size was located 1.55 m from the sample and offset by ≈ 20 cm in the horizontal direction to give a higher q range of ≈ 0.05 to 4 nm-1, corresponding to a feature size length scale of 12.6 to 1.6 nm ($d \approx 2\pi/\lambda$). Scattering from a control (Fe-14wt.%Cr-3wt.%W-0.4wt.%Ti), that does not contain Y, was subtracted from the alloy of interest to isolate the NF scattering and the resulting signal was fit to determine average diameter (<d>), number density (N), and volume fraction (f) from the sample using the method given by Alinger et al. [5].

2.4 STATUS AND PROGRESS

2.4.1 Milled and annealed powders

The TEM micrograph in Figures 2.1a shows a bimodal grain structure in the 1150ºC-annealed powder, with a mixture of small grains, <0.5 μm, and larger grains, several μm in size. The FIBed sample was too small for an accurate overall grain size measurement. Figure 1b shows the NF distribution, shown by the small dark spots, with an average diameter (<d>) ≈ 1.5 nm, a number density (N) of ≈ $6.5x10^{23}$ m^{-3}, and a nominal volume fraction (f) of 0.18%.

Three APT tips from the 850ºC annealed powder were analyzed (≈10 million ions) and five tips were analyzed from the 1150ºC annealed powder (≈34.5 million ions). In all cases, a high NF number density was observed. The average bulk composition for both annealing temperatures is shown in Table 2.1. The bulk composition for the various annealing temperature were generally similar, except that the 1150ºC anneal had a Y content of 0.044 at.% while the 850ºC anneal was 0.076 at.%. Although the Y was lower in the 1150ºC anneal, the range from 0.044 to 0.076 at.% Y is not unexpected and is consistent with previous studies. The low value of Y may be due to the inhomogeneity of the NF distribution or larger Y precipitates that are not observed by APT due to their small number density and the small sample size. There is also a possibly of undercounting Y ions that are undetected in the atom probe analysis. A small amount of N was observed and indicates that the milling procedure minimized contamination compared to some previous alloys.

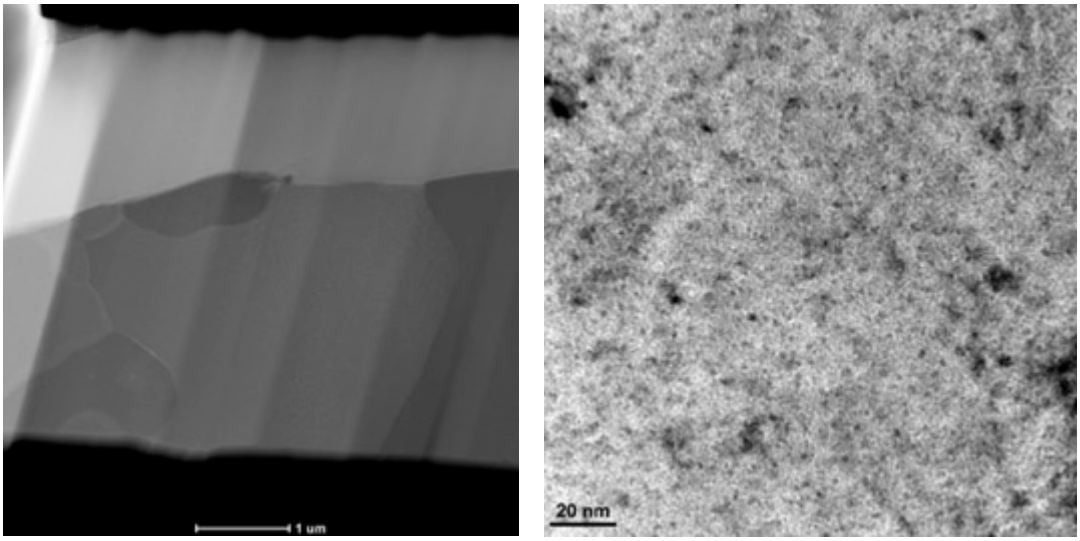

Figure 2.1. TEM images of 1150ºC annealed powder showing a) bimodal grain size and b) fine dispersion of NF.

Table 2.1. The average APT bulk composition (at.%) in the V540 850 and 1150ºC annealed powders.

	Fe	Cr	W	Ti	Y	O	C	Si	N
850ºC Anneal	82.61	15.41	0.998	0.381	0.076	0.263	0.064	0.073	0.002
1150ºC Anneal	83.10	15.13	0.980	0.361	0.044	0.225	0.017	0.063	0.002

Table 2.2 shows the matrix composition, excluding NFs, for the two samples. Again the composition is similar for the two aging temperatures. Except for large reductions in the Ti, Y, and O that are associated with the NFs there is little change between the bulk and matrix compositions. The Ti and O are reduced by ≈ 50% while the Y is reduced by more than 70%.

Table 2.2. The average APT matrix composition (at.%) in the V540 850 and 1150ºC annealed powders.

	Fe	Cr	W	Ti	Y	O	C	Si	N
850ºC Anneal	83.07	15.38	0.996	0.185	0.018	0.131	0.052	0.066	0.001
1150ºC Anneal	83.482	14.988	0.975	0.241	0.012	0.156	0.013	0.060	0.002

Table 2.3 shows the average composition of the clusters after correcting for iron and other matrix atoms. Again both alloys show similar average NF composition. There is significant Cr content in the NF of ≈20% and the Y/Ti ratio is ≈ 0.36, typical of other NFAs

Table 2.3. The average APT NF composition (at.%) in the V540 850 and 1150ºC annealed powders after removing matrix atoms.

	Cr	W	Ti	Y	O
850ºC Anneal	21.76	0.77	29.24	10.71	34.97
1150ºC Anneal	19.91	0.24	28.99	10.20	38.27

Although the overall average NF composition was similar for the 850ºC and 1150ºC anneals, one 850°C annealed APT tip showed a population of NFs with Y/Ti ratios > 1. In this particular case, the upper portion of the tip had many NFs that were mostly Y and O as shown in Figure 2.2. In the bottom 1/3 of the tip, below a possible grain boundary, most of the NF had lower Y/Ti ratios more typical of those found in other NFAs. Since the NFs with higher Y/Ti ratios were only observed in one sample, it is difficult to draw broad conclusions; however, since this alloy was annealed at a lower temperature the NFs may suggest that the Y and O features are present before annealing or cluster first, before reacting with Ti.

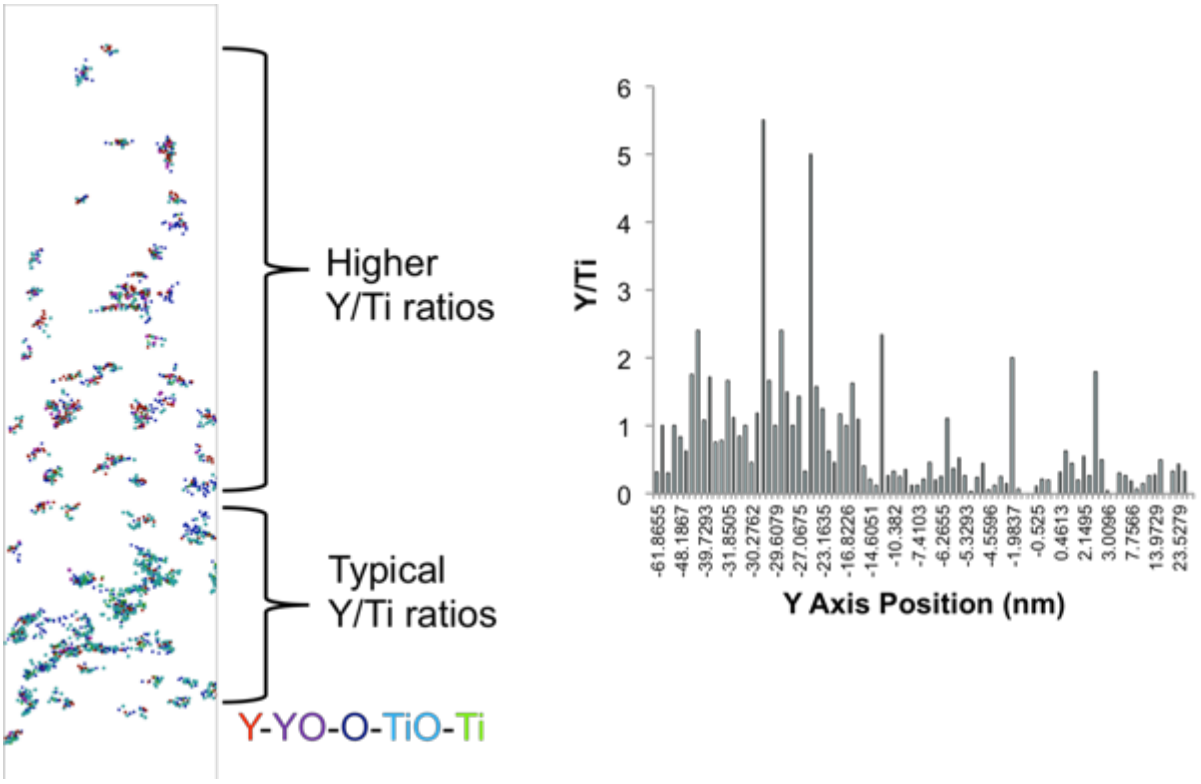

Figure 2.2. APT analysis on 850ºC sample showing two populations of NF with one set having Y/Ti ratios > 1.

The average NF size (<d>), number density (N), and clustered solute fraction (f_{solute}) for the two powders anneals are shown in Table 2.4. As expected, the 850ºC anneal had a higher number density and smaller size than the 1150ºC condition. Despite the high Y/Ti ratio found in some NF, in one 850ºC APT tips the overall NF Y/Ti/O ratio was nearly identical.

Table 2.4. The average NF <d>, N, f and Y/Ti/O ratio measured by APT.

Conditions	<d> , nm	N (1023/m3)	f_{solute} (%)	Y/Ti/O
850 ºC	1.8	10.0	0.51	14/39/47
1150ºC	2.1	4.8	0.38	14/38/48

Figure 2.3 shows atoms maps of one large precipitate that was found on a grain boundary in the 850ºC annealed powder. This precipitate was composed mainly of Ti, Si, and C with trace amounts of N in the center. No other larger precipitates were observed in either the 850 or 1150ºC tips.

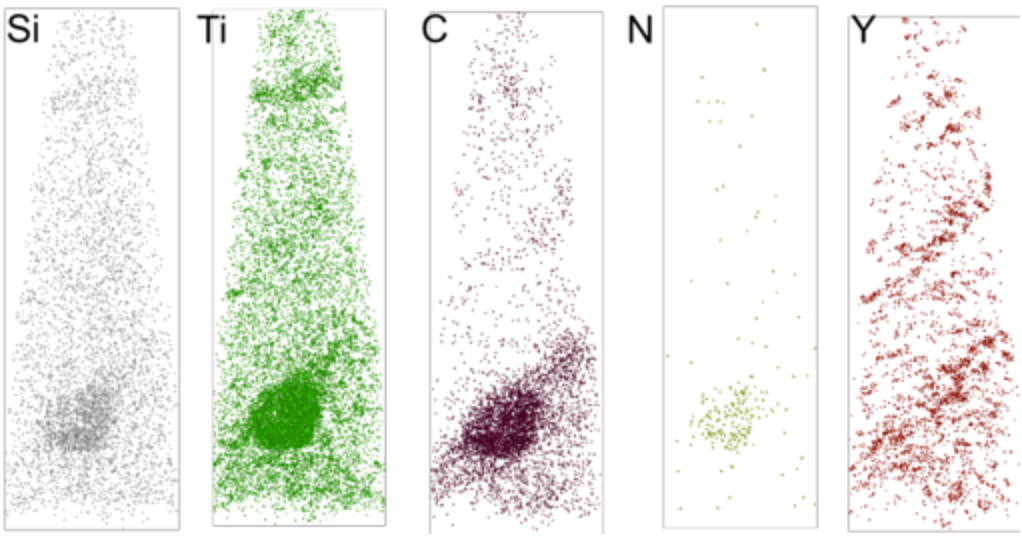

Figure 2.3. Atom map showing large Ti-Si-C-N precipitate on possible grain boundary in 850ºC annealed powder.

2.4.2 Extruded alloy FCRD-NFA1

The FCRD-NFA1 alloy consolidated by extruding at 850ºC and subsequently cross-rolled to50% thickness after annealing for 1 h at 1000ºC was analyzed by TEM, APT, and SANS. The microstructure is shown in the TEM images in Figure 2.4. This alloy showed a unimodal grain size distribution with the average size of ≈ 0.5 µm. This is similar to the previous extruded alloy, PM2.

EDX analysis on some of the larger precipitates showed that they were mainly composed of Ti and N, indicating some contamination may have occurred. An example TEM image showing the larger precipitates on grain boundaries is shown in Figure 2.5. TEM also showed the presence of the smaller Y-Ti-O NF and measured the <d>, N and f to be 2.1±1.3 nm, 1.6×10^{23} m^{-3}, and 0.25%, respectively. EDX was performed on larger NF from 5 to 20 nm in diameter. The measured Y/Ti ratio in these larger NF ranged from 0.5 to 1.3. SANS analysis was also performed on the FCRD-NFA1 and showed slightly larger NF (3 nm) with higher number density (6.0×10^{23} m^{-3}) and volume fraction (0.82%) compared to the TEM results. Figure 2.6 compares the 45±15º scattering curves of the FCRD-NFA1 alloy with NFA alloy MA957 and a Fe14Cr control. Overall, the scattering is slightly higher in the FCRD-NFA1 but still comparable to that for MA957.

Almost all the tips FCRD-NFA1 atom probe tips fractured early when encountering large Ti rich precipitates. Figure 2.7 shows atom maps from one sample with two large precipitates composed mainly of Ti, O, C, and N. Smaller Y-Ti-O NF were found in the rest of the sample. The NF Y/Ti/O ratio for FCRD-NFA1 is 14/42/45 with slightly higher, but still similar compared to the milled and annealed powders. The Y/Ti/Cr/O was 11/32/24/34, again showing high 20% Cr in the NFs. This alloy included a processing step at 1000ºC between the powder temperatures annealing

temperature, and the N and <d> fell between the annealed powders at 6.9×10^{23} m^{-3} and 2.02±0.78, respectively. The f was ≈ 0.74%.

The APT bulk and matrix composition from the FCRD-NFA1 sample without large Ti-rich precipitates is shown in Table 2.5. Again the majority of Y, Ti, and O are found in the precipitates and not in the matrix. This tip also has higher C content compared to the annealed powder (0.138 at.% vs 0.064 at.%). Part of this C contamination may come from the can used during extrusion, since the APT tip was taken near the sample/can interface.

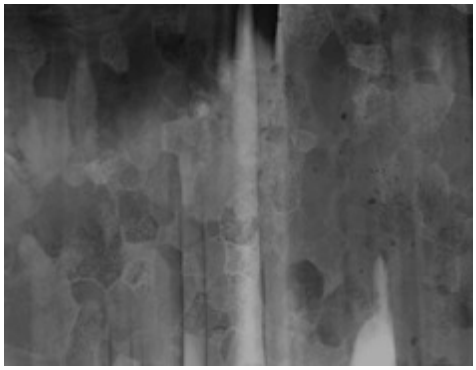

Figure 2.4. TEM image showing grain structure in FCRD-NFA1 alloy.

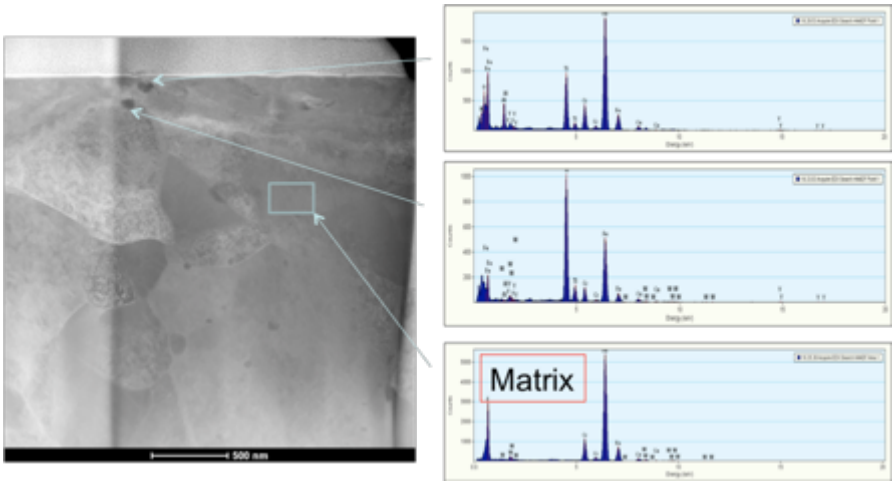

Figure 2.5. TEM image of the FCRD-NFA1 alloy showing the presence of larger precipitates on grain boundaries that are mainly composed of Ti and N.

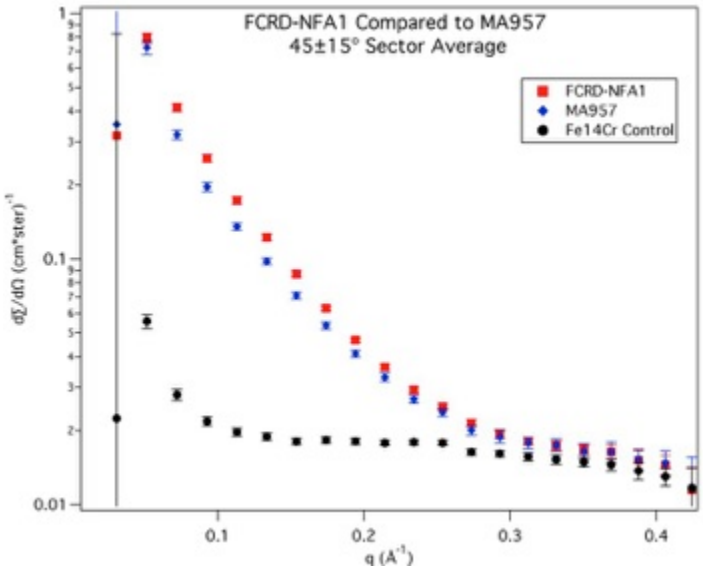

Figure 2.6. SANS 45º scattering curves comparing FCRD-NFA1, MA957, and Fe14Cr control.

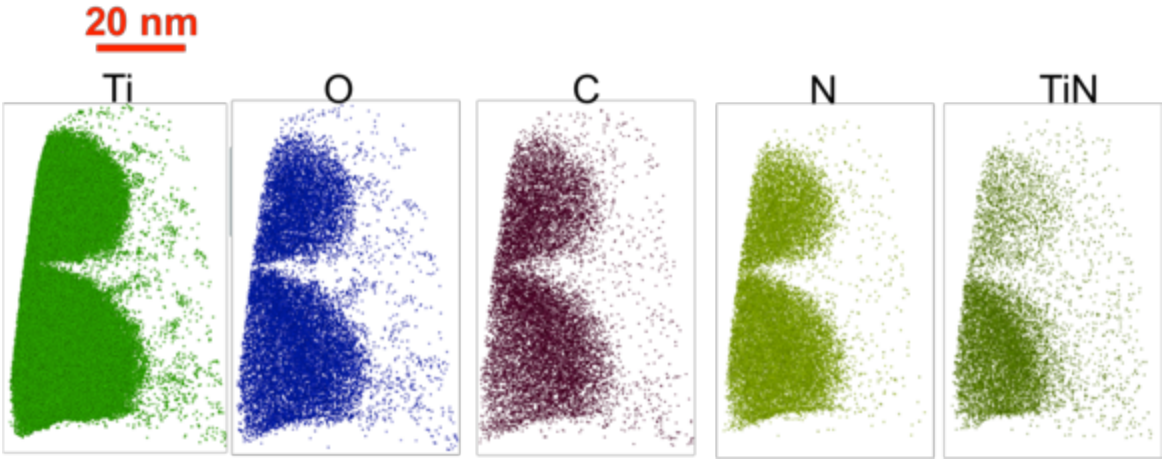

Figure 2.7. Atom maps showing large precipitates in FCRD-NFA1 composed of Ti, O, C, and N.

Table 2.5. The APT bulk and matrix composition (at.%) in the FCRD-NFA1 extruded alloy.

	Fe	Cr	W	Ti	Y	O	C	Si	N
Bulk	82.94	15.05	0.967	0.283	0.090	0.366	0.138	0.076	0.006
Matrix	83.57	14.97	0.969	0.056	0.016	0.125	0.127	0.073	0.005

Table 2.6 compares two previously characterized NFAs with the newest FCRD-NFA1 alloy. Alloy PM2 was the smaller batch precursor to FCRD-NFA1 and MA957 is an older NFA that has been extensively studied. The results from different characterization methods are shown along with the corresponding average <d>, N and f. The APT Y/Ti/O ratio, μH, and grain size are also given. The newer 14YWT NFAs have slightly smaller NFs compared to MA957, but similar number densities and compositions. The microhardness is slightly higher in the newer 14YWT alloys and they have a smaller average grain size. The grains are only slightly elongated in the newer extrusions compared to MA957.

2.4.3 High temperature aging

SANS was performed on the 850 and 1150ºC HIP consolidated alloys as well as aged specimens. All the HIP condition were aged at 1200ºC for 48, 96, 144, and 228 h. Currently only the 48 h aging SANS data has been analyzed. Results from the longer aging times will be reported in the future and will be compared to previous aging performed on MA957. As noted above, the 850ºC HIP baseline alloy had the smallest NF and highest number density at <d> = 2.1 nm and N = 2.93×10^{24} m^{-3}. This corresponded to a nominal NF volume fraction of 1.5% and resulted in a μH of 495±16. The 1150ºC HIP had a <d> = 3.0 nm, N = 7.2×10^{23} m^{-3}, and f = 1.0% resulting in a μH of 357±17. After aging at 1200ºC for 48 h the NF populations in the two conditions were nearly identical. The aged 850ºC HIP had a <d> = 3.6 nm, N = 3.6×10^{23} m^{-3}, and f = 0.90%. The aged 1150ºC HIP had a <d> = 3.7 nm, N = 3.3×10^{23} m^{-3}, and f = 0.9%. The microhardness in the 850 and 1150ºC HIPs after aging were 304±36 and 308±34, respectively. The magnetic to nuclear scattering ratio (M/N) was similar in both alloys at 1.2 for the HIP at 850ºC and 1.1 for the 1150ºC HIP consolidation. This is slightly below the expected value of 1.4 for a population of $Y_2Ti_2O_7$ NF. The M/N in the un-aged alloys is similar to the FCRD-NFA1 alloy with M/N = 1.2. After aging the M/N increased to 1.5 and 1.6 in both cases.

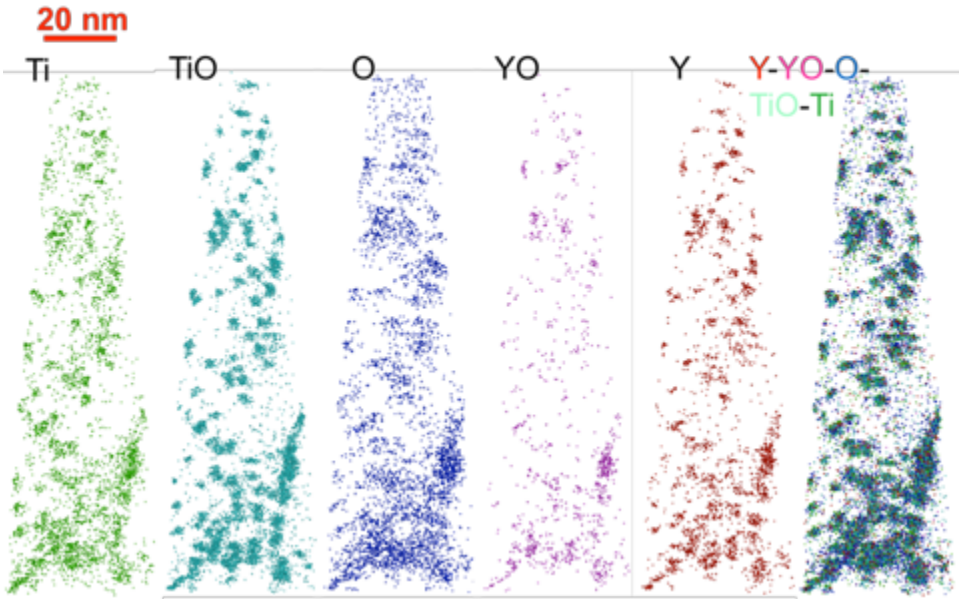

Figure 2.8. Atom maps showing high number density of Y-Ti-O NF in FCRD-NFA1.

Table 2.6. Comparison of 14YWT alloys FCRD-NFA1 and PM2 with MA957.

Technique	NFA1	PM2	MA957
TEM <d> (nm)	2.1	1.4	2.8
APT <d> (nm)	2.0	2.1	2.7
SANS <d> (nm)	3.0	2.8	2.7
Average (nm)	2.4	2.1	2.7
TEM N (10^{23} m^{-2})	1.6	5.8	2.6
APT N (10^{23} m^{-2})	6.9	11.0	5.1
SANS N (10^{23} m^{-2})	6.0	8.9	9.0
Average (10^{23} m^{-2})	4.8	8.6	5.6
TEM f (%)	0.25	-	0.40
APT f (%)	0.74	-	0.51
SANS f (%)	0.82	1.00	0.90
Average (%)	0.60	1.00	0.60
APT Y/Ti/O	14/42/45	12/43/40	14/46/40
μH	359±18	401±15	336±8
Grain Size (μm)	454	424	1.47x0.63

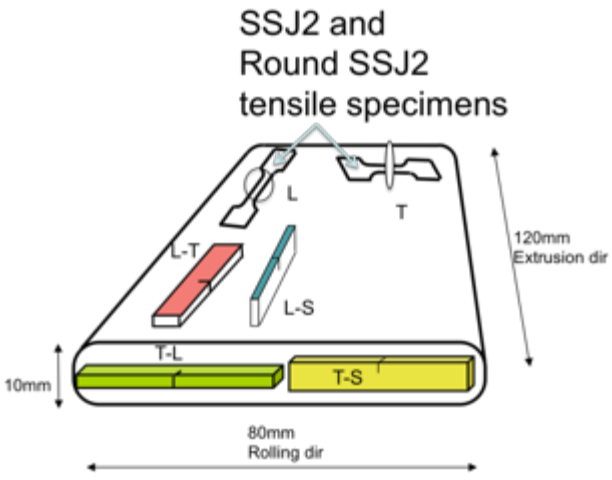

Figure 2.9. Mechanical test specimen layout in extruded and cross-rolled FCRD-NFA1.

2.5 CONCLUSIONS AND FUTURE WORK

The new extruded and cross-rolled FCRD-NFA1 larger heat has a similar microstructure and NF distribution to the previously processed, smaller precursor batch PM2 alloy. In both cases high number densities of Y-Ti-O NFs were observed with a similar character. One notable exception is that there appears to be a greater number of larger, Ti-rich precipitates in the FCRD-NFA1. These larger precipitates were observed both in TEM and APT.

Further comparison between PM2 and FCRD-NFA1 will evaluate the mechanical properties. Limited mechanical property data from PM2 showed promising creep resistance as well as acceptable fracture toughness. The larger volume of FCRD-NFA1 material will allow for a more comprehensive mechanical property investigation. Figure 9 shows the type of samples and orientations that are currently being tested. Fracture testing will occur using one-half-1/3 bend bar specimens in four orientations: L-T, T-L, T-S and L-S. The first letter corresponds to the direction normal to the crack plane in the directions of the length of the specimen, and the second letter corresponds to the crack propagation direction. Two types of tensile specimens were produced. The flat, 0.5 mm thick specimens will be used for tensile testing both at room temperature and at elevated temperature. The round gauge length specimens will be used for creep testing by performing strain-rate jump tests.

ACKNOWLEDGMENT

This work is part of a multi-laboratory collaboration between LANL, UCSB and ORNL. The research was supported by DOE Office of Nuclear Energy under a NEUP grant 119430 and by a subcontract from the LANL FCRD program. Partial support was also provided the DOE Office of Fusion Energy. We acknowledge the support of the National Institute of Standards and Technology, U.S. Department of Commerce, in providing the neutron research facilities used in this work. This work was made possible through use of the Microscopy and Microanalysis facility at the California Nanosystems Institute (CNSI) at UCSB.

REFERENCES

1. N. J. Cunningham, “Study of the Structure, Composition, and Stability of Y-Ti-O nm-Scale Features in Nano-Structured Ferritic Alloys,” Ph.D. Thesis, University of California - Santa Barbara, Santa Barbara, CA (2012).

2. Y. Wu, N. J. Cunningham, A. Etienne, E. Haney, G. R. Odette, “The Effect of Bulk Oxygen Concentration on the Micro-Nanostructure and Strength of a 14Cr Nanostructured Ferritic Alloy,” DOE Fusion Reactor Materials Program Semiannual Progress Report for the Period Ending June 30, 2011, DOE/ER-0313/50 2011.

3. C. Oberdorfer and G. Schmitz, “On the Field Evaporation Behavior of Dielectric Materials in Three-Dimensional Atom Probe: A Numeric Simulation,” Microsc. Microanal. 17, 2011, 15-25.

4 K. Thompson, D. Lawrence, D. J. Larson, J. D. Olson, T. F. Kelly, and B. Gorman, “In Situ Site-Specific Specimen Preparation for Atom Probe Tomography,” Ultramicroscopy 107, 2007, 131.

5 M. J. Alinger, G. R. Odette, and D. T. Hoelzer, “On the Role of Alloy Composition and Processing Parameters in Nanocluster Formation and Dispersion Strengthening in Nanostructured Ferritic Alloys,” Acta Mater. 57, 2009, 392-406.

SECTION 2: REPORT ON CHARACTERIZATION OF FCRD NFA-1 PROCESSED COMPONENTS

CHAPTER 1: TENSILE PROPERTY CHARACTERIZATION of 14YWT NANOSTRUCTURED FERRITIC ALLOY NFA1

The main objective of this study is to characterize the high temperature tensile property of a newly developed larger best practice heat of 14YWT nanostructured ferritic alloy, NFA1, in different orientations.

1.1 SUMMARY

FCRD NFA-1 is a new larger heat of best practice nanostructured ferritic alloy (NFA) that was produced by ball milling argon atomized Fe-14Cr-3W-0.4Ti-0.2Y (wt.%) and FeO powders, followed by consolidation and a thermo-mechanical processing sequence consisting of extrusion at 850°C followed by annealing and cross-rolling at 1000°C. Uniaxial tensile tests were performed on flat, dog-bone shaped specimens in six different orientations at different temperatures ranging from 23 to 800°C. NFA1 exhibits excellent strength with up to a 0.2% yield strength (YS) of 1144 MPa and ultimate tensile strength (UTS) of 1253 MPa in the extrusion and cross-rolled directions (LT and TL). This high strength is accompanied by good total elongation ductility of ~10%. In contrast, loading in the short plate thickness direction (S) at ambient temperature exhibited much lower strength of ~800 MPa, with a flat, facet fractured surface, and low total ductility of less than ~0.5%. The low strength and total strain in the plate thickness direction can be attributed to the presence of pre-existing microcracks that run parallel to the plate surfaces. Upon loading, the microcracks propagate by brittle cleavage. The brittle to ductile fracture mode transition begins above 23°C and is complete at 200°C. At 800°C, the NFA1 exhibits up to 251 MPa YS, 278 MPa UTS and 17% total strain LT and TL direction and 200 MPa YS, 209 MPa UTS and 16.4% total strain at S directions.

1.2 BACKGROUND

Background on NFA and further details on NFA-1 are reported elsewhere and will not be reviewed here [1,2].

1.3 EXPERIMENTAL

The as fabricated NFA-1 was characterized using a scanning electron microscope (SEM) equipped with energy dispersive spectroscopy (EDS) and electron backscatter diffraction (EBSD). Polished (down to 20 nm colloidal silica) surfaces were observed in a FEI X30 SEM (Netherland) to characterize the surface morphology before testing. EBSD was used to measure the crystallographic grain morphology with respect to extrusion and cross-rolling directions. Tensile tests were performed on SSJ-2 type dog-bone shaped and sub-sized flat specimens with a gage section length, width and thickness of 5.0x1.2x0.5 mm. The tests in air were performed for six orientations, namely LT, TL, LS, TS, SL and ST where L, T and S represent longitudinal (rolling), transverse (cross-rolling) and short thickness directions, respectively (see Fig.1.1). The tests were conducted at varying temperatures from ambient to 800°C, using a 810 MTS servo-hydraulic universal testing machine equipped with a clam shell furnace. All specimens were sanded down to 1500 grit to remove any surface contamination or residual stresses due to the EDM machining before testing. The specimens were heated to the target temperature in atmosphere environment, and held for 10 minutes before testing. Testing was carried out at a crosshead speed of 0.30 mm/min or a strain rate of $\approx 10^{-3}$/s. Except for the small size of the specimens, the tensile properties were determined in accordance with ASTM Standard E8M-13. Extensive SEM/EDS was carried out on the post-test fracture surfaces.

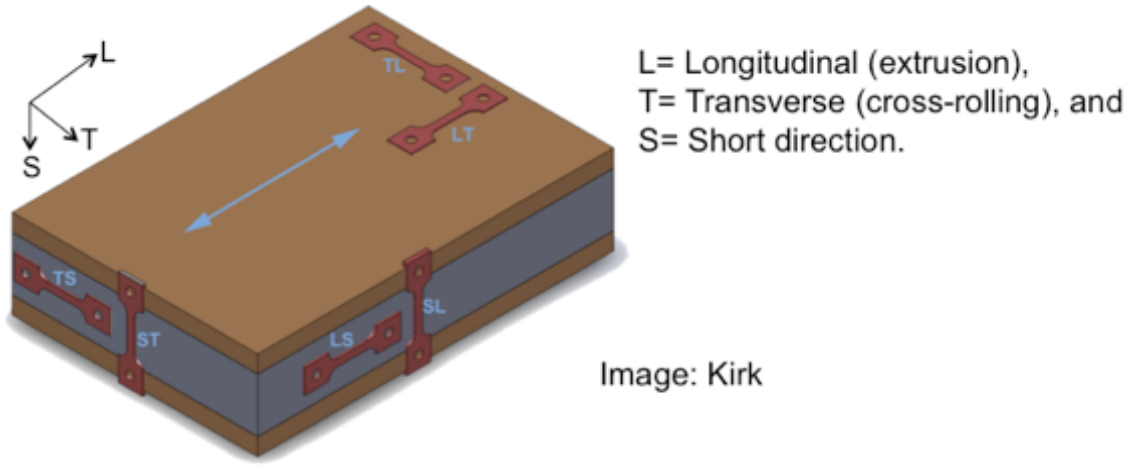

Figure 1.1. NFA1 specimen orientations labeled with respect to the extrusion, cross-rolling and plate thickness directions.

1.4 STATUS AND PROGRESS

Pre-Test Characterization

SEM micrographs on non-deformed polished and etched NFA-1 plate normal surfaces in Fig. 1.2a do not show any cracks or pores. In contrast, Figs. 1.2b and c show anisotropic banding in the thickness cross section plane oriented along cross-rolling (plane B) and extrusion (plane C) directions. EBSD used to characterize the grains imaged in all three planes. The inverse pole figure (IPF) maps in Fig. 1.3 highlight the existence of strong preferential crystallographic fiber texture, with most grains <110> oriented along the extrusion direction. Plane A showed the smallest average grain size of ≈ 235 ± 212 nm, with the lowest grain aspect ratio (GAR) of ≈ 1.7 ± 0.6. Fig. 1.3b shows the presence of surface cracks along the transverse direction. Most of the grains are extended along the transverse (cross-rolling) direction (Fig. 1.3b). Very large (2-5 micron) and elongated grains are often observed in the vicinity of the surface cracks. Plane C also reveals relatively larger 349 ± 247 nm grains with the highest GAR ≈ 3.3. Fig. 3c reveals that the elongated grains oriented along the extrusion directions are also often associated with surface cracks.

Tensile Properties

Room temperature tensile tests were conducted in six different orientations shown in Fig. 1.1. Examples of the results are shown in Fig. 1.4. The LT orientation showed the highest ambient temperature strength with a YS average of 1144 MPa 0.2% and UTS average of ≈ 1253 MPa. The corresponding ST oriented specimens showed the lowest average strength of ≈ 765 MPa and 832 MPa for the YS and UTS, respectively. The fracture surfaces in all six orientations are shown in Fig. 1.5. There is a similarity in properties and fracture patterns that fall three different categories: group 1 LT and TL orientations (group 1) with high strength and intermediate total strain; LS and TS (group 2) with the highest total strain; and SL and ST (group 3) with the lowest strength with negligible total strain and brittle fracture surfaces.

Delaminations occurred in the group 1 normal to the thickness direction in planes parallel to the plate surfaces. In group 2, delaminations form through the width direction along the gage length normal to the thickness direction, which is basically a 90^{o} rotation from group 1. Stress-strain curves in Fig. 1.4 show multiple-stage post necking load drops associated with a sequence of delaminations. The load drops are

due to the corresponding to reductions in the necking constraint in the width direction. Difference between group 1 and 2 are related to the brittle orientation of the brittle planes with respect to the direction of necking reduction. The LT/TL oriented specimens neck in the thickness direction whether as LS/TS oriented specimens neck in width direction. Specimens loaded in the short directions (group 3) failed almost in a brittle manner, mostly in its elastic regime. In this case the weak planes and laminated layers are perpendicular to the loading direction and easily break during tensile loading at much lower stress compared to other orientations. The fractured surface are quite flat, in this case, with almost no/minimal area reduction. Group 2 specimens exhibited the highest uniform and total elongations. The LS orientation exhibits an average uniform elongation (UE) of ≈ 8.1% and a total elongation (TE) is as high as 21.8%. Group 1 specimens exhibited lower total strain with averages of ≈ 5.0 % UE and ≈ 10% TE. The higher strength of group 1 specimens comes at the expense of total strain, compared to group 2 specimens. In contrast, group 3 specimens exhibited both lower strength and total strain (≤ 0.5% UE and TE) compared to the other groups. Figure 1.6 shows higher magnification SEM images of fractured samples that revealed the extensive presence of ductile shear zones in group 1 and ductile dimples in group 2 in contrast to the cleavage brittle fracture features in group 3 specimens.

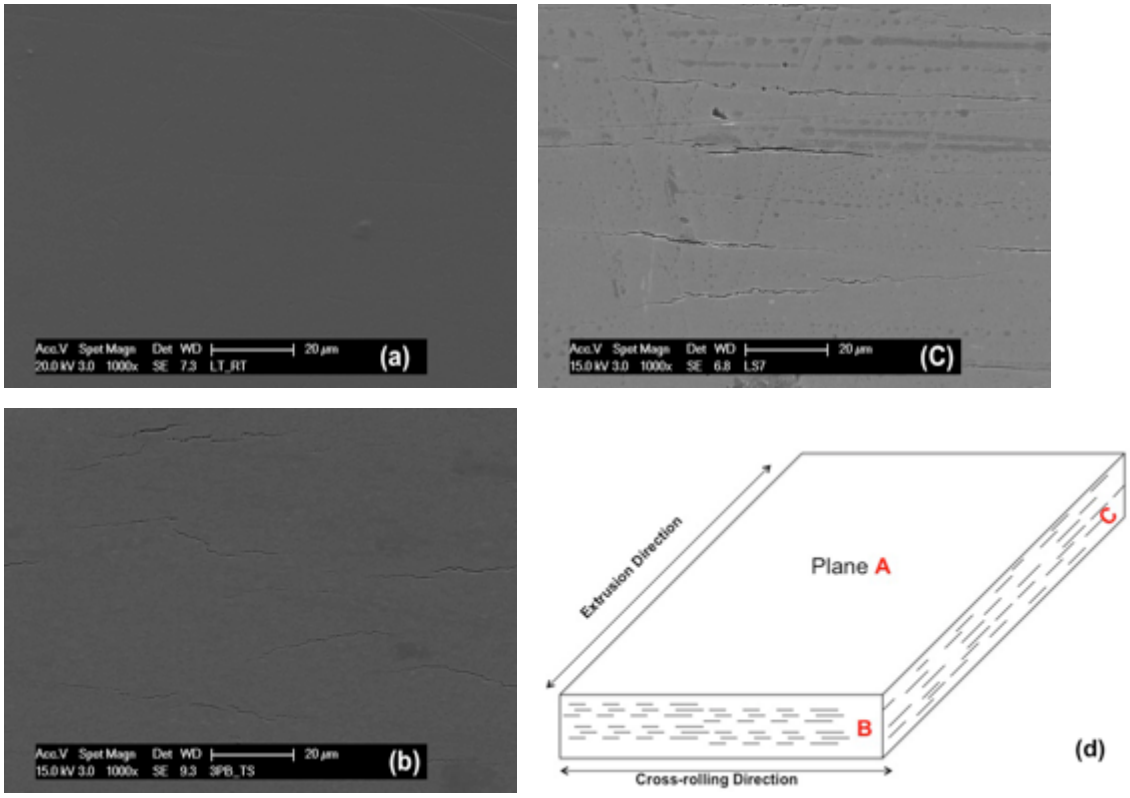

Fig. 1.2. SEM images showing the non-deformed surface morphology of: (a) Plane A, (b) Plane B, and (c) Plane C of 2(d), respectively. 2(d): Schematics of delamination of NFA1.

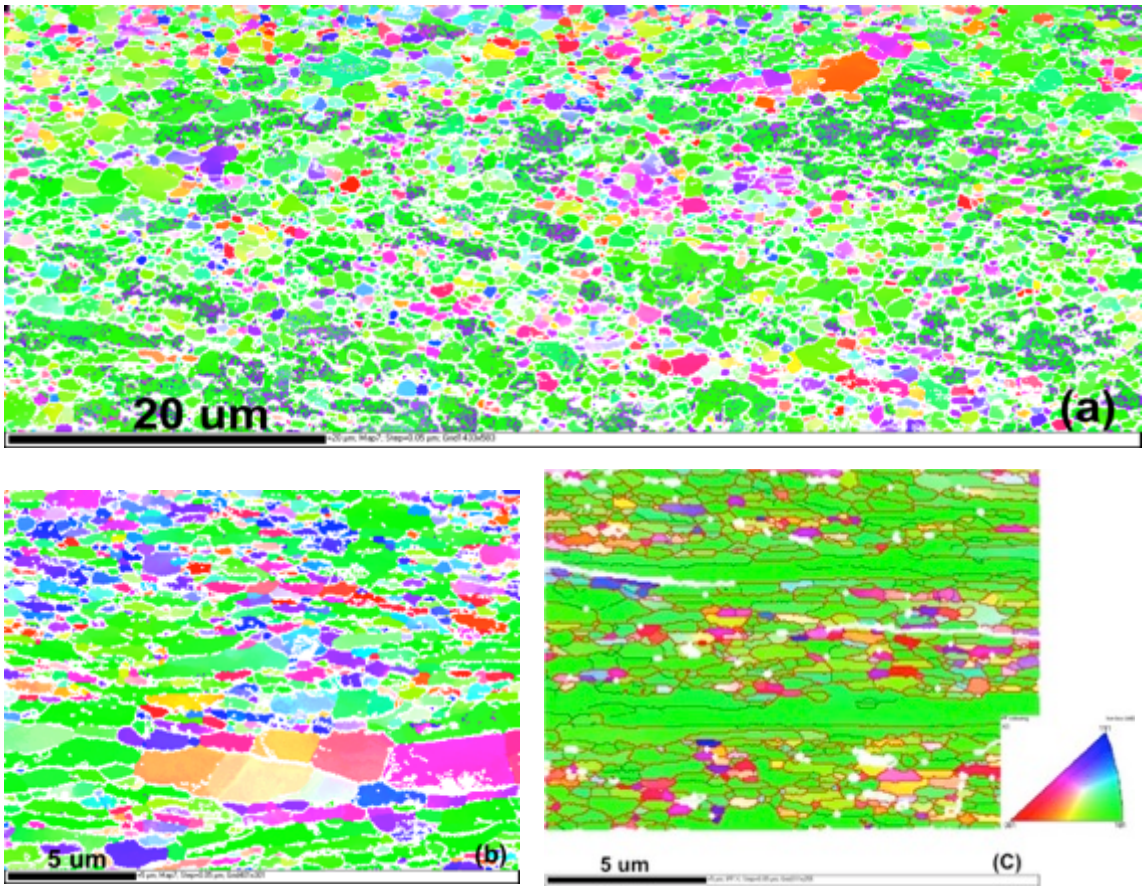

Fig. 1.3. Inverse pole figure (IPF) maps obtained by EBSD on the: (a) Plane A, (b) Plane B, and (c) Plane C of 1.2(d), respectively.

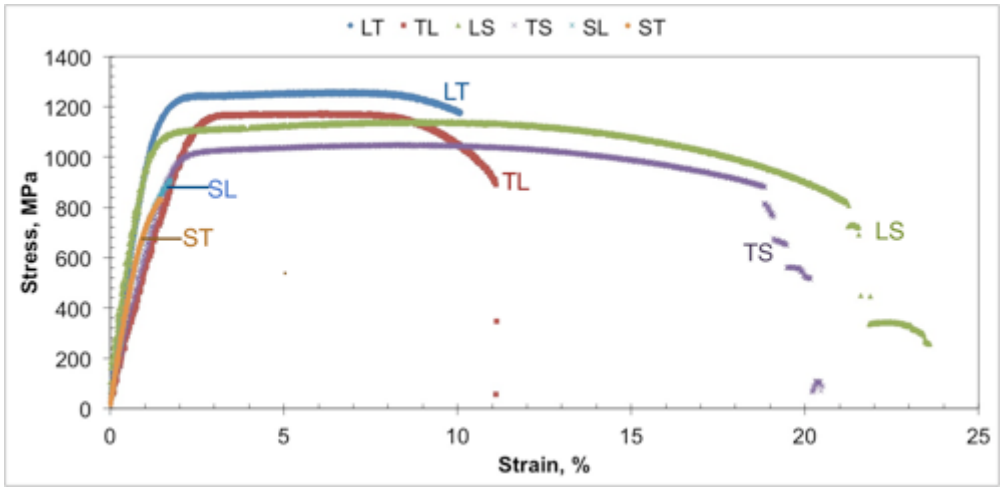

Fig. 1.4. Room temperature engineering stress-strain curves of NFA1 specimens tested in all six orientations.

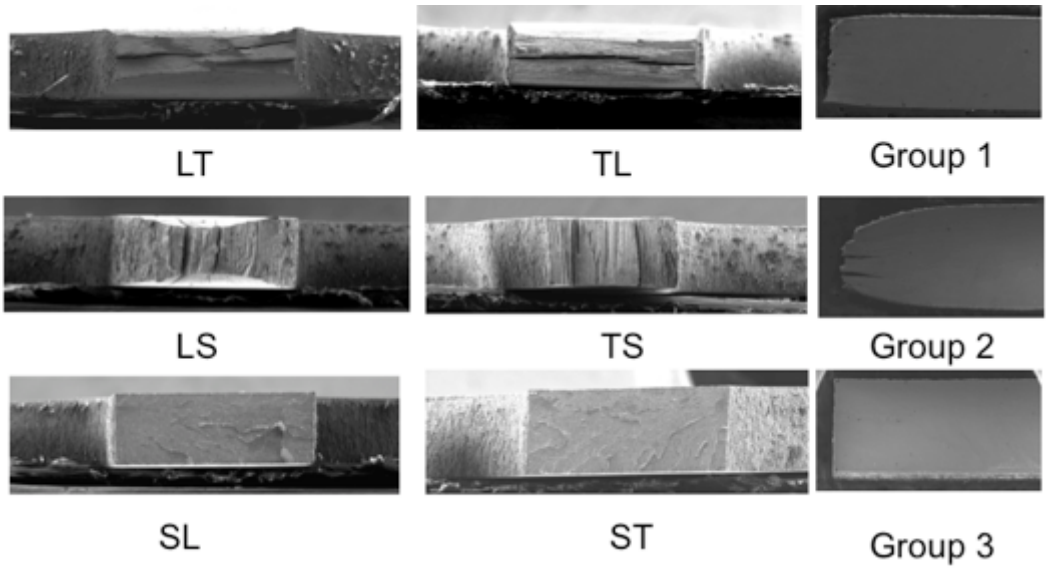

Fig. 1.5. Low magnification SEM fractographs of room temperature tensile fracture surfaces in different orientations.

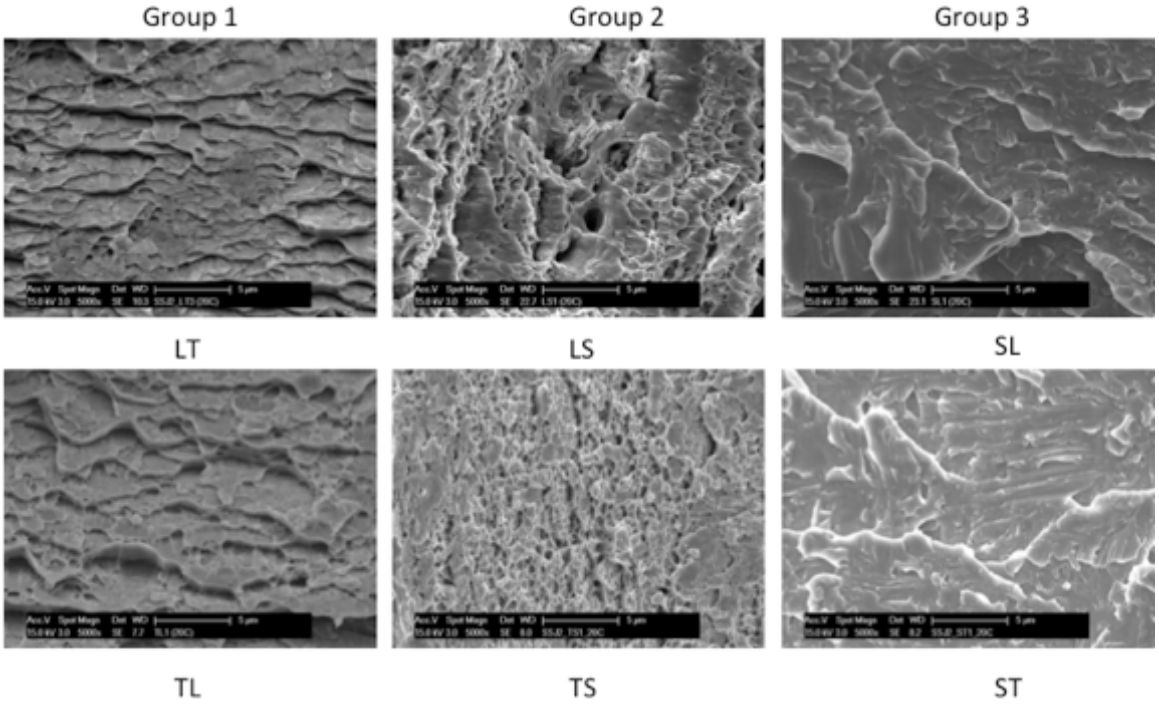

Fig. 1.6. SEM fractographs of NFA-1 tensile specimens showing by group: (1) shear-leaps like features for LT/TL, (2) dimple like features for LS/TS, and (3) cleavage features for SL/ST orientations, respectively.

Tensile curves for tests performed at 600^{o}C in all six orientations are shown in Fig. 1.7. Like room temperature tensile properties, LT oriented specimen again showed the highest strength with an average value of 584 MPa 0.2% YS and 630 MPa UTS. TL orientations again exhibited similar tensile properties

as for LT, but with slightly lower strength. The LS and TS orientations (group 2) have intermediate strength (528-543 MPa 0.2%YS and 555-589 MPa UTS) with the highest total strain (~23%). Whereas group 3 (SL and ST) specimens failed in a brittle manner with lower strength at room temperature, at 600°C the same orientations exhibited comparable strength (~ 483 MPa 0.2%YS and ~535 MPa UTS) as the other groups. As shown in Figure 1.8, all the orientations failed in a completely ductile manner with the total elongation as high as 23.5%. In all cases, the uniform elongation is quite low, varying between 1.1-2.3%. No delaminations were observed in any case. Since the overall strength and ductility are comparable at 600°C, an important conclusion is that NFA-1 exhibits nearly isotropic tensile behavior at higher temperature.

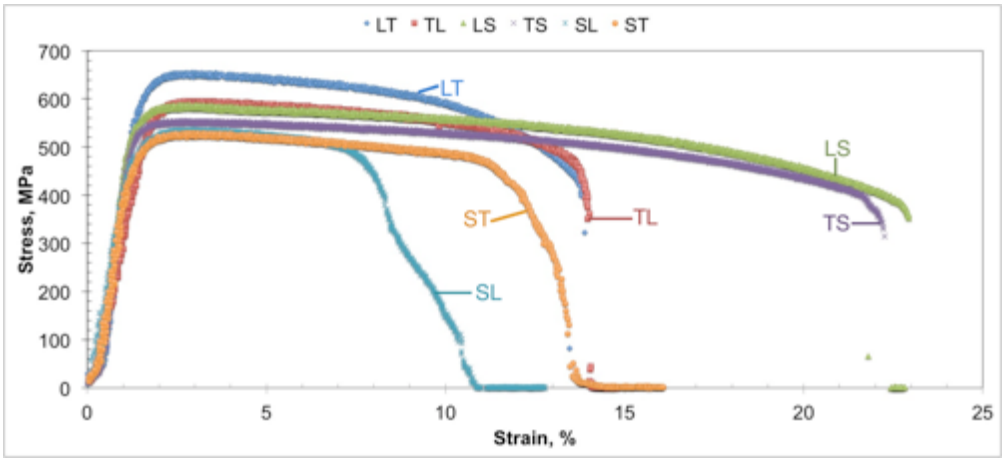

Fig. 1.7. Engineering stress-strain curves of NFA1 tensile specimens tested at 600oC all six orientations.

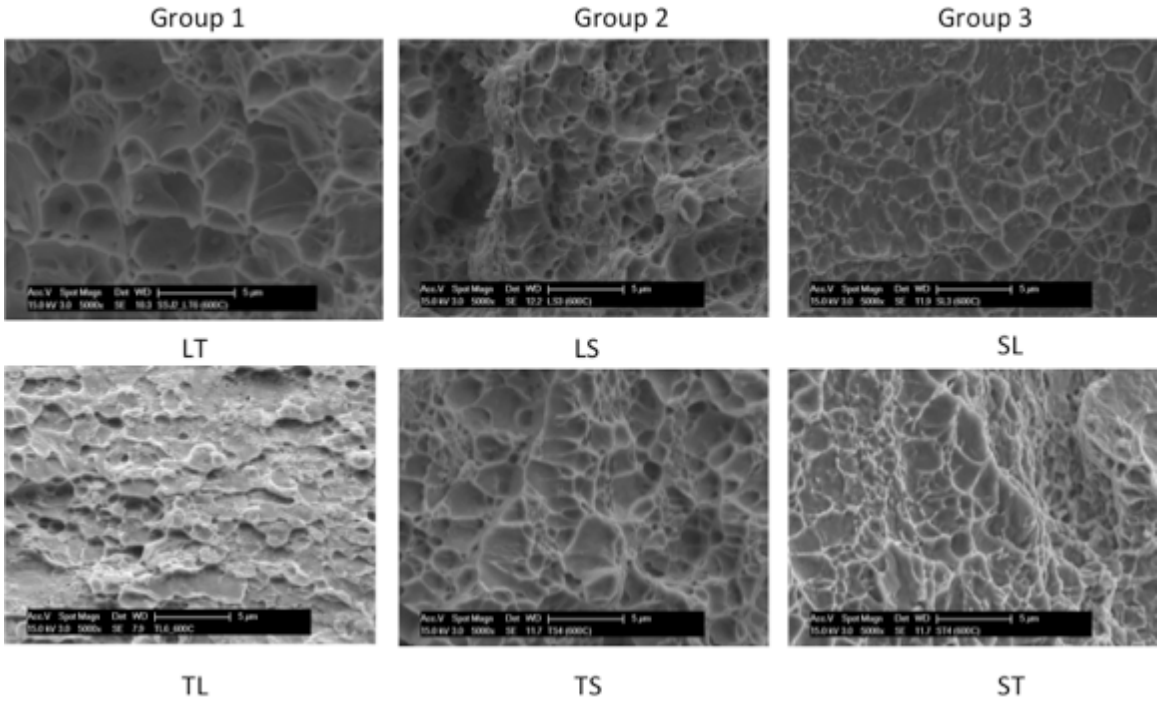

Fig. 1.8. High magnification (x5000) SEM fractographs of NFA-1 tensile specimen fracture surface at 600°C showing dimple like features in all six orientations.

The tensile properties were characterized in the strongest (LT) and the weakest (ST) orientations from ambient temperature to 800°C and the results are shown in Figs. 1.9 and 10, respectively. Figure 1.9a shows the typical stress-strain curves of LT specimens as a function of temperature and Fig. 9b summarizes the various tensile properties. It can be clearly seen that the strength was decreased with increasing temperature. However, the rate of change of strength is much lower below ≈ 500°C, followed by a sharp decrease from 500°C to 800°C. This might be due to associated with a transition to viscoplastic creep even at the high strain rate of 10^{-3}/s. The strength of the NFA1 material at LT orientation is still high (>250 MPa) at 800°C. Despite the high strength, the material also exhibited relatively high total elongation (10-18%) over the entire temperature range. The uniform and total elongation were almost constant up to 400°C and then followed by a decrease in the uniform elongation up to 700°C while total elongation increased to 18% at 800°C due to the viscoplastic creep behavior.

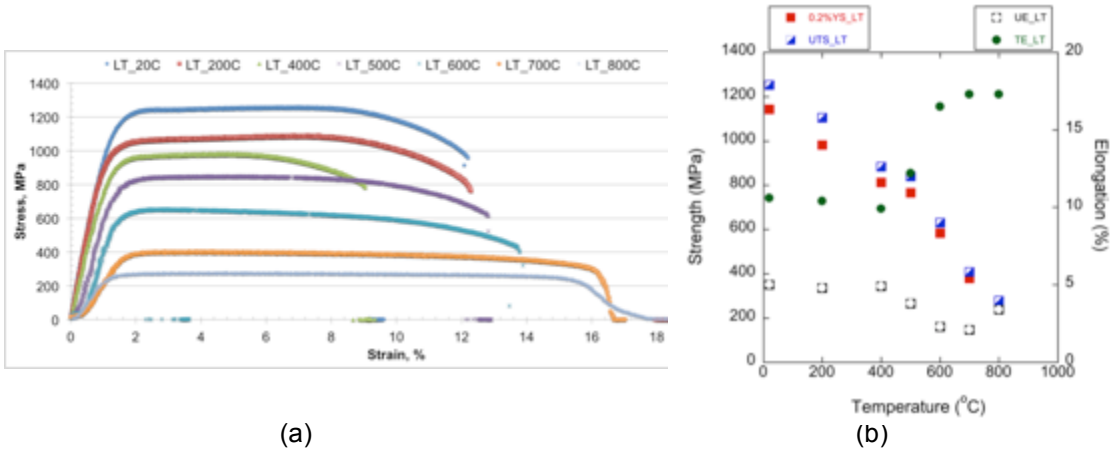

(a) (b)

Fig. 1.9. (a) Engineering stress-strain curves for the LT oriented NFA1 tensile specimens as a function of temperature, and (b) summary of their tensile properties.

Fig. 1.10a shows the tensile curves for the ST orientation. Fig. 1.10b plots the various corresponding tensile properties of ST oriented specimen as a function of temperature. A small amount of yielding and strain hardening is observed at 100°C that but the specimen again fails in a brittle manner. Significant strain occurred at 200°C with failure by ductile fracture. The maximum stress was similar in all three cases ranging from 850 to 900 MPa. The total elongation increased almost linearly with temperature, from 0.5% at ambient temperature to 16% at 800°C, while the corresponding uniform elongation increased from 0.5% at ambient temperature to 5% at 200°C, then decreasing up to 800°C. The low temperature behavior in the ST orientation can be rationalized by a ductile to brittle transition in the alloy matric toughness that permitted cleavage cracking only between ambient temperature and 100°C.

While not the topic of this report, the corresponding fracture toughness of NFA-1 is also strongly affected by the pre-existing cracks lying in planes parallel to the plat surface and normal to the thickness direction. In this case the delamination actually increase the fracture toughness. The fracture data are shown in Fig. 1.11 and discussed in some detail elsewhere [1]. We only briefly note that the enhanced toughness and very low ductile to brittle transition temperature In NFA-1 are due to the relaxation of high triaxial crack tip stresses upon delamination accompanied by a transition from a plane strain to a plane stress state condition.

Finally, creep rate and creep rupture time and ductility are also highly anisotropic and affected by the underlying deformation structure. However, as shown in Larson-Miller plot of the minimum creep rate shown in Figure 1.12, NFA-1 has a high temperature strength that is comparable to other similar alloys such as MA957.

Discussion and Summary

The tensile property of FCRD NFA1 material was fully characterized at six different orientations at varying temperature up to 800°C. In contrast to the LT orientation, NFA-1 failed in the brittle elastic region much at a much lower stress at ambient temperature when loaded in S (short) direction. The causes of this behavior are under investigation.

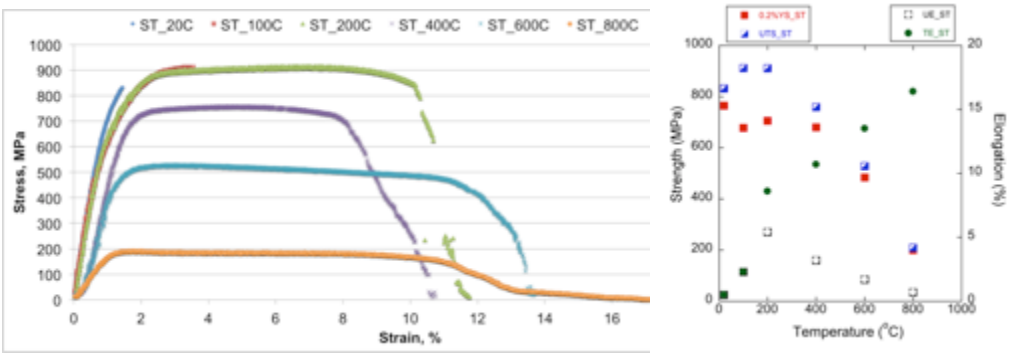

(a) (b)

Fig. 1.10. (a) Engineering stress-strain curves of ST oriented NFA1 tensile specimens as a function of temperature, and (b) summary of their tensile properties.

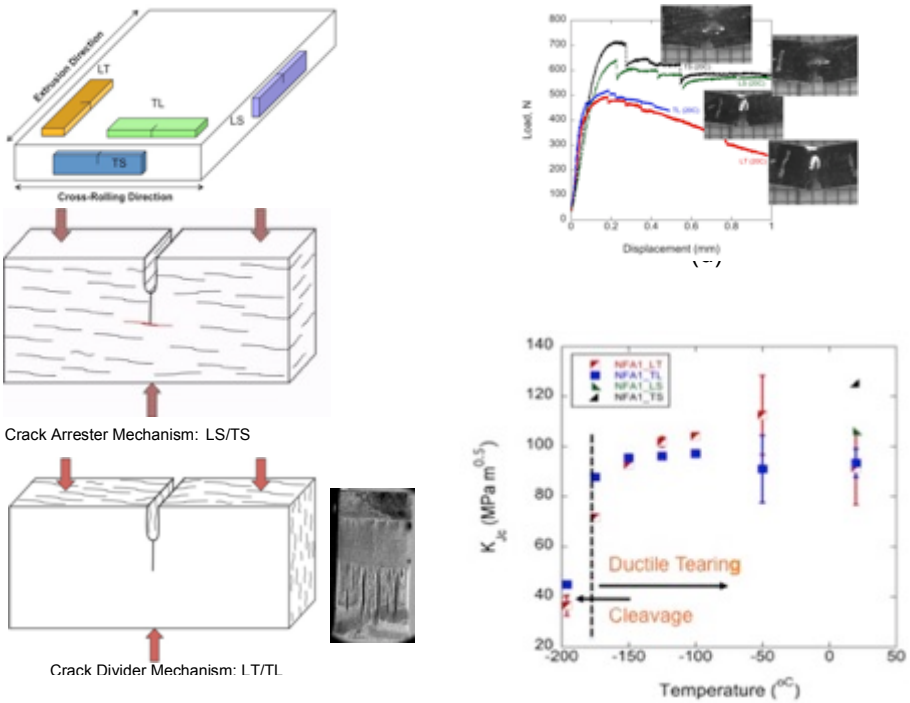

Figure 1.11. A pictorial summary pictorially illustrating the effect of delamination cracking on the fracture behavior of NFA-1 as discussed in more detail elsewhere [1]

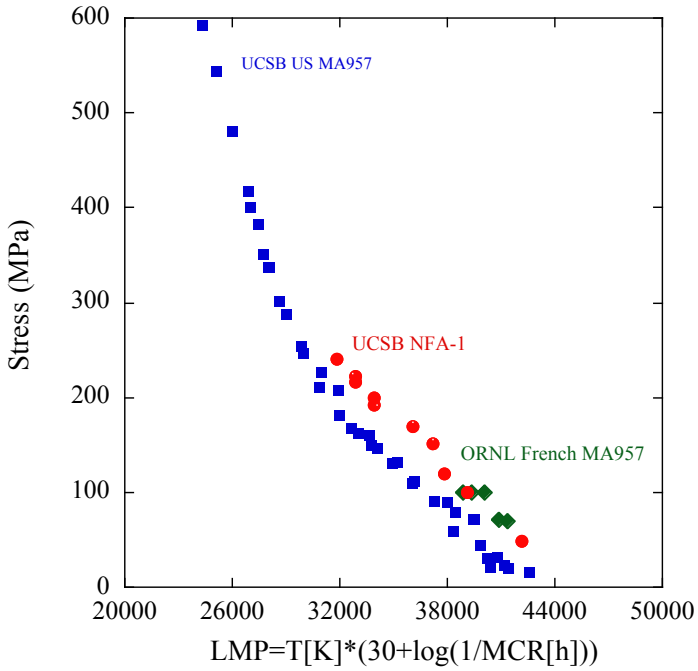

Figure 1.12. A comparison of the creep strength of NFA-1 with US and French heats of MA957 based on a Larson Miller minimum creep rate plot.

Acknowledgments

This work is part of a multi-laboratory collaboration between LANL, UCSB and ORNL. The DOE Office of Fusion Energy Sciences supported some of the mechanical testing reported here. NFA-1 was produced with the sponsorship of the DOE Office of Nuclear Energy under both a NEUP grant and the FCRD programs.

References

1. G.R. Odette, “Recent progress in developing and qualifying nanostructured ferritic alloys for advanced fission and fusion applications,” JOM. 66 (2014) 2427.

2. N.J. Cunningham, Y. Wu, G.R. Odette, D.T. Hoelzer, S.A. Maloy, “ Characterization of a larger best practice heat of 14YWT in annealed powder, HIP consolidated and extruded forms,” DOE/ER-0313/54 (2013), DOE Fusion Reactor Materials Program Semiannual Progress Report (2013).

CHAPTER 2: CRACK HEALING BY ANNEALING IN 14YWT NANOSTRUCTURED FERRITIC ALLOY, FCRD NFA-1

2.1 OBJECTIVE

The objective of this study is to explore the effects of annealing on the microstructural and mechanical properties of a newly developed larger best practice heat of 14YWT nanostructured ferritic alloy, NFA-1.

2.2 SUMMARY

FCRD NFA-1 is a new 14YWT nanostructured ferritic alloy (NFA) processed to form a 12.5 mm thick plate. Plane sections parallel to the broad plate surface have a nearly equiaxed, ultrafine grain structure. In contrast, the plane sections parallel to the narrow plate thickness side contain pancake shaped grains with a trimodal size distribution, including some that are very large, and a population of microcracks running normal to the thickness direction. At 23°C tensile specimens loaded in the short thickness direction have flat, faceted fracture surfaces and no ductility due to cleavage initiation of the microcracks. The corresponding tensile ductility increases with test temperature due to a brittle to ductile transition. A 1300°C/1h anneal appears to heal the microcracks, resulting in ductile fracture for short thickness direction axis loading. Annealing also appears to alter the grains and reduces the 23°C yield stress by ≈ 13%. Tensile tests at 600°C showed relatively isotropic properties in both conditions, and a smaller reduction in strength following annealing.

2.3. PROGRESS AND STATUS

2.3.1 Materials and Methods

The nanostructured ferritic alloys (NFAs) are a promising candidate alloy class for the advanced nuclear fission and future fusion reactor applications, since they have high tensile, fatigue and creep strengths over a wide range of temperature, as well as unique irradiation tolerance and outstanding thermal stability up to 1000°C. These attributes derive from the presence of submicron size grains, high dislocation densities and especially an ultrahigh population of nanometer size Y-Ti-O rich multifunctional nano-oxides (NO) [1]. NFA-1 was developed in collaboration between UCSB, ORNL and LANL to explore including Y in the Fe-14Cr-3W-0.4Ti-0.2Y melt prior to gas atomization by ATI Powder Metals (Pittsburgh, PA). However, the Y was phase separated after atomization. Thus a low interstitial alloy powder (15 kg) variant was ball milled for 40 hours with FeO (52.5 g) to increase the O content and to mechanically alloy the Y into solution. The milling was carried out by Zoz GmbH (Wenden, Germany) using a CM100b attritor mill with a ball mass-to-charge ratio of 10:1 and ball size of 5 mm. The milled powders were then consolidated at ORNL by hot extrusion at 850°C. The extruded bar was annealed for 1 hour and then hot cross-rolled to a ≈ 50% thickness reduction, both at 1000°C, to produce an ≈ 12.5 mm thick plate [2]. The as-fabricated plate has been extensively characterized as reported elsewhere [3]. Tensile specimens extracted from the plate wrapped in a molybdenum getter foil were annealed in a low pressure Ar environment at 1300°C for 1 h.

The as fabricated and annealed NFA-1 conditions were characterized using a scanning electron microscope (SEM) equipped with energy dispersive spectroscopy (EDS) and electron backscatter diffraction (EBSD) detectors. The tensile specimens were ground (to 1500 grit) and polished (to 20 nm colloidal silica), then etched with Kroll's reagent (92% distilled water, 6% nitric acid and 2% hydrofluoric acid) prior to examination in a FEI x30, Netherland SEM. Longest (l) and shortest (s) individual grain dimensions were tabulated from the SEM micrographs using 'ImageJ64' software. The effective grain diameter was taken as d = (l+s)/2 and the aspect ratio as r = l/s. EBSD was used to characterize the texture in the plate induced by hot extrusion and cross rolling. Vickers microhardness measurements

were performed on polished coupon surfaces at a 500g load using LECO M-400A semi-automated hardness tester, based on the average of 10 to 15 indents. Tensile tests were performed on flat dog-bone shaped sub-sized specimens with a gage section length, width and thickness of 5.0x1.2x0.5 mm^3. The tensile tests were performed for longitudinal (L), transverse (T) and short (S) thickness directions as illustrated in Fig. 2.1, at both room temperature and 600^oC, on a 810 MTS servo-hydraulic universal testing machine equipped with a clam shell furnace. The tensile specimens were sanded with 1500 grit to remove surface contamination, minor defects and local residual stresses due to the EDM used to fabricate them. The specimens were heated to the target temperature in atmosphere, and held for 10 minutes before testing. Loading was carried out at a crosshead speed of 0.30 mm/min, or a strain rate of ≈10^{-3}/s. Except for the small size of the specimens, the tensile properties were determined in accordance with ASTM Standard E8M-13. The fracture surfaces of the broken tensile specimens were extensively characterized by SEM.

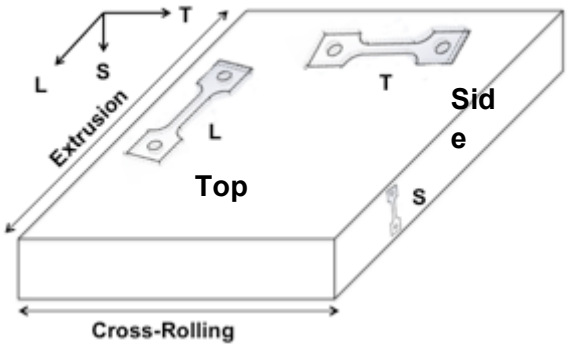

Figure 2.1. NFA-1 specimen orientations labeled with respect to the extrusion, cross-rolling and plate thickness directions.

2.3.2 Results and Discussion

Microstructure

Figs. 2.2a and d show SEM micrographs of the plate normal (L-T or top) view with nearly equiaxed, unimodal and ultrafine grains, in both the as fabricated and 1300^oC annealed conditions. The grains are ≈ 20% larger following annealing. Figs. 2.2b and c show that the as-fabricated L-S (side) plane contains a number of microcracks running on planes normal to the plate thickness direction. The corresponding grains are elongated and pancake-shaped with a tri-modal grain size distribution (many < 1 μm, some 1-10 μm and a few very large grains). As shown in Figs. 2.2e and f, microcracks are not observed in the L-S (side) view of the annealed specimens. Both the corresponding grain size and aspect ratio appear slightly smaller in the annealed versus as-fabricated condition. An EDS scan indicates the presence of Ti-rich precipitates in stringers along the extrusion direction. High temperature annealing appears to heal the cracks, presumably by surface diffusion, perhaps assisted by recrystallization and grain boundary migration [4].

Table 2.1 Grain morphology and microhardness of as-fabricated and 1300 ^{o}C annealed NFA1

Location, Condition	Grain Size (nm)	Aspect Ratio	Microhardness (Hv)
Top, as-fabricated	454 ± 142	1.2 ± 0.2	376 ± 18
Side, as-fabricated	(1077 ± 509) x (397 ± 124)	2.7 ± 1.1	352 ± 39
Top, annealed	705 ± 346	1.2 ± 0.4	294 ± 13
Side, annealed	(822 ± 516) x (341 ± 115)	2.4 ± 1.4	304 ± 17

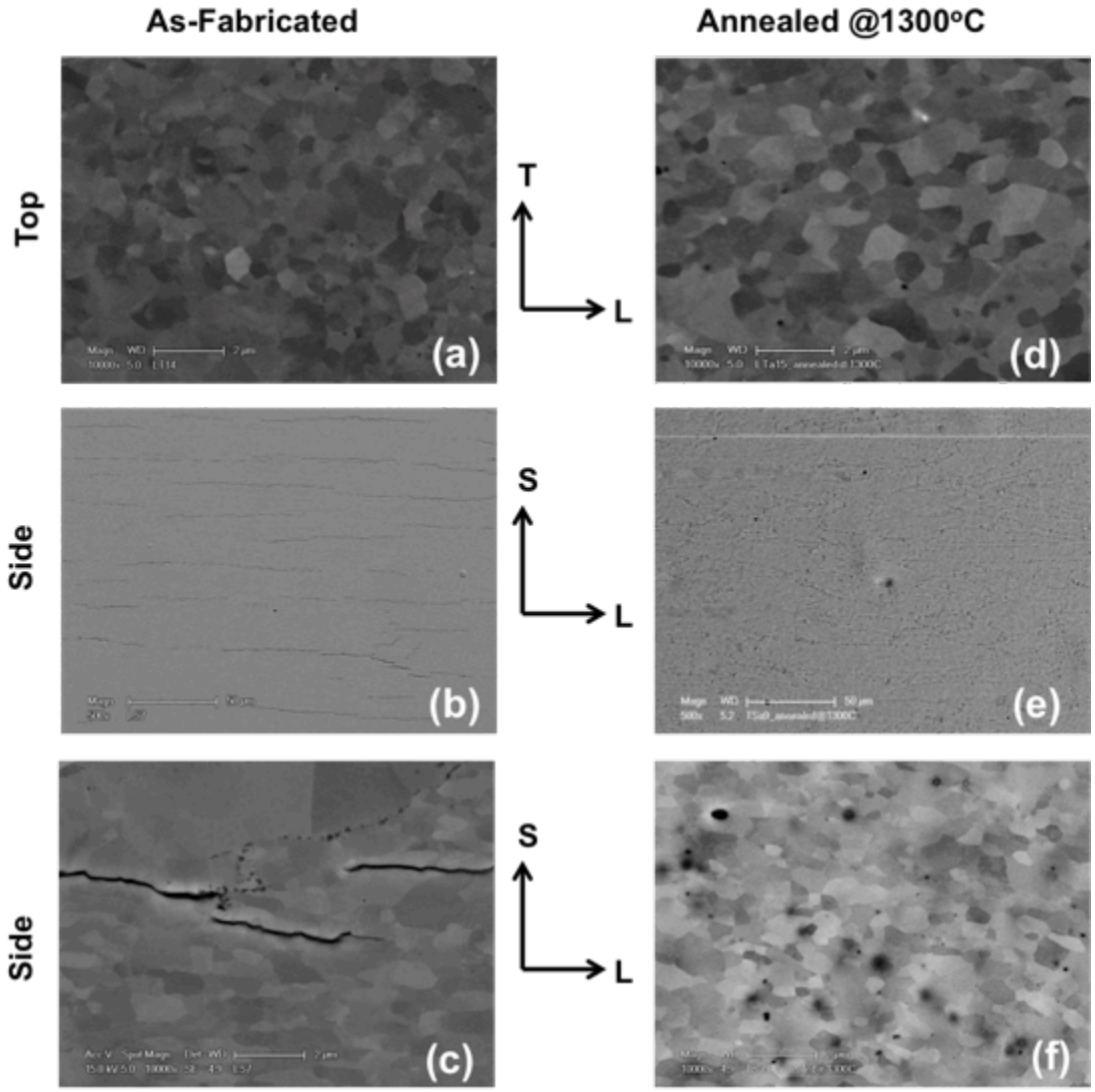

Figure 2.2. SEM images showing plate's: (a) top, and (b,c) side view morphology, respectively, for as-fabricated (left) and 1300 oC annealed samples (right).

Figure 2.3 shows EBSD inverse pole figure (IPF) maps for as-fabricated and annealed conditions with both top and side views. Subgrains and grains were characterized by > 3° (red) and > 15° (black) grain boundary misorientation angles. Consistent with the SEM observations, Fig. 2.3a shows small and nearly equiaxed grains in the plate's L-T (top) view, while Fig. 2.3b shows larger and grains elongated in the extrusion direction in the side views in the as-fabricated condition. Some very large and highly elongated grains are also observed, including one in the vicinity of a microcrack. Low angle grain boundaries are found inside the larger grains (marked as red). The IPF highlights the strong preferential crystallographic orientation of most of the grains with a <110> α-texture along the extrusion directions. As shown elsewhere [5], the texturing is accompanied by the development of (100) planes normal to the thickness direction, thus creating a corresponding (100)<110> texture, which is the most brittle cleavage system for bcc Fe. In combination with stress concentrations, this leads to the formation of the population of microcracks. In contrast, the side view of the annealed condition is crack-free, relatively equiaxed, untextured and bimodal grain distribution (Fig. 2.3d).

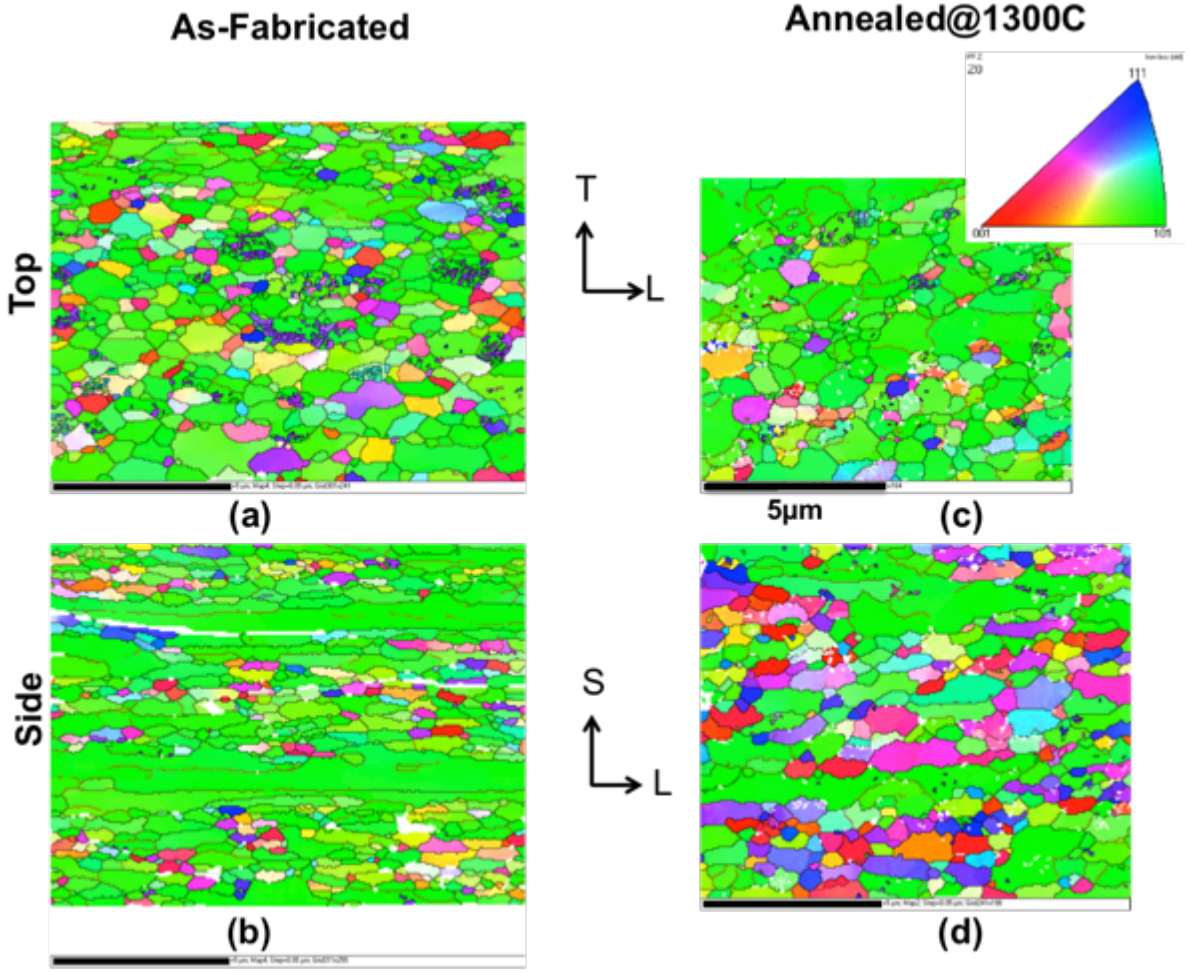

Figure 2.3. IPF maps obtained by EBSD for the as-fabricated condition (left) with a) top and b) side views; the corresponding IPF map for the annealed condition (right) with c) top and d) side views.

Microhardness

Vicker's microhardness (H_v) data for the NFA-1 are also summarized in Table 2.1. For the as-fabricated condition H_v averages 376 ± 18 (kg/mm^2) for the top surface and 352 ± 39 (kg/mm^2) for the side surface for specimens. These differences can probably be attributed to some coarsening of the NO and grains. The lower H_v and higher standard deviation for the side surface might be due to softening associated with delamination. The H_v is lower after annealing and similar for the two surfaces, with smaller standard deviations.

Tensile Properties

Fig. 2.4 shows engineering stress-strain s(e) curves from room temperature tensile tests in the three L, T and S orientations (see Fig. 2.1), for both the as-fabricated and annealed conditions. The as-fabricated L and T orientations have similar s(e), with 0.2% yield stress (YS) and ultimate tensile strength (UTS) values varying from 951-961 MPa and 1062-1082 MPa, respectively. The total elongations range from 12.8 to 15.3%. In contrast, the as-fabricated S orientation has the lowest strength with YS = UTS = 652 MPa, fracturing in the elastic region, without any plastic strain. The s(e) for the L and T oriented annealed condition are also similar to each other, with ≈ 14% lower strength than the as-fabricated condition. While the as-fabricated S oriented tensile specimen failed in the elastic region at room temperature, the corresponding annealed condition has a large total elongation of ≈ 18%, with slightly higher YS ≈ 700 MPa and a significantly higher UTS of ≈ 874 MPa compared to the as fabricated condition. The strength and ductility for annealed condition in the S orientation is comparable to the annealed L and T oriented specimens. These improvements in strength and ductility are associated with the absence of microcracks (Table 2.1 and Fig. 2.2). The lower YS in this case is due to a lower stress marking the deviation form the elastic loading line. But this may be an experimental artifact since all three orientations have otherwise very similar s(e) curves.

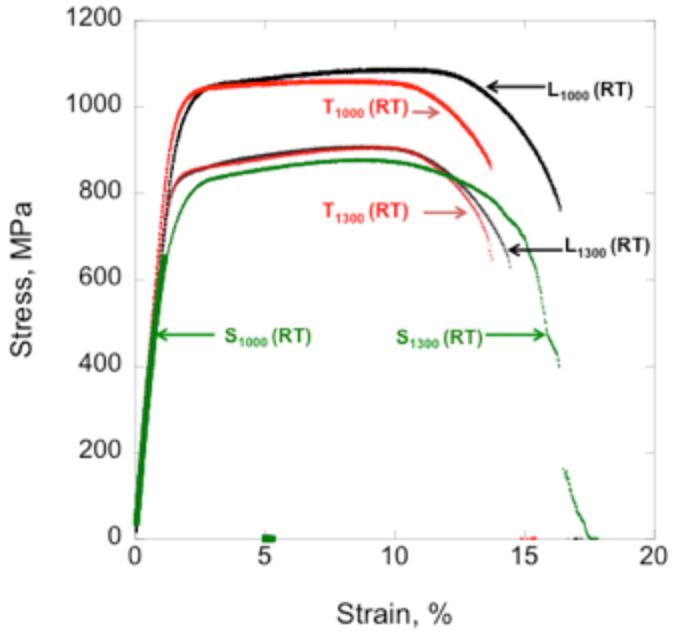

Figure 2.4. Room temperature engineering stress-strain curves of as-fabricated (1000°C) and annealed (1300°C) NFA-1 specimens tested in three different orientations.

Figs. 2.5 and 2.6 show the fracture surfaces of the broken tensile specimens. Delaminations occurred in both the as-fabricated condition L and T specimens normal to the thickness direction in planes parallel to the plate surfaces. In contrast, the annealed condition is delamination-free. Again the fracture surface is flat and brittle for the S orientation in the as-fabricated condition, in contrast to fully ductile fracture in the annealed condition. Corresponding higher magnification images in Fig. 2.6 show ductile dimples in the all of the annealed conditions along with shallow crater-like features, which might be partly responsible for lower strength along with higher grain size compared to the as-fabricated specimens. The crater like features may partially healed microcracks.

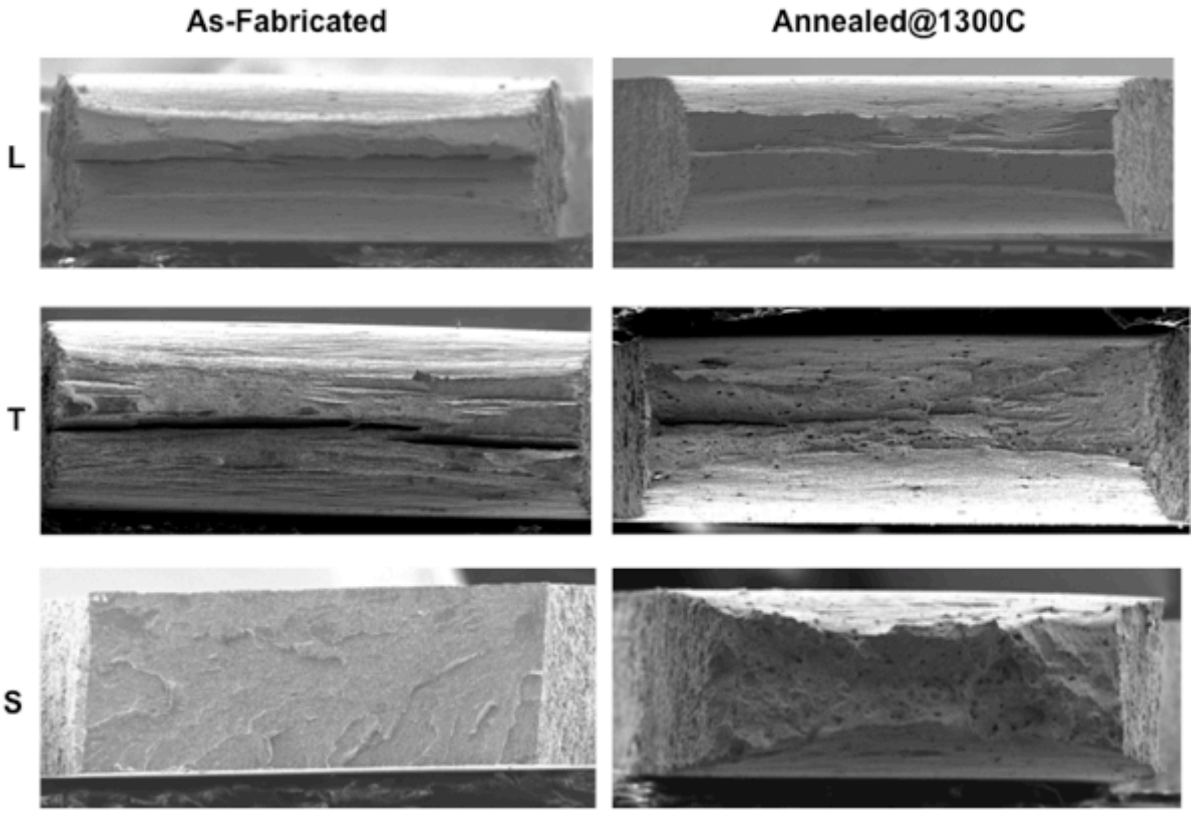

Figure 2.5. Low magnification SEM fractographs of room temperature as-fabricated and annealed tensile fracture surfaces for different orientations.

Fig. 2.7a shows the s(e) for tensile test on annealed T and S oriented specimens at 600^{o}C. Both the strength (YS and UTS) and ductility decrease at higher temperature. In both cases, the uniform elongations are quite low (~1.3%) compared to at room temperature (7-8%). However, the annealed specimens retained significant strength levels of YS = 432-489 MPa and UTS = 469-502 MPa, and ductility, with total elongation strains of 9-10%. This compares to corresponding as-fabricated strength and ductility values of YS ≈ 484-547 MPa, UTS ≈ 529-580 MPa and total elongation strains of 13.5-

14.4%. As seen in Fig. 2.7b, no delaminations are observed in the annealed condition. Relatively flat fracture surfaces were observed for both T and S orientations with reductions in area of ≈31% and ≈12%, respectively. Higher magnification SEM images in Fig. 2.7c, show dimples associated with coarser oxide particles in both cases, along with crater-like features. However, the dimples for the S orientation appear to be composed of larger and smaller features. The larger features are filled with small dimples on their sidewalls. Note the surfaces are oxidized during high temperature testing. In the annealed condition L, T and S orientations strength and ductility values are comparable both for the room temperature and 600°C tests. Thus NFA-1 exhibits nearly isotropic behavior when annealed at 1300°C.

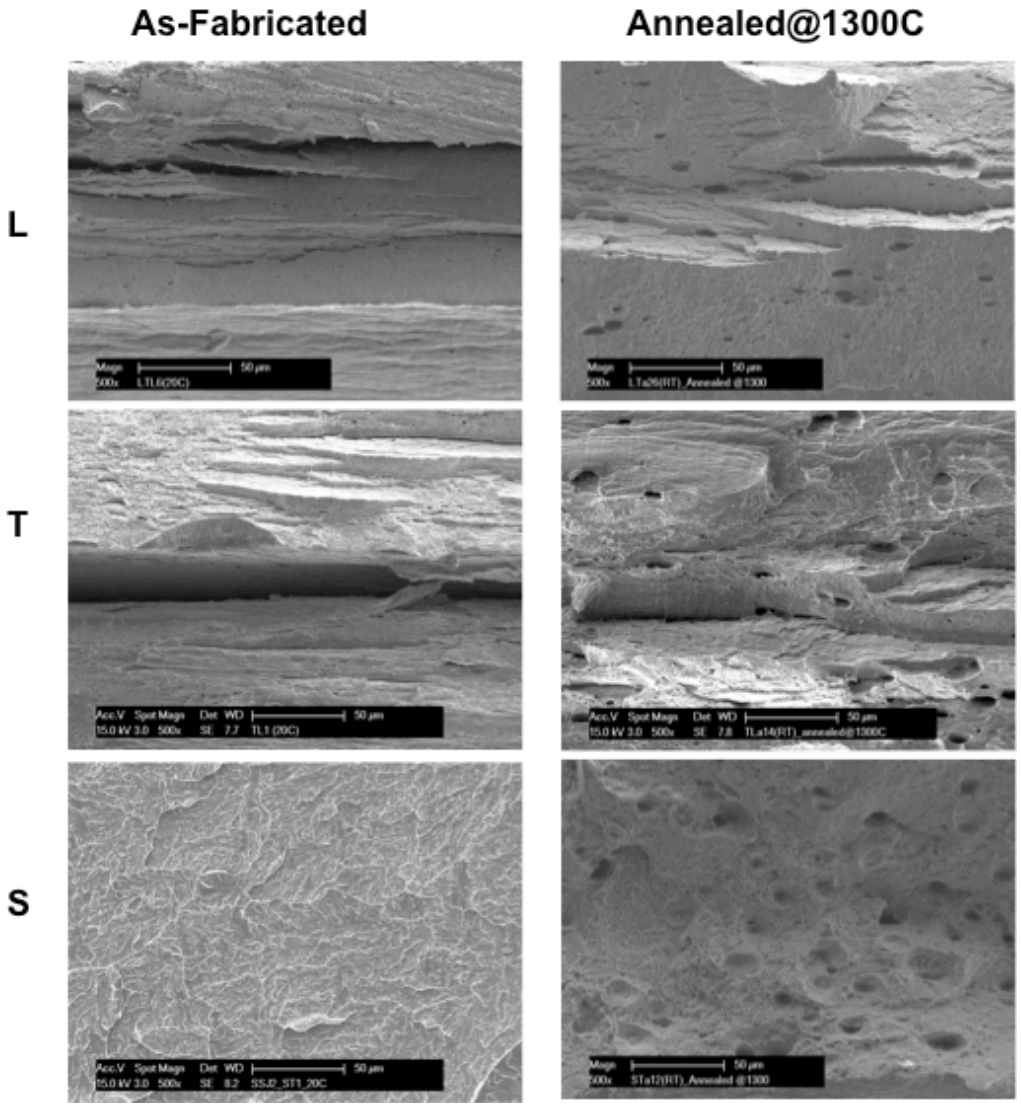

Figure 2.6. High magnification SEM fractographs of room temperature as-fabricated and annealed tensile fracture surfaces at different orientations.

2.3.3 Summary and Future Work

The effect of annealing 1300°C for 1 h on as-fabricated NFA-1 was characterized in terms of grain structures, microcracks, microhardness and tensile properties. High temperature annealing appears heal the microcracks that exist in the as-fabricated plate. Annealing also increases the average grain size by ≈ 20% reduces both the microhardness by ≈ 18% and room temperature tensile YS and UTS by ≈ 13% lower. The room temperature tensile properties are more isotropic after annealing.

The effect of different annealing temperatures and times will be explored and more detailed observations on microcrack healing will be obtained along with the corresponding effects on the grain, dislocation and NO nanostructures will be characterized. Mechanical property measurements will be extended to fracture toughness.

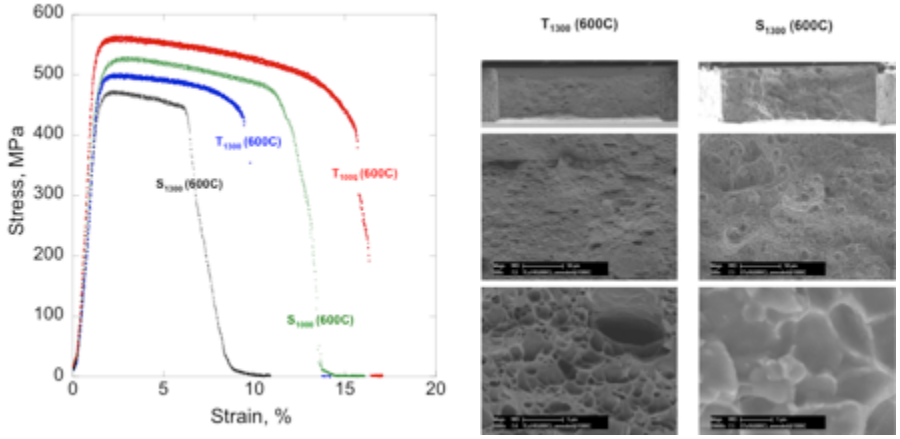

(a) (b)

Figure 2.7. (a) Engineering stress-strain curves of annealed specimens tested at 600oC, and (b) their SEM fractographs.

REFERENCES

[1] G.R. Odette, “Recent progress in developing and qualifying nanostructured ferritic alloys for advanced fission and fusion applications,” JOM. 66 (2014) 2427.

[2] N.J. Cunningham, Y. Wu, G.R. Odette, D.T. Hoelzer, S.A. Maloy, “ Characterization of a larger best practice heat of 14YWT in annealed powder, HIP consolidated and extruded forms”, Fusion Materials Semiannual Progress Report for Period Ending June 30, 2013, DOE/ER-0313/54, U. S. Department of Energy, 15.

[3] M.E. Alam, K. Fields, G. R. Odette, D. T. Hoelzer and S. A. Maloy, “Tensile property characterization of 14YWT nanostructured ferritic alloy NFA1” Fusion Materials Semiannual Progress Report for Period Ending December 31, 2014, DOE/ER-0313/57, U. S. Department of Energy, 39.

[4] K.W. Gao, L.J. Qiao, and W. Y. Chu, “In situ TEM observation of crack healing in □α-Fe”, Scripta Materialia, 44 (2001) 1055.

[5] A. G. Junceda, M. H. Mayoral and M. Serrano, “ Influence of the microstructure on the tensile and impact properties of a 14Cr ODS steel bar”, Materials Science and Engineering A, 556 (2012) 696.

CHPATER 3: MICROSTRUCTURAL AND MECHANICAL BEHAVIOR OF AS-FABRICATED AND ANNEALED 14YWT NFA-1 ALLOY – M.E. Alam, S. Pal, D. Gragg, G. R. Odette (UCSB), D. T. Hoelzer (ORNL) and S. A. Maloy (LANL)

3.1 OBJECTIVE

The objective of this study is to perform statistical analysis of grains, precipitates and microcracks of as-fabricated 14YWT FCRD NFA-1 material, and also to explore the effects of annealing on the microstructural and mechanical properties on it.

3.2 SUMMARY

FCRD NFA-1 is a new 14YWT nanostructured ferritic alloy (NFA) processed to form a 12.5 mm thick plate. Ultrafine, nearly equiaxed grains dominate the plate's face (LT), while the front (LS) and side (TS) views contain pancake-shaped, trimodal grains with very large aspect ratios, along with a population of embedded microcracks that are readily visible in profile. Low temperatures tensile test on longitudinal (L) direction shows a delamination driven ductile fracture, even at liquid nitrogen temperature, with strengths up to 1563 MPa. In contrast, the room temperature tensile specimen loaded in the short thickness (S) direction fails prematurely in its elastic regime, with a flat, faceted fracture surface. Annealing at 1300^{o}C for 1 and 5 hrs helps to alter the grains towards equiaxed in all plane views, heals the microcracks that results in much improved room temperature tensile ductility. However, microhardness, tensile strength and fracture toughness have been compromised, and the fracture mechanism has also been changed from delamination driven to microvoid coalescence dimple fracture.

3.3 PROGRESS AND STATUS

3.3.1 Materials and Methods

The nanostructured ferritic alloys (NFAs) are a promising candidate alloy class for the advanced nuclear fission and future fusion reactor applications, since they have high tensile, fatigue and creep strengths over a wide range of temperature, as well as unique irradiation tolerance and outstanding thermal stability up to 1000°C. These attributes derive from the presence of submicron size grains, high dislocation densities and especially an ultrahigh population of nanometer size Y-Ti-O rich multifunctional nano-oxides (NOs) [1]. NFA-1 was developed in collaboration between UCSB, ORNL and LANL to explore including Y in the Fe-14Cr-3W-0.4Ti-0.2Y melt prior to gas atomization by ATI Powder Metals (Pittsburgh, PA). However, the Y was phase separated after atomization. Thus, a low interstitial alloy powder (15 kg) variant was ball milled for 40 hours with FeO (52.5 g) to increase the O content and to mechanically alloy the Y into solution. The milling was carried out by Zoz GmbH (Wenden, Germany) using a CM100b attritor mill with a ball mass-to-charge ratio of 10:1 and ball size of 5 mm. The milled powders were then consolidated at ORNL by hot extrusion at 850°C. The extruded bar was annealed for 1 hour and then hot cross-rolled to an ≈ 50% thickness reduction, both at 1000°C, to produce an ≈ 12.5 mm thick plate [2]. The basic microstructural and mechanical properties of the as-fabricated plate have been reported elsewhere [3-4]. However, due to the anisotropic nature of the plate along with through-thickness grain variation, the measured grain size of three different planes (face: LT, front: LS and side: TS, see Fig. 3.1) were found inconsistent since the specimens were selected randomly. Therefore, in this present study, a 5mm 5mmx5mm cube has been EDM cut from the middle of the plate thickness and grain size of all three plane views were characterized. In detail crack statistics as well as processed induced impurities were also analyzed. Low temperature tensile tests were performed. Later, as-fabricated specimens from the

plate were wrapped in a molybdenum getter foil and annealed in vacuum at 1300°C for 1 hr and 5 hrs. Microstructural and mechanical characterizations were also performed on the annealed specimens.

Metallurgically ground (up to 1500 grit sand paper) and polished (up to 20 nm colloidal silica) as-fabricated and annealed specimens were observed in scanning electron microscope (SEM, FEI x30) equipped with energy dispersive spectroscopy (EDS) to characterize the pre-test surface morphology. Polished samples were then etched with Kroll's reagent (92% distilled water, 6% nitric acid and 2% hydrofluoric acid) prior to image for grains using SEM and dual beam Scanning Electron Microscope/Focused Ion Beam (SEM/FIB, FEI Helios 600). Longest (l) and shortest (s) dimensions of ~ 500 individual grains from each planes were tabulated from the micrographs using 'ImageJ64' software. The effective grain diameter was taken as d = (l+s)/2 and the aspect ratio as r = l/s. Coarser precipitates were identified using both the SEM and transmission electron microscopy (TEM), equipped with EDS. SEM images were used to measure the average precipitate size, inter-precipitate spacing and stringer spacing. Precipitates were found to be arranged in stringers, rather than random. Therefore, the inter-precipitate spacing along the stringer and stringer spacing along the thickness was considered. Microcracks were also characterized in terms of crack width, crack separation distance, crack length and number density of crack per unit area. Relatively low magnification (x1000) SEM images were chosen to characterize the crack length and their number. Vickers microhardness measurements were performed on polished coupon surfaces at a 500g load using LECO M-400A semi-automated hardness tester, based on the average of 10 to 15 indents. Tensile tests were performed on flat dog-bone shaped sub-sized specimens with a gage section length, width, and thickness of 5.0x1.2x0.5 mm^3. The tensile tests were performed for the as-fabricated longitudinal (L) directions as illustrated in Fig. 1, from room temperature down to liquid nitrogen temperature, on a 810 MTS servo-hydraulic universal testing machine equipped with a cooling chamber. Controlled liquid nitrogen-air mixture was injected into the cooling chamber to achieve the targeted cryogenic temperature, and held for 30 to 45 minutes before testing. However, both L and short (S) oriented as-fab and annealed tensile specimens were tested at room temperature. The tensile specimens were sanded with 1500 grit to remove surface contamination, minor defects and local residual stresses due to the EDM used to fabricate them. Loading was carried out at a crosshead speed of 0.30 mm/min, or a strain rate of $\approx 10^{-3}$/s. Except for the small size of the specimens, the tensile properties were determined in accordance with ASTM Standard E8M-13. Fracture toughness tests of as-fabricated and annealed specimens were conducted at room temperature on the L-T oriented fatigue pre-cracked single-edged notch three point bend (3PB) bar specimens with nominal dimensions of 16 mm in length, 3.3 mm in width and 1.65 mm in gross thickness and a/W ≈ 0.5. Same 810 MTS servo-hydraulic testing machine was used for this purpose. The toughness (K_{Jc}) was calculated at the maximum load. Fracture surfaces of the broken tensile and toughness specimens were extensively characterized by SEM.

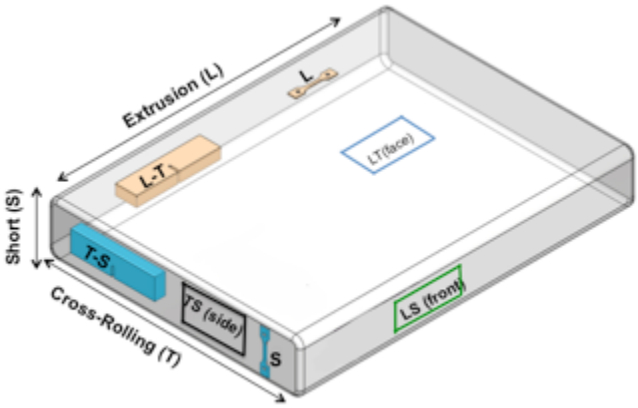

Figure 3.1. NFA-1 specimen orientations labeled with respect to the extrusion, cross-rolling and plate thickness directions.

3.3.2 Results and Discussion

Microstructure

The microstructure of the as-fabricated FCRD NFA-1 material has been characterized in terms of: (a) grain morphology, (b) presence and distribution of coarser precipitates, and (c) crack statistics at all three different planes (see Tables 3.1 to 3 and Figs. 3.1 to 3). Figures 2a and b show the low magnification SEM, and high magnification SEM/FIB images of the as-fabricated and pre-test NFA-1 at different planes, respectively. Plate's face (LT) reveals crack or pore free surface. High magnification SEM/FIB images also characterize nearly uniform, equiaxed and ultrafine grain morphology of the corresponding plane (see Table 3.1). In contrast, the front (LS), and side (TS) views reveal a number of microcracks embedded on planes normal to the plate thickness direction. The corresponding plane's grains are elongated and pancake-shaped that oriented parallel to the extrusion (LS) or cross-rolling (TS) direction with a tri-modal grain size distribution (many are <1μm, some are 1-10 μm and few are >10 μm, see Fig. 3.3a). Through thickness grain size variation has also been observed. Relatively smaller grains are found near the top and bottom of the plate's thickness while the larger grains at the middle.

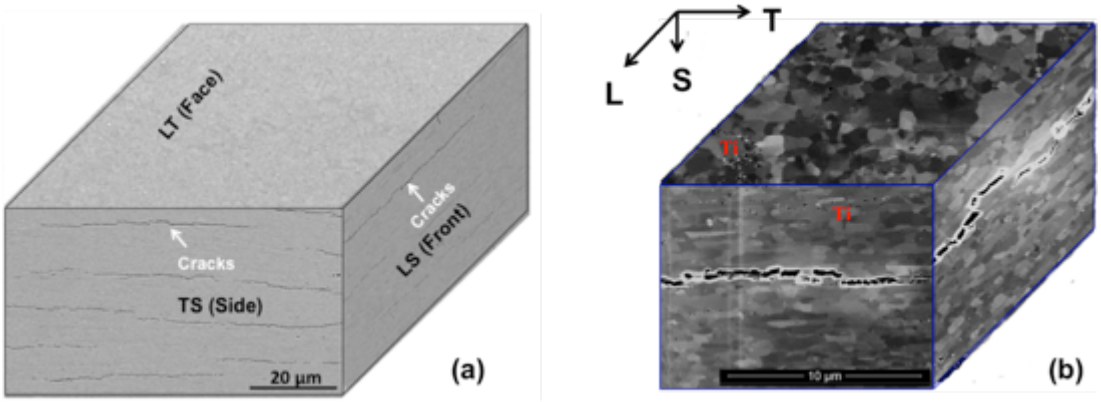

Figure 3.2. Different plane views of the as-fabricated NFA-1 plate captured by: (a) SEM at low magnification, and (b) SEM/FIB at high magnification.

Table 3.1 Grain morphology and hardness of as-fabricated NFA-1 specimens

Planes	Long, l (μm)	Short, s (μm)	Avg, d= l+s)/2 (μm)	Aspect ratio, r = l/s	Microhardness, HV, (Kg/mm^2)
LT (Face)	0.767 ± 0.566	0.517 ± 0.355	0.642 ± 0.450	1.5 ± 0.4	376 ± 18
LS (Front)	0.792 ± 0.638	0.301 ± 0.108	0.546 ± 0.343	2.7 ± 1.6	368 ± 25
TS (Side)	0.799 ± 0.833	0.296 ± 0.180	0.548 ± 0.482	2.7 ± 1.3	352 ± 39

Despite having uniformly distributed Y-Ti-O rich nano-oxides (NOs) (size: 2.1 nm, number density: 1.6 x 10^{23} m^{-3} and volume fraction: 0.25%) all over the NFA-1 matrix, reported elsewhere [2], the material also reveals the presence of relatively coarser precipitates (Figs. 3.2b and 3b) in the matrix, and summarizes in Table 3.2. These precipitates are predominantly located at or near the grain boundaries in a form of stringers (Fig. 3b). EDS equipped with SEM and TEM, identify them mostly as Ti-rich (darker) with some as Y-rich (relatively gray) oxides [5]. These stringers are oriented randomly at the plates' face but parallel to the extrusion or cross-rolling direction at the front and side views, respectively, with an average stringer separation distance 2.6 to 2.8 μm (Table 2 and point 1 of Fig. 3.3b). Average precipitate size is measured ≈60 nm, with a range varies between 10 nm and 262 nm. Fig. 3.3c shows the distribution of coarser precipitate size. Table 2 also summarizes the spacing among the precipitates that averaged ~ 200 to 300 nm.

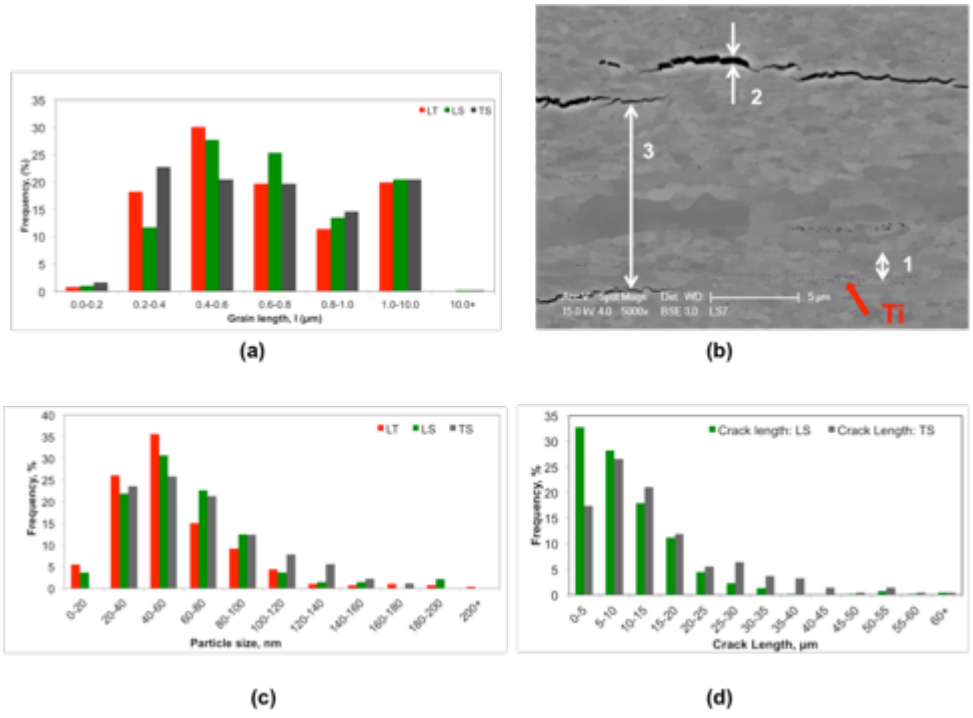

Figure 3.3. (a) Distribution of grain's length, l, (b) point 1, 2 and 3 showing the inter-stringer spacing, crack width and crack separation distance, respectively, (c) coarser particle size distribution, and (d) crack length distribution of as-fabricated NFA-1 plate at different plane views.

Table 3.2 Ti/Y rich precipitates of as-fabricated NFA-1

Planes	Ti/Y rich particle size (nm)	Interparticle spacing along x (nm)	String spacing along thickness (μm)
LT (Face)	57 ± 33	228 ± 106	Random
LS (Front)	62 ± 32	303 ± 210	2.6 ± 1.0
TS (Side)	68 ± 33	279 ± 160	2.8 ± 1.0

Fig. 3.2 also shows the presence of microcracks running normal to the plate thickness direction both for the front (LS) and side (TS) plate views and their statistics are summarized in Table 3.3. The micromechanism of these crack formation has been reported elsewhere [5]. The average crack width (point 2 in Fig. 3.3b), which is believed to be the initiation of crack front, is ~250 nm. The crack separation distance is measured between the layers of crack in the short thickness direction (point 3 in Fig. 3.3b) and found almost same (~16μm) for both the front and side views. Length of the cracks is also recorded and averaged ~10μm (front) to 15μm (side) with a span ranges from 2μm to 105μm. Smaller cracks might join together to form the larger cracks. In some cases, cracks are separated by a very small ligament (<1μm) and might have minimal resistance during loading, and thus considered as a single large crack. Fig. 3.3d shows almost similar crack size distribution for both front and side planes and found ~75% cracks are below 15μm with very few are over 50μm. Nevertheless, these larger cracks supposed to serve as weaker links during fracture. The number density of crack is also measured and found 2.5 times higher at the front than the side plane.

Table 3.3 Side surface crack statistics of as-fabricated NFA-1

Planes	Crack opening width (nm)	Crack separation distance (μm)	Crack length (μm)	Crack density (m^{-2})
LS (Front)	252 ± 142	16.3 ± 4.7	10.2 ± 8.9	3.45×10^9
TS (Side)	205 ± 130	15.2 ± 4.8	14.9 ± 12.6	1.34×10^9

Since the front and side plate view shows almost similar microstructural features for as-fabricated conditions, only the plates' side view (TS) has been considered for annealing along with its face (LT) view. Fig. 3.4 and Tables 3.4 and 3.5 show the grain morphology and statistics of the face and side planes after annealing at 1300^{o}C for 1hr and 5 hrs. Results show that the introduction of annealing (1300 ^{o}C/1hr) increases the grain size up to 10%, which further increases with time (5hrs) ≈ 25% when compared with the as-fabricated condition. Aspect ratio of the side plane reduces from 2.7 for the as-fabricated condition to 1.8 for annealed at 1300^{o}C/5h condition (Table 3.5). Grains larger than 10μm were also not observed for any annealed specimen. Higher annealing temperature might recrystallize the larger grains. High temperature annealing also appears to heal the cracks, presumably by surface diffusion, perhaps assisted by recrystallization and grain boundary migration [6]. However, crater-like pores were observed in all the annealed specimens, and the size of these pores increases (with number decreases) with annealing time.

Table 3.4 Grain morphology and hardness of NFA-1 as a function of annealing condition and plate views

Planes*	Long, l (μm)	Short, s (μm)	Avg, d= l+s)/2 (μm)	Aspect ratio	Microhardness, HV, (Kg/mm^2)
LTa131	0.842 ± 0.493	0.547 ± 0.285	0.695 ± 0.367	1.6 ± 0.4	294 ± 13
TSa131	0.849 ± 0.544	0.354 ± 0.144	0.602 ± 0.320	2.4 ± 1.3	304 ± 17
LTa135	0.979 ± 0.481	0.694 ± 0.325	0.837 ± 0.390	1.4 ± 0.4	252 ± 7
TSa135	0.963 ± 0.371	0.537 ± 0.197	0.750 ± 0.266	1.8 ± 0.5	247 ± 13

*LT: As-fabricated, LTa131: Annealed at **1300**°C for **1** hr, LTa135: Annealed at **1300**°C for **5** hrs

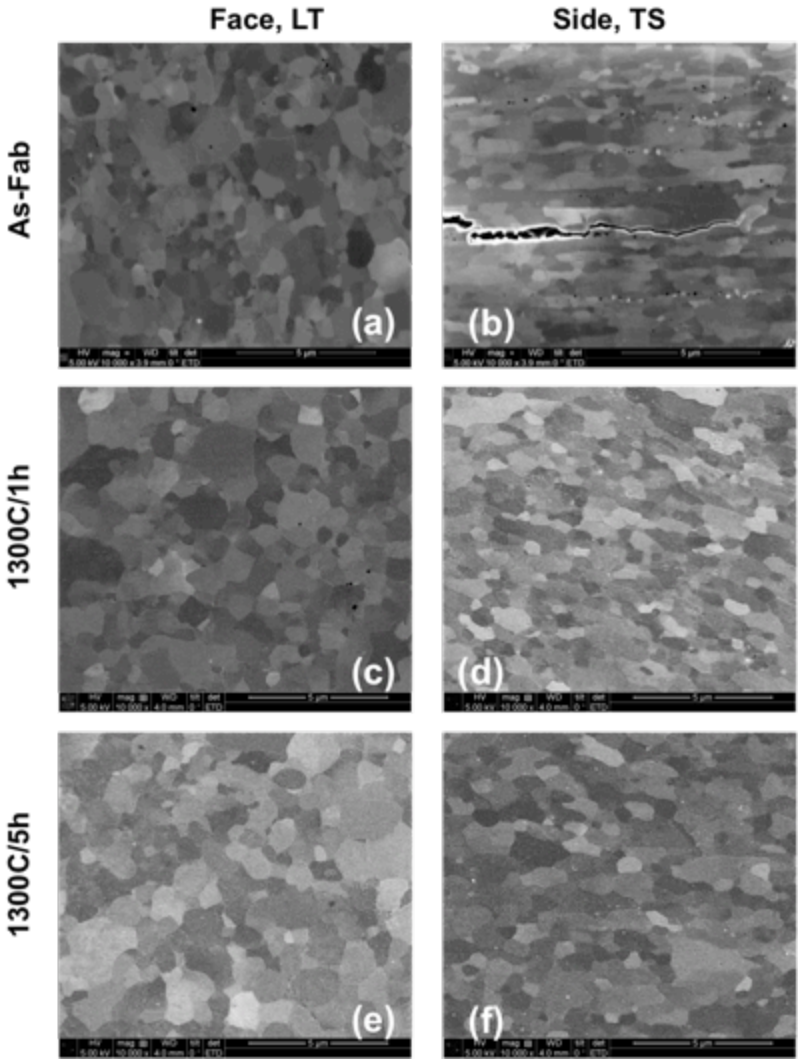

Figure 3.4. SEM/FIB images of the as-fabricated (a,b) and annealed (c-f) NFA-1 specimens for face (left column), and side (right column) planes, respectively.

Microhardness

Vicker's microhardness (H_v) data for the as-fabricated and annealed NFA-1 are summarized in Tables 3.1 and 3.4, respectively. H_v averages 376 ± 18 (kg/mm^2) and 352 ± 39 (kg/mm^2) when indented at face and side plane, respectively. Hardness reduces ≈30% with the annealing for 1300^{o}C/5hr. These differences can probably be attributed to the presence of pores and grain coarsening. However, unlike as-fabricated condition, hardness variation among different planes is negligible for annealed specimen.

Table 3.5 Grains aspect ratio, number and area fraction as a function of plates view, for as-fab and annealed conditions

Planes	Range (μm)	Length, l (μm)	Aspect ratio, r	No. freq. of grains, (%)	Area fraction, (%)
	0-1	0.57 ± 0.20	1.5 ± 0.4	80	60
LT (Face)	1-10	1.57 ± 0.80	1.6 ± 0.4	20	40
	10+	-	-	-	-
	0-1	0.60 ± 0.19	2.2 ± 0.7	79.3	64.6
LS (Front)	1-10	1.42 ± 0.50	4.5 ± 2.0	20.5	33.2
	10+	11.3	15.8	0.2	2.2
	0-1	0.56 ± 0.22	2.2 ± 0.9	79.3	59.5
TS (Side)	1-10	1.59 ± 0.94	4.1 ± 1.5	20.5	37.9
	10+	12.94	10.0	0.2	2.6
	0-1	0.63 ± 0.19	1.5 ± 0.4	72.6	56
LT131 (face)	1-10	1.40 ± 0.60	1.8 ± 0.6	27.4	44
	10+	-	-	-	-
	0-1	0.60 ± 0.20	2.0 ± 0.7	72.8	55.2
TS131 (side)	1-10	1.51 ± 0.61	3.5 ± 1.7	27.2	44.8
	10+	-	-	-	-
	0-1	0.71 ± 0.19	1.4 ± 0.4	61.1	45.2
LT135 (Face)	1-10	1.39 ± 0.50	1.5 ± 0.3	38.9	54.8
	10+	-	-	-	-
	0-1	0.72 ± 0.16	1.7 ± 0.4	59	45.6
TS135 (Side)	1-10	1.31 ± 0.29	2.0 ± 0.5	41	54.4
	10+	-	-	-	-

Tensile Properties

Results of low temperature uniaxial tensile test on L oriented specimens are shown in Table 3.6 and their engineering stress-strain s(e) curves at Fig. 3.5. Unlike most of the metallic materials, the NFA-1 material shows a concurrent increase in strengths and ductilities (except at -196^{o}C) at subzero temperatures. For example, ~32% higher yield strength (YS) and ~65% higher uniform elongation (UE) has been observed for -150^{o}C when compared to room temperature test. This exceptional phenomenon can be attributed to the presence of microcracks that creates delamination during the test (see Fig. 3.6a). This delaminations splits the thickness of the tensile specimen even smaller and drive them towards plane stress condition, and thus, suppress the effect of friction stress or Peierls force. Strengths continue to increase (1469 MPa YS and 1563 MPa UTS) at liquid nitrogen temperature, while both the uniform and total elongation decreases to 1.0% and 8.4%, respectively. Relatively lower ductility at -196 ^{o}C might be due to the activation of Peierls stress, which might take control over delamination, or it might only happen to this particular specimen. Low magnification fracture image for -196^{o}C, shown in Fig 3.6a, shows relatively shiny fracture surface. Nevertheless, higher magnification images of the fractured specimens tested at all different temperatures reveals almost identical flake-like shallow dimples, attributed for ductile tearing (Fig. 3.6b). It is worth noting that the NFA-1 material showed remarkably low ductile brittle transition temperature (≈ -185 ^{o}C), reported previously [3], which makes the NFA-1 material to achieve near record strength-toughness combination. In contrast, The S tensile specimen tested at room temperature fails in a complete brittle manner, mostly in its elastic zone, with almost 0% ductility. The fractured surface shows very flat, shiny face with cleavage like brittle features (see Figs. 3.6 and 3.7). Upon loading, the pre-existing micro cracks that run perpendicular to the loading direction propagate by brittle cleavage.

Table 3.6 Low temperature tensile test results of L oriented NFA-1 specimens

Temperature (^{o}C)	0.2%YS (MPa)	UTS (MPa)	UE (%)	TE (%)
20	970	1062	6.4	13.9
-50	1046 ± 64	1143 ± 37	9.2 ± 0.3	16.1 ± 0.4
-100	1123	1249	9.9	16.0
-150	1283	1380	10.6	16.6
-196	1469	1563	1.0	8.4

YS= Yield strength, UTS= ultimate tensile strength, UE = uniform elongation, TE= total elongation.

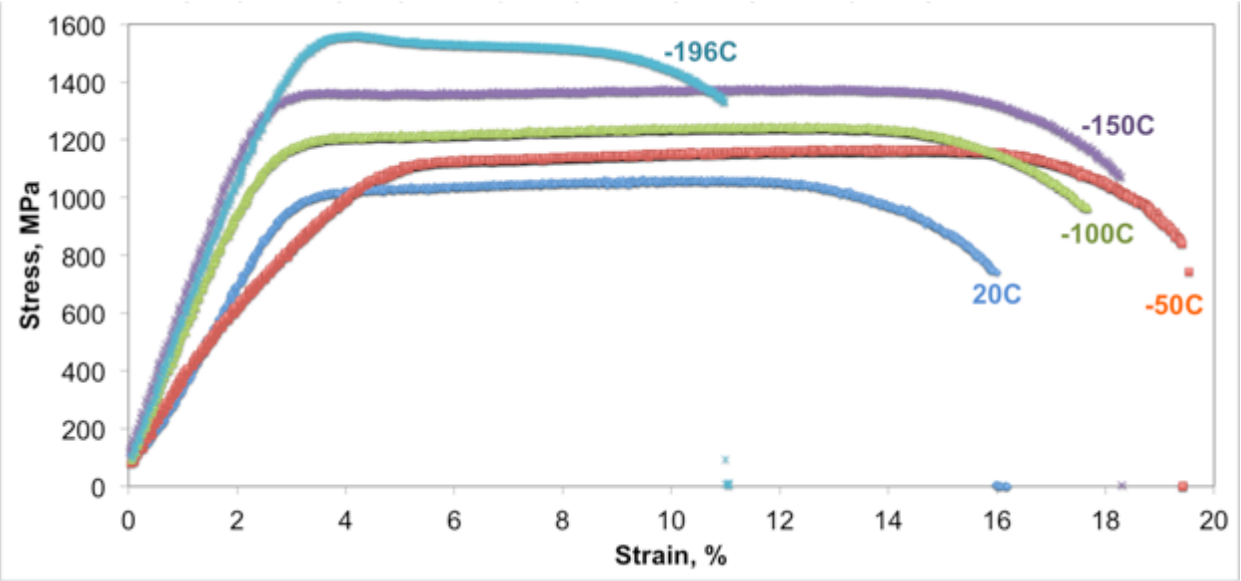

Figure 3.5. Engineering stress-strain curves of L-oriented NFA-1 specimens tested at lower temperatures.

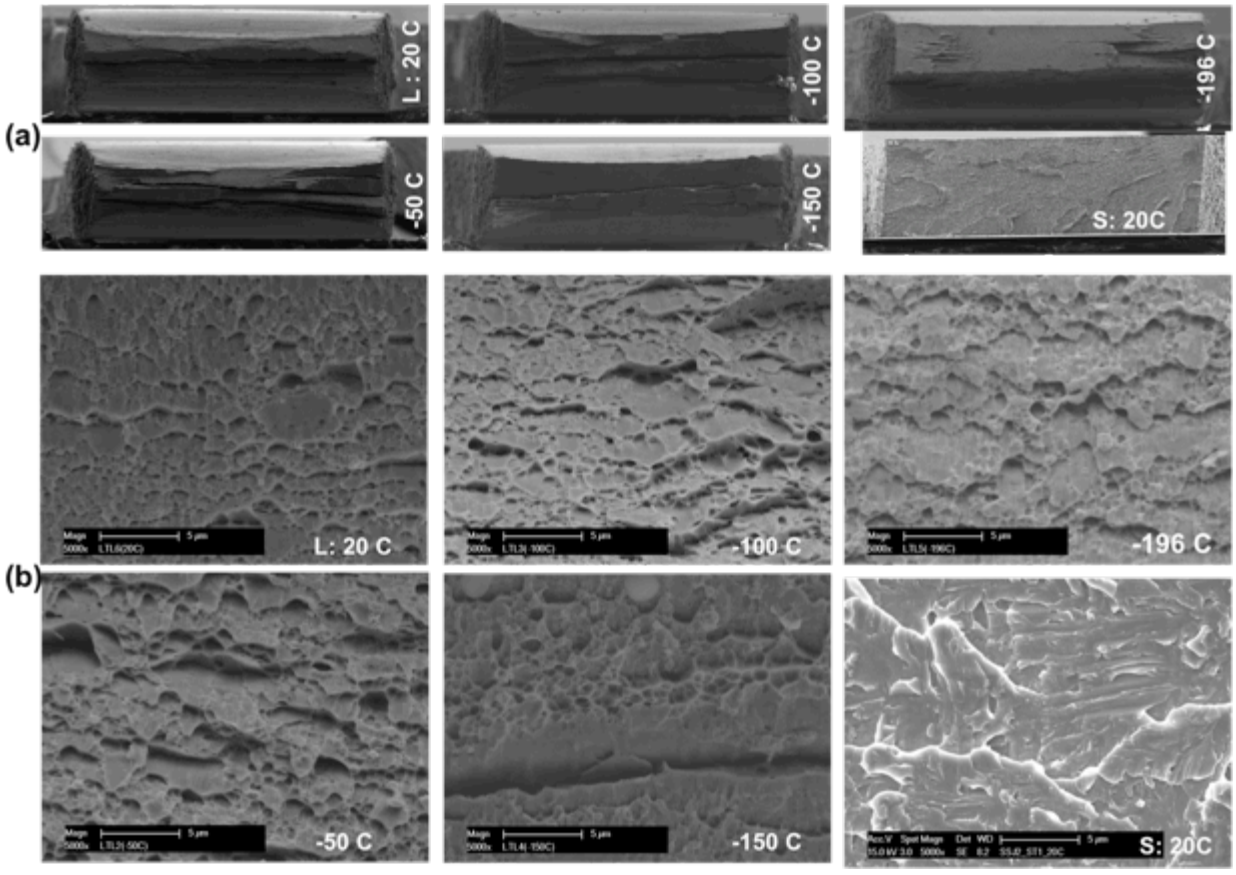

Figure 3.6. Low (a), and high (b) magnified SEM images of the L and S-oriented tensile fracture surfaces

The room temperature tensile s(e) curves and their respective SEM fractographs of as-fabricated and annealed (with varying times) conditions for L and S oriented NFA-1 specimens are shown in Fig. 3.7. Figure 3.8 also plots the summary of their properties. Annealing at 1300^{o}C for 1h and 5 hrs lower the tensile strength for L by ~14% and ~24%, respectively, than their as-fabricated condition. Uniform and total elongation remain almost similar at all conditions though the fracture mechanism changes from delamination driven for as-fabricated specimens to microvoid coalescence dimple fracture with some presence of crater-like features for annealed specimens. These craters might be partly responsible for lower strength along with higher grain size compared to the as-fabricated specimens. While the as-fabricated S oriented tensile specimen failed in the elastic region at room temperature, the corresponding 1h annealed specimen has a large total elongation of ≈ 18% with a significantly higher UTS of ≈ 874 MPa compared to the as-fabricated condition (≈ 652 MPa). Annealing at 1300^{o}C for 5h further improves the total ductility to 23%, while tensile strength drops slightly (≈ 802 MPa), but still high enough when compared with the as-fabricated condition. Fracture surface has also been changed from flat, shiny brittle fracture for as-fabricated specimens to dimple dominated ductile fracture with some craters for annealed specimens. The crater-like features may partially heal microcracks and help to increase the ductility. The room temperature strength and ductility of the L and S oriented annealed specimens are comparable to each other. These improvements in strength and ductility are associated with the absence of microcracks and grains larger than 10μm (see Table 3.5 and Fig. 3.4).

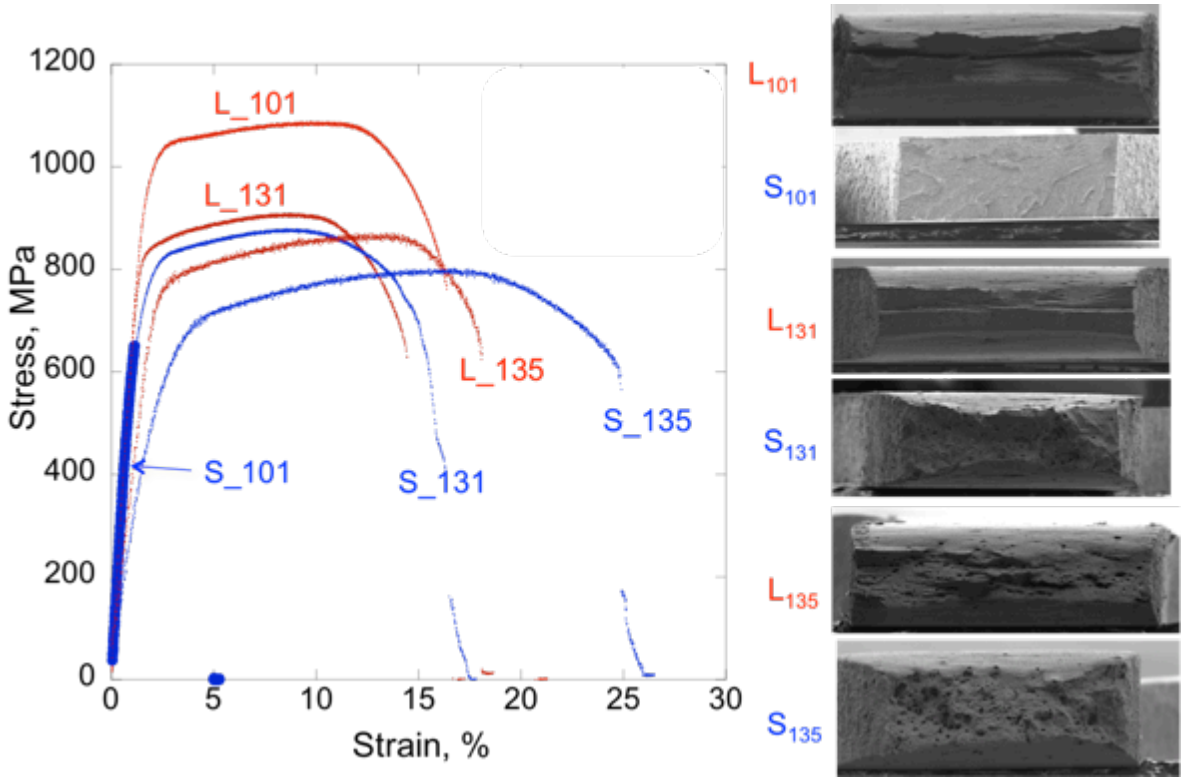

Figure 3.7. Room temperature engineering stress-strain curves for the as-fabricated and annealed L (red) and S (blue) oriented tensile specimens and their respective SEM fractographs. Codes 101, 131 and 135 mean as-fab, annealed at 1300oC/1hr and annealed at 1300oC/5hr conditions, respectively.

Fracture toughness

Room temperature fracture toughness test were conducted on L-T oriented as-fabricated and annealed (1300^{o}C/1hr) specimens and their load-displacement curves along with fracture surfaces are shown in Fig. 3.9. The result shows that the toughness reduces ≈ 22% for the annealed specimen when compared with the as-fabricated specimen. This lower toughness for annealed specimen might be associated with the relatively higher grain size, lower strength, formation of crater-like pores and absense of microcracks in favourable orientations. Fracture mode has also been changed from delamination driven for the as-fabricated specimens to the classical dimple fracture by microvoid coalescence for annealed specimen.

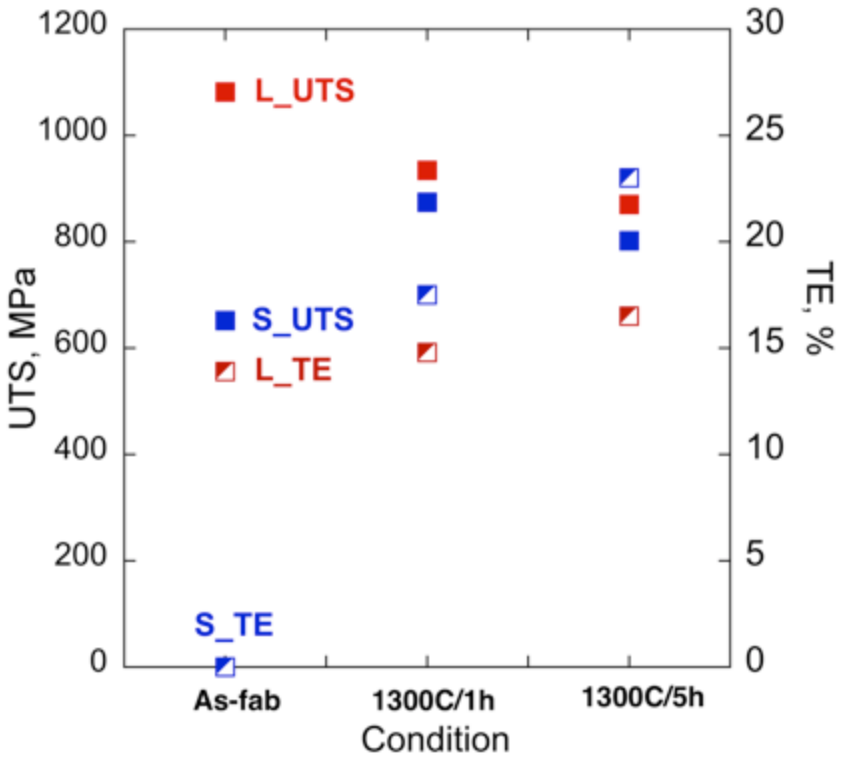

Figure 3.8. Room temperature ultimate tensile strength (UTS) and total elongation (TE) of L (red) and S (blue) oriented tensile specimens as a function of annealing conditions.

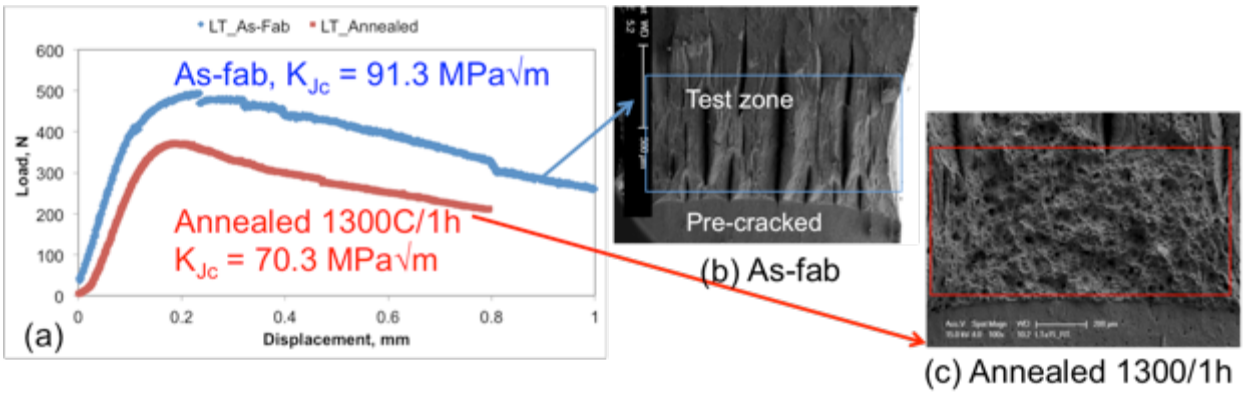

Figure 3.9. Room temperature fracture toughness test for L-T oriented specimens: (a) load-displacement curves, (b) delamination driven fracture for the as-fabricated specimen, and (c) dimple fracture surface for annealed at1300oC/1hr specimens.

3.4 Summary and Future Work

The statistical analysis of microstructural features of as-fabricated and annealed NFA-1 material has been studied. High temperature annealing at 1300°C for 1 hr and 5 hrs appears to heal the microcracks and altars the pancake-shaped grains towards more equiaxed that exist in the as-fabricated plate. Annealing for 1 and 5 hrs also increases the average grain size by ≈ 10% and ≈ 24%, reduces the microhardness by ≈ 18% and ≈ 30%, respectively. The room temperature L loaded tensile strengths also lower by up to 24%. Interestingly, the strength increases up to ≈ 34% for the S loaded annealed tensile specimens. Total ductility was also observed ≈23% for annealed condition, when compared to the as-fabricated condition that showed ≈0% ductility. The room temperature tensile properties are more isotropic after annealing.

The effect of different annealing temperatures (1100 and 1200 °C) and times (1 hr and 5 hrs) will be explored and more detailed observations on microcrack healing will be obtained along with the corresponding effects on the grain, dislocation and NO nanostructures will be characterized.

REFERENCES

[1] G.R. Odette, “Recent progress in developing and qualifying nanostructured ferritic alloys for advanced fission and fusion applications,” JOM. 66 (2014) 2427.

[2] N.J. Cunningham, Y. Wu, G.R. Odette, D.T. Hoelzer, S.A. Maloy, “ Characterization of a larger best practice heat of 14YWT in annealed powder, HIP consolidated and extruded forms”, Fusion Materials Semiannual Progress Report for Period Ending June 30, 2013, DOE/ER-0313/54, U. S. Department of Energy, 15.

[3] M.E. Alam, NJ Cunningham, D. Gragg, K. Fields, G. R. Odette, D. T. Hoelzer and S. A. Maloy, “Mechanical Properties Characterization of a Larger Best Practice Heat of 14YWT NFA1”, Fusion Materials Semiannual Progress Report for Period Ending June 30, 2014, DOE/ER-0313/56, U. S. Department of Energy, 63-69.

[4] M.E. Alam, K. Fields, G. R. Odette, D. T. Hoelzer and S. A. Maloy, “Tensile property characterization of 14YWT nanostructured ferritic alloy NFA1” Fusion Materials Semiannual Progress Report for Period Ending December 31, 2014, DOE/ER-0313/57, U. S. Department of Energy, 39.

[5] S. Pal, M. E. Alam, G. R. Odette, D. Hoelzer and S. Maloy, " Microstructure, texturing, microcracking and delamination behavior of NFA-1", DOE/ER-0313/58 (2015), DOE Fusion Reactor Materials Program Semiannual Progress Report, 58 (2015) 66-82.

[6] K.W. Gao, L.J. Qiao, and W. Y. Chu, "In situ TEM observation of crack healing in □α-Fe", Scripta Materialia, 44 (2001) 1055.

CHAPTER 4: MICROSTRUCTURE, TEXTURING, MICROCRACKING AND DELAMINATION BEHAVIOR OF NFA-1

4.1 OBJECTIVE: The objective is to determine the origins of microcracking in 14YWT NFA-1 plate.

4.2 SUMMARY: NFA-1 was processed by gas atomization of powders, mechanical alloying by powder ball milling, consolidation by hot extrusion and annealing followed by hot cross rolling. NFA-1 exhibits highly anisotropic microstructures and mechanical properties. Sub-μm roughly, equiaxed grains from ~ 0.2-0.7 μm are observed on view planes parallel to the plate to surface (LT – see Fig. 4.1). View planes parallel to the plate side thickness (LS) reveal elongated pancake shaped grains of ~ 0.5μm average thickness and aspect ratios of 2-3. Larger and a few much larger grains are also observed**.** Deformation processing (extrusion and cross rolling) induces a strong <110> fiber texture, accompanied by a high volume fraction of brittle {001}<110> cleavage system planes and directions observed in the side LS view, throughout the thickness of the plate. Formation of sessile dislocations with a burger vector of <001> on {001} planes along low angle subgrain boundaries accommodates the initial stages of deformation. Further deformation results in dislocations pile-ups at the subgrain boundaries, creating stress concentrations and opening displacements ultimately nucleate microcracks on the brittle cleavage system. Microcrack propagation is further driven by residual stresses that develop during the deformation.

4.3 PROGRESS AND STATUS:

4.3.1 Introduction: Hot extruded and cross-rolled FCRD-NFA-1 is severely microcracked on planes perpendicular to the normal direction of the as processed plate [1-2]. The microcracks form during thermo-mechanical processing. This work is aimed at identifying the detailed micro-mechanisms leading to microcracking and subsequent delamination.

4.3.2 Experimental Methods: Microstructural characterization was carried out using SEM, TEM. EBSD was used for texture characterization. Selected region TEM lamellas were fabricated by the FIB lift out method and examined using a variety of imaging, diffraction and micro analytical methods.

4.3.3 Results: Deformation processed nano-structured ferritic (NFA-1) alloy exhibits strong anisotropy in both its mechanical properties and microstructures [1]. A significant difference in the measured values of fracture toughness and tensile strength along the thickness and longitudinal directions is observed [1-2]. The sample geometry and directions are schematically shown in Fig. 4.1.

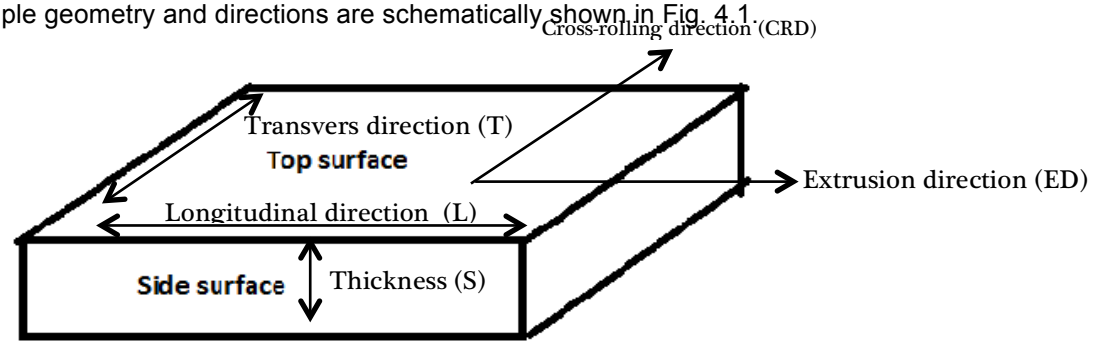

Figure 4.1. A schematic of the NFA-1 plate showing longitudinal (L), transverse (T) and short thickness (S) directions. Planes parallel to the side surface is defined as LS, parallel to the top LT and parallel to the front face as TS. Extrusion and cross rolling of the plate was carried out along the L and T direction as marked accordingly.

Microstructural characterization using SEM also reveals a significant difference in grain morphology and apparent sizes along the plane parallel to top surface, versus parallel to the thickness direction, as described in Fig. 4.2. Equiaxed ~ 0.2-0.7 μm grains are observed on the plane parallel to top surface (LT view), whereas the plane parallel to thickness direction (LS view) contains elongated “pancake” shaped grain of thickness ~0.2-0.5 μm and an aspect ratio of ~ 6-7.

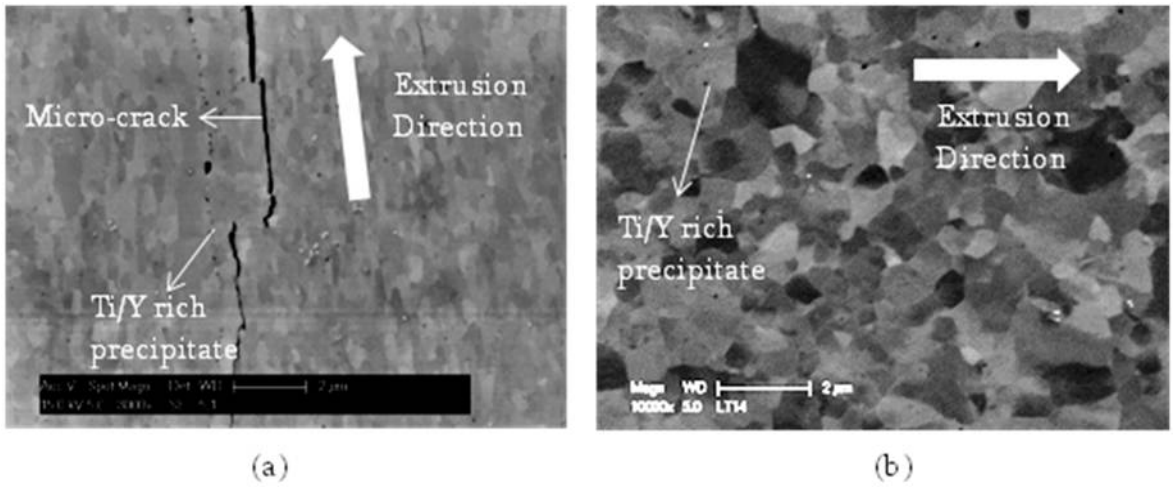

Figure 4.2. a) Polished SEM micrograph of the plate’s LS view; and, b) LT view. The microstructural features (visible in the SEM micrographs) and extrusion direction for the sample are labeled accordingly.

SEM images of both the LS and LT views show presence of Ti and Y rich precipitates, which are detrimental to mechanical properties. Compositional maps for both the LS view shown in Fig. 4.3a to f and the LT view shown in Fig. 4.4a to f were characterized using electron probe microanalysis (EPMA). The elemental composition map shown in Figs. 4.3 and 4.4 confirm the presence of Ti and Y rich precipitates in the hot extruded and cross-rolled plate. The number density of the Y rich precipitates is lower compared to the Ti rich features, as seen in Figs. 4.3b and d and Figs. 4.4b and d. The precipitates are aligned in stringers along the extrusion direction, as seen from the Fig. 4.3d and 4.4d. EPMA maps also show that cracked region contains oxidation peaks. Elemental maps for the LT and LS views are similar. A more detailed investigation of this Ti/Y rich particles was carried out by TEM EDX in the high angle annular dark field (HAADF) mode as shown in Fig. 4.5a. It was previously proposed that the microcracks might nucleate at the coarse precipitates, especially along prior powder particle boundaries. This now does not seem to be the case, since TEM clearly reveals that these features do not influence microcrack nucleation. The precipitates, that span a size range from about 15 to 150 nm and are found both in the matrix and on grain boundaries, degrade the ductility of NFA-1. The compositions of the precipitates and matrix are summarized in Table 4.1.

Table 4.1: EDS composition analysis of the Ti/Y rich precipitates and the matrix

Feature	Composition (atom %)					
	Fe	Cr	W	Ti	Y	Cu*
Ti rich particle	2.91	1.13	-	78.94	-	16.97
Y rich particle	40.02	8.96	-	-	40.02	8.71
Matrix	78.38	14.74	0.94	-	0.28	5.22

* Cu in the EDS spectrum is due to use of a Cu grid

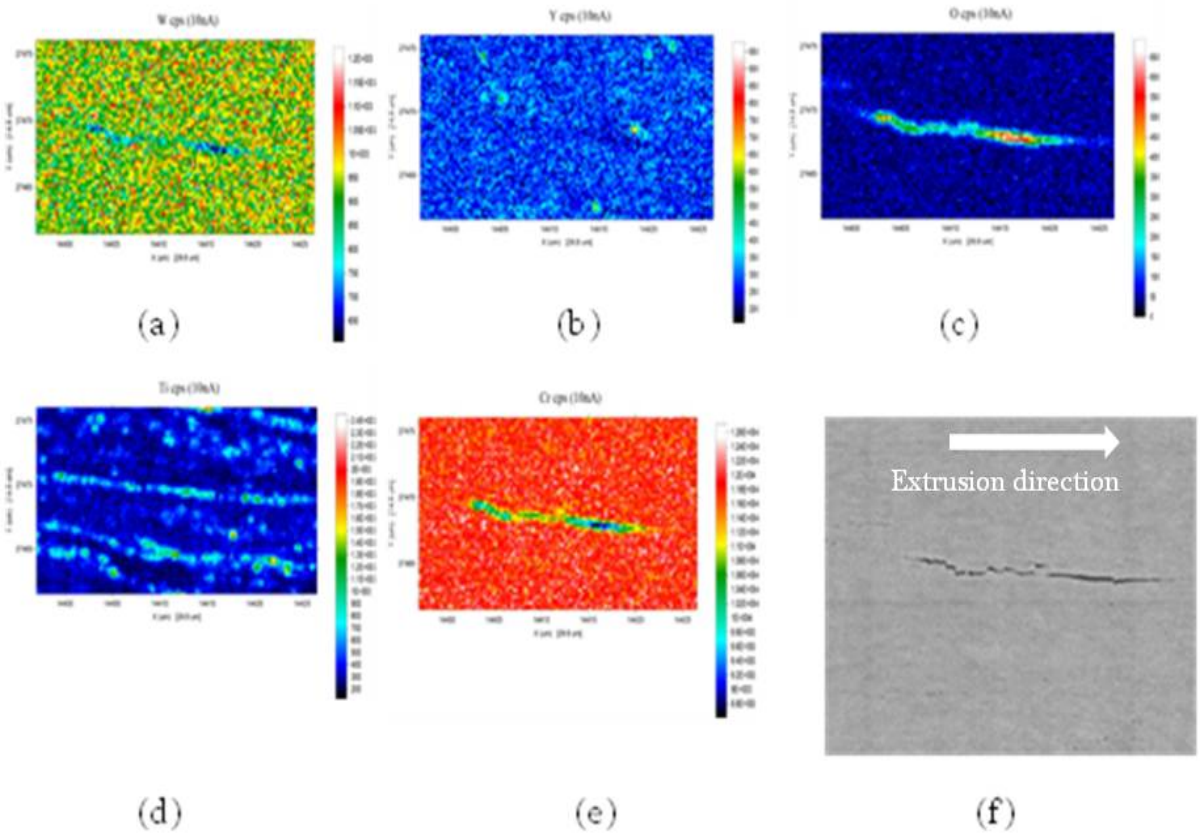

Figure 4.3. Elemental compositional maps for the LS view and the cracked region of interest.

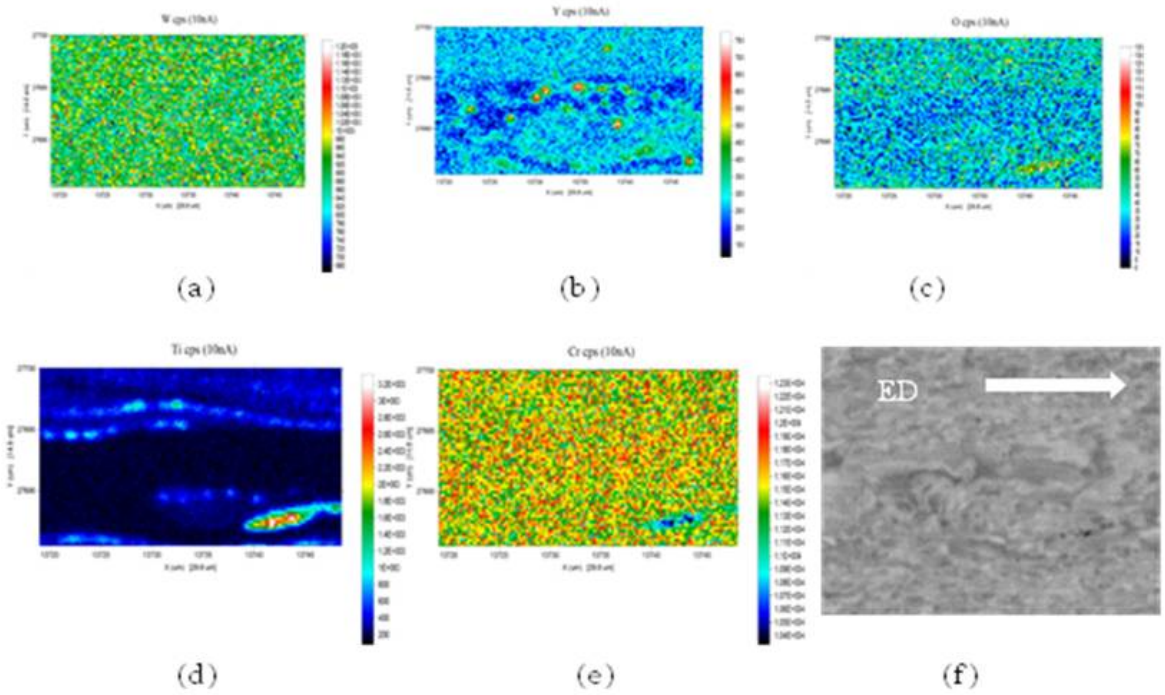

Figure 4.4. Elemental compositional maps of LT view and the cracked region of interest.

Microcracks are observed only in the plate side SL view, running throughout the plate thickness (S). Similar microcraking has been previously reported in the literature [3-4]. The microcrack size, number density, inter-crack spacing and opening dimensions are summarized in Table 4.2. The microcracks play a very critical role in determining the fracture toughness of NFA-1, especially by nucleating delaminations that relax the tri-axial stress state towards a plain strain condition, thereby lowering internal stresses, and suppressing cleavage; alternately delaminations cause crack deflections for LS orientations. However, microcracks reduce the tensile ductility and strength in the thickness (S) direction [1].

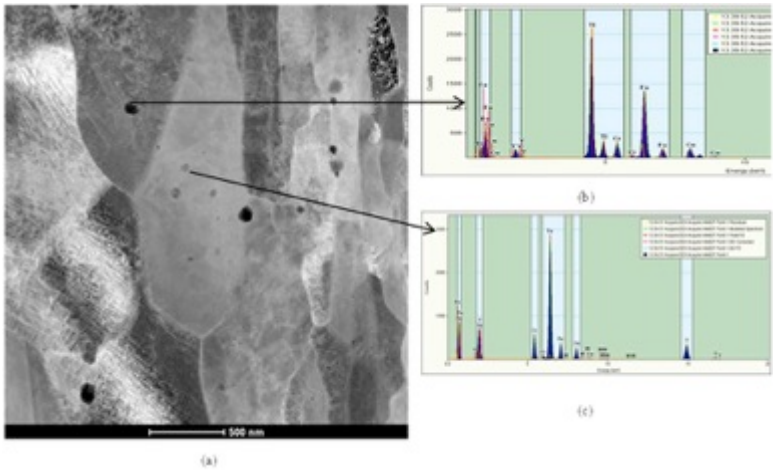

Figure 4.5. a) HAADF image showing Ti/Y rich precipitates with darker contrast; b) EDS spectrum of the Ti rich precipitates; and, c) EDS spectrum for the Y rich precipitates.

Table 4.2: Microcrack Statistics

Item	Number	Standard Deviation
Av. crack separation (μm)	~ 16.3	± 4.7
Crack length (μm)	~ 10.2	± 8.9
Number density (/m^2)	~ $3.45x10^9$	± $1.2x10^9$
CMOD (nm)	~ 252	± 142

Texture characterization:

Fig. 4.6 shows the directions and planes that are used to define texturing with respect to the primary deformation orientations. Texture measurements for different views of the plate planes were first carried out by pole figure (PF) analysis. Projections of two major deformation axes, along with the plate normal direction, are shown in stereogram in Fig. 4.6b and c for both the LT and LS views, respectively.

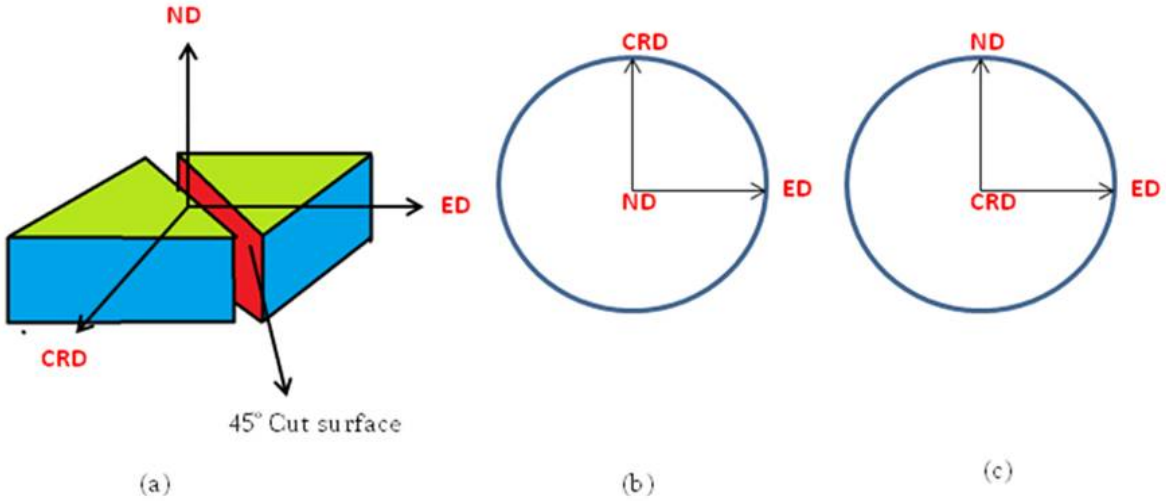

Figure 4.6. a) A schematic representation of the plate along with primary deformation axes of extrusion (ED), cross-rolling (CRD) and normal direction to the plate (ND); and, b) and (c) show stereogram equivalent deformation axes directions for the LT and LS views, respectively.

EBSD PF maps in Fig. 4.7a show that the plate has an expected strong α-fiber texture (<110>) along the extrusion direction. Fig. 4.7b shows that a partial α-fiber also develops along the cross rolling direction. This suggests that both the primary deformation processes (hot extrusion and cross-rolling) induce a similar type of <110>-fiber texture. PF analysis also shows that the texture component developed along the surface normal direction is <001>. EBSD characterization of surface cuts at 45° with respect to the extrusion direction (as illustrated in Fig. 4.6a) in Fig. 4.8 also show that texture for the LT plate surface

normal is predominantly <100>. The PF analysis in Fig. 4.8 also shows that the planes parallel to the 45° cut surface are {100}-type. These observations are further corroborated by the inverse pole figure (IPF) analysis in Fig. 4.9.

More quantitative and accurate determination of the texture components was carried out based on an orientation distribution function (ODF) analysis. The Φ_2 = 0 and 45° ODF sections, shown in Fig. 4.10a and b, demonstrate that a strong {001}<110> texture is dominant in the plate. This is also the low tough toughness cleavage system in bcc Fe.

Taken together, the most important conclusion is that a strong {001}<110> texture system develops in the thickness direction of the extruded and cross rolled plate.

Characterization of crack propagation and initiation by TEM:

A brittle crack is characterized by its direction and plane of propagation. TEM was used to characterize the propagation plane-direction and the microcrack formation mechanism. TEM lamellas in Fig. 4.11b and d, taken from locations shown in Fig. 4.11a and c, were prepared using FIB-lift out method. The largest separation between the crack surfaces indicates the crack initiation site.

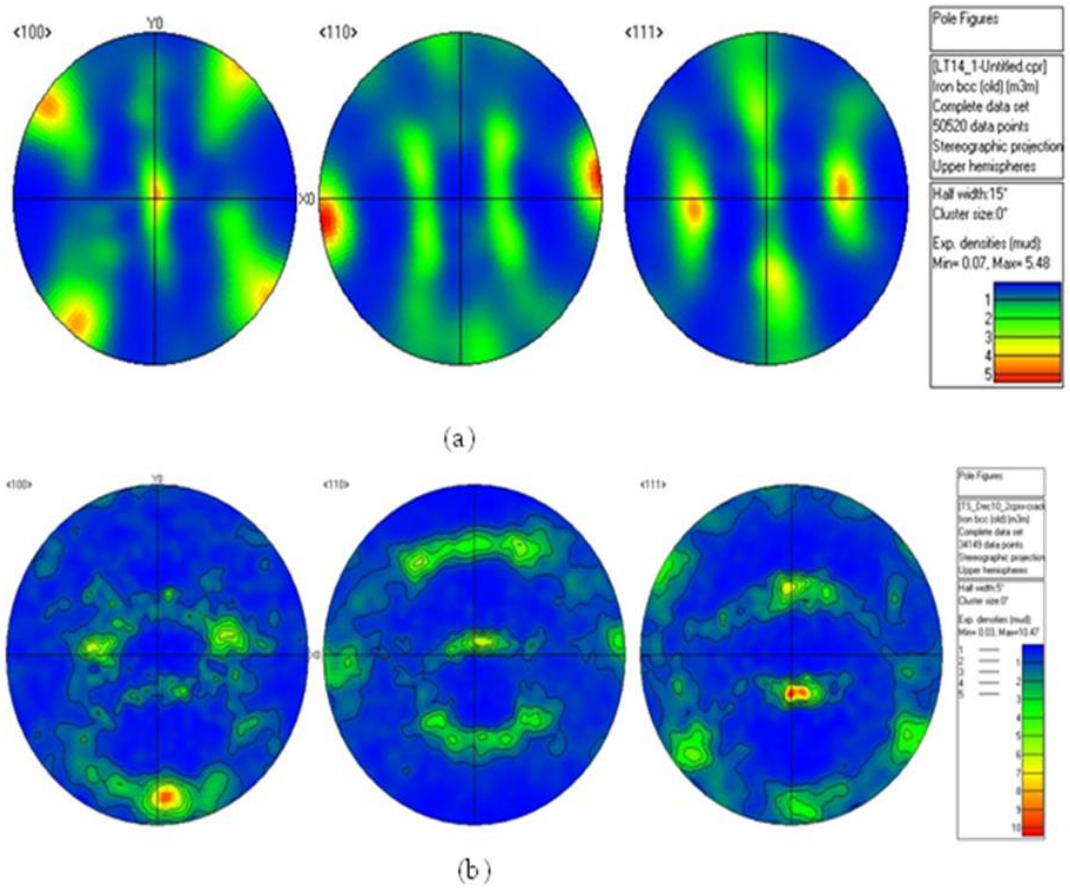

Figure 4.7. Pole figures of a) LT view, b) LS view of the as extruded plate showing projection of <100>, <110> and <111> poles.

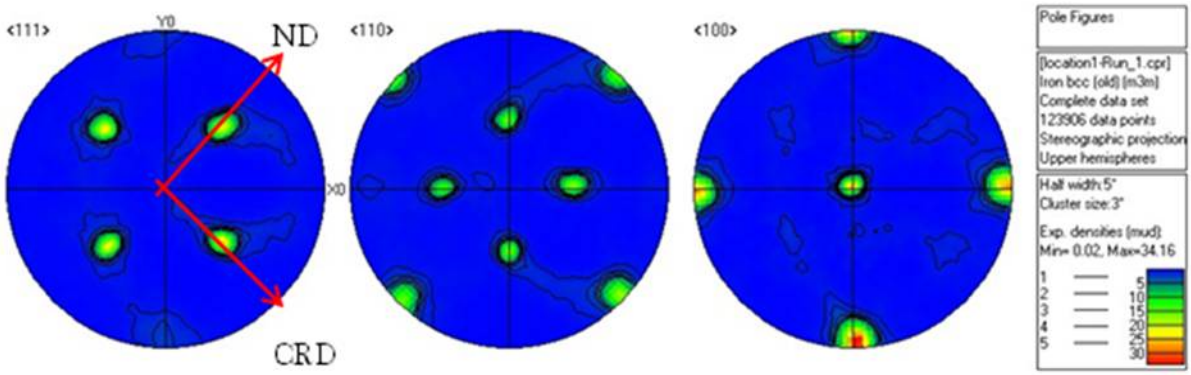

Figure 4.8. PF for the 450 cut surfaces showing <100>, <110> and <111> projections. The deformation directions for the plate for the <111> projection.

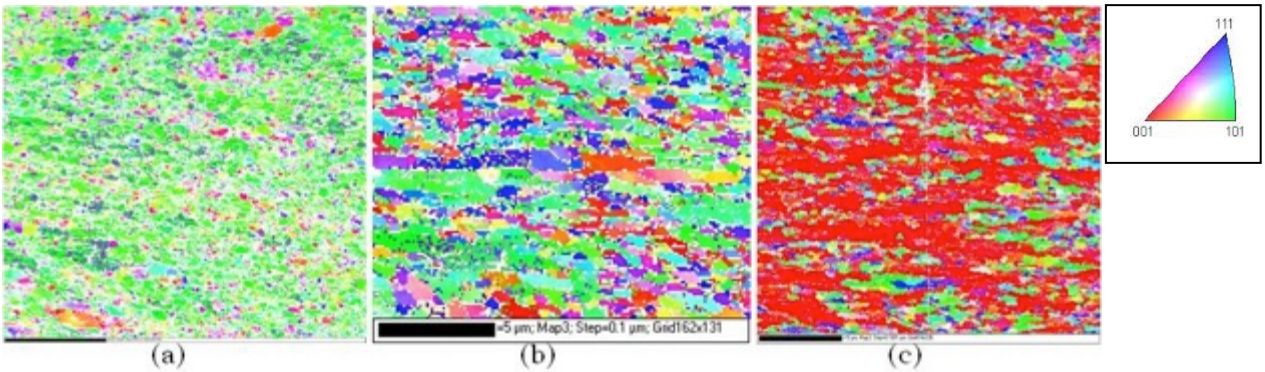

Figure 4.9. IPF maps of a) LT, b) TS and c) 45° cut section showing density of the planes parallel to the surface of respective samples.

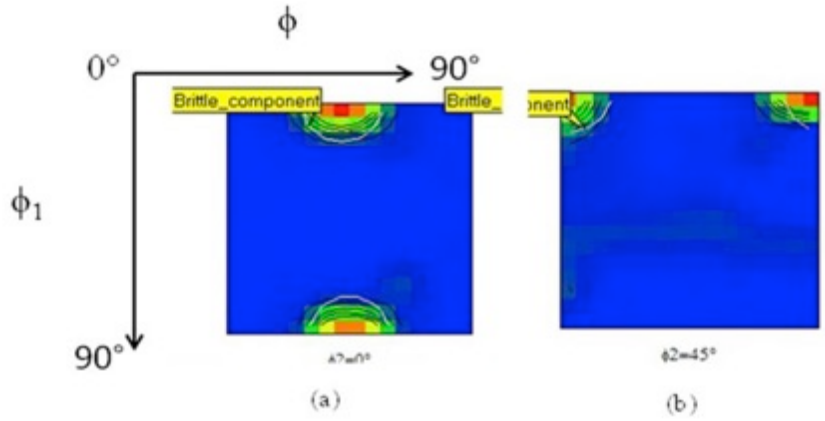

Figure 4. 10. a) Φ2 = 0; and, b) Φ2 =45° ODF sections of the plate.

Fig. 4.11a and c show the FIB locations where TEM lamellas were extracted along both the propagated crack front and initiation site. Fig. 4.12a is a bright field (BF) TEM image of the propagation front lamella shown in Fig. 4.11b. The crack runs through a single grain with a contrast variation due to a high dislocation density and a low angle boundary. Selected area diffraction (SAD) patterns for the marked locations in Fig. 4.12a, along with dark field (DF) imaging, confirm that the crack is confined to a single (001) oriented grain. The SAD patterns from the near crack tip locations, marked as 1 and 2 in Fig. 4.12a, show that the foil normals are near <110>, that are only slightly misoriented with respect to each other. The weak beam dark field (WBDF) image in Fig. 4.13b, for the (002) reflection, marked by the dashed circle in Fig. 4.12c, is taken in the g-3g condition. Dislocations, seen as the bright contrast in the Fig. 4.13b, are concentrated around the crack and low angle boundary.

A BF image of the propagating crack region is shown in Figure 4.13a. The WBDF in Fig. 4.13b, and the HAADF image in Fig. 4.13c, also show dislocation pile-ups in the vicinity of a crack. Further, Fig. 2.13 suggests that a low angle sub grain boundary is formed in a grain by the accumulation of dislocations. Contrast in HAADF images is sensitive to variations in mass-thickness and local strain fields. Since the FIB lamella thickness is nearly uniform, the contrast variation in the Fig. 4.13c can be largely ascribed to corresponding variations in the local strain fields. Eight TEM lamellas were prepared from the crack initiation regions and illustrative BF and DF images are shown in Figs. 4.14a and c. along with the corresponding SAD patterns in Fig. 4.14b. Clearly, the microcrack nucleates on a {100}-type plane and propagates in a transgranular mode.

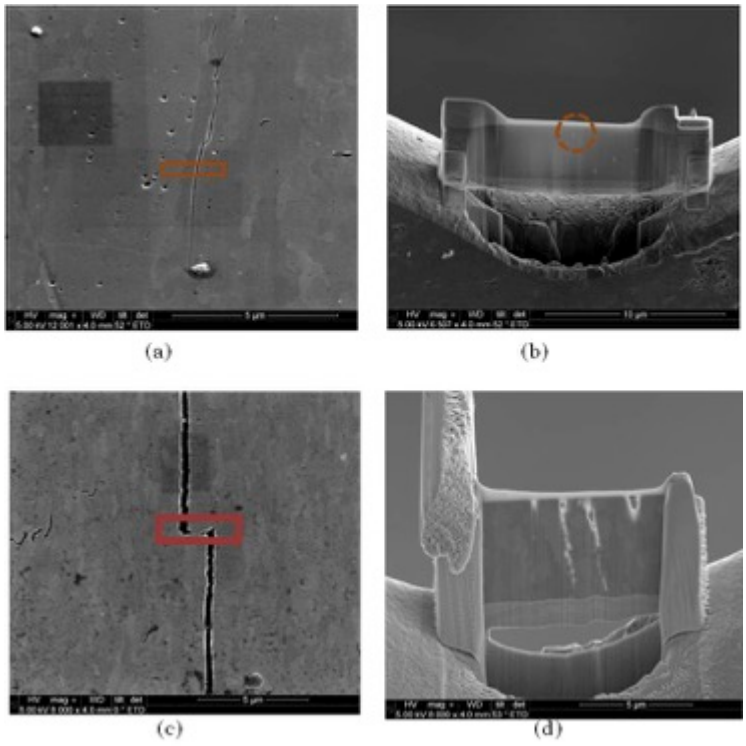

Figure 4.11. a) The marked location where the TEM lamella was extracted to characterize the crack propagation front; b) the corresponding FIBed lamella; c) the marked location crack initiation front where the TEM lamella was extracted; and, d) the corresponding FIBed lamella.

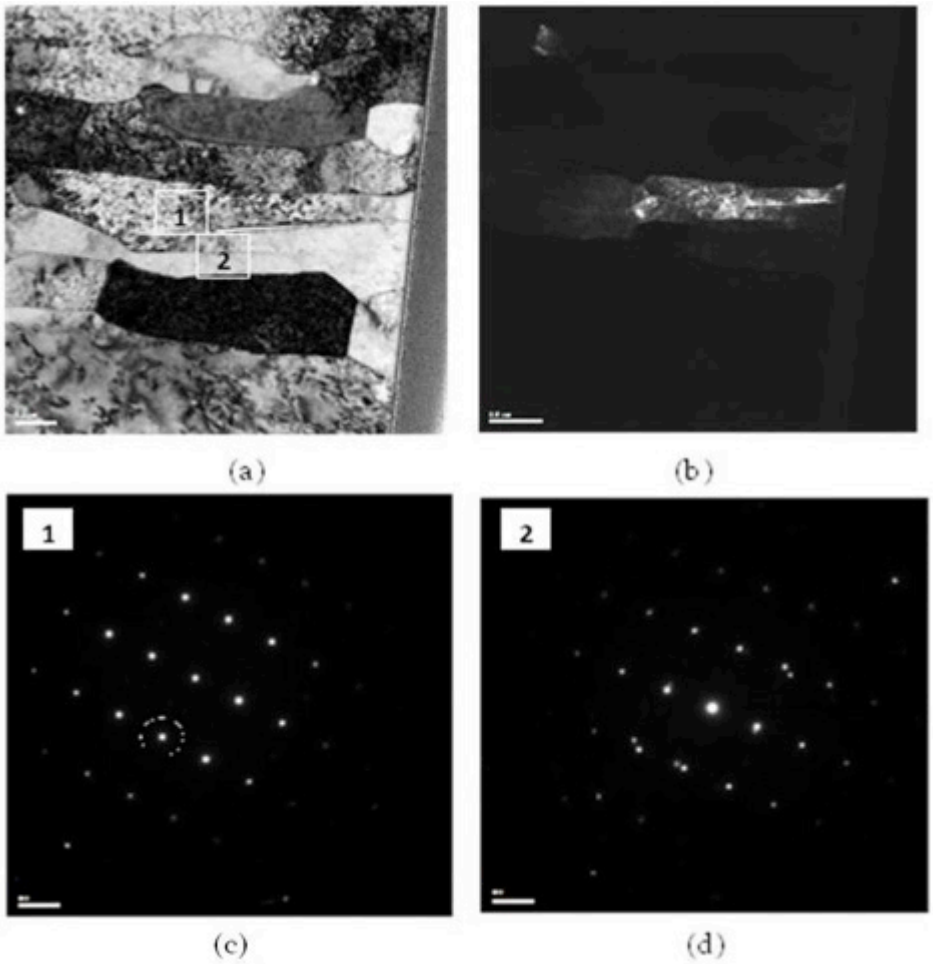

Figure 4.12. a) a BF image; b) a CDF image; c) and d) SAD patterns for the marked locations in Fig. 4.12a using the (002) reflection marked in Fig. 4.12c.

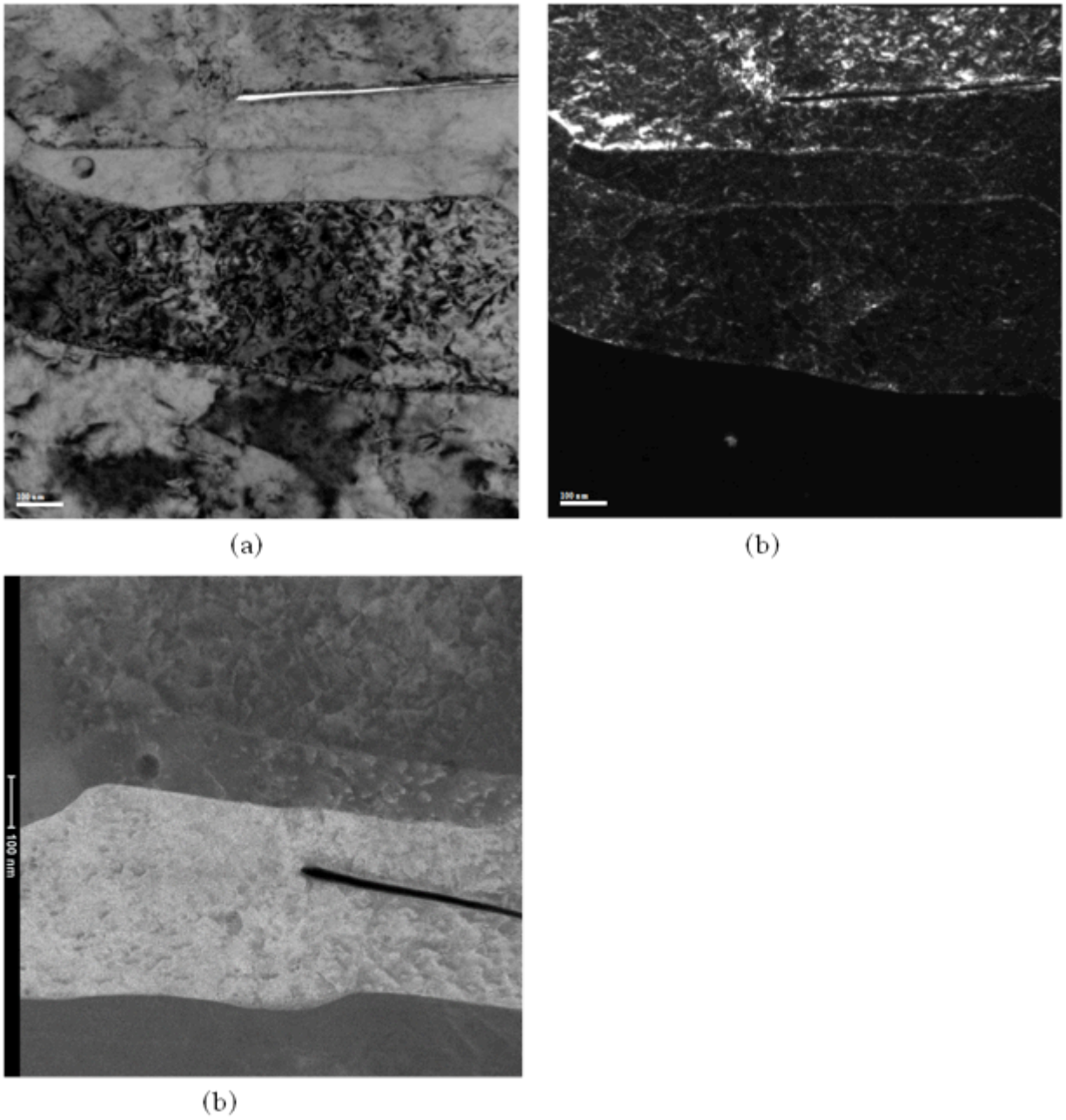

Figure 4.13. a) A BF; b) WBDF; and, c) HAADF image of the crack propagation plane.

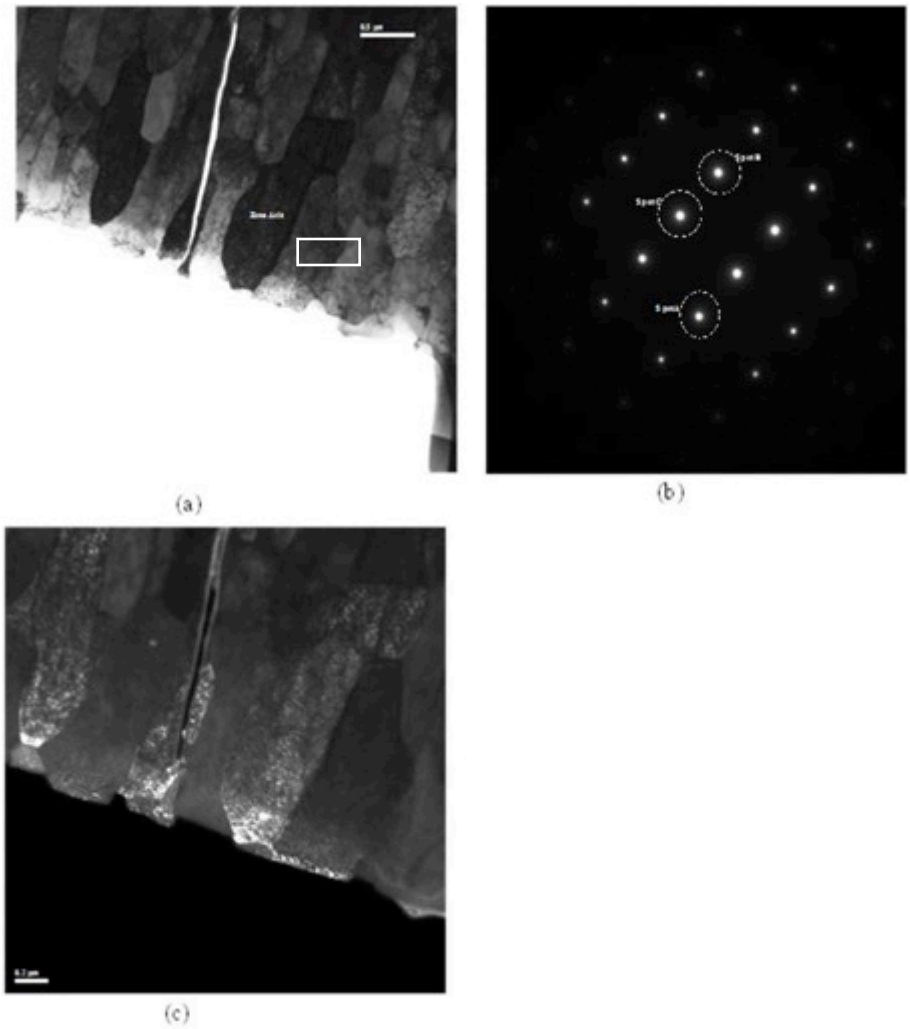

Figure 4.14. a) BF image of the crack initiation front. Marked grain is tilted to the zone axis conditions; and, b) SAD pattern captured from the grain marked in Fig. a). SAD pattern of <110> zone axis captured from the grain marked using white box in Fig. a); and, c) DF image captured from the (002) spot labeled in Fig. b).

The higher magnification view of the crack region in Fig. 4.15 shows that very diffuse boundary like contrast parallel to the crack. Dislocations tangles are clearly seen inside the grain in Fig. 4.15a and b. Fig. 4.15b shows that cracks propagate along the sub grain boundary which originated from dislocation a pile up.

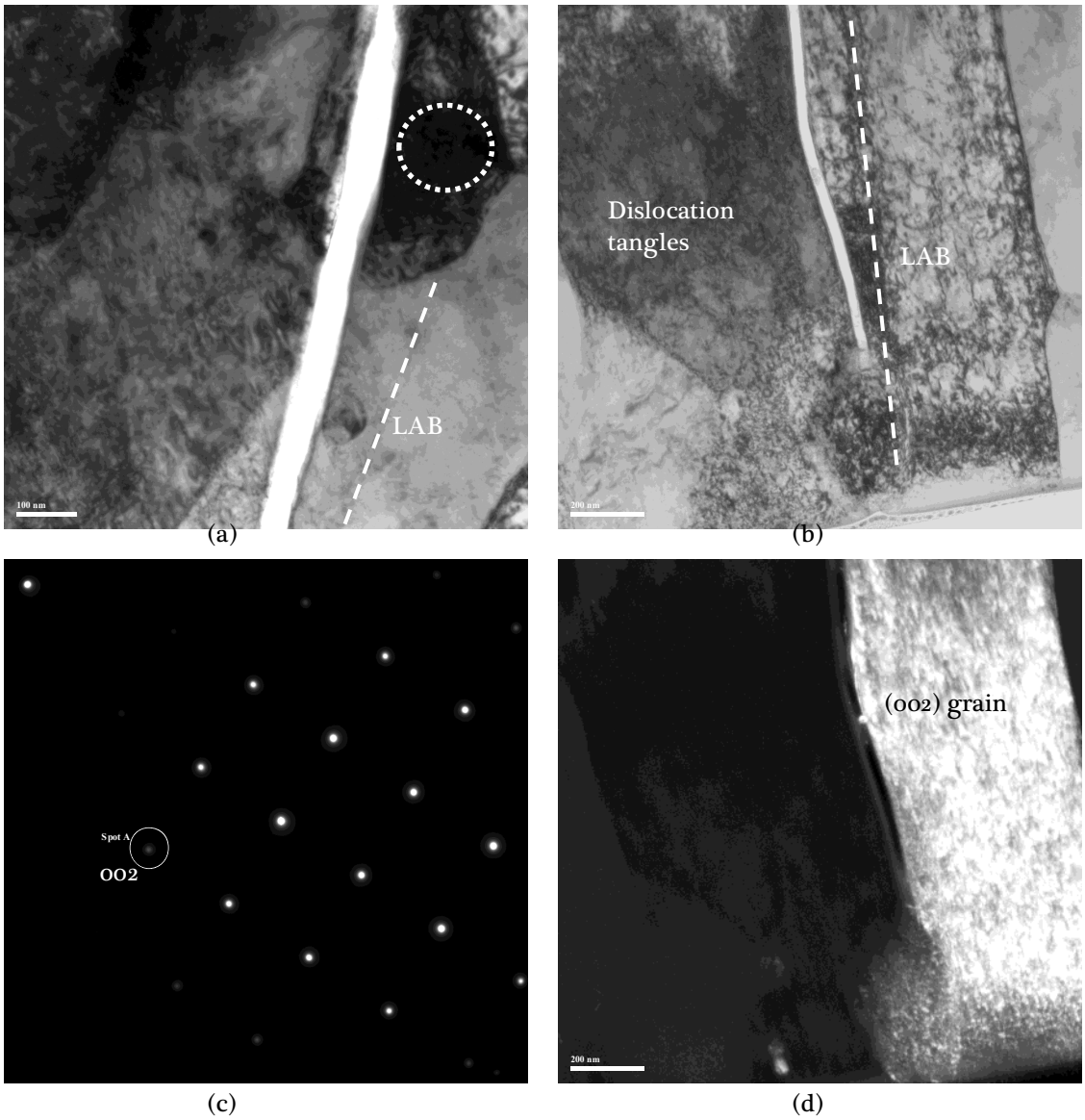

Figure 4.15. a) A BF image of a cracked region showing low angle boundary (LAB) in a grain; b) a BF image of the same location under different tilting conditions; c) the SAD pattern from the marked region in Fig. 4.15a showing the grain orientation <110>; and, d) a DF image corresponding to the (002) reflection of the SAD pattern shown in Fig. 4.15c.

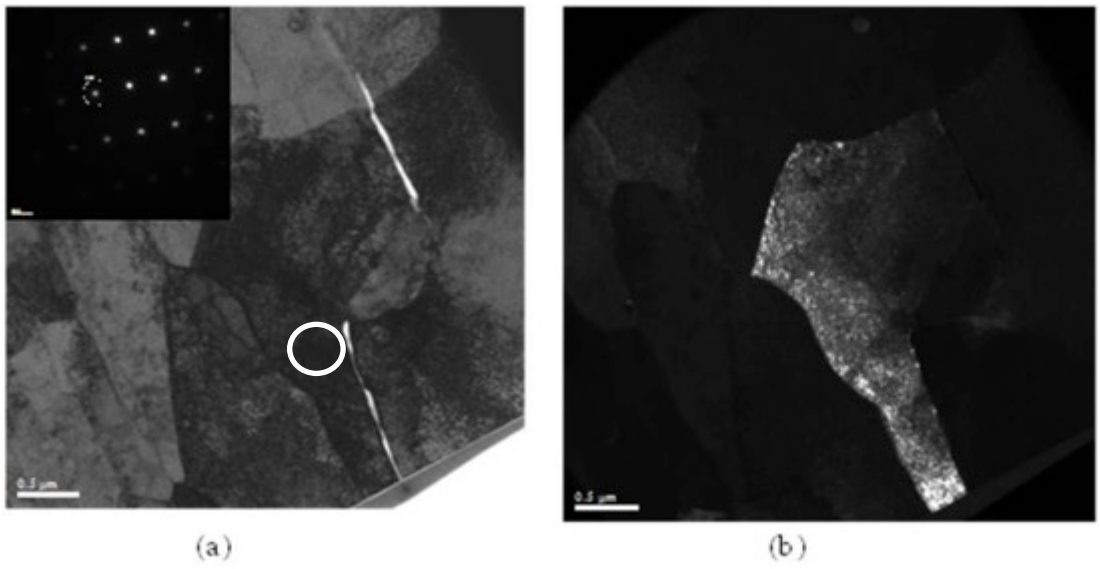

Figure 4.16. a) A BF image of the cracked region, where the insert shows the SAD pattern for the (110) zone axis at the marked location; and, b) a DF image corresponding to the (002) reflection in the inset SAD pattern of Fig. 2.16a.

Figs. 4.16 and 4.17 lend additional support to our hypothesis regarding the nucleation of microcracks associated with dislocation pile at low angle subgrain boundaries. Fig. 4.16 again shows that crack originates on a {001} plane in a grain that contains a high density of dislocations. The SAD area patterns shown in Fig. 4.17 for different locations near the crack, as marked by red circles in the BF image, show that all the SAD patterns belong to a nearly common zone axis with only minor deviations from <110>. These results clearly demonstrate that cracks are formed in association with low–angle grain boundary by dislocations pile-ups. All the microstructural components are contained in the HAADF image in Fig. 4.18, taken from the same locations seen in Fig. 4.16a and Fig. 4.17. The HAADF micrograph clearly shows the low angle boundary parallel to crack and that dislocation pile-ups develop the boundary.

Thus we hypothesize that the sequence of events leading to microcracking is as follows: a) the initial deformation is accommodated by formation of low angle dislocation subgrain boundaries; b) further deformation creates dislocations pile-ups at these low angle subgrain boundaries; c) the local stress concentrations and accumulated opening displacements nucleate microcracks on {100} type planes; d) once nucleated, the microcracks propagate transgranularly along the low angle subgrain boundaries on {100} type cleavage planes.

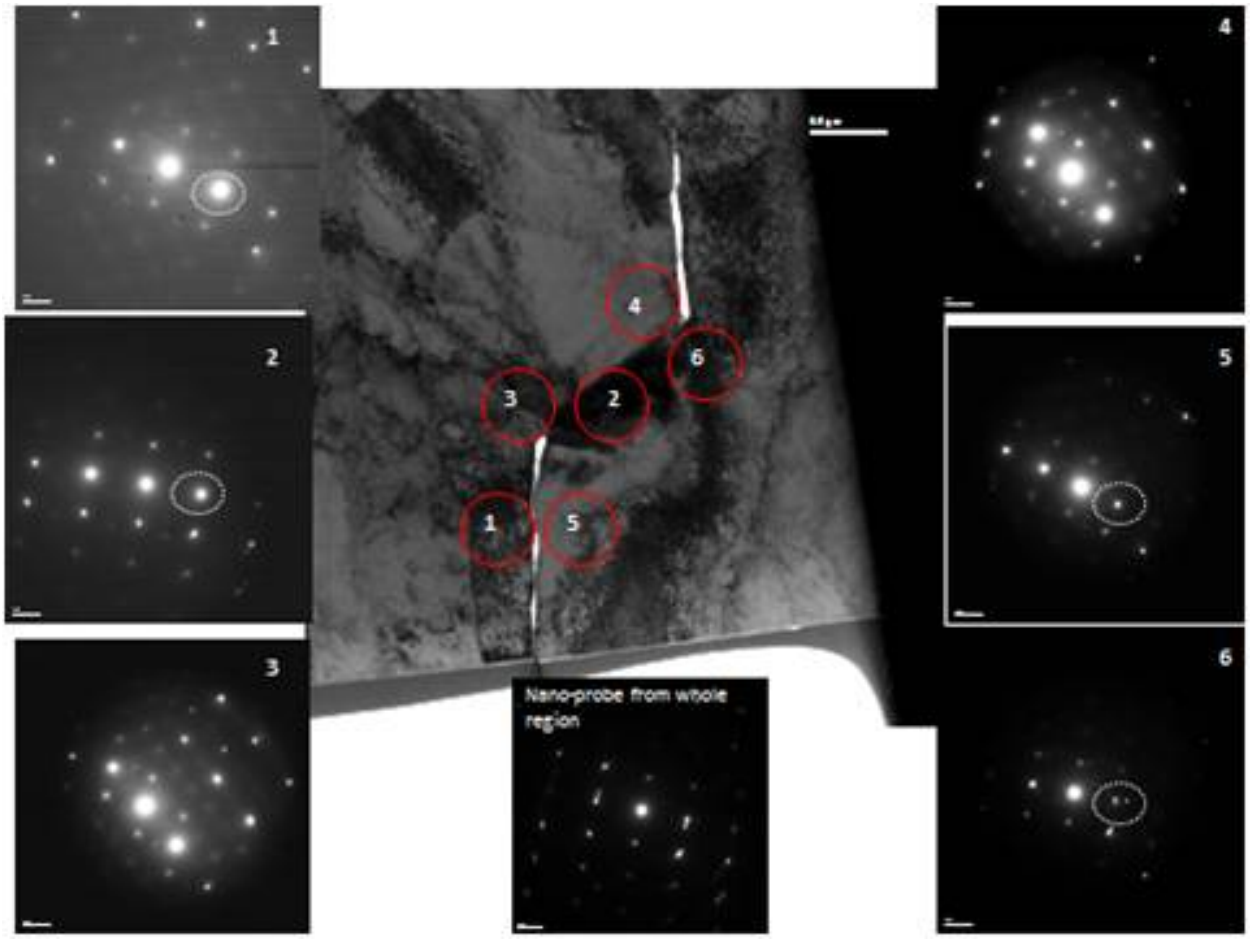

Figure 4.17: showing the same locations of Fig. 4.17 and SAD patterns are captured from the marked locations and shown in the same image. The misorientations between all the patterns are very less.

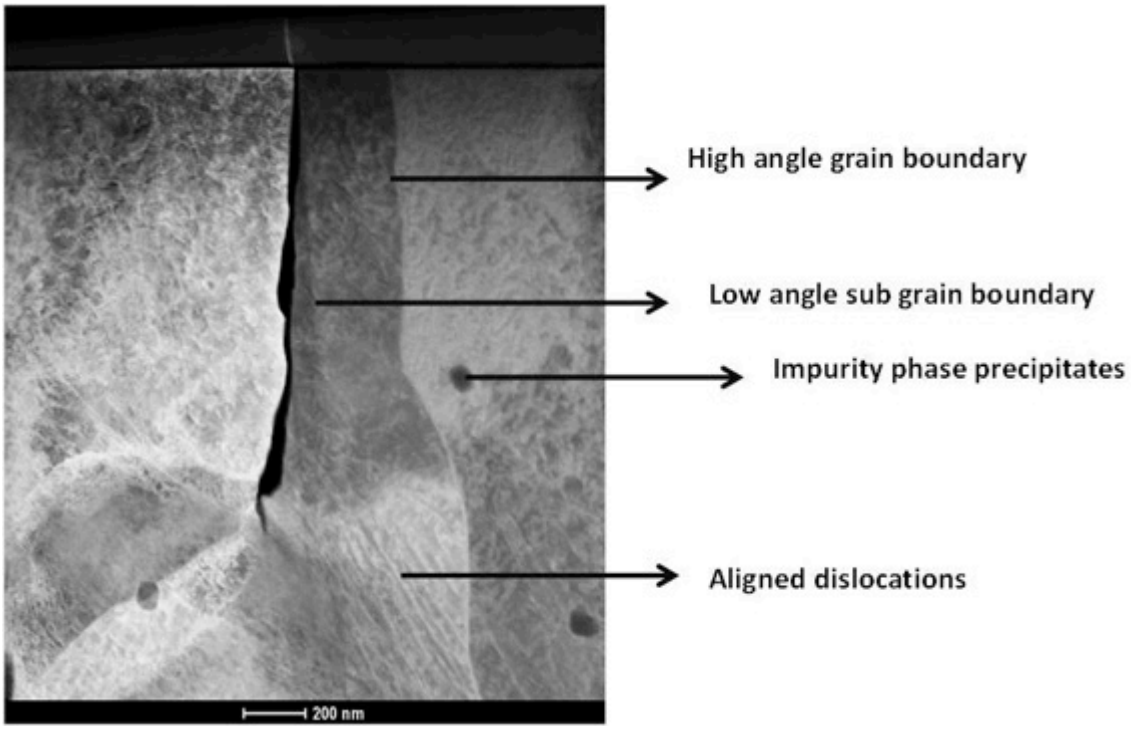

Figure 4.18: HAADF image of the crack front showing different microstructural components.

4.3.4 Summary and Discussion:

Microcracking and delamination in pipeline steels are well-established phenomena. Various reasons for this behavior have been proposed, including: inter phase boundary fracture; presence carbide and inclusion particles; texture; banding; and anisotropic plastic deformation [3-4]. Unfortunately a clear responsible micro-mechanism operating during thermo-mechanical processing and texture development is not in hand. Most of these reported results are for dual phase steels containing combinations of ferrite/austenite/martensite constituent grains and their biphasic interfaces [3-4]. In the present investigation microcracking and delamination occurs in a fully ferritic steel (14YWT NFA-1). The extruded and cross-rolled NFA-1 plate exhibits a strong α-fiber texture (<110>∥ ED). ODF analysis coupled with IPF maps show that presence of a {001}<110>-texture component in planes normal to the short, plate thickness direction. This is the most brittle cleavage system in of bcc Fe. TEM clearly shows that cracks nucleate and propagate on {100}-type planes and run along low angle subgrain boundaries parallel to {100} in the <110> direction. Since {110} are the easy glide planes in bcc structures, grains containing these planes become elongated along the extrusion direction. In contrast, glide is difficult on {100}-type planes. Under sufficiently high stress, two a/2[111] + a/2[-1-11] dislocations react on a {001} plane to form a sessile [001] dislocation [5]. Subsequent dislocation pile-ups create stress concentrations and opening displacements that nucleate a microcrack. The fracture toughness for the {001} <110> cleavage system is extremely low of order ~ 5-10 MPa√m. This microcrack growth is further driven by the residual stresses that develop during the thermo-mechanical processing.

The existence of residual stress is supported by streaking in the SAD patterns in Fig. 4.19b collected from different locations near the cracks within a single grain marked in Fig. 4.19a. These SAD patterns are

taken along the <111> zone axis of BCC Fe. Streaking of the diffraction spots usually could be attributed to residual stress that generates strain even within a single grain. Initially the deformation is accommodated through low angle subgrain boundary formation on {001} planes by creating sessile <001> dislocations that form subgrain boundaries. These subgrain boundaries are also aligned along the primary deformation direction. Further deformation causes dislocations pile-ups and produces crack opening displacements. These cracks propagate on the brittle cleavage system {001}<110> aligned along the subgrain boundaries.

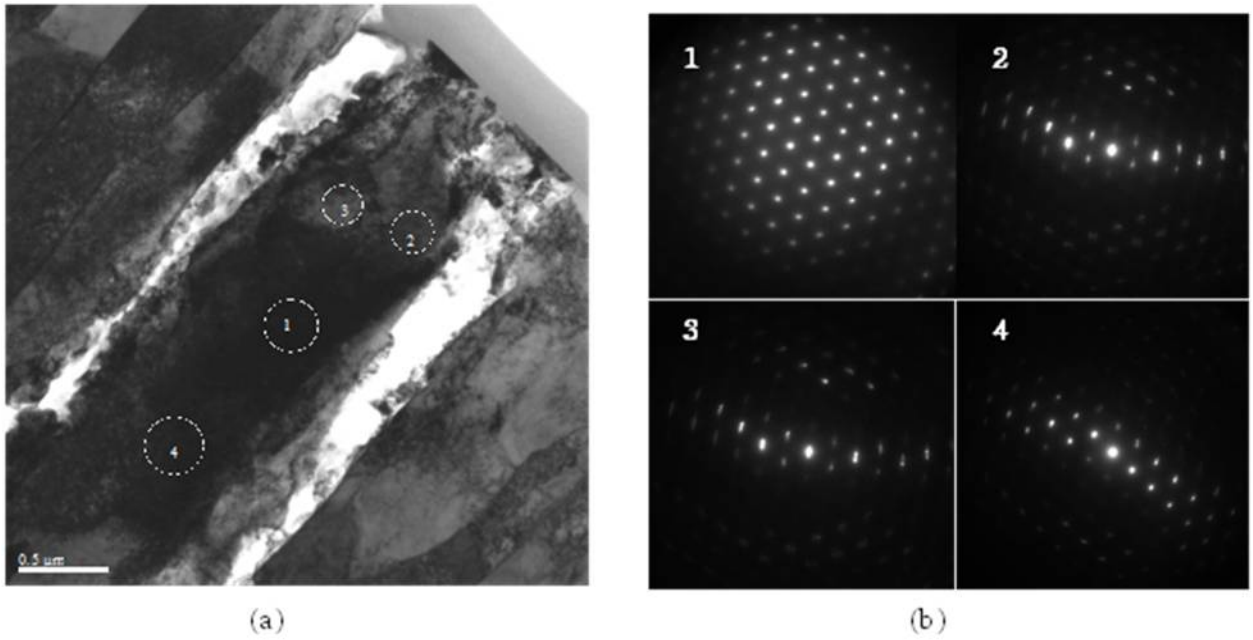

Figure 4.19. a) A BF image of the cracked regions; and, (b) streaked SAD patterns from the locations marked in the BF image.

4.3.5 Conclusions:

- Thermo-mechanical processing of the NFA-1 alloy produces microstructure containing a trimodal distribution of small (< 1 μm), medium (1 – 10 μm) and large grains. The pancake shaped grains are compressed in the plate reduced thickness direction and elongated in the cross rolling and especially extrusion directions with aspect ratio ranging from when viewed along a side LS view surface.

- NFA-1 contains coarser Ti or Y rich precipitates/inclusions in the size range of ~ 15-150 nm. However, these features do not have appeared to affect microcracking.

- Microcracking of as processed NFA-1 alloy is related to texture development during deformation processing. The plate develops α-fiber texture along the extrusion and cross rolling directions, and results alignment of {001}<110> brittle cleavage plane-direction system normal to the plate thickness direction.

- Initial deformation accommodated by a/2[110] dislocation glide that react to form low angle subgrain boundaries composed of sessile a[001]-type of dislocation on {001} planes. Further deformation leads to additional dislocation pile-ups at the subgrain boundaries that create stress concentrations and opening displacements that nucleate a cleavage microcrack. Transgranular cleavage microcrack propagation occurs on the {001}<110>-cleavage system and is further driven by residual stresses that develop during deformation processing.

REFERENCES:

[1] G.R. Odette, “Recent progress in developing and qualifying nanostructured ferritic alloys for advance fission and fusion applications” JOM, 66-12 (2014) 2427.

[2] M. E. Alam, N. J. Cunningham, D. Gragg et al., **“**Mechanical property characterization of a larger best practice heat of 14YWT NFA1**”**, DOE/ER-0313/56 (63-69)

[3] H.C.Chao, “Mechanism of anisotropic lammellar fractures”, Met. Trans. A, 9A (1978) 509.

[4] D. L. Bourell and O. D. Sherby “Texture induced cleavage delamination of warm-rolled low carbon steel”, Met. Trans. A, 14A (1983) 2563.

[5] A.H. Cottrell, “Theory of brittle fracture in steel and similar metals**”,** Trans. A.M.I.E, 212 (1958), 192-203.

CHAPTER 5. CHARACTERIZATION OF THE MICROSTRUCTURE AND TEXTURE OF NFA-1 FOR TWO DEFORMATION PROCESSING ROUTES

5.1 OBJECTIVE

The objective of this research is to characterize the effect of different processing routes on the microstructural development and texture evolution of the FCRD-NFA-1alloy to facilitate the fabrication of component structures.

5.2 SUMMARY

Our previous investigation showed that NFA-1 produced through ball milling and hot extrusion followed by hot cross rolling suffers from severe micro-cracking on planes parallel to the plate surface and normal to the thickness direction. The microcracking inhibits fabrication of components, such as thin wall tubing, by conventional processing routes. This work reveals that a strong {001}<110> brittle texture component develops in NFA-1 during thermo-mechanical processing. Dislocation pile-ups at low angle boundaries result in formation of cleavage micro-cracks on {001} planes. In contrast, tubes formed by hydrostatic extrusion develop a strong {110}<211> “J1-shear texture” component and low angle grain boundaries. Since preferred slip occurs on {110} planes in bcc Fe, deformation is readily accommodated by easy dislocations glide in the hydrostatic tube extrusion case. This is in contrast to {001} slip planes with pile ups that lead to stress concentrations and micro-crack nucleation in the extruded and cross rolled plate.

5.3 PROGRESS AND STATUS

5.3.1 Introduction

A nanostructured ferritic alloy (NFA), called FCRD NFA-1, was processed and is being qualified as part of collaboration between UCSB, LANL and ONRL [1-2]. Processing the plate involved a series of steps, including: 1) ball milling to produce powders with dissolved Y, Ti and O; 2) consolidation by hot extrusion at 850°C that also precipitated nano-oxides; and, 3) annealing and cross rolling at 1000°C. Following steps produce the base material, in the form of a plate, which is later used as a starting material for the thin wall tube formation through cold working process, such as pilgering. Presence of severe micro-cracks in the through thickness direction of plate, shatters the whole component during tubing by propagating along the radial direction of the tube. Very recently, hot hydrostatic extrusion method has been employed to produce tube from this NFA-1 alloy at Case Western University. It is well reported that application of hydrostatic pressure can change the ductility and fracture behavior of a brittle monolithic metal [3]. Component fabrication from brittle intermetallic material such as NiAl was successfully carried out using hydrostatic extrusion method near to its brittle to ductile transition temperature [4]. Present study is a prelude to understand the microstructural development and texture formation; when, same NFA-1 alloy processed through two different routes, hot extrusion followed by cross-rolling and hydrostatic extrusion.

5.3.2 Materials and Methods

The nominal composition of NFA-1 is 14Cr-3W-0.4Ti-0.21Y-balance Fe. Hot consolidation results in precipitation of an ultrahigh density (order $5x10^{23}$ /m^3) of Y-Ti-O nano-oxides (NO), primarily $Y_2Ti_2O_7$, with average diameters of 2-3 nm. These NO provide exceptional strength accompanied by high ductility, thermal stability and irradiation tolerance, including trapping helium in nm-scale bubbles at their interfaces.

The processing sequence described above resulted in a 12.5 mm thick plate that is characterized by pancake shaped grains. The grain size is taken as the average of the long (l) and short (s) dimensions d

= (l + s)/2 and the grain aspect ratio as r = l/s. The plates also contain a high density of micro-cracks on planes parallel to the plate surface and normal to the thickness direction. The cross rolled plate (or as extruded bar) can, in principle, serve as the starting point for subsequent fabrication of NFA components.

However, the micro-cracks severely limit the conventional cold workability of NFA-1, and more generally similarly processed NFA [1, 2]. For example, tube processing typically involves multiple room temperature pilgering and high temperature annealing step sequences [5-7]. Very recently, hot hydrostatic extrusion was used to produce a small length of thin wall tubing from the NFA-1 plate with remarkable success [8]. Hot extrusion was performed two times with an area reduction ratio of 4:1, which is equivalent to 44% applied strain. An aluminum mandrel was used to promote uniform wall thickness and stable deformation. The final product is completely free from micro-cracking. This motivated in-depth characterization of the microstructure and texture of NFA-1, for both of these processing routes. The microstructure of the plate and hydrostatically extruded tube were observed by SEM, TEM on FIBed liftouts and EBSD were used to characterize the corresponding textures. The characterization studies led to a micromechanical hypothesis regarding formation of the microcracks. The plate and tubing reference directions and specimen orientation are schematically illustrated in Figure 5.1.

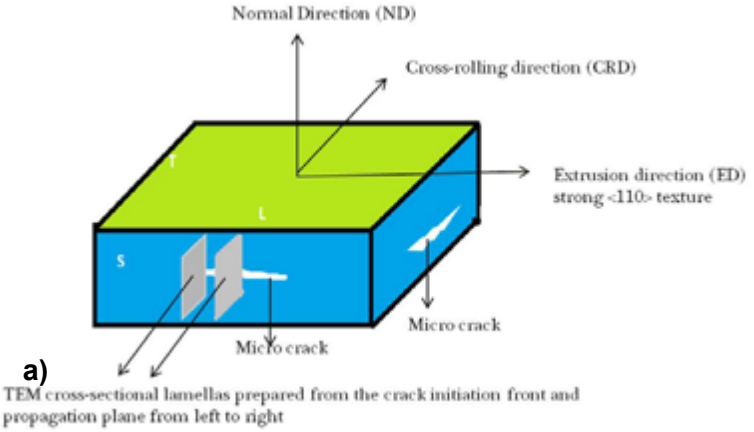

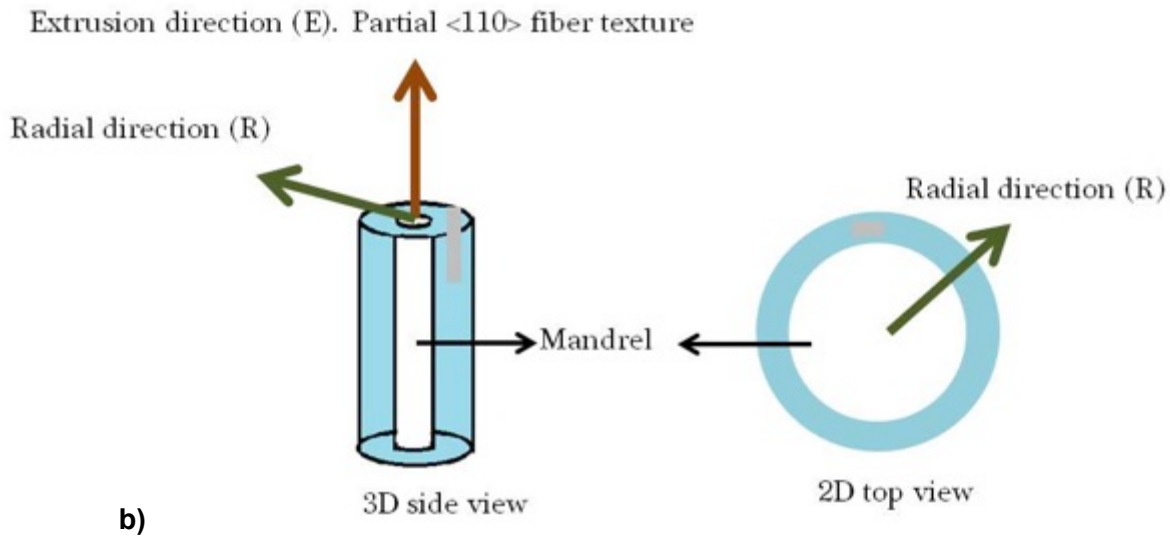

Figure 5.1. a) Schematic of a plate orientations referenced to the prime deformation directions. Micro-cracks, which are also shown in the image, run perpendicular to the short (S)-thickness direction. The

tensile and cracked specimen orientation (L, T, and S) convention is also shown in Figure 3.1a. and, b) a schematic of the hydrostatically extruded tube showing the two key extrusion (E) and radial (R) directions. The region from where the TEM lamella is prepared is marked by grey box.

For cracks this convention is that the first letter defines the direction parallel to the front: L, T and S, and the second letter the direction of propagation. For tensile tests the letter defines the specimen axis. Planes and surfaces can also be defined in terms of L, T, S as parallel to the top (LT), side (LS) and front (ST).

5.3.3 Results

The two NFA-1 conditions characterized are: a) plates deformation processed by hot extrusion, annealing and cross rolling; and, b) tubes fabricated by hydrostatic extrusion. The hot extrusion, at Case Western University, was carried out starting with a gun drilled thick wall tube on a mandrel. The tube was taken from the cross-rolled plate with its axis in the extrusion direction. Therefore, it is very important to define the primary deformation orientations for both processing conditions by referencing physically relevant directions. Figure 5.1a shows a schematic of the plate, defining the longitudinal (L), transverse (T) and short (S) directions as labeled accordingly along with primary deformation extrusion (L) and cross-rolling (T) coordinate system. Figure 3.1b shows the two relevant radial and extrusion directions for hydrostatic processing.

Microstructural characterization by SEM

Figure 5.2a and b show SEM images for LS and LT views, respectively, of the NFA-1 plate. Grains are elongated in the extrusion direction in case of LS view. Black Ti/Y rich precipitates along with the micro-cracks are seen in the SEM image for the LS view in Figure 5.2a, No microcracks are found for the LT view shown in Figure 5.2b. In case of tube, Figure 5.3 shows the SEM image of the polished surface of the sectioned tube normal to the extrusion direction.

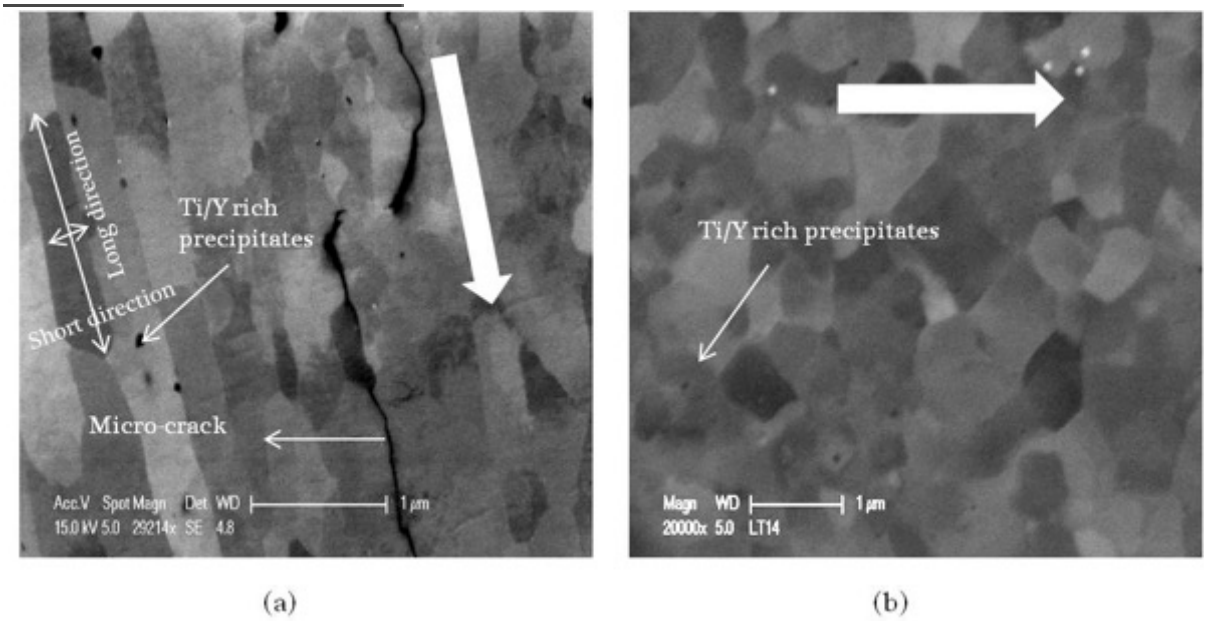

Figure 5.2. a) A SEM image for the LS view; b) a SEM image for the LT view.

The large arrows mark the extrusion direction. Other components of the microstructure are labeled. The long and short dimensions of an individual grains are seen in the Figure 5.2a. The same method for grain size measurement is followed for the microstructural characterization of both tube and plate.

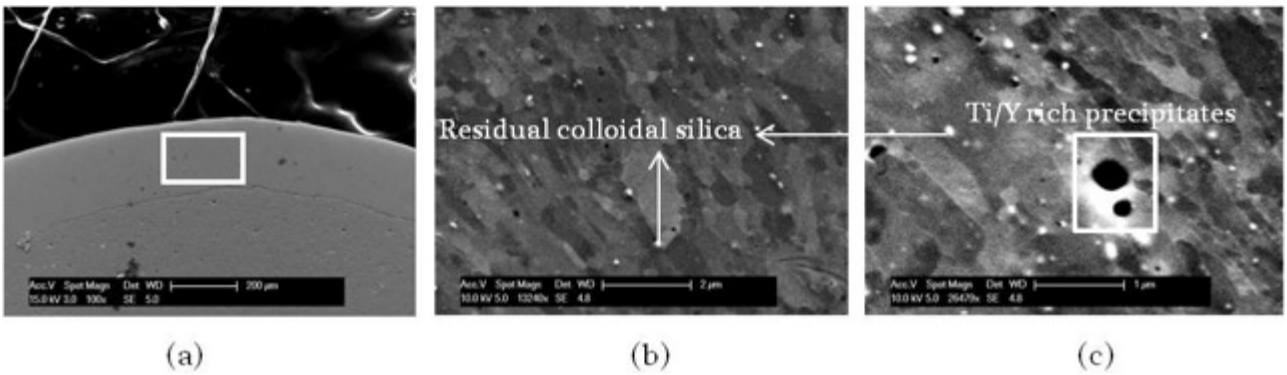

Figure 5.3. a) A low magnification SEM micrograph showing the tube wall cross section with the mandrel. The extrusion direction is normal to the image plane; b) a magnified view of the location marked by the white box in Figure 3.3a and, c) grains elongated in the radial direction (maximum sheer stress direction) of the hydrostatically extruded tube (see Figure 5.1b), where the dark particles are either Ti and Y rich precipitates, while the bright particles are residual colloidal silica.

The corresponding average grain sizes and standard deviations for the plane parallel to the top (LT) and side surface (LS) of the plate are summarized in Table 5.1. Here the grain size is taken as the average of the long and short dimension and the aspect ratio as the long divided by short dimension. The grains observed in the LS view parallel to the thickness direction have “flattened” shapes and are elongated along the observed extrusion direction. The grain size distributions and aspect ratio for the tube are also given in Table 5.1. The SEM micrographs of the tube section in Figure 5.3b and c reveal grains elongated in the radial direction. SEM images in Figure 5.2a and Figure 5.3c clearly show the plate’s side (LS) view, the contrast-orientation differences between the elongated grains are much stronger in comparison to the tube. Most notably, hydrostatic extrusion does not result in the formation of the microcracks.

Table 5.1. Showing the grain size and aspect ratio for the plate and tube conditions.

Sample surface	Average grain size (μm)	Grain aspect ratio
LT plane for plate	454 ± 142	1.2 ± 0.2
LS plane for plate	1077 x 397	2.7 ± 1.1
Cross-sectional plane for tube	590 ± 210	2.1 ± 1.1

Microstructural characterization by TEM

Figure 5.4a shows a SEM image of the tube cross-section indicating the location of a FIB lift out at a ≈ 45° angle to the radial, maximum shear, direction. The FIBed foil face is parallel to the extrusion direction as shown in Figure 5.4b.

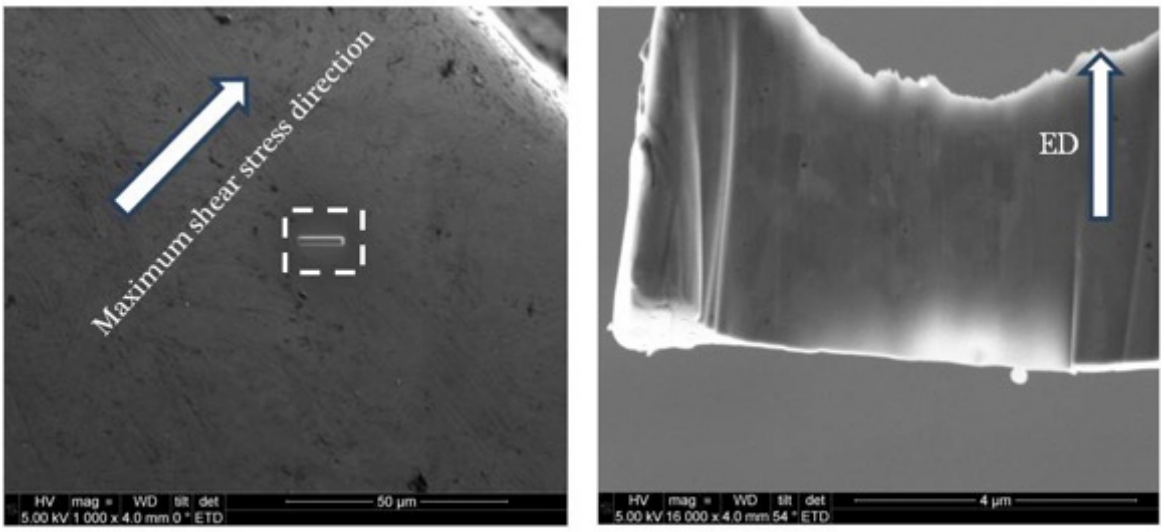

Figure 5.4. a) The location of TEM lift-out for the tube; and, b) the corresponding FIBed TEM foil.

The bright field (BF) TEM images in Figures 5.5a to d clearly demonstrate that hydrostatically extruded tube contains a significant population of dislocations in the vicinity of a low angle boundary, marked in Figures 5.5c and d. The boundary between the grains, marked by the dashed box, is ill defined, with minimum contrast between the two sides, indicating a low angle character.

In order to accurately determine the grain sizes in the tube, the circled grain in Figure 5.6a is tilted in a two- beam condition (see Figure 5.6b) and the corresponding dark field image is shown in Figure 6c. The SAD pattern from the circled region using the smallest 20μm aperture in Figure 5.6b, shows overlap of the near <111> grains, with only a small angle of misorientation. The corresponding dark field (DF) image in Figure 5.6c shows that all the bright grains are roughly equiaxed. These observations lead to the conclusion that low angle grain boundaries exist in what appear in BF to be elongated grains. This also confirms our SEM observation of grains elongated along the radial direction of the tube with a minimal contrast between grains of either side of the boundary, as shown in Figure 5.3b and c. Both SEM and TEM observe a similar average small grain diameter of ~ 0.5μm.

Figure 5.7 show BF and DF TEM images of the plate side LS view, where the foil area is perpendicular to the extrusion direction. Figure 3.7a shows that microcracks track the elongated grain with lengths of ~ 0.4 ± 0.1 and ~ 3± 1 μm along the short and elongated directions, respectively. The plate condition contains a high dislocation density. SAD patterns, at a 0° tilt, are shown in Figures 5.7b and c, for the two circled regions in Figure 5.7a. The SAD patterns show the two bcc <110>-zone axis are only slightly misoriented with respect to each other. The DF image in Figure 5.7d shows a trans-granular crack propagating through a (001) grain (the corresponding (002) spot is marked in Figure 5.7b with a white circle). The BF image shown in Figure 5.7e is for a <110>-zone axis. These results show that, in contrast to the tubing, in the NFA-1 plate condition, elongated grains are separated by high angle boundaries.

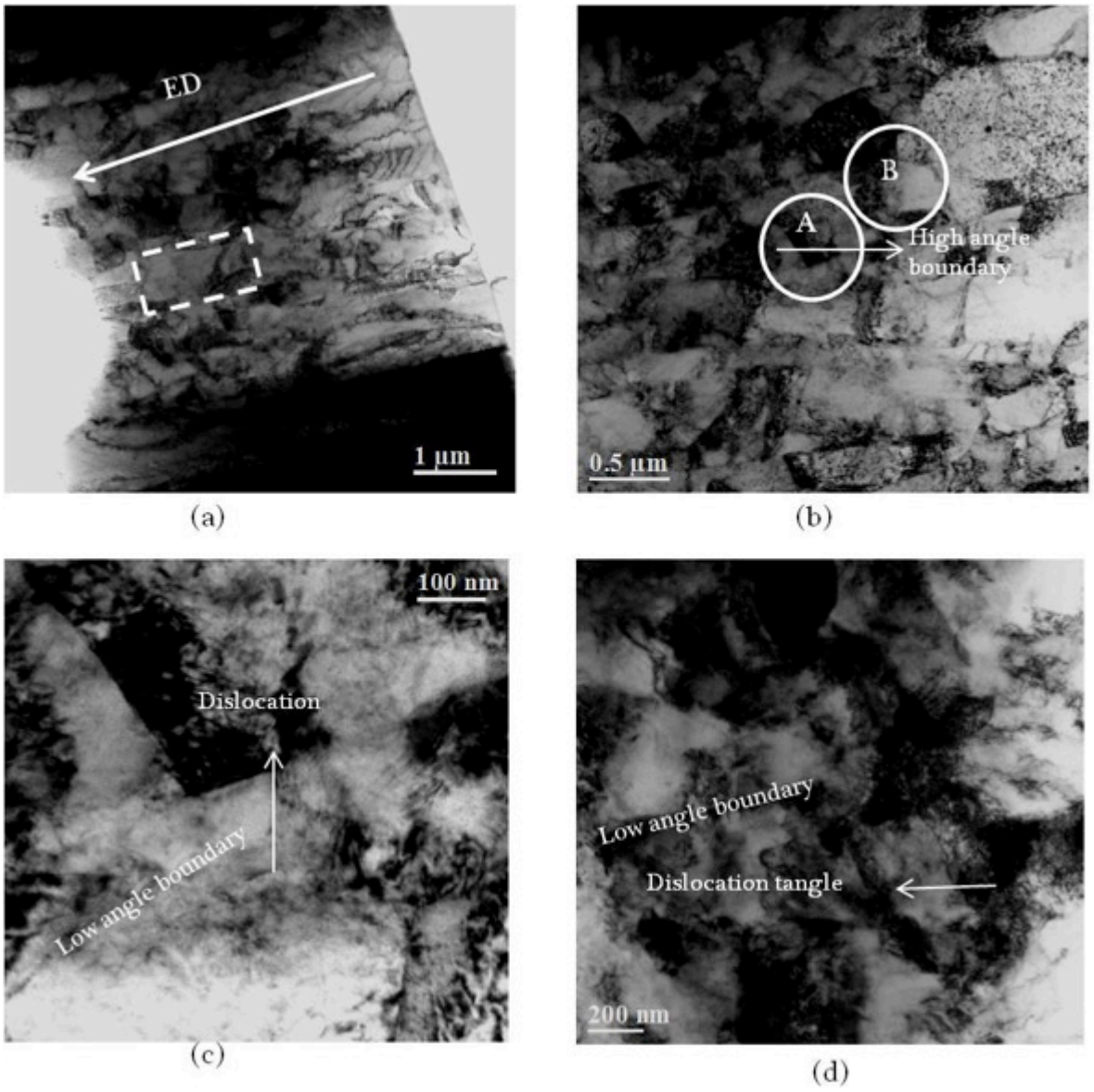

Figure 5.5. A bright field image of the tube microstructure at different magnifications: a) the extrusion direction elongated grain structure; b) a high angle grain boundary; c) a magnified view of region marked as (A) in Figures 5.5b; d) a magnified view of region marked as (B) in Figure 5b showing low angle boundaries and dislocations tangles.

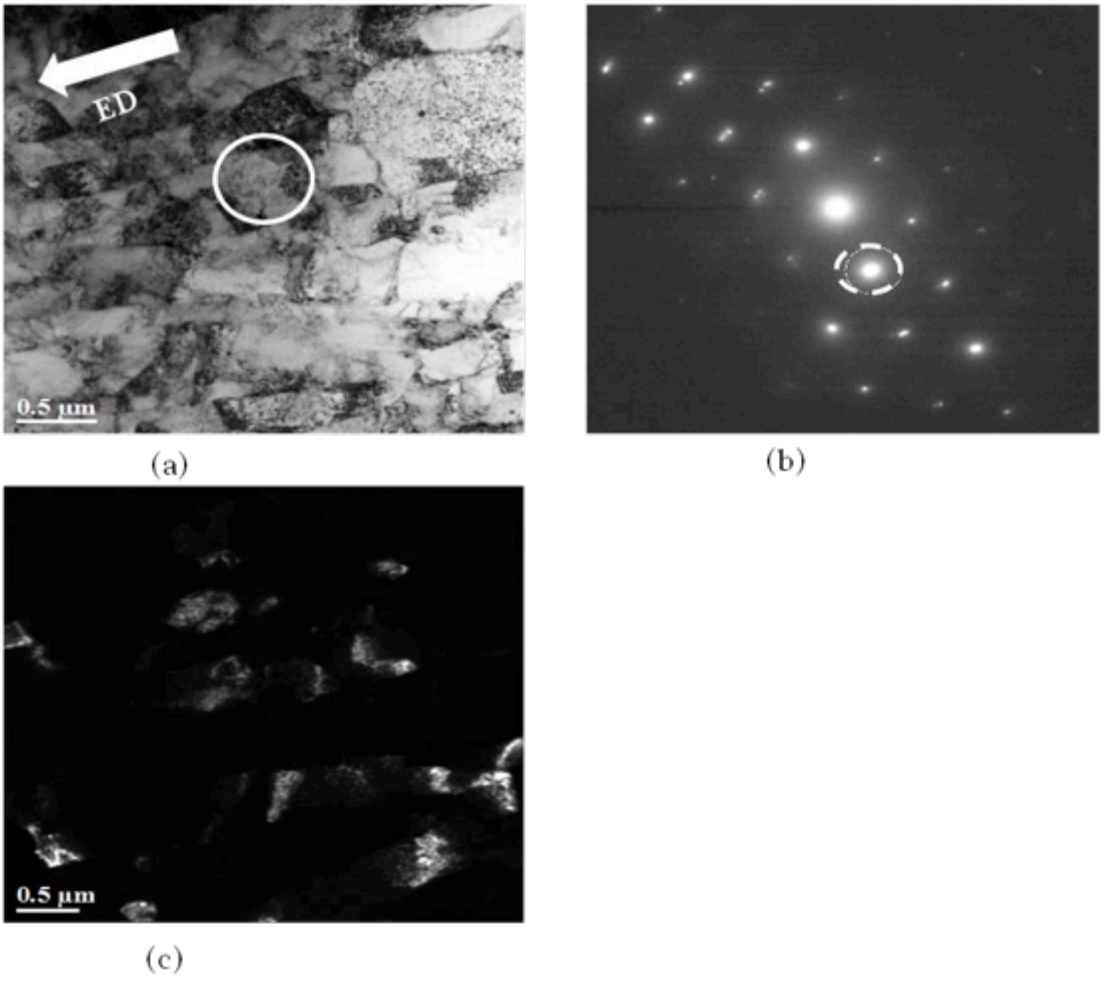

Figure 5.6. a) BF image of the tube microstructure; b) the SAD pattern for the circled region along the <111> zone axis under two beam conditions with the (110) bright spot circled; and, c) the dark field image of the (110) spot

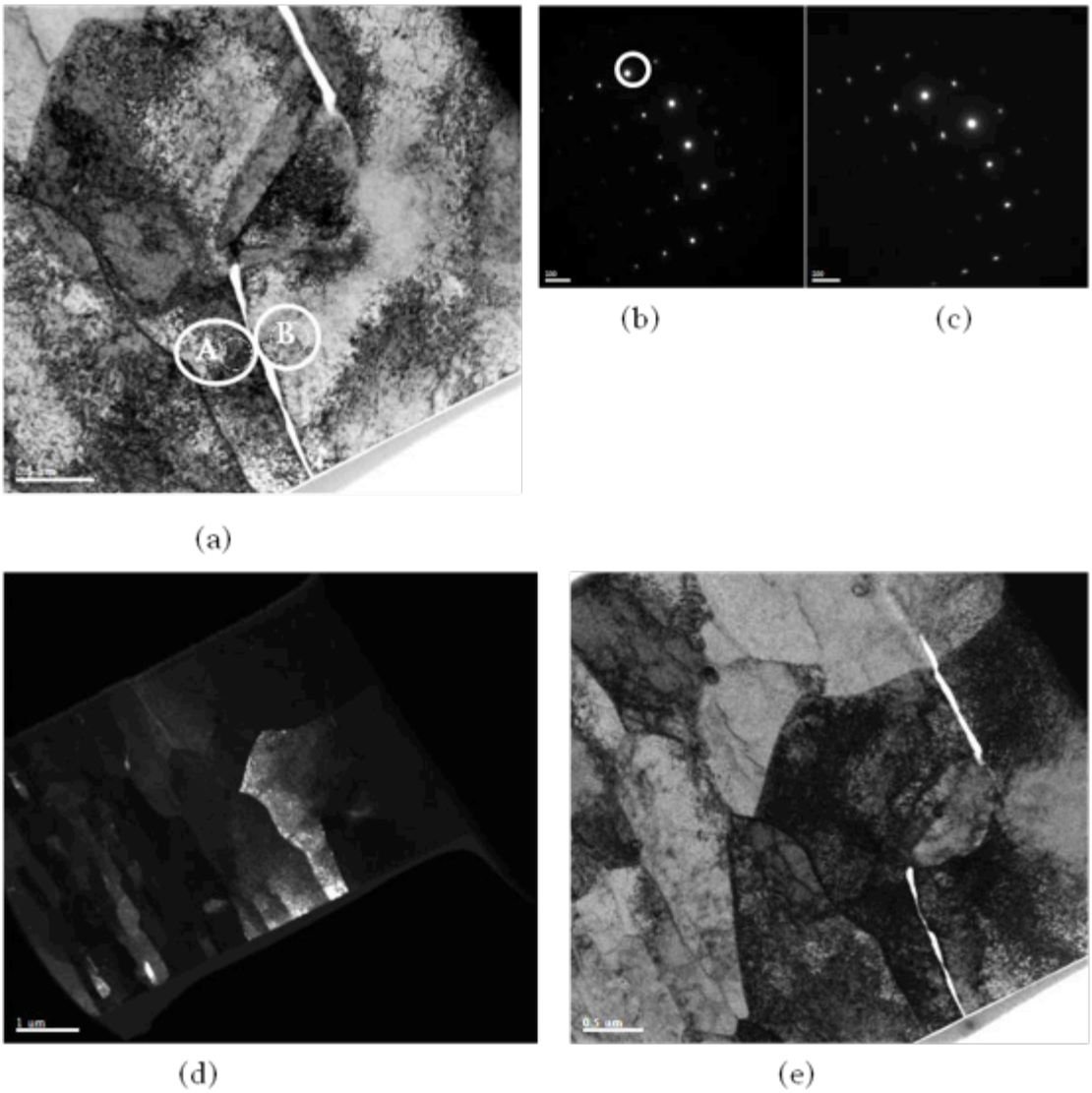

Figure 5.7. a) shows the BF image of the LS sample; b) and c) are the SAD patterns from the circled regions in a; d) a DF image from the circled SAD spot in Figure 5.7b; and, e) a BF image for a<110> zone axis.

Texture Characterization by EBSD

Texture measurements for both the NFA-1 processed conditions were carried out by EBSD. For the plate, EBSD was carried out on both the side-parallel (LS) and top-parallel (LT) views (as shown in the schematic Figure 5.1a). Pole figure (PF) maps for the LT and LS parallel surface planes are shown in Figure 5.8. The PF show that the plate contains strong α-fiber texture along the extrusion direction with a partial α-fiber along the cross-rolling direction. A prominent <100>-texture component is observed in the direction normal to LT parallel surface planes.

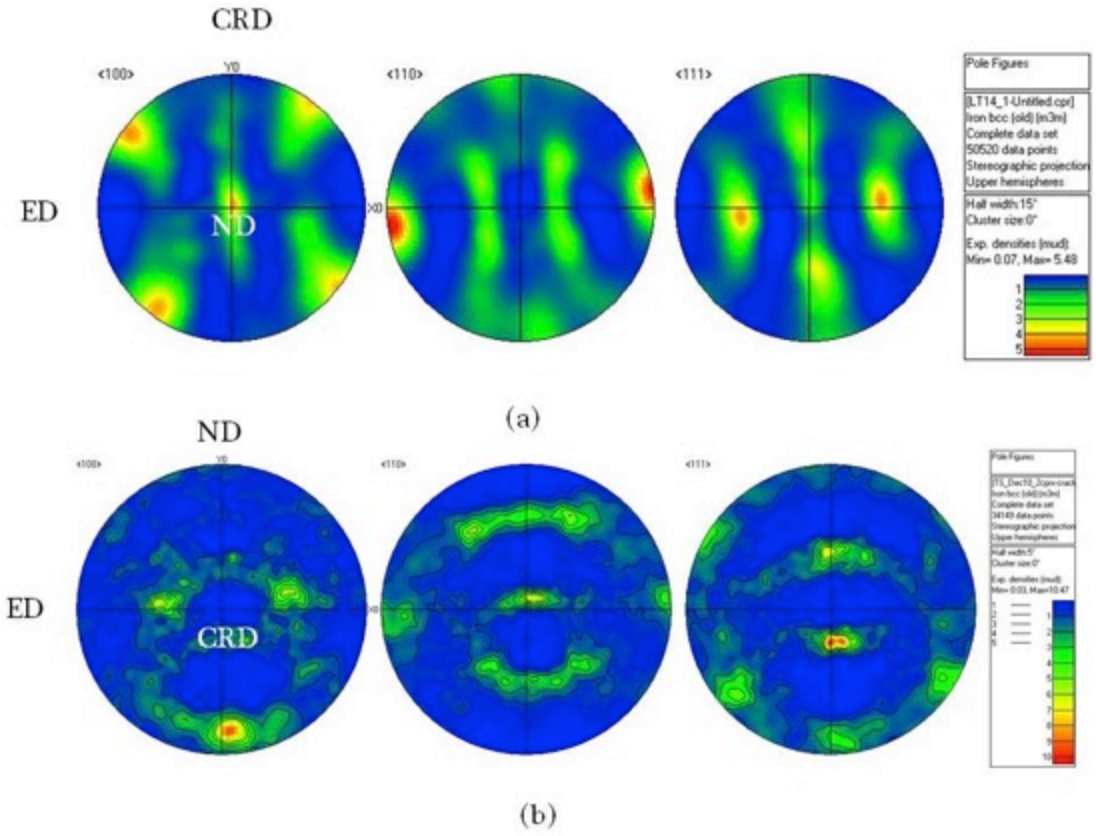

Figure 5.8. a) LT, and b) LS views: EBSD <100>, <110>, <111> poles of the plate sample, respectively. Equivalent deformation directions for the plate are also shown in the PF respectively by following the convention defined in Figure 5.1a and following text.

Texture measurements were carried out on a polished surface shown in the Figure 5.3a, normal to the extrusion direction. The texture of the tube is quite different compared to the plate as shown in Figure5.9. The tube has a partial α-fiber texture in the extrusion direction.

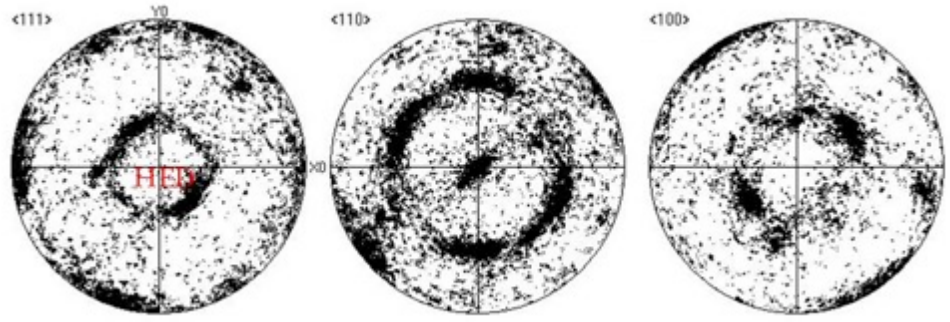

Figure 5.9. Pole <111>, <110>, <100> poles figures of the tube. Hydrostatic extrusion direction for the tube, schematically shown in Figure 5.1b, is also marked in the <111> pole figure of <111> pole.

PF analysis shows development of α-fiber along the extrusion direction for both the tube and the plate, while for the direction normal to the plate surface parallel planes and tube radius, the texture components are <100> and <111>, respectively. This observation is further corroborated in the inverse pole figures (IPF) in Figure 3.10, which show density of pole projections on a stereographic triangle with <001>, <110> and <111> vertices for the plate in the prime deformation directions.

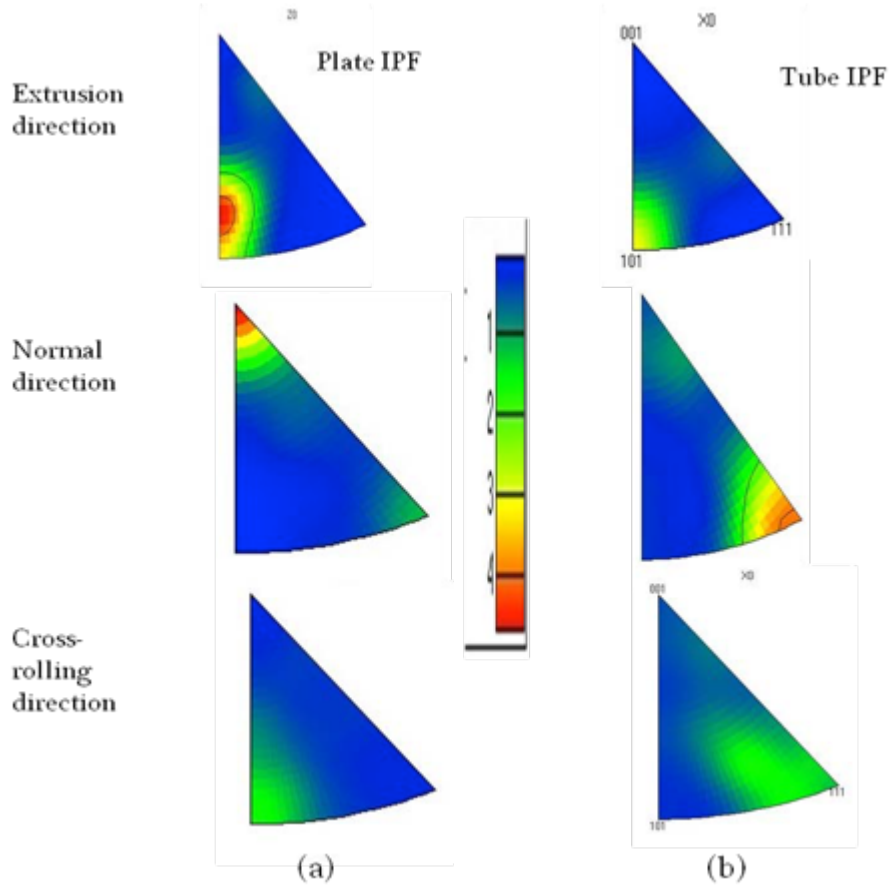

Figure 5.10. IPF maps of the tube and plate: a) the plate IPF for extrusion, surface normal and cross-rolling directions following the convention in Figure 3.1a; b) the tube radial direction, which is equivalent to the both cross-rolling and normal directions for the plate (see Figure 3.1b.) The extrusion direction is the same for both tube and plate.

The IPF analysis clearly demonstrates that while along the extrusion direction texture is similar for both the tube and plate, it differs in the normal direction: a strong <100> in along the normal direction for the plate, and <111> in the normal radial direction for the tube. The latter is also the direction of the maximum sheer stress in the case of the hydrostatic extrusion.

PF and IPF maps are basically a 2D stenographic projection of either crystallographic directions or the deformation directions for the plate or tube. A fully accurate description of the texture and its components is not possible using PF or IPF plots. A more accurate way of representing texture requires an orientation distribution function (ODF) analysis. All the possible orientations in a sample are projected in a 3D Euler space (defined by three Euler's angles of, φ, φ_1 and φ_2) as shown in Figure 5.11. Preferred orientations

produce a high-density region around a certain combinations of these angles. Figure 5.11 shows a 3D ODF plot created from the PF data using the series expansion method [9]. For the ease of visualization, 2D sections of the 3D cube containing φ and φ_1 from 0 to 90° for constant value of φ_2 is shown in Figure 5.12.

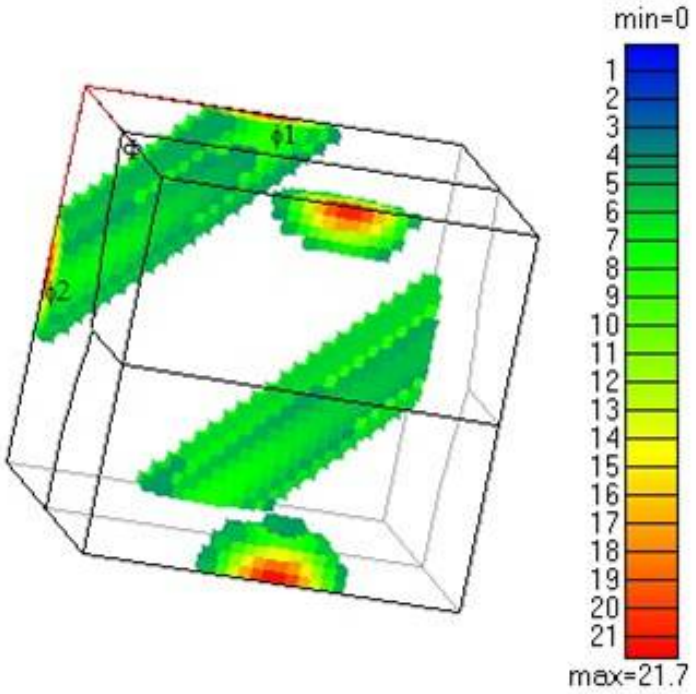

Figure 5.11. A 3D ODF plot for the plate.

The most important texture components for bcc steels occur at φ_2 = 0 and 45° sections [8], which are shown in Figures 5.12a, d and 5.12b,e for the plate and tube, respectively. Figures 5.12c and f show the ideal texture components for bcc steels (reproduced from Ref. [8]). These sections show the texture is completely different in the plate versus the tube. These ODF maps are compared with ideal φ_2 = 0 and 45° sections of bcc steel [8] shown in Figures 5.12c and f.

The texture components in the plate and tube are also shown on the ideal ODF plots as brown circle (plate) and blue box (tube), respectively. Notably the plate contains strong {001} <110> brittle cleavage texture components. Note, the PF and IPF analysis mainly showed a <110> α-fiber in the plate. However, the ODF analysis shows that α-fiber family contains three strong texture components: {001}<110>, {112}<110>, {111}<110>, with {001} <110> being by far the most dominant. Again, the {001}<110> α-fiber texture is also the most brittle cleavage system in bcc iron. This partly explains the origins of microcracking on (001) planes in the plate. The texture of the tube is quite different with dominant components of {011}<211> and a lower fraction of {011}<111>. These two components belong to the ζ-fiber texture family as shown by the brown line in Figure 5.12c.

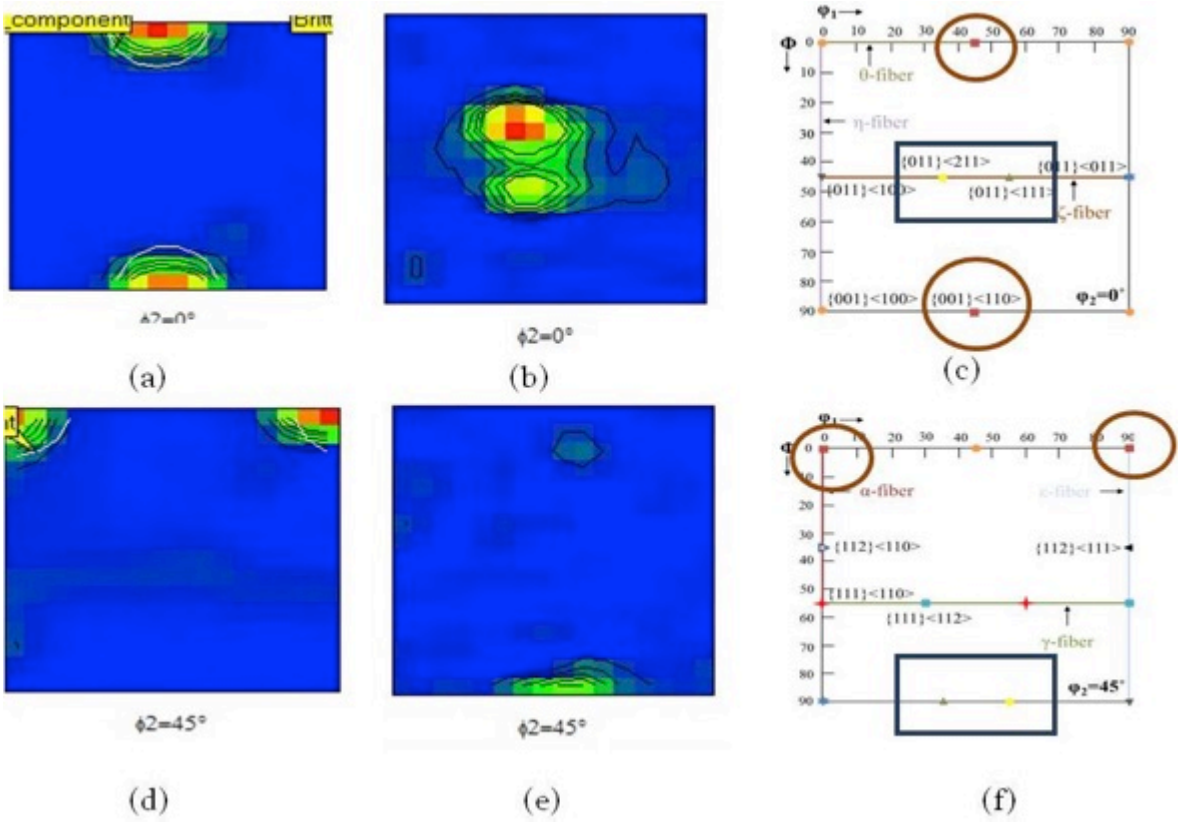

Figure 5.12. a), b) and c) (top) are φ2 = 0 sections for the plate, tube and ideal ODF texture components for bcc steel, respectively [8]. Figures 3.12 d), e) and f) (bottom) are for the corresponding φ2 = 45° section.

5.3.4 Conclusions

• Various characterization methods have been used to explore the microstructures and crystallographic textures that develop in NFA-1 under two deformation processing paths.In the case of the hot extruded and cross-rolled plate, the grains are elongated along the extrusion direction and a strong α-fiber texture develops along with a brittle cleavage {100} <011>-fracture system. This restricts glide on {100} planes lead to dislocation pile ups and stress concentrations with increasing strain, resulting in formation of corresponding population of micro- cracks.

• In case of hydrostatic extrusion of tubes, the grains are elongated along the maximum sheer stress direction and develop corresponding sheer texture components of {110} <112> and {110}<111>. Deformation occurs on {110}-bcc easy glide planes and is accompanied by formation of low angle sub grain boundaries. These microstructures and textures are not brittle, hence, cracking is not observed in the hydrostatically extruded tube.

REFERENCES

[1] G.R. Odette, “Recent progress in developing and qualifying nanostructured ferritic alloys for advance fission and fusion applications”, JOM, Vol-66, Number-12, 2012, 2427-2441.

2. M.E. Alam, N. J. Cunningham, D. Gragg, K. Fields, G. R. Odette, D. T. Hoelzer and S. A. Maloy, “Mechanical Properties Characterization of a Larger Best Practice Heat of 14YWT NFA1”, Fusion Reactor Materials Program, June 30, 2014, *DOE/ER-0313/56 – Volume 56.*

[3] J.J. Lewandowski and P. Lowhaphandu, “Effects of hydrostatic pressure on mechanical behaviour and deformation processing of materials”, International Materials Review, 43(4), (1998), 145-187.

[4] J.J Lewandowski, B. Berger, J.D. Rigney, and S. N. Patankar, "Effects of Dislocation Substructure on Strength and Toughness in Polycrystalline NiAl Processed via High Temperature Hydrostatic Extrusion", Philosophical Magazine A, 78 (3), (1998), 643-656.

[5] S. Ukai, “Perspective of ODS alloys application in nuclear environments”, Journal of Nuclear Materials, 307-311, (2002), 749-757.

[6] B. Leng, “Recrystallization texture of cold-rolled oxide dispersion strengthen ferritic steel”, ISIJ International, 51 (2011), 951.

[7] L. Toualbi, “Assessment of a new fabrication route for for Fe-9Cr-1W ODS cladding tubes”, Journal of Nuclear Materials, 442 (2013) 410-416.

[8] Un-published work – “Effect of tube processing methods on the texture and grain boundary characteristics of 14YWT Nanostructured Ferritic Alloys” - work carried out in LANL.

[9] H.J. Bunge, “Texture Analysis in Material Science: Mathematical methods”, Butterworths, London, p-323, 1982.

CHAPTER 6. CHARACTERIZATION OF PROCESSING INDUCED IMPURITY PHASE PRECIPITATES IN THE AS PROCESSED FCRD-NFA-1 ALLOY

6.1 OBJECTIVE: This study is aimed to characterize the microstructure and chemistry of the impurity phase precipitates produced in the as processed NFA-1 alloy, and, its effect on the high-temperature mechanical properties of the alloy.

6.2 SUMMARY: Microstructure observation of the as processed NFA-1 alloy reveals that the as processed alloy contains some impurity phase along with the desirable nano-oxides (NOs). This impurity phase precipitates appear as black, near to round shaped, particle-like features in SEM micrographs, with a size distribution of 10-260nm. These particles are arranged as strings in the direction of primary deformation axes, hot extrusion, and cross-rolling. Chemical analysis using electron probe micro-analyzer demonstrates that these particles are either rich in Ti or Y. TEM observation of these particles reveals that they are nucleated at the grain boundary as an incoherent precipitate, even sometimes at the triple junction. EDS analysis using TEM further confirms that it is composed of either Ti-O or Y-O; whereas, numbers of the Ti precipitates are more compared to the Y rich ones. High-temperature heat treatment of this alloy at 1300°C/5 hr shows the complete dissolution of these precipitates, suggesting these are a metastable phase. These precipitates can act as nucleation sites for the ductile fracture at high temperature; hence, the premature fracture may happen before attaining their expected toughness value at elevated temperature.

6.3 PROGRESS AND STATUS:

6.3.1 Introduction: Nanostructured ferritic alloys (NFA) are targeted to design in such a manner that it should contain 1-3 nm fine dispersions of Y-Ti–O nano-oxides to achieve, a high radiation tolerance by managing helium, and, exceptionally high thermal stability up to ~1300°C [1-3]. The alloy also poses a very high tensile strength and high temperature creep strength [1, 3]. It has been postulated that the excellent creep and radiation tolerance of this alloy is due to the presence of these fine scale nano oxides, which impede dislocation and boundary movements during high-temperature deformation. On the other hands, it can effectively trap helium in nanometer scale bubbles and prevents to form a big void [1 2]. An enormous effort has been put forward to characterize the structure and chemistry of these nano-oxides using different characterizations techniques, such as TEM, APT, SANS, SAXS [4, 5]. However, microstructural characterization also reveals that the alloy also consists of some bigger size precipitates 10-150 nm, rich in either Ti or Y [6, 7]. Chemical analysis of these precipitates using EDS and EELS suggest that there are formed as precipitates of Ti-C-O-N or sometimes pure Y_2O_3, originated as a processing induced inhomogeneity [1, 6, 7]. A little effort has been given to characterize the exact structure and chemistry of these precipitates, as well as its role on determining the mechanical properties of this alloy. The present investigation is a prelude towards that path.

6.3.2 Materials and methods: The present investigation was carried out on a newly develop NFA alloy, FCRD-NFA-1, a variant of ODS class of steel. This alloy has been developed with a close collaboration between UCSB, LANL, and ORNL. The nominal composition of the alloy is 14Cr-3W-0.4Ti-0.3Y and balance Fe. The alloy powder is first ball milled, then canned and degassed at 400°C, and, hot extruded at 850°C, which is further annealed and cross-rolled along perpendicular to the HE direction at 1000°C. Microstructural characterizations were carried out using SEM and TEM. The elemental chemical analysis was performed using electron probe micro-analyzer (EPMA) and energy dispersive spectroscopy attach with a TEM. Thin TEM lamellas are prepared using FIB-Lift out methods. In order to characterize the thermal stability of the impurity phase precipitates, as processed alloy sample is annealed at 1300°C for 5 hr inside a vacuum furnace.

6.3.3 Results: Figure 6.1 shows a representative SEM micrograph of the side surface (LS) of NFA-1 plate, where the grains are elongated in the extrusion direction. The impurity phase precipitates appear as a black particle-like features, and, collectively those are arranged as strings along the extrusion direction. The particles are looked like near round shaped. Size distribution, the average spacing between two particles, measured from the SEM micrographs of the top, side and front surfaces, are listed in Table 6.1.

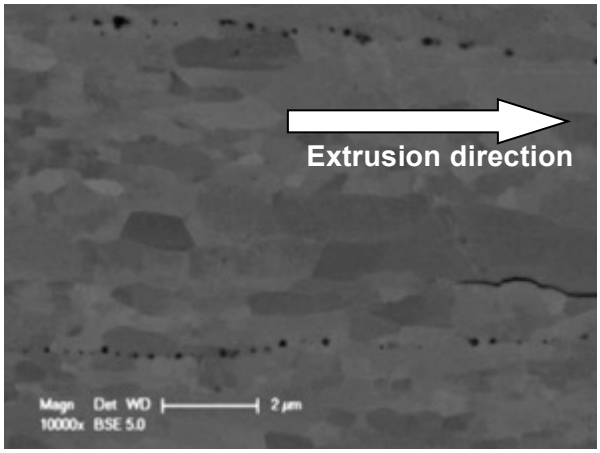

Figure 6.1. SEM micrographs of the LT view or plane parallel to the top surface of NFA-1 as processed plate shows impurity phase precipitates as a black particle like feature. Extrusion direction is marked with a white arrow.

Table 6.1. Statistics of particles size and interparticle spacing for planes parallel to the top (LT), side (LS) and front (TS) of as processed NFA-1 plate.

Sample Orientation	Ti/Y rich particle size (nm)	Interparticle spacing along x (nm)
LT/ Top surface	57 ± 33 Range: 10-262	228 ± 106
LS/Side surface	62 ± 32 Range: 11-188	303 ± 210
TS/ Front surface	68 ± 33 Range: 22-180	279 ± 160

Figure 6.2a-f and 6.3a-f display the compositional maps of the plane parallel to the top (LT) and side (LS) surfaces of the NFA-1 plate, measured using an electron probe micro analyzer. Fe, Cr, and W are homogeneously distributed throughout the map; whereas, Ti and Y form clusters. SEM micrographs together with EPMA maps confirm that those precipitates are rich in Ti and Y. The numbers of Ti-rich clusters are much more compared to the Y rich one.

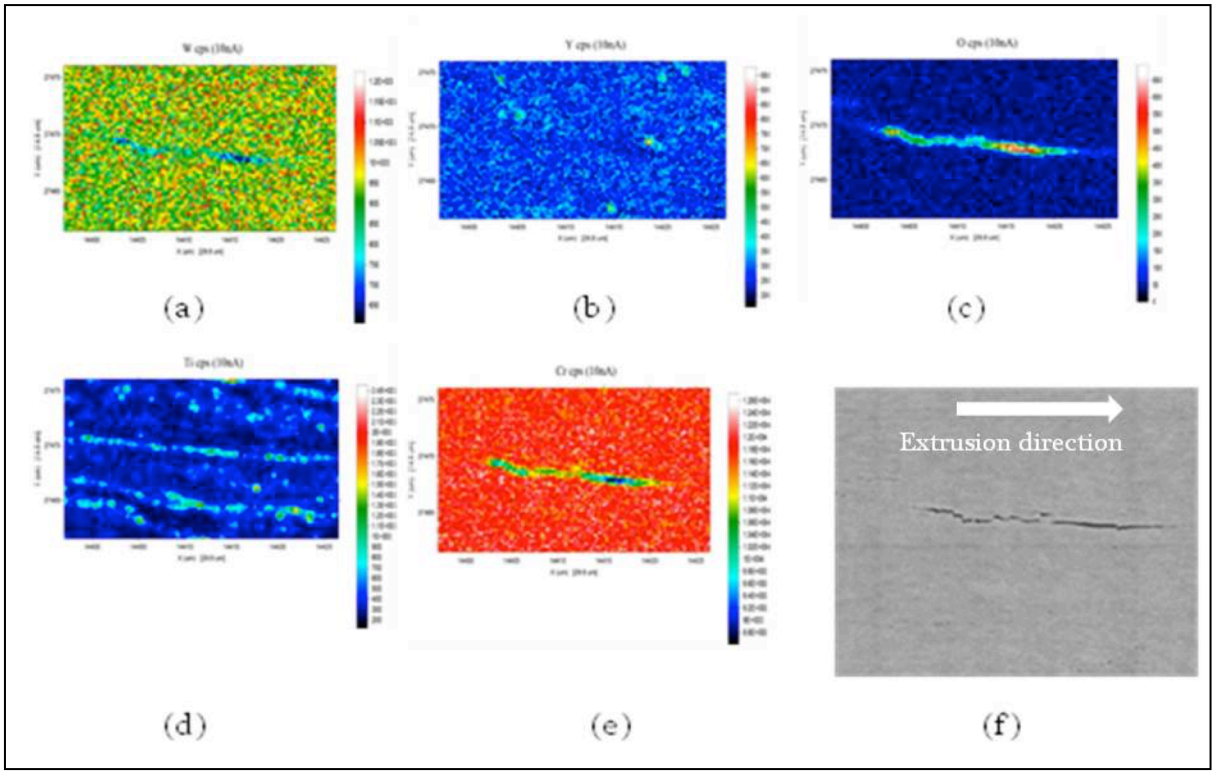

Figure 6.2. a-e) Elemental compositional maps for the LS view and f) the cracked region of interest

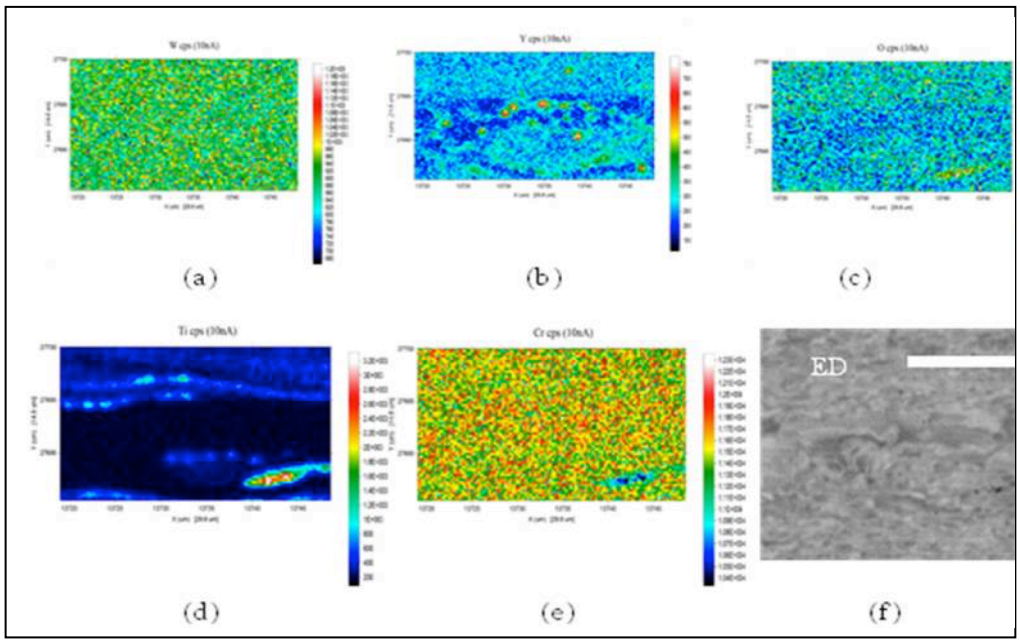

Figure 6.3. a-e) Elemental compositional maps for the LS view and f) the region of interest

An in-depth microstructural characterization and chemical analysis of these impurity phase precipitates were performed using TEM. Similar to SEM micrographs, these precipitates are also appeared as dark particles like features in an STEM-HAADF image, see Figure 6.4. BF-TEM images of two of these precipitates are shown in Figure 6.5a and 6.5b. From the micrographs, it is clearly evident that those precipitates are nucleated at either grain boundary or grain boundary triple junction. Both the precipitates have a size of ~ 50 nm.

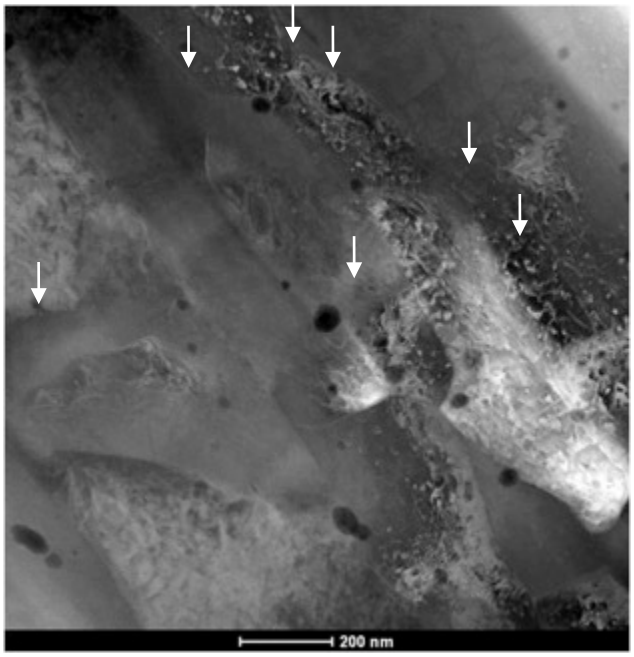

Figure 6.4. STEM–HAAD image of the NFA-1 alloy shows impurity phase precipitates as black particles, marked in the figure using arrows.

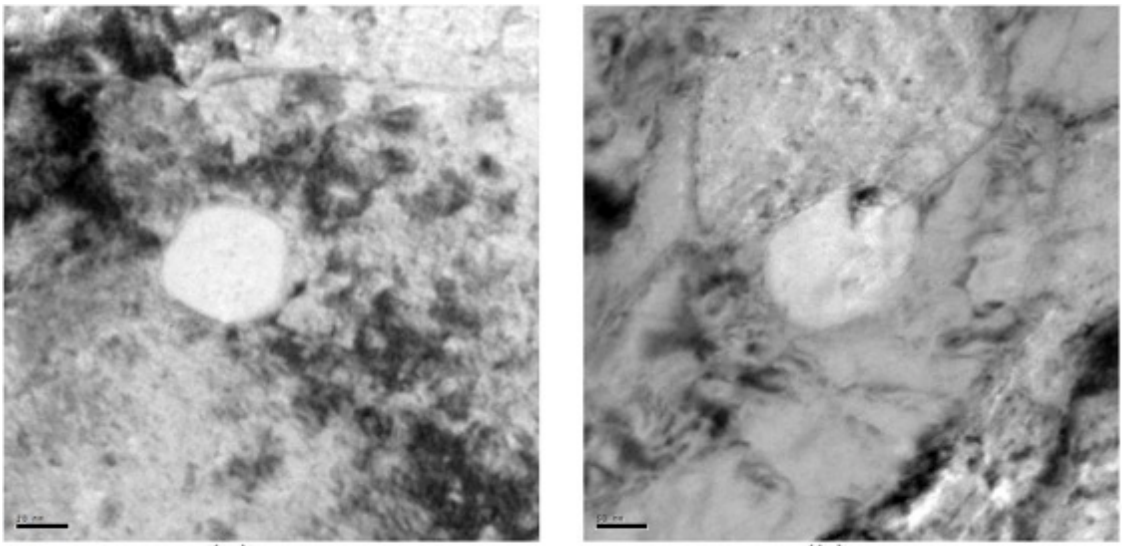

Figure 6.5. a) and b) BF-TEM image of an impurity phase precipitate nucleated at a grain boundary and triple junction, respectively.

Lattice fringe image of the precipitate, shown in Figure 6.6a, clearly displays that the interface between the matrix and precipitate is completely incoherent. The shape of the precipitate is not spherical; rather it takes a faceted polyhedral shape. The fast furrier transform (FFT) pattern of the precipitate captured from the region, marked as 2, displays that the precipitate has a different structure than NOs of $Y_2Ti_2O_7$ or $Y_2Ti_2O_5$, seen in Figure 6.6b [5]. Amorphous like appearance of the region, marked as 1, implies that this portion of the precipitate does not satisfy a zone axis condition, whereas region 2 does satisfy a near zone axis condition. This gives an indication of strongly faceted nature of the precipitate. Higher magnification view of the lattice fringe image of Figure 6.6a, shown in Figure 6.7, does not exhibit continuous lattice fringes. Even within the precipitate, regions of discontinuous lattice fringes with a dark contrast is clearly visible. STEM-HAADF image of the same particle also shows inside the precipitates some white particles like contrast, see Figure 6.8a. EDS spectrum collected from the precipitate, shown in Figure 6.8b, indicates that this particle is enriched with Y and O.

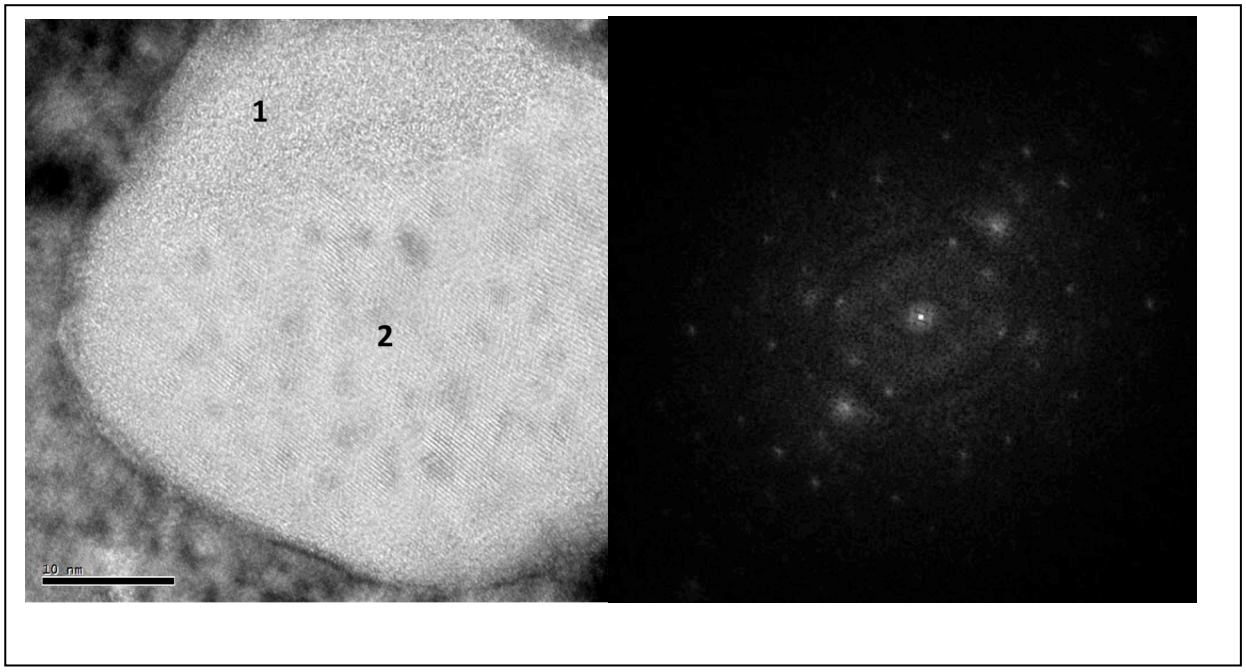

Figure 6.6. a) HR-TEM image of the precipitates shown in Figure 6.5a). b) FFT pattern of the PPT captured from the location, marked as 2 in Figure a).

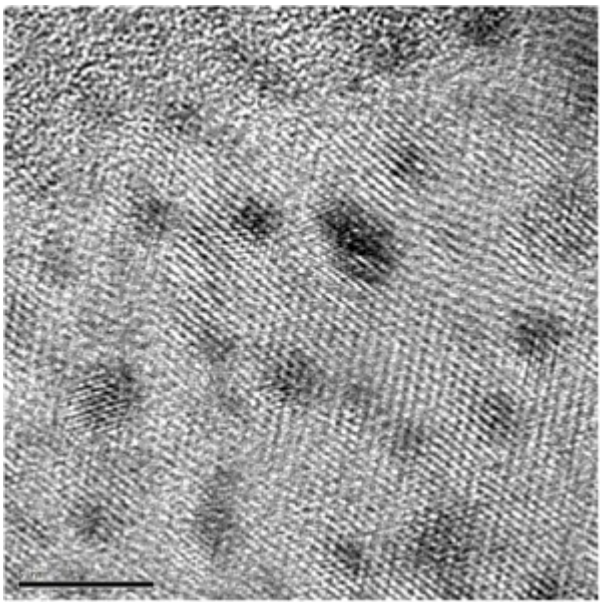

Figure 6.7. Higher magnification view of the Lattice fringe image of the precipitates shown in Figure 6.5a.

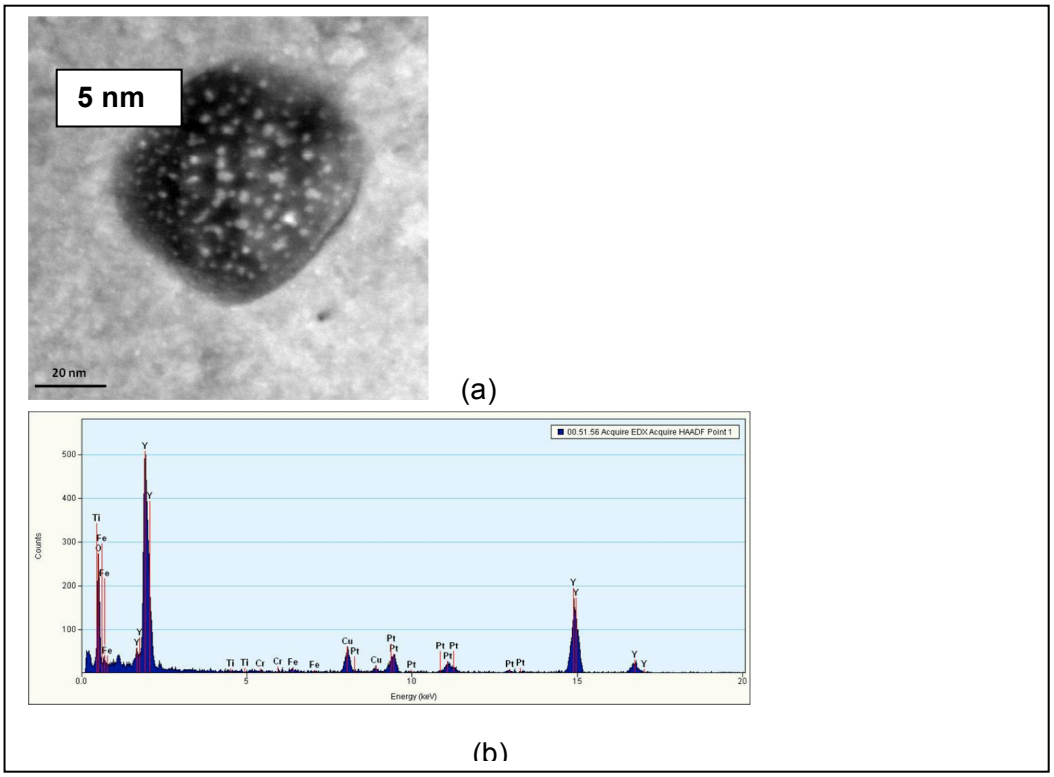

Figure 6.8. a) STEM-HAADF image of a Y-rich precipitates b) corresponding EDS spectrum.

STEM –HAADF imaging coupled with EDS line profile also show that there are precipitates, which are rich in Ti, see Figure 6.9. A dark contrast inside these precipitates has been observed, which shows higher oxygen concentration compared to the brighter portion of the precipitates. Ti signal follows the

opposite trend of oxygen signal inside the particle. Inside the particle Fe and Cr signal has not been detected. The numbers of Ti-rich precipitates are more compared to the Y rich one.

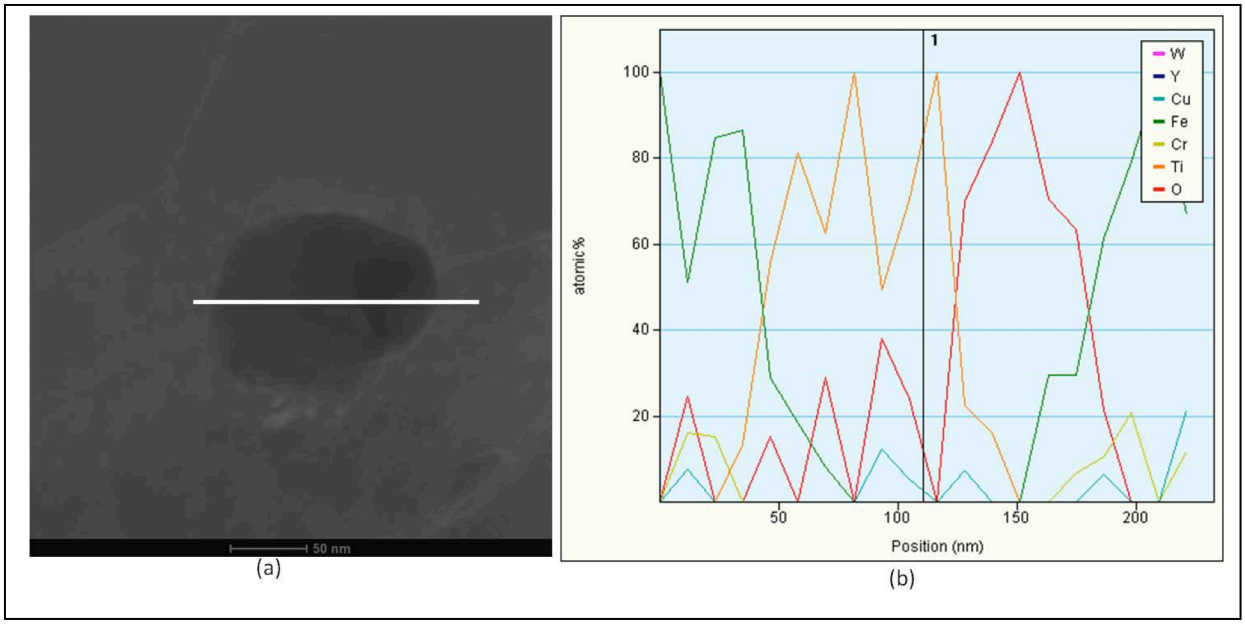

Figure 6.9. a) STEM-HAADF image of an impurity phase precipitates, b) corresponding EDS composition profiles of different elements present in the alloy, captured along the marked line in Figure 6.7a.

Effect of high-temperature heat treatments on the impurity phase precipitates: Effect of high-temperature heat treatments on these precipitates is quite profound, and, it has been observed that these precipitates are not thermally stable. Figure 6.10a shows that the large precipitates do not even exist after a heat treatment of 1300°C for 5 hr.

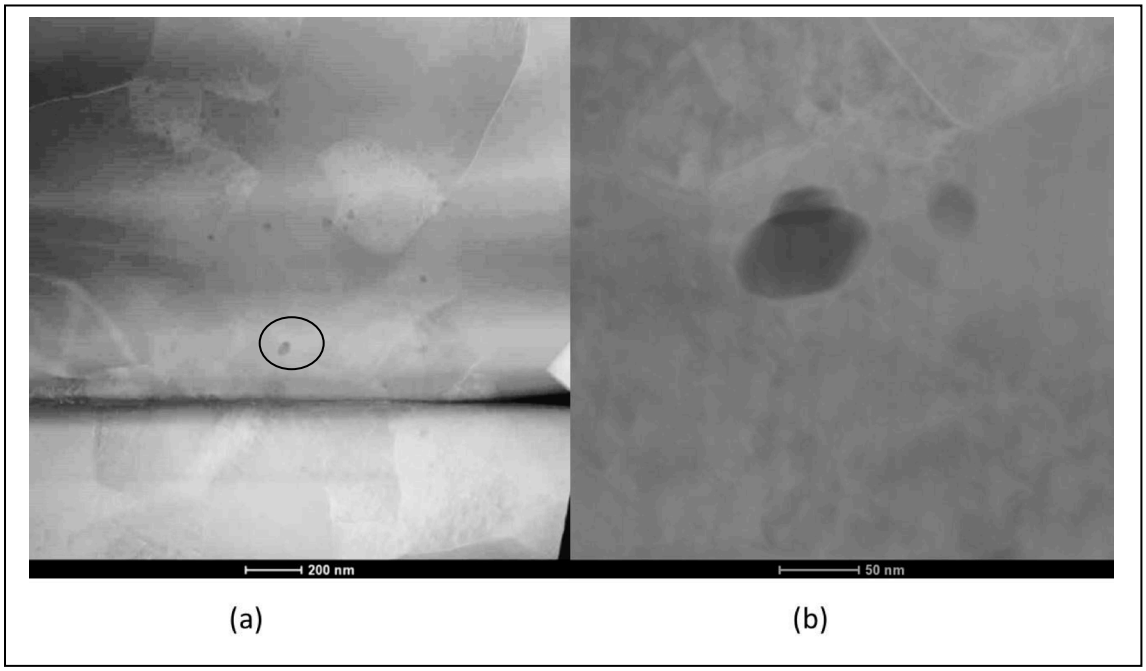

Figure 6.10. a) STEM-HAADF image of 1300°C/5 hr. heat treated sample. b) Magnified view of the precipitate marked in Figure 6.10a using a black circle.

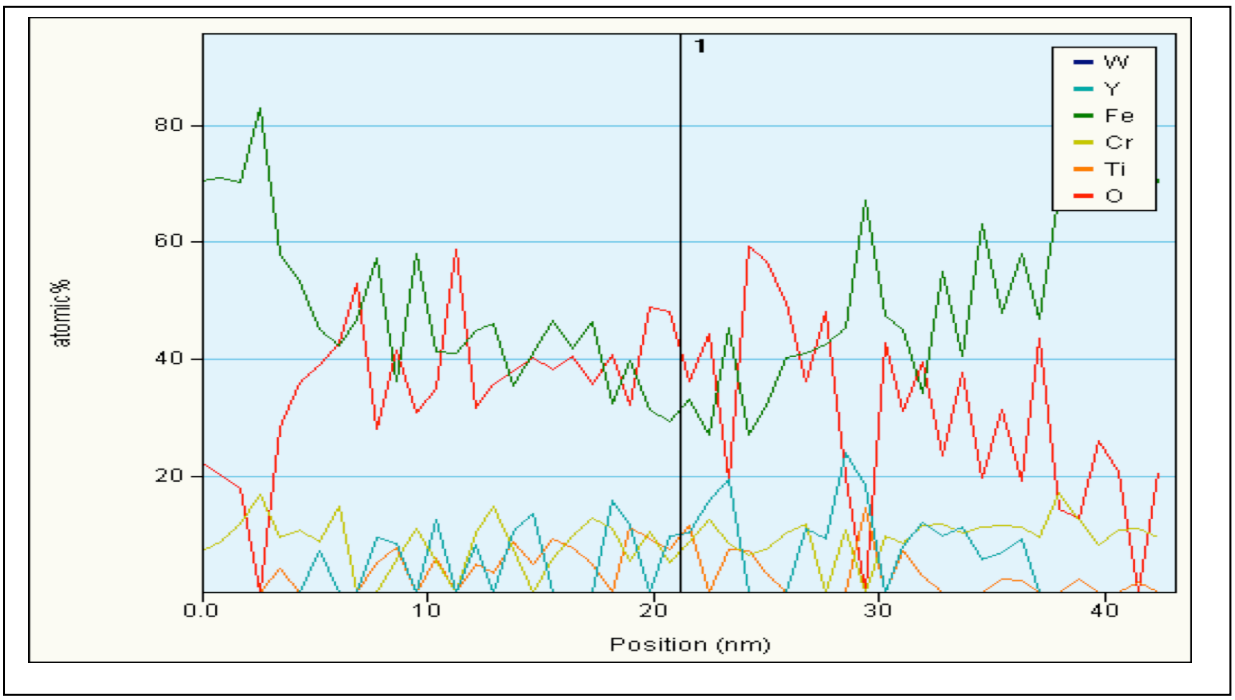

Figure 6.11. Composition profile of the different elements presents in the NFA alloy measured along the marked line in Figure 6.10b).

EDS line profile analysis, see Figure 6.11, depicts that after heat treatments of 1300°C/5 hr Ti and Y content of the precipitates are significantly reduced; whereas, in as processed condition precipitates are enriched with either Ti or Y, seen in Figure 6.7 and 6.8 b. The measured average ratio of Y, Ti and O is ~ 1/1/3.5. This suggests that the imaged precipitate is not the same impurity phase precipitates; rather, it is a nano-oxide of $Y_2Ti_2O_7$ coarsens during the heat treatment. On the hand it is well known that growth kinetics of NOs are extremely sluggish, therefore coarsening of a NOs up to a size of ~ 60 nm, see Figure 11b, is extremely difficult for the present heat treatment conditions [1]; rather, it is more probable for the precipitates to transform into a NOs. Figure 6.11b also shows that inside NOs significant amount of Fe and Cr coexist, suggesting a core-shell kind of structure of these NOs. This kind of core-shell kind of structure of NOs is also reported by other researchers [6, 7]. Though the kinetics of dissolution and thermal stability of the impurity phase precipitates has not been understood properly; but experimental evidence suggest these impurity phase precipitates are metastable. Surprisingly for the present instance, we have not found any of the impurity phase precipitates in 1300°C/5 hr annealed sample.

Effect of impurity precipitates on high-temperature tensile behavior:

Figure 6.12 shows the variation of yield strength with temperature for FCRD-NFA-1 alloy, where test specimens were made from three different orientations of the plate top, side and front surfaces. The plots suggest that there might be two different mechanisms operative: one from room temperature to 400°C

and another one above 400°C. A similar kind of dependence of fracture toughness of NFA alloy on temperature is also reported by Byun et.al [8]. At room temperature fracture of the alloy is controlled by mesoscopic features; whereas, above 200°C continuous reduction in the toughness is caused by the shallow plastic zone formation due to the nanostructure of the alloy itself. It was also observed that at 700°C fracture occurs through debonding of low toughness grain boundaries [8].

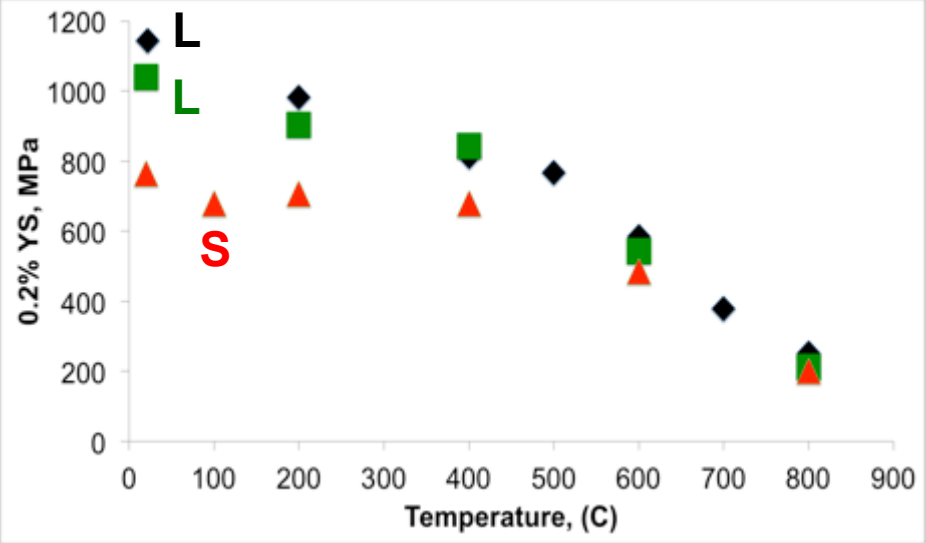

Figure 6.12 . Yield strength of NFA-1 alloy tested at different temperatures.

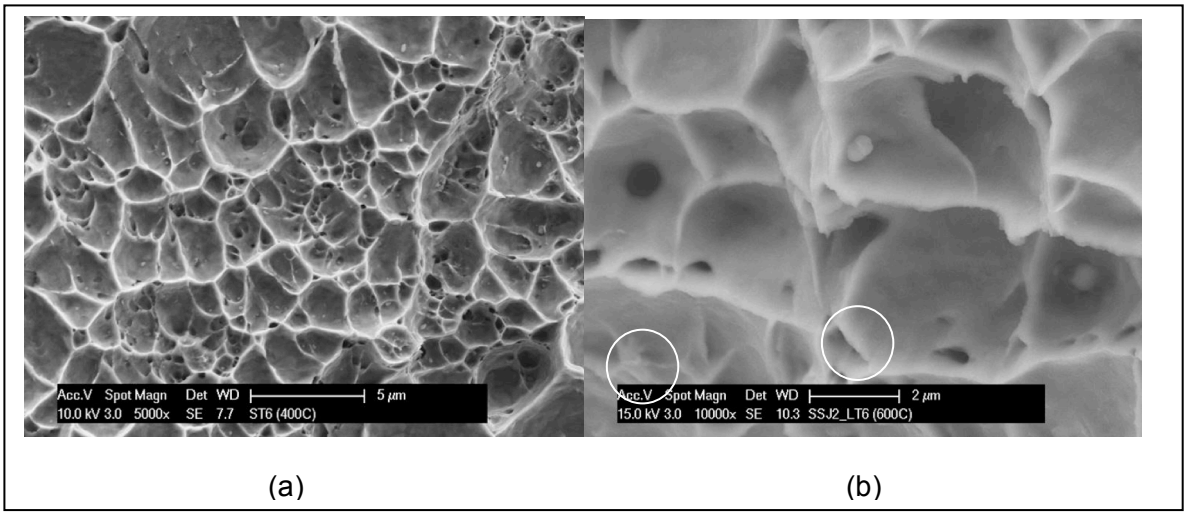

Figure 6.13. a) and b) show the both low and high mag image of the fracture surface of a tensile sample tested at 600°C. Particles are marked using a white circle in Figure 6.13b).

Fractography of the 600°C tensile tested specimen clearly demonstrates that the failure of the alloy at elevated temperature occurs by ductile failure mode with dimple formation. A closer observation of the fracture surface see Figure 6.12a and b, reveal that fracture process at high temperature occurs through debonding of the grain boundary, which initiates from those impurity phase precipitates. Notably, all these

impurity phase precipitates are only observed at the grain boundaries and incoherent in nature. This altogether suggests that this impurity phase precipitates have an important role on determining the high-temperature behavior of this alloy.

6.4 Summary: Experimental evidences clearly demonstrate that the large size precipitates are not same as the NOs, usually found in the NFA alloys. These precipitates are neither oxynitride nor oxycarbaide, particles as reported previously [6, 7]. It is usually bigger in size, lesser in numbers compared to the NOs and form only at the grain boundary. These precipitates are incoherent in nature and do not have any significant effect on the room temperature mechanical properties of these alloys; but, decohesion of these precipitates during high-temperature deformation may degrade the high-temperature mechanical properties of the alloy.

REFERENCES:

1. "Recent Progress in Developing and Qualifying Nanostructured Ferritic Alloys for Advanced Fission and Fusion Applications", G.R.Odette, JOM, 66 (2014) 2427-2441.
2. "Recent Developments in Radiation resistant Steels" G.R.Odette, Annu. Rev. Mater. Res, 38 (2008) 471-503.
3. "Creep behavior and deformation mechanism in a nanoclustered strengthen ferritic steel" M.C.Brandes, Acta Materialia, 60 (2012) 1827-1839.
4. "A new method for the quantitative analysis of the scale and composition of nanosized oxide in 9Cr-ODS steel" M.Ohnuma, Acta Materialia, 57(2009), 5571-1839.
5. **"**Transmission electron microscopy characterization of the nanofeatures in nanostructured ferritic alloy MA957" Y.Wu, Acta Materialia, 60(2012), 3456-3468.
6. "Morphology, structure, and chemistry of nanoclusters in a mechanically alloyed nanostructured ferritic steel" M.C.Brandes, J.Mater. Sci, 47 (2012), 3913-3923.
7. "Role of alloying elements in nanostructured ferritic steel" M.K.Miller, Material Science and Technology, 27 (2011) 729-734.
8. "High-temperature fracture characteristics of a nanostructured ferritic alloy (NFA)"- Thak Sang Byun, Journal of Nuclear Materials, 407 (2010) 78-82.

CHAPTER 7. DETERMINATION OF THE RESIDUAL STRESS IN THE AS PROCESSED NFA-1 ALLOY PLATE

7.1 OBJECTIVE: The aim of the present study is to quantify the amount of residual stress developed within the as processed NFA-1 alloy plate using depth-sensing nanoindentation technique.

7.2 SUMMARY: Hardness and modulus of the as processed NFA-1 alloy plate have been measured using nanoindentation (NI) as well as to probe the nature and magnitude of the residual stresses due to thermo-mechanical processing. The residual stresses were quantified from the (NI) load-displacement curves following the methodology proposed by Suresh et. al. In the as-processed condition, states of the surfaces are in compression near the surfaces and in tension in the middle of the plate. The magnitude of the tensile residual stress in the mid thickness of the plate is ~ +500 MPa, decreasing to ~ +75MPa tension near to the plate surface and finally possess a residual compressive stress of ~ -29 MPa at the surface. The micro-crack population perpendicular to the short thickness direction of the plate also tracks the measured residual tensile stress profile. The residual stresses were further quantified using the conventional $\sin^2\psi$ x-ray diffraction method. The residual stress measured near to the top surface of the plate exhibits more or less the same value when measured using both nanoindentation and x-ray diffraction (XRD).

7.3 PROGRESS AND STATUS:

7.3.1 Introduction: Nanostructured ferritic alloys are an attractive structural material for advanced nuclear fission and fusion reactors due to their radiation tolerance, high-temperature strength, high fracture toughness and remarkably low value of BDT [1,2]. However, bulk processing of NFA is extremely difficult due to a highly anisotropic α-fiber texture [3]. UCSB has collaborated with LANL and ORNL to develop a large heat NFA 14YWT variant called FCRD-NFA-1. The extruded and cross rolled plate contains a large population of microcracks lying perpendicular to the short thickness direction of the as processed plate, running in the primary deformation directions. Our previous investigation showed that during high-temperature thermo-mechanical processing, stress concentration builds up ahead of the dislocation pile-ups at {001}<110> type low angle tilt boundaries. The tilt boundaries are composed of sessile <001> dislocations formed by reactions between two <111> dislocations gliding on {110} planes. The dislocation pile-up lead high stress concnetrations and the summed Burger's vectors can directly nucleate a crack. The {001}<110> boudary is a low toughness brittle cleavage system for the crack nuclie and residual stresses that develop during thermo-mechanical processing drive cleavage crack propagation to form microcracks. The presence of residual stresses in the cracked region was previously shown using selected area diffraction, where streaking of the diffraction spots was clearly visible [3]. Therefore it is critically important to quantify the residual stresses. Here, we use a nanoindentation technique to estimate the residual stresses based on a method proposed by Suresh et.al [5] as well as by XRD using the $\sin^2\Psi$ method. We show that the though-thickness micorcrack density approcimately tracks the residual stress profiles.

7.3.2 Materials and Methods: For the present study, a larger heat variant of the nanostructured ferritic alloy, called FCRD-NFA-1, containing 14Cr-3W-0.4Ti-0.3Y and balance Fe was studied. NFA-1 was developed in a close collaboration between UCSB, LANL, and ORNL. NFA-1 was hot extruded at 850°C, the annealed, and hot cross rolled at 1000°C perpendicular to the extrusion direction to a final plate plus can thickness of 12.5 mm thick plate at.

The nanohardness (NH) and reduced modulus (E_r) of the as processed were measured using a nanoindenter (Hysitron, Tribo-indenter). Depth sensing instrumented nanoindentation provides a load vs. displacement curve. The load-displacement curve, not only not only characterizes NH and Er, but also

provides information on strain hardening, creep, bi-axial residual stresses and yield strength. Here we evaluate the bi-axial residual stresses present in the as processed NFA-1 alloy following the methodology proposed by Suresh et. al [5].

Fig. 7.1 shows a typical load displacement curve obtained from a nanoindentation test where h_f are the final plastic depth and h_{max} is the maximum depth of penetration. The method of calculating hardness and modulus of a material from the load-displacement curve of the nanoindentation test was first proposed by Oliver and Pharr [6].

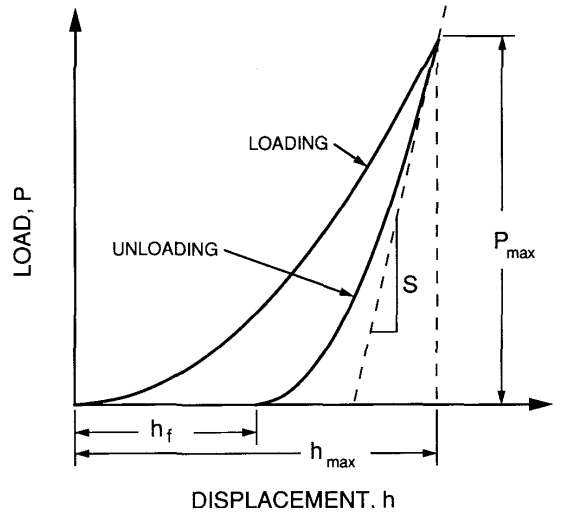

Fig. 7.1. A typical load-displacement curve for the nanoindentation experiment.

The reduced Young modulus (E_r) of an indented substrate is related to the slope of the initial unloading period of the load–displacement curve (S) and contact area (A_r) between the indenter and the indented material by the relationship.

$$S = \frac{dP}{dh} = \frac{2}{\sqrt{\pi}} * \sqrt{A_r} * E_r \tag{1}$$

The reduced modulus, E_r, is,

$$\frac{1}{E_r} = \frac{1-\nu_1^{\,2}}{E} + \frac{1-\nu_2^{\,2}}{E_i} \tag{2}$$

Here the E and E_i are the Young moduli of the indented and indenter, respectively; and, ν_1 and ν_2 are the Poisson ratios of the indented and indenter, respectively. The slope of the unloading portion of the load-displacement curve is determined by least squares fitting:

$$P = A(h - h_f)^m \tag{3}$$

Typical values of *m* fall between 1.2 to 1.6, depending upon the material. Therefore, we have considered only those load-displacement curves with *m* in that range. The NH is the average contact pressure at the maximum load, defined by,

$$H = \frac{P_{\max}}{A_r} \tag{4}$$

If the indentation region is subject to an equi-biaxial residual stress, the shape of the indentation curve is modified relative to a stress free case as illustrated in Fig. 7.2.

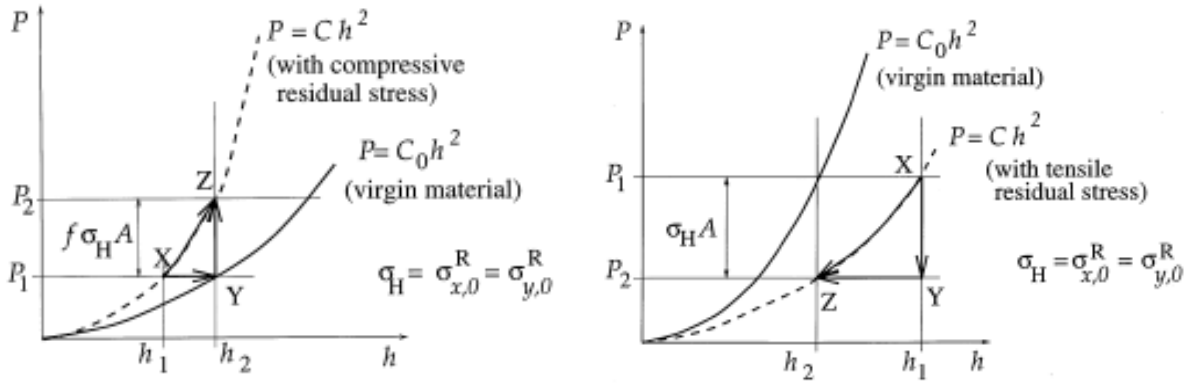

(a) (b)

Fig. 7.2. Schematic of the load-displacement curves of a virgin material and the same material containing a) compressive residual stress b) tensile residual stress [5].

The basic physics of the modification of the P-h loading curves is easy to understand as illustrated in Fig. 3. If the region is under compression it takes a higher load to create a given indentation depth and the load is lower in the case of a tensile stress. Expressions describing the effect of residual stress on the curvature of the load-displacement curve, expressed in terms of the average contact pressure and area (hardness), were derived by Suresh et. al [5].

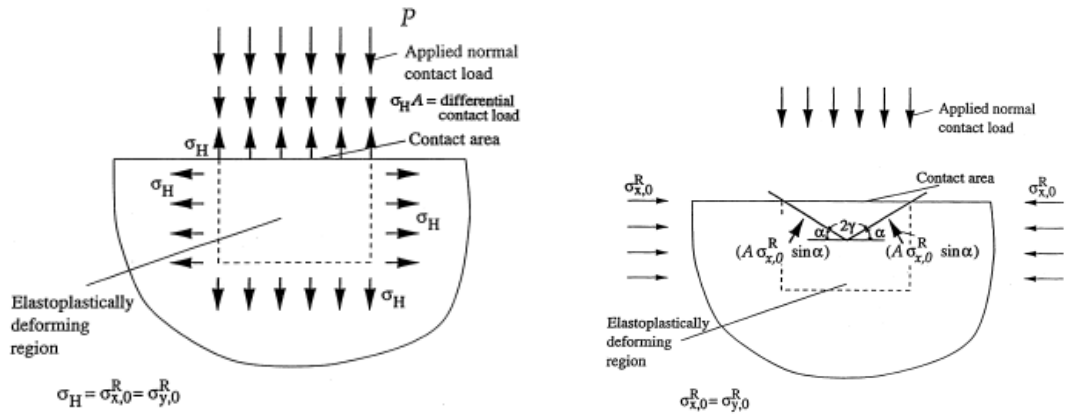

(a) (b)

Fig. 7.3. Schematic of the role of elastic residual stress at the indented surface a) tensile b) compressive residual stress, respectively [5].

The hardness of a material defines its ability to resist plastic deformation. For a sharp indenter, the amount of plastic strain is not affected by pre-existing elastic residual stress. However, for an elastoplastic material, the apparent contact area can change in the presence of a residual tensile stress during indentation, by adding a finite hydrostatic stress component, σ_H, to the indentation stress tensor, including in the loading direction, for a specified indentation depth. The same hydrostatic stress is subtracted in the case of constant load indentation. Similarly, compressive residual stress can either add or subtract a hydrostatic stress component, $\sigma_H \sin\alpha$, along the direction of indentation. How an elastic bi-axial residual stress on the indented surface is equivalent to either tensile or compressive hydrostatic stress component is illustrated in Fig. 7.3. Therefore based on the equivalence of the mean contact pressure, the relation between apparent contact area, residual contact stress, and mean contact pressure was established. The change in contact area due to elastic residual stress is related to mean contact pressure through the following equation:

$$\frac{A_r}{A_0} = \left(1 - \frac{\sigma_H}{P_{ave}}\right)^{-1} \quad \text{for tensile residual stress} \tag{5}$$

$$\frac{A_r}{A_0} = \left(1 - \frac{\sigma_H \sin\alpha}{P_{ave}}\right)^{-1} \quad \text{for compressive residual stress} \tag{6}$$

Here, α is the semi-apex angle of the indenter. For the sharp Berkovich indenter α = 24.8° and A_0 is the contact area between the indenter for a residual stress free condition, and P_{ave} is the corresponding average contact pressure, or hardness [5].

Through thickness microstructural characterization of a 45°, cut surface of the plate was carried out using FIB-SEM (Helios600, FEI) has been reported previously [3]. Residual stress measurement using XRD were carried out in a two-axis goniometer instrument (XPertPro, PAN-Analytical) using CuKα radiation. The (112) planes, with a peak in bcc Fe occur at 2θ = 83.219°, was chosen to measure changes in the d spacing, because of the higher sensitivity of the measurement at a large Bragg angle. Since the NFA-1 alloy has a strong texture, an initial θ-ω scan was performed to identify the ω angle with a maximum intensity for the (112) peak. The d spacing measurements were performed using θ-2θ scan with a series of positive and negative ψ tilt.

7.3.3 Results: Fig. 7.4 shows a schematic of the NFA plate deformation directions. Since we are interested in evaluating the residual stress profile developed within the short thickness direction of the plate, therefore it is more feasible to perform measurement on a 45° cut surface, rather perfoming indentation on the side surface of the plate.

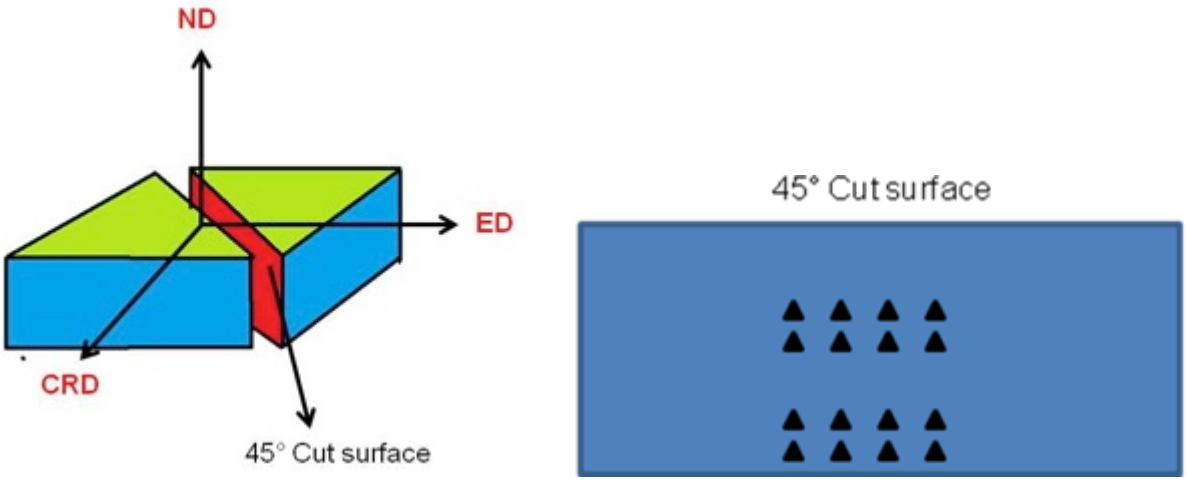

(a) (b)

Fig. 7.4. (a) Schematic of the plate geometry along with the deformation direction, the top surface of the plate is colored with green, and, short thickness direction is marked with blue. (b) Schematic of the top view of 45°cut surface of the plate shows the location, where nanoindentations are performed.

Determination of the residual stress from the nanoindentation load-displacement curve requires a stress-free standard. Therefore a small rectangular shape specimen was cut from the thickness direction of the plate and annealed at 1000°C for 5 hrs to completely remove the residual stress, present in the specimen. The standard sample was chosen from the thickness direction of the plate to maintain a microstructural and textural similarity between the stressed and standard stress-free specimen. The annealing condition was chosen in such a way that there should not be any change in the microstructure of the specimen, which can affect the test results. It was previously reported that a 32.4 kh treatment of the NFA-1 alloy at 1000°C causes minimal change in its microstructure [1]. Fig. 7.5 displays the measured hardness and modulus of the 45° cut surface from the as processed plate, and, 1000°C/5 hrs annealed specimen which is used as a residual stress-free standard for the present case. The annealed specimen has the highest hardness, whereas the modulus.

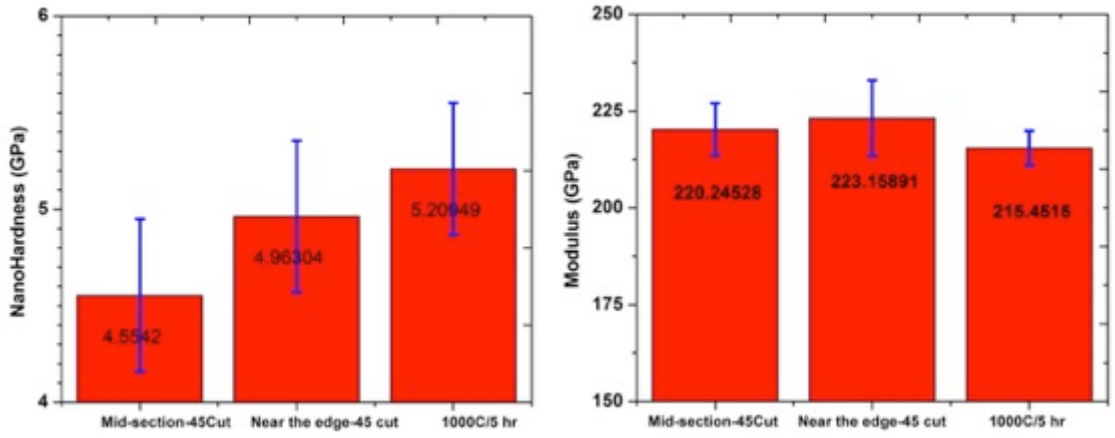

(a) (b)

Fig. 7.5. a) Hardness and b) modulus of all the indented specimens.

Representative load-displacement curves for the three indented specimens are shown in Fig. 7.6. The curvature of the initial loading portion of the load-displacement curve depends on the nature of the residual stress (compressive or tensile) exist into the indented region, as described by Suresh et. al [5]. It is clearly visible that the curvatures of both the curves obtained from indenting the 45° cut plate surface are lower compared to the 1000°C/5 hr heat treated specimen. Since the annealed sample is stress-free and the curvature of the load-displacement curve is higher than the curves obtained from indenting the 45° cut surface. Therefore, we can effectively report that the as processed plate possess a tensile residual stress in their through thickness direction.

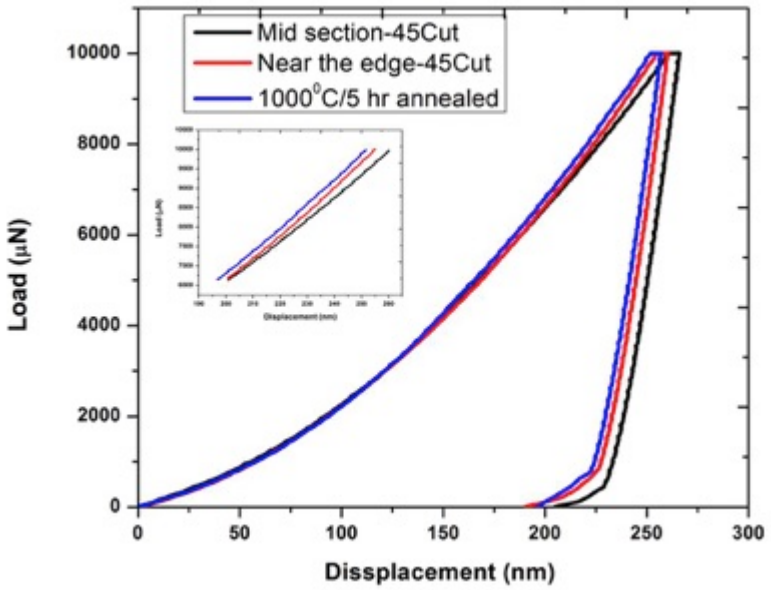

Fig. 7.6. load-displacement curves obatined from the near to the edge and mid section of the 45°cut specimen, as well as 1000°C/5 hr annealed speimen. Inset shows a magnified version of the loading portion.

The curvatures of the loading P-h curve for the three indented specimens were least square fit using a generalized Kick's law, where the load (P) is related to penetration depth (h) through the following relation:

$$P = Ch^n \tag{7}$$

where *C* determines the magnitude of the loading portion and n is an empirical exponent depends on the indenter geometry.

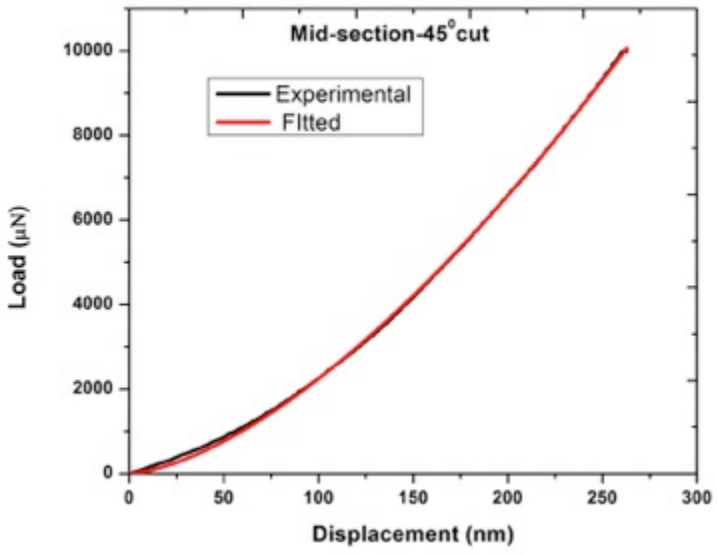
Mid-section-45° cut
Experimental
FItted
Load (μN)
Displacement (nm)
0
2000
4000
6000
8000
10000
0
50
100
150
200
250
300

(a)

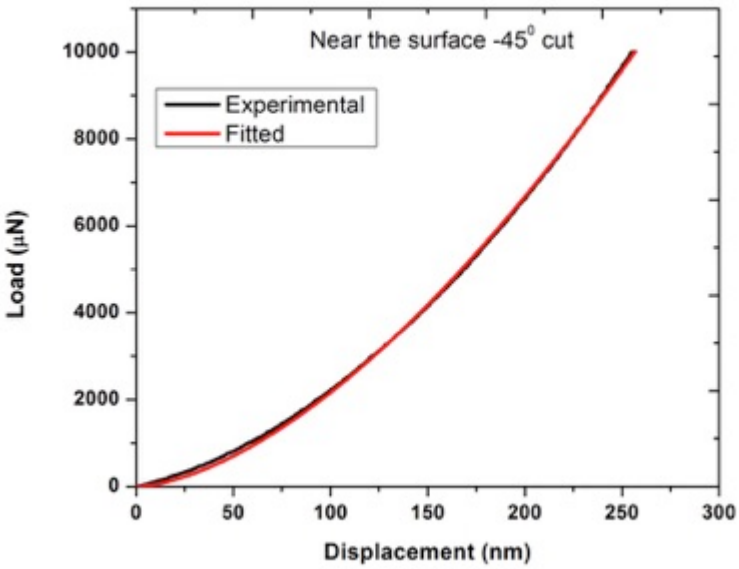
Near the surface -45° cut
Experimental
Fitted
Load (μN)
Displacement (nm)
0
2000
4000
6000
8000
10000
0
50
100
150
200
250
300

(b)

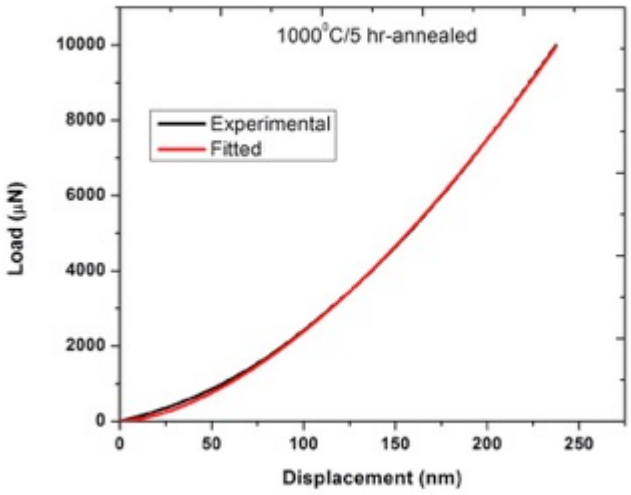

(c)

Fig. 7.7. Loading portion of the indentation curve and the fitted curve a) 1000°C/5 hr b) mid-section c) near to the edge of the 45° cut plate surface.

The exponent n is ≈ 1.65 in all three cases, consistent with a material that has significant strain hardening [7]. Eqs 5 and 6 hold for the n = 1.65 and the residual stress is given the Eq. 5.

The values for C and n obtained using the least square method, and calculated residual stress values are tabulated in the Table. 7.1. The contact area for the stressed and stress-free sample, and average contact pressure or hardness was evaluated from the load-displacement curve, see Fig. 7.7. The curvature of the loading portion of the curve, which is determined by the double derivative of the governing equation at a fixed depth of 200 nm for the three indented specimens, is also listed in Table. 1 From the table 1, we can easily say that the 45° cut sample possess residual tensile stress compared to 1000°C/5 hr annealed specimen.

Table 7.1. display the values of C, n, curvature at a fixed depth of 200 nm and residual stress obtained from the nanoindentation curve.

Sample	C	n	Double derivative at 200 nm depth	Residual stress (MPa)
45Cut-Mid	0.937	1.662	1.029825	496.296
45Cut-near edge	0.943	1.675	1.06663821	75.54873
1000C/5 hr	1.167	1.655	1.26383691	-

Near to the mid-thickness of the plate, the value of tensile residual stress is around ≈ 500 MPa, decreasing to ≈ 75 MPa near to the top edge of the plate. Not the plate is contained inside a can so it is expected that compressive residual stresses would exist near the canned plate surface. These residual stress estimates are approximate but are consistent with data in the literature, for example in a cold rolled-ferritic steel [8]. The residual tensile stress drives crack propagation. Notably the stress distribution is consistent with the through thickness variation of the crack density determined from the low magnification FIB-SEM images shown in Fig. 7.8. Fig. 7.9 shows the variation of the microcrack density in the through-thickness direction plate. The mid-section of the plate has the highest crack density and the maximum residual tensile stress, whereas near to the plate edge both the crack density and the residual tensile stresses are low. Figure 7.8 and 7.9 and in Figure 7.9 show the distance is measured from the center of the plate

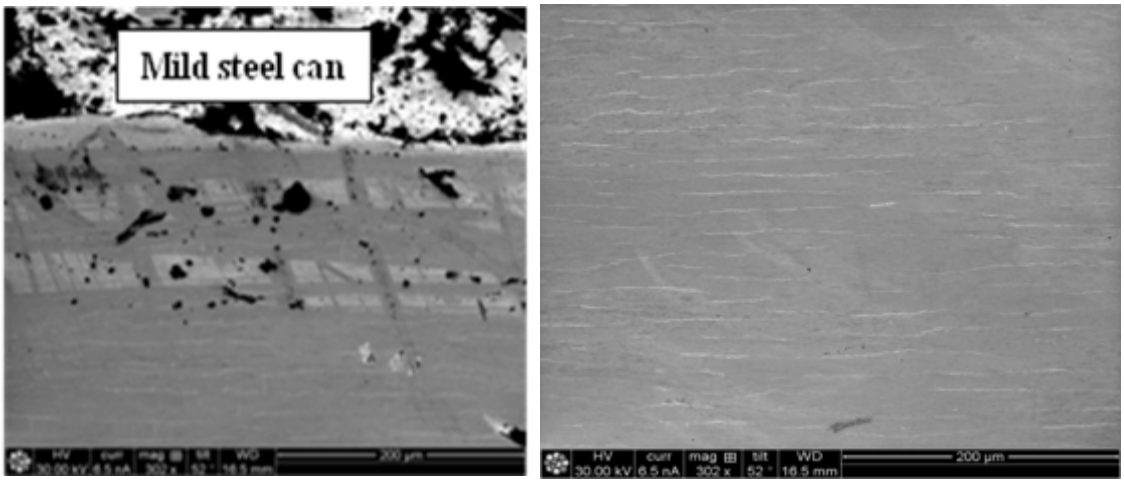

(a) (b)

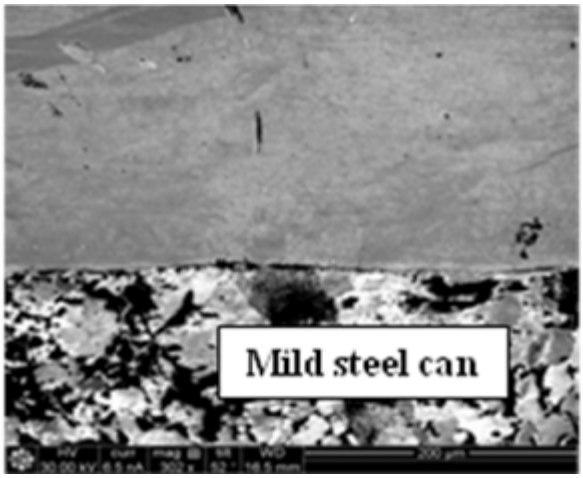

©

Fig. 7.8. FIB-SEM low magnification micrographs of the 45° cut surface of the plate thickness show a) near the top edge b) midsection c) near the bottom edge. The mild steel can is marked in the images.

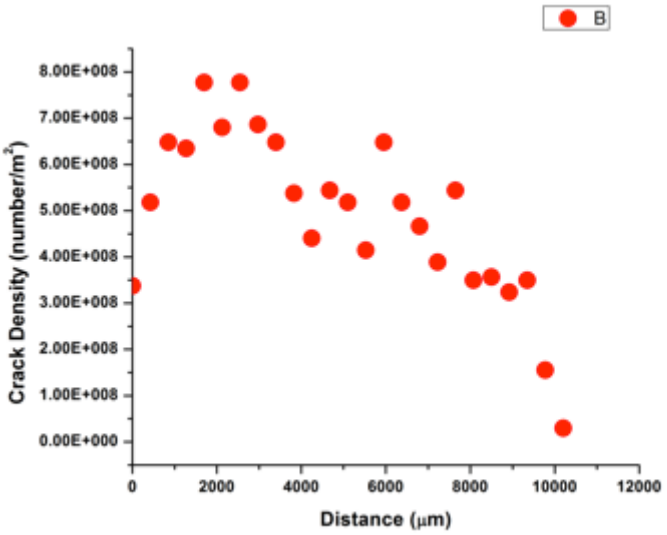

Fig. 7.9. The distribution of crack density along the thickness of the 45° surface of the plate.

The residual stresses in the top surface of the canned plate were measured by the XRD $\sin^2\psi$ method and found to range from ≈ -29 (compression) to +64 (tension). Details of this analysis will be reported in the future along with through thickness measurements that are planned. The qualitative variation the residual stress is shown in Fig. 7.10.

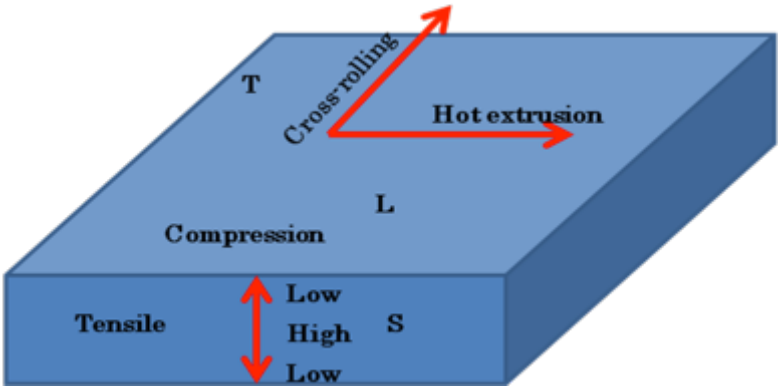

Fig. 7.10: A schematic of the alloy plate showing the residual stress profiles along the different direction.

7.4 Summary and Discussion:

We reported for the first time estimates of the residual stress distribution in the processed NFA-1 alloy. The results are qualitative but show robust trends. The mid-thickness region of the plate exhibits a very high tensile residual stress of ≈ 500 MPa coincident with a very high micro-crack population. The residual tensile stresses near the edge of the canned plate are ≈ 75 MPa with a correspondingly low microcrack density. XRD techniques were used to characterize the stresses on the top surface of the canned plate that were also low and in one case compressive. Future measurements will be carried out at synchrotron and neutron residual stress measurement facilities.

REFERENCES:

1. G. R. Odette, "Recent Progress in Developing and Qualifying Nanostructured Ferritic Alloys for Advanced Fission and Fusion Applications," *JOM,* vol. 66, no. 12, pp. 2427-2441, 2014.

2. M. E. Alam, N. J. Cunningham, D. Gragg, K. Fields, G. R. Odette, D. T. Hoelzer and S. A. Maloy, "MECHANICAL PROPERTIES CHARACTERIZATION OF A LARGER BEST PRACTICE HEAT OF14YWT NFA1," *Fusion Reactor Materials Program,* vol. 56, no. DOE/ER-0313/56, pp. 63-69, 30 June 2014.

3. S. Pal, M.E. Alam, G. R. Odette, D. T. Hoelzer and S. A. Maloy (LANL) "Microstructure, Texturing, microcrakinga and Delamination of NFA-1", *Fusion Reactor Materials Program*, DOE/ER-0313/58, pp. 66-82, 30 June 2015.

4. S. Pal, M.E. Alam, G. R. Odette, J. Lewandowski, D. T. Hoelzer and S. A. Maloy (LANL) "Characterization of the Microstructure and Texture of NFA-1 for Two Deformation Processing Routes", *Fusion Reactor Materials Program*, DOE/ER-0313/58, pp. 29-41, 30 June 2015.

5. S.Suresh, A.N. Giannakopoulus, "A new method of emstimating residual stress by instrumented sharp indenation", Acta Materialla, vol. 46, No. 16, pp. 5755-5767, 1998.

6. W.C.Oliver and G.M.Pharr, "An improved technique for determining the hardness and modulus using load and displacement sensing indentation experiments" J. Mater. Res., Vol. 7, No. 6, 1564-1583, June 1992.

7. S. V. Hainsworth, H. W. Chandler, and T. F. Page, "Analysis of the nanoindentation load-displacement curve" J. Mater. Res., Vol. 11, No. 8, 1987-1995, August 1996.

8. J.M. Atienza , M.L. Martinez-Perez , J. Ruiz-Hervias, F. Mompean , M. Garcia-Hernandez , M. Elices " Residual stress in cold drawn ferritic rods" Scripta Materialia, Vol. 52, pp. 305–309, 2005.

ACKNOWLEDGEMENTS

This work is part of a multi-laboratory collaboration between LANL, UCSB and ORNL. The DOE Office of Fusion Energy Sciences supported some of the mechanical testing reported here. NFA-1 was produced under the sponsorship of the DOE Office of Nuclear Energy through both a NEUP grant and the FCRD program.

Research at UCSB was supported by the Department of Energy Office of Fusion Energy Sciences (Grant No. DE-FG03-94ER54275) and the Office of Nuclear Energy (Grant No. DE-FC07-07ID14825). Most of the specimen preparation and some of the TEM measurements were carried out in the UCSB Materials Research Laboratory Microstructure and Microanalysis Facility, supported by the Materials Research Science and Engineering Center Program of the National Science Foundation under Award No. DMR05-20415. The authors thank our UCSB colleagues P. Wells for insight on APT issues, Dr. T. Yamamoto for his many general contributions to our research program, T. Stan for helpful discussions of the interfaces and many others in the Odette Group for their assistance in various parts of this research. We also acknowledge helpful discussions regarding XRD with D. Sprouster and L. Ecker at BNL, and D. Morgan

L. Barnard at the University of Wisconsin for their outstanding modeling insight and and Y. Jiang at the Central South University in China sharing the DFT results shown in Figure 5. Electron microscopy experiments were performed at the NCEM facility of the Molecular Foundry, which is supported by the Office of Science, Basic Energy Sciences of the U.S. Department of Energy under Contract DE-AC02-05CH11231. The authors would like to thank M. Libbee and C. Song for their support on TEM sample preparation and training at the Molecular Foundry. Finally, we acknowledge the assistance of M. Toloczko at PNNL in providing the irradiated MA957 characterized in this study and S. Maloy at LANL and D. Hoelzer at ORNL for their role as UCSB collaborators in developing FCRD NFA-1.

SECTION 3: INTERIM PROGRESS REPORT ON TOUGHNESS OF 14YWT COMPONENTS

CHAPTER 1: DELAMINATION MEDIATED FRACTURE TOUGHNESS OF FCRD NFA-1

1.1 OBJECTIVES

The objective of this research is to understand the effect of pre-existing microcrack on delamination and fracture toughness properties of 14YWT FCRD NFA-1.

1.2 SUMMARY

The FCRD NFA-1 is a high strength, irradiation tolerant nanostructured ferritic alloy (NFA) produced by ball milling argon atomized Fe-14Cr-3W-0.35Ti-0.25Y (wt.%) and FeO powders, followed by hot extrusion at 850ºC, and subsequent annealing and cross-rolling at 1000ºC. The microstructure of ≈ 10 mm thick NFA-1 plates is dominated by ultrafine sub-micron pancake shaped grains and a population of microcracks lying on planes perpendicular to the plate faces. Pre-cracked fracture toughness bend tests show stable crack growth by ductile tearing, with peak load K_{Jc} from ≈ 88 to 154 MPa$\sqrt{m}$ at ambient temperature. Crack tearing is accompanied by extensive delamination, due to the propagation of the microcracks, that persists down to ≈ -175°C. Depending on the specimen orientation, this highly unusual behavior is either due to reduction of stresses in thin ligaments formed by the delaminations, or 90° deflection of cracks initially running normal to the delaminations, both suppressing cleavage.

1.3 BACKGROUND

The success of the Gen IV nuclear fission and future fusion as a source of large-scale power production depends on the development of new, high-performance structural materials that can safely support safe extended component lifetimes under the extremely hostile environment [1]. Nanostructured ferritic alloys (NFAs), which are a variant of oxide dispersion strengthened (ODS) steels, have high tensile, fatigue and creep strengths over a wide range of temperature, excellent thermal stability up to more than 900ºC and unique irradiation tolerance, especially in managing high levels of helium [2-4]. These outstanding properties are due to the presence of an ultrahigh number density of order $5x10^{23}$ /m^3, ≈ 2.5 nm Y-Ti-O nano-oxides (NOs), submicron grains and high dislocation densities [2-5].

Recently a 14Cr-Y-W-Ti (14YWT) NFA was developed in a collaboration between Los Alamos National Laboratory (LANL), Oak Ridge National Laboratory (ORNL) and the University of California at Santa Barbara (UCSB). So-called FCRD NFA-1 was processed by first ball milling Fe-14Cr-0.25Y-3W-0.35Ti (wt.%) atomized powder with FeO powder to dissolve the Y and provide a proper balance of Ti and O [4, 6]. The mechanically alloyed powders were then canned, degassed, hot extruded at 850^{o}C, annealed for 1 h and cross-rolled to an ≈ 50% thickness reduction, both at 1000^{o}C, to form an ≈ 10 mm thick plate.

While enjoying a host of outstanding properties, NFAs often have poor fracture toughness and high brittle-to-ductile transition (BDT) temperatures that are highly anisotropic [7-15]. Toughness is lower when the crack propagates parallel to the principal deformation (e.g., extrusion) direction, but is usually much lower for propagation for the transverse orientations. In most cases, the fracture toughness of NFA has been reported only for the toughest directions. Thus, one objective of this study is to characterize fracture

toughness for all significant loading direction orientations over a range of temperatures from ambient (23°C) down to -196°C. In order to better understand the underlying mechanisms of fracture in NFA-1, the meso-microstructures and fracture surfaces were thoroughly characterized. Tensile tests in longitudinal extrusion direction were also conducted at lower temperatures to evaluate the combination of strength-toughness of NFA-1, and to support finite element analysis simulations of the load-displacement curves of the pre-cracked bend bars. NFA-1 tensile properties at higher temperature are reported elsewhere [16].

1.4 STUTUS AND PROGRESS

1.4.1 Materials

NFAs are typically processed by ball milling Fe-Cr-Ti-W and Y_2O_3 powders to mechanically alloy Y and O into solid solution. The powders are then consolidated at high temperature [3-4]. NOs precipitate during hot consolidation, at sizes (d) and number densities (N), that depend on the alloy composition and processing temperature history [4, 17]. Typically, the consolidated NFA must be deformation processed a final net shape, while maintaining or improving performance-sustaining properties. In the case of NFA-1, Y was included in the melt prior to gas atomization and rapid solidification. This was intended to explore the possibility of minimizing, or eliminating, the ball-milling step and to produce more uniform distributions of NOs. ATI Powder Metals (Pittsburgh, PA) provided the atomized Fe-14Cr-3W-0.4Ti-0.2Y powders with a controlled range of O contents. However, the Y was found to be phase-separated after atomization, hence, low O atomized powders were ball milled for 40 h with 10 mesh FeO powders to increase O to ≈ 0.125 wt.% O. The ball milling was carried out by Zoz GmbH (Wenden, Germany) in a CM100b attritor mill, with a ball mass-to-charge ratio of 10:1 and ball size of 5 mm. After ball milling the Y was uniformly distributed in the powders. The powders were then sealed in a 100 mm diameter mild steel can, degassed at 400ºC, and hot extruded at 850ºC through a 64 x 30mm^2 rectangular die. The extruded bar was annealed for 1 h, and then hot cross-rolled to an ≈ 50% thickness reduction, both at 1000°C, to form an ≈15mm thick section including the can, containing an ≈10 mm plate [16].

1.4.2 Microstructural characterization

Characterization of the NO and dislocation structures in NFA-1 are described elsewhere [6]. Figure 1.1a shows the orientations of the NFA-1 fracture specimens with respect to the extrusion, cross rolling and thickness directions. Here we use the notation of L, T and S for the extrusion (L), cross-rolling (T) and thickness (S) directions, respectively. The corresponding plane section view direction are defined L, T and S, and include: the extrusion direction view defined by the T and S (TS); the cross-rolling view direction defined by the L and S (LS); and the thickness view direction defined by L and T (LT). The corresponding three-dimensional (3D) mesostructure of the plate, composed of grains and microcracks, is shown in Figure 1.1b and c. The fracture surfaces were characterized by various combinations of: a) optical and scanning electron microscopy (SEM, FEIx30) equipped with energy dispersive spectroscopy (EDS); b) a dual beam Scanning Electron Microscope/Focused Ion Beam (SEM/FIB, FEI Helios 600); c) electron backscatter diffraction (EBSD, FEI Quanta 400F); and, d) transmission electron microscopy (FEI Titan and Technai TEMs) equipped with EDS and electron energy loss spectroscopy (EELS). Specimens used for mesostructure characterization were ground (1500 grit) and polished down to 20 nm colloidal silica. Some polished samples were etched with Kroll's reagent (92% distilled water, 6% nitric acid and 2% hydrofluoric acid) prior to SEM, SEM/FIB and EBSD imaging.

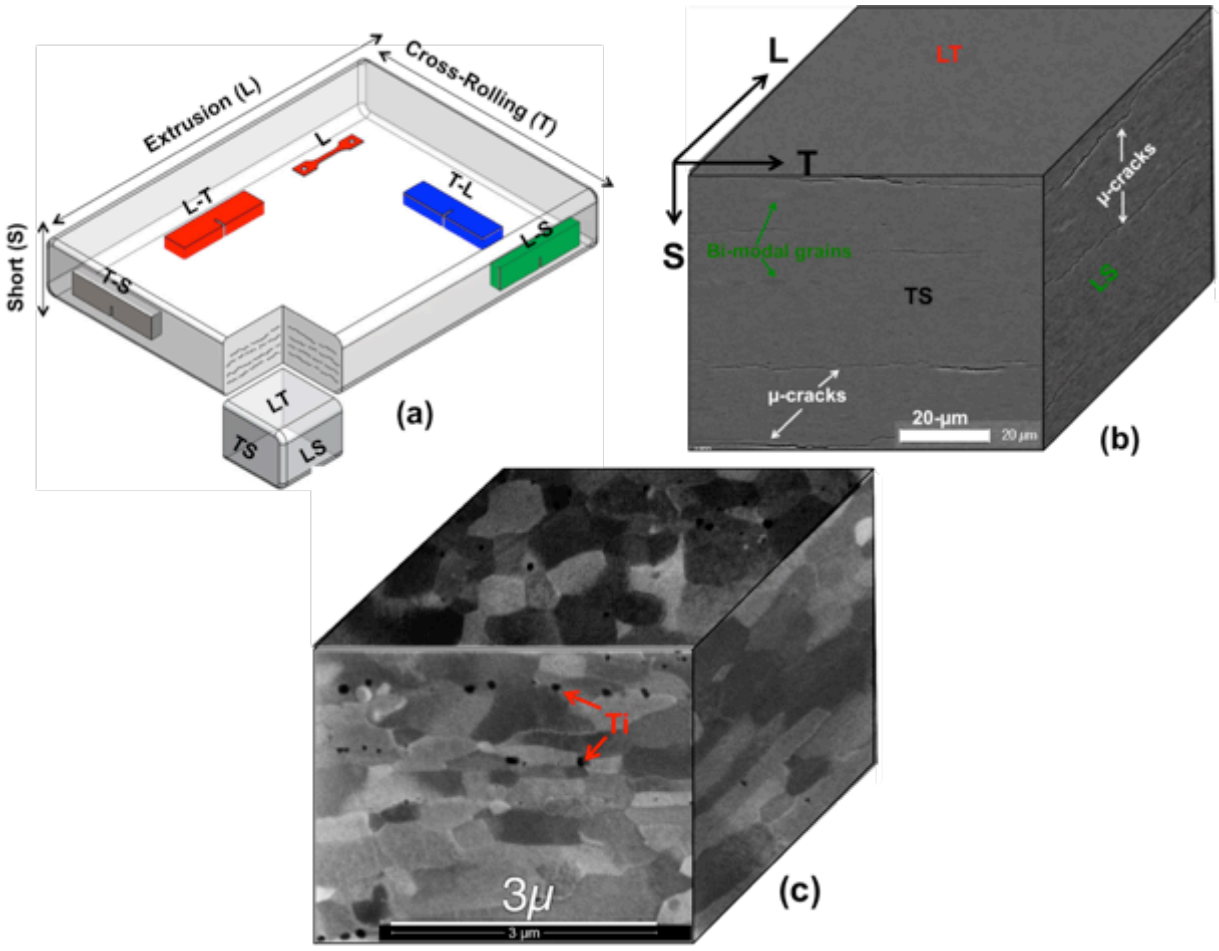

Fig. 1.1 NFA-1: (a) Orientation of the plate sections and test specimens; (b) pre-existing microcracks; (c) the grain substructure.

The grains are pancake shaped due to the extrusion and cross rolling deformations. In the short (LT planes) section view direction, the grains are roughly equiaxed, while in the extrusion and cross rolling views (TS and LS planes), the grains are elongated in both cases. The longest (l) and shortest (s) dimensions of ~500 individual grains were tabulated from micrographs using 'ImageJ64' software. The average grain size was taken as (l+s)/2 grain, while the grain aspect ratio (GAR) is defined by r = l/s. The grain statistics are summarized in Table 1.1 and further details are given in [16].

SEM was used to image ≈ 250 (extrusion direction TS section views) and ≈ 500 (cross rolling direction LS section views) cracks, as illustrated by the low magnification image in Figs. 1b and 2a. These images were used to characterize the crack length, number, maximum opening width, separation distance, and number density per unit area on the sectioned surface. Note that in many cases adjacent cracks on the same plane were separated by only small, intact bridging ligament. In this case, they were counted as a single crack when the ligament size was ≤ 1 μm. EBSD (voltage: 20KeV, spot size: 4, step size: 0.05μm and working distance: 10mm) was used to characterize the texture induced by hot extrusion and cross rolling for the different plate views. TEM was used to investigate the micro-mechanisms of crack formation as described in detail elsewhere [18]. Optical microscopy provided macroscopic images of the

fracture surfaces, and SEM was used for higher magnification fractography to detail delamination and the local fracture micro-mechanisms, both for the tensile and toughness tests.

SEM was also used to characterize 150 to 270 of the coarser precipitate inclusions, since they act as nucleation sites for microvoids. The inclusions are most often arrayed in stringers along the extrusion direction. SEM and TEM were used to characterize the average size and spacing of the inclusions, as well as the stringer spacing. SEM and TEM with EDS and EELS were used to identify the compositions of inclusions.

1.4.3 Tensile testing

The uniaxial tensile tests were performed on flat dog-bone shaped, sub-sized SSJ-2 type specimens with a gauge section dimensions of 5.0 mm length, 1.2 mm width and 0.5 mm thickness [16]. The tensile specimens were loaded in the longitudinal (L) direction (see Fig. 1a). All specimens were ground by 1500 grit paper to remove any surface contamination, minor cracks or local residual stresses due to the electric discharge machining (EDM). The tests were conducted from ambient temperature (≈ 23°C) down to the liquid nitrogen temperature (LN_2 ≈ -196ºC) on an 810 MTS servo-hydraulic universal testing machine equipped with cooling chamber. Controlled liquid nitrogen-air mixture was injected into the cooling chamber to achieve the targeted temperature, and held for 30 to 45 minutes before testing. The tensile tests were conducted at a displacement rate of 0.30 mm/min, equivalent to a strain rate ≈ 10^{-3}/s.

1.4.4 Fracture toughness

Fracture toughness tests were conducted from ambient temperature down to LN_2 temperature on the fatigue pre-cracked single-edged notch three point bend (3PB) specimens with nominal dimensions of 16 mm in length, 3.3 mm width and 1.65 mm thickness. The same 810 MTS servo-hydraulic universal testing machine equipped with cooling chamber was used for this purpose. Fracture toughness tests were conducted in four orientations as illustrated in Figure 1a (L-T, T-L, L-S and T-S, where the first letter designates the direction normal to the crack plane and second letter designates the anticipated direction of crack propagation). The specimens were fatigue pre-cracked under a nominal cyclic load of 0 to 420 ± 50 N at 20 Hz to a nominal crack length-to-specimen width ratio (a/W) of ≈ 0.5. The fracture tests were conducted generally based on the ASTM 1921 standard practice [19], including constraint requirements. Of course, the E1921 procedure is not strictly valid for deflected cracks. However, the significant metric is the load and displacement at initiation, that is reasonably reflected by K_{Jc}. The K_{Jc} was calculated at the maximum load, sometimes coincident with a small pop-in. Above -175°C crack initiation was followed by extensive stable crack growth by ductile tearing (except one L-T specimen tested at -150ºC). Crack tearing is signaled by a decreasing load (P) in the P-displacement (D) curve.

The crack initiation and final a/W were readily visible on the fracture surface after the specimen is broken in LN_2. The precrack a/W was measured as the average of 5 to 7 points along the crack front. The a/W during crack growth was not measured by a method such as unloading compliance. However, the a/W at a given P-Δ can be estimated by finite element simulations, e.g. the key curve method [20, 21]. A minimum of 2 tests we conducted in all case and 3 for LT at 23 and -150ºC and TL at 23ºC. The number of test was limited by the available plate material. However, since the fracture process at and above -175°C is by ductile tearing, rather than cleavage, and since the corresponding K_{Jc} statistics are generally limited to small pop-in events, with the one exception at -150°C, the limited number of individual tests is not likely a serious issue in establishing the general fracture mechanisms and toughness trends in NFA-1.

1.5. RESULTS AND DISCUSSION

1.5.1 Microstructural characterization

The microstructure of the hot extruded and cross rolled FCRD NFA-1 material was characterized in terms of the: (a) grain morphology; (b) presence and distribution of coarser precipitate-inclusions; (c) crack statistics; and, (d) texture as summarized in Tables 1.1 to 1.3 and Figs. 1.1 to 1.4. Figure 1.1b and c shows a low magnification SEM, and high magnification SEM/FIB 3D images of the NFA-1 plate. The thickness direction (LT) sections reveals nearly uniform, equiaxed and predominantly ultrafine grains (see Table 1.1). The average extrusion to cross-rolling direction GAR is ≈ 1.5. The extrusion and cross rolling direction views of the TS and LS sections, reveal a large number of microcracks lying on planes normal to the plate thickness direction. The pancake-shaped grains are elongated in the extrusion and cross-rolling directions. Most grains (≈ 80%) are < 1 μm, while fewer are in the range of 1-10 μm, and very few are more than 10 μm (see Fig. 1.2a). The average LS section length to thickness GAR is 2.7, varying from ≈ 2 to 16. Further details of the grain statistics can be found elsewhere [16].

Table 1.1 Grain morphology of FCRD NFA-1 material

Views	Long, (nm)	Short, s (nm)	Avg grain size, d=(l+s)/2, nm	Aspect ratio, l/s
LT	767 ± 566	517 ± 355	642 ± 450	1.5 ± 0.4
LS	792 ± 638	301 ± 108	546 ± 343	2.7 ± 1.6
TS	799 ± 833	296 ± 180	548 ± 482	2.7 ± 1.3

The fine scale Y-Ti-O NO statistics (d ≈ 2.4 nm, N ≈ 4.8 x 10^{23} m^{-3} and f ≈ 0.6%) are also reported elsewhere [6]. NFA-1 also contains coarser precipitates-inclusions as shown by the red arrows in Fig. 1.2a and summarized in Table 1.2. These inclusions are predominantly located at or near the grain boundaries in a form of stringers (Figs. 1.1c and 1.2a). EELS on FIB lift out TEM and EDS with SEM, respectively, identified these phases a mostly as Ti-rich (Ti-N-O: darker) oxinitrides, with fewer Y-rich (Y-O: gray) oxides (see Fig. 1.3). Microvoids initiate from these inclusions and degrade the ductility of NFA-1 (see 1.3b). The stringers are aligned parallel to the extrusion and cross-rolling directions. The average stringer through-thickness separation distance is ≈ 2.8 μm (Table 1.2 and Fig. 1.2a). As shown by the histogram in Fig. 1.2b, the coarser inclusions ranged from ≈ 10 to 260 nm, averaging ≈ 60 nm. The inclusion spacing along the stingers averaged ≈ 200 to 300 nm.

Figs. 1.1b, and 1.2a show microcracks running through the extrusion and cross rolling directions. The corresponding microcrack statistics for the section views are summarized in Table 1.3. The average opening at the crack center is ≈ 250 nm (Fig. 1.2a). The average distance between layers of cracks in the thickness direction is ≈ 16 μm. As shown in Fig. 1.2b, the cracks length ranged from ≈ 2 to 105 μm. About 75% cracks are below 15μm, and very few are over 50μm. The corresponding observed averages are ≈10 μm in the extrusion direction and 15μm in the cross rolling direction. In some cases, two cracks are separated by a small ligament (<1μm), thus were be considered as a single large crack with some degree of bridging. The larger cracks are important since they serve as weak links that initiate cleavage fracture.

The apparent number density per unit area varies from $1.3x10^9/m^2$ (in the extrusion direction) to 3.45 x $10^9/m^2$ (in the cross rolling direction view).

Table 1.2 Statistics of coarser precipitates of NFA-1 at different plate views

Views	Ti /Y-rich particle size (nm)	Interparticle spacing along stringer (nm)	Stringer spacing along thickness (μm)
LT	57 ± 33	228 ± 106	Random
LS	62 ± 32	303 ± 210	2.6 ± 1.0
TS	68 ± 33	279 ± 160	2.8 ± 1.0

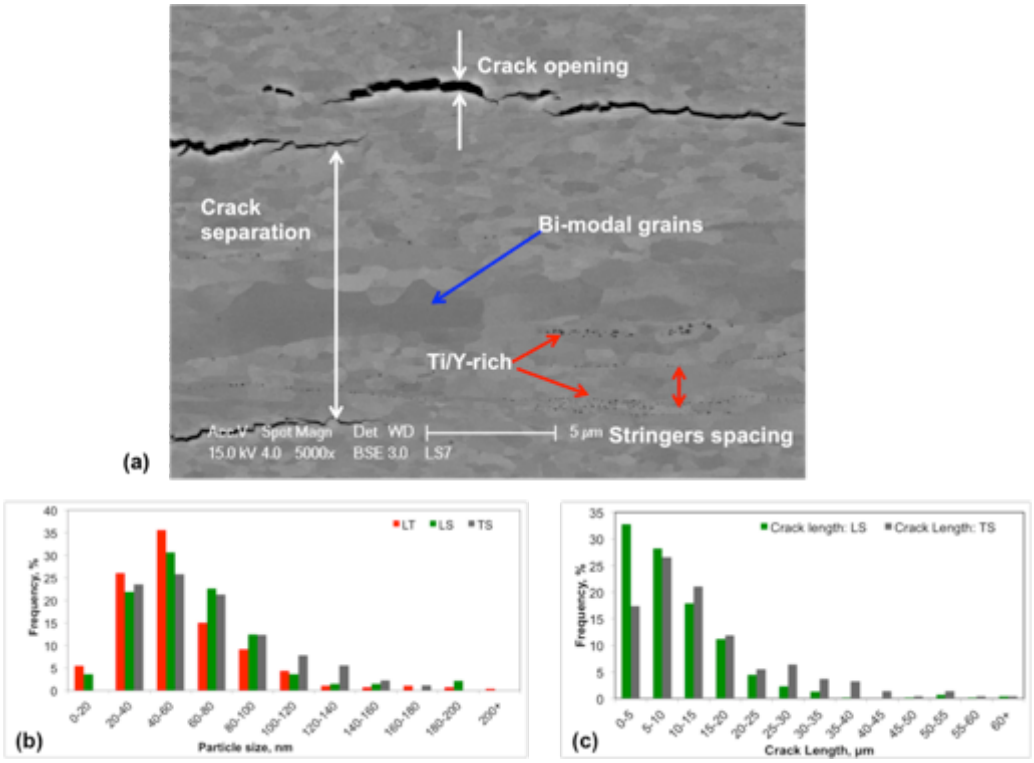

Fig. 1.2 (a) A representative higher magnification image of the NFA-1 microcracks and inclusion stringers as well as how crack spacing, opening and separation distance are defined; (b) the size distribution of coarser precipitates; and, (c) the distribution of microcrack lengths.

Figure 1.4 shows a 3D EBSD images of the grains and grain orientations for the x, y and z direction plate views. The color-coding indicates the orientation distribution along the extrusion (x), cross-rolling (y) and plate thickness compression (z) directions. The x-y (L-T) plate face, coded for poles in the z-direction, is almost 100% red, indicating the dominance of (001) planes. The grains are nearly equiaxed in the LT

plate face view. The LS view, coded for the x extrusion direction, is almost 100% green, indicating the dominant {110}-fiber texture. In this section view, the grains are elongated in the extrusion direction and thinned (compressed) in the z direction due to the extrusion and cross rolling. The grain morphology is similar in the TS section view, that again shows strong {110} a-fiber texture in the y cross-rolling direction. The texture index and GAR slightly higher in the extrusion direction, 4.83 and 2.71 ± 1.6, compared to the cross rolling direction, 4.45 and 2.65 ± 1.3. Low angle grain boundaries are found inside the larger grains.

Table 1.3 Crack statistics of NFA-1 at different plate views

Views	Crack opening width (nm)	Crack separation distance (μm)	Crack length (μm)	Crack density (m^{-2})
LT	-	-	-	-
LS	252 ± 142	16.3 ± 4.7	10.2 ± 8.9	3.45×10^9
TS	205 ± 130	15.2 ± 4.8	14.9 ± 12.6	1.34×10^9

These observations clearly show that extrusion and cross rolling creates {100}<110> plane-direction combinations that are a brittle cleavage system in bcc Fe [22-26]. Of course the a-fiber texture is very common in deformation processed steels [15, 27-29]. Junceda *et al.* [27] and Kimura *et al.* [28] reported that the grains are oriented in <110> along the extrusion direction in a hot extruded 14WYT ODS steel, and on a tempered martensitic steel, respectively. Ukai *et al.* [15] also reported {100}<110> textured grains in parallel to rolling planes and rolling directions in a hot extruded, recrystallized and cold-rolled 15YWT ODS alloy, whether as Bourell [29] also found similar texture component in a warm-rolled low carbon steel.

It was previously believed that the microcracks nucleated at the coarser precipitates, especially along prior powder grain boundaries [22, 30-31]. However, this does not seem to be the dominant mechanism of microcrack formation in NFA-1. Extrusion and cross rolling induce a strong <110>-fiber texture, accompanied by the formation of {001}<110> cleavage plane-direction systems, lying on planes perpendicular to the plate thickness. Notably, the brittle {100}<110>-cleavage system has a low temperature toughness of ≤ 4 MPa√m and the temperature range of low toughness increases with alloy strength [24-26, 32-34].

As reported by S. Pal et. al [18], the responsible deformation mechanism is as follows. High temperature deformation first produces sessile a[001] dislocations on {001} planes by a/2[111] + a/2[-1-11]→a[001] dislocation reactions. The resulting stack up of a[100] sessile dislocations forms a low angle sub-grain tilt boundary. Further deformation leads to pile up of a/2{111} slip dislocations at the {100} boundary, and a correspondingly high stress-concentration. The leading dislocations can create a cleavage crack opening nucleus on the {100} sub boundaries that partly relaxes the very high local pile-up stresses, as initially proposed by Cottrell [35]. The subsequent activation of the cleavage crack nuclie to form a population of microcracks is likely driven by deformation induced residual stresses as the plate cools to a temperature below the cleavage brittle-to ductile transition temperature (BDTT).

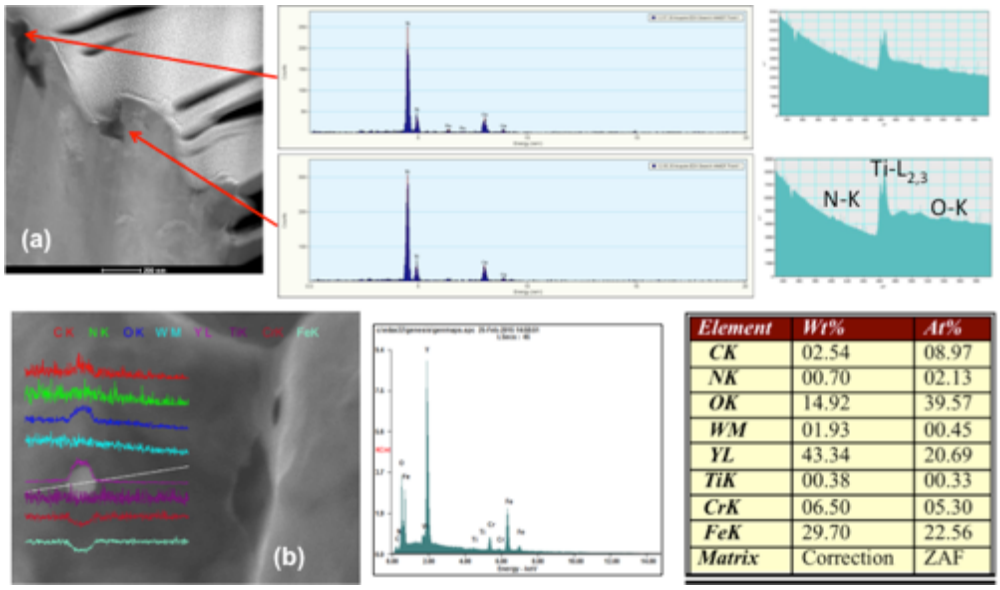

Element	Wt%	At%
CK	02.54	08.97
NK	00.70	02.13
OK	14.92	39.57
WM	01.93	00.45
YL	43.34	20.69
TiK	00.38	00.33
CrK	06.50	05.30
FeK	29.70	22.56
Matrix	Correction	ZAF

Fig. 1.3 NFA-1: (a) EDS and EELS spectra showing the Ti-N-O rich precipitates; and, (b) SEM/EDS showing Y-O rich precipitates.

Fig. 1.5a shows a bright field (BF)-TEM image of the crack propagation path, where the cross-sectional FIB lift-out is perpendicular to the crack propagation front. Here, the hot extrusion direction is normal to the TEM lamella. The micrographs clearly show that the crack propagates within a single pre-existing grain in a transgranular manner. The selected area diffraction pattern (SAD) from the locations marked 1 and 2 in Fig.1.5a show that the foil normal is <110>. The microcrack front propagation direction is <110> along the primary deformation direction, which is normal to the TEM lamella in Fig. 1.5a. Similarly, weak beam dark filed imaging (WBDF) corresponding to the (002) spot in Fig. 1.5b, shows dislocation pile-ups of crack at the low angle subgrain boundary parallel to the crack. SAD patterns, shown in the insert in Fig. 1.5a, taken near the crack tip at the marked locations, show the general grain orientation is <110>. However, the pattern for location 2 is slightly misoriented respect to the pattern for location 1 in the same grain, even though they maintain the same general common orientation of <110>. This indicates the presence of a low-angle subgrain boundary parallel to the crack propagation direction. Thus these TEM observations fully support our hypothesis regarding this microcrack nucleation and propagation mechanisms. In general these observations are consistent with the more qualitative early findings of Tetelman and co-workers [36-38].

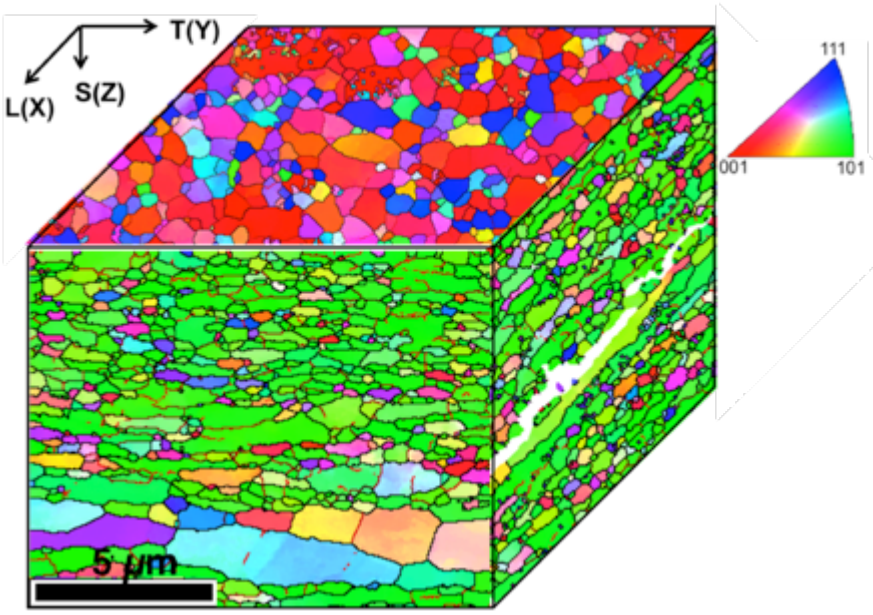

Fig. 1.4 An EBSD inverse pole figure (IPF) showing strong {110} texture along the extrusion direction (ED) and (001) plane grains lying parallel to the L-T plate section face.

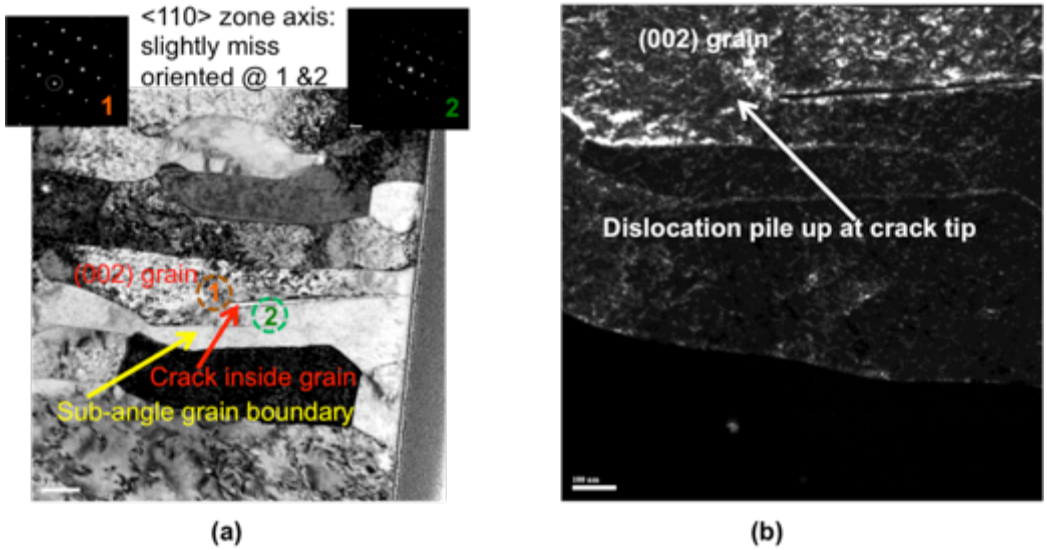

Fig. 1.5 Microcrack formation microstructures in NFA-1: a) A BF-TEM image of the crack propagation front at a subgrain boundary; and, (b) a weak beam dark field image for the (002) spot highlighting dislocations around the crack. The crack in this grain containing is on a (002) plane with the foil normal to <110> as indicated by a SAD pattern taken ahead of the crack tip (not shown).

1.5.2 Tensile test

Results of low temperature uniaxial L-axis tensile tests are summarized in Table 1.4 and the corresponding engineering stress-plastic strain (s-e_p) curves are shown in Fig. 1.6, starting at the standard 0.2% plastic offset strain. As expected the yield (s_y) and ultimate (s_u) stresses increase with decreasing temperature reaching a $s_y \approx 1555 \pm 121$ MPa and $s_u \approx 1643 \pm 112$ MPa at -196°C. Notably, the tensile total elongation strains (e_t) remain high down to -196°C. In all cases the fracture surfaces are characterized by shallow dimples (Fig. 1.7b).

Table 1.4 Low temperature tensile test results of NFA-1 samples at L orientation

Temperature (^oC)	s_y (MPa)	s_u (MPa)	e_u (%)	e_t(%)	RA, %
25	1042 ± 102	1133 ± 100	3.8 ± 3.7	12.9 ± 1.5	56 ± 8
-50	1073 ± 65	1183 ± 76	6.9 ± 4	15.7 ± 0.7	58 ± 7
-100	1162 ± 54	1293 ± 62	5.7 ± 6	14.8 ± 1.8	56 ± 14
-125	1326 ± 25	1416 ± 10	1.3 ± 0.7	15.3 ± 3	47 ± 2
-150	1332 ± 69	1453 ± 103	6 ± 6.5	13 ± 5	50 ± 4
-175	1424 ± 59	1502 ± 93	1.8 ± 1.1	10.9 ± 1.3	44 ± 2
-1951	1555 ± 121	1643 ± 112	1.0 ± 0	7.9 ± 0.7	31 ± 6

s_y= yield stress, s_u= ultimate tensile stress, e_u= uniform elongation, e_t= total elongation, RA = reduction of area

1.5.3 Fracture toughness at ambient temperature

Normalized ambient temperature (AT ≈ 23°C) load-displacement (P-D) curves, for the four different orientations (see Figure 1.1a) are shown in Fig. 1.8a. This normalization involved adjusting the P-Δ data to a common a/W=0.5, so that the curves can be better inter compared. The L-S and T-S peak load (P_{max}, marked by circle) are roughly similar and somewhat higher than those for the L-T and T-L orientations, which are also in themselves similar. The corresponding maximum load average K_{Jc} are ≈ 88 and 97 MPa√m for L-T and T-L, respectively; and ≈ 154 and 140 MPa√m for L-S and T-S, respectively. The P-D curves show a series of small pop-ins and an otherwise quasi continuous load drop with increasing Δ following P_{max}. The P-D curve is associated with stable crack growth, and strong resistance curve behavior. Note, we did not construct resistance curvse per se, in part due to the complications introduced by the delaminations. The P-D curves can be viewed as measures of cracked body strength and ductility. None of the specimens fully fractured in tests above -196°C. The larger K_{Jc} for the S orientations is due to a higher P_{max} and D_{pmax} for deflected cracks. The K_{Jc} vary somewhat from specimen-to-specimen as shown by the scatter bars.

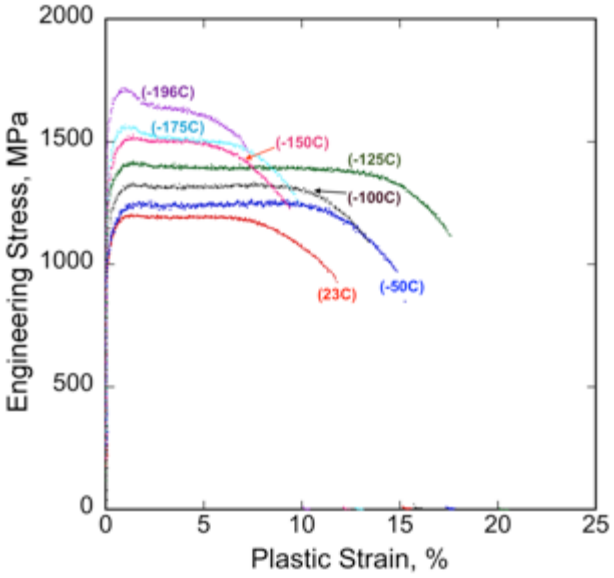

Fig. 1.6 (a) Engineering stress- plastic strain curves of L oriented tensile specimens tested at room to liquid nitrogen temperatures.

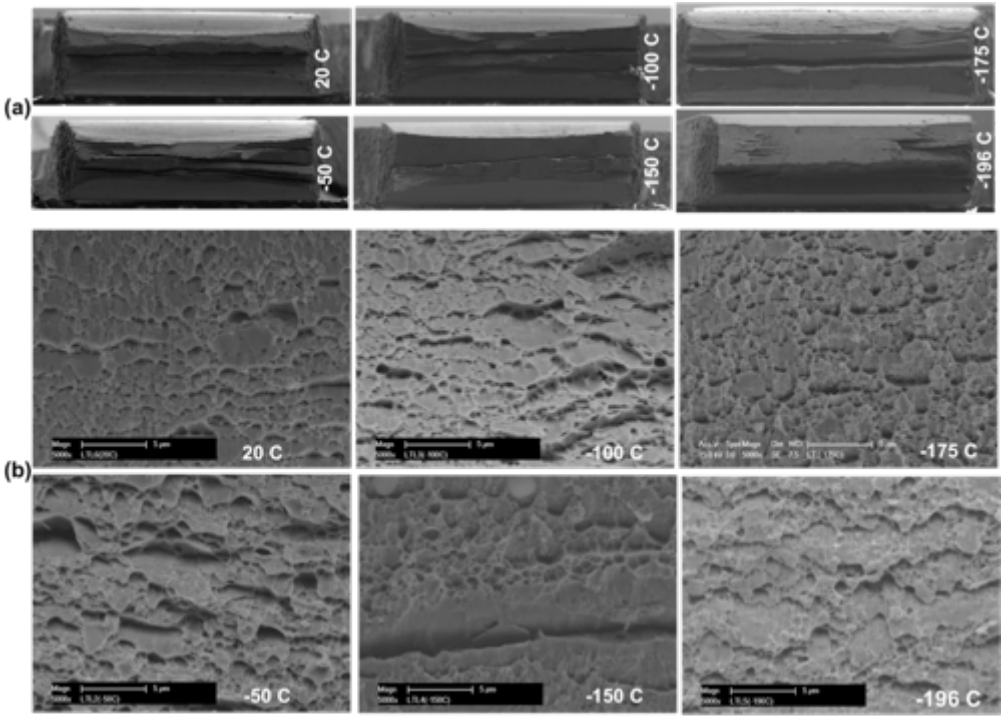

Fig. 1.7 Low (a) and high (b) high magnification SEM images of the fracture surfaces for L-orientation tensile tests at different temperatures showing ductile fracture down to -196ºC.

Table 1.5 Low temperature fracture toughness (K_{Jc}) of NFA-1 at L-T and T-L orientations

Temp (°C)	L-T (MPa√m)	T-L (MPa√m)
20	88 ± 12	97 ± 8
-50	113 ± 16	91 ± 13
-100	101 ± 4	96 ± 2
-125	102 ± 2	93 ± 5
-150	79 ± 23	92 ± 5
-175	70 ± 2	86 ± 3
-196	37 ± 4	44 ± 2

Post-test side-section images of the specimens in Fig. 1.8b, show that the cracks run in plane for L-T and T-L tests, but deflect by ≈90°, to form Mode II cracks , in both the L-S and T-S orientations. The deflected cracks run down delaminations parallel to the plate faces. The L-S and T-S P-D curves show a series of larger pop-ins, reflecting a larger distance between delamination microcrack initiation and arrest.

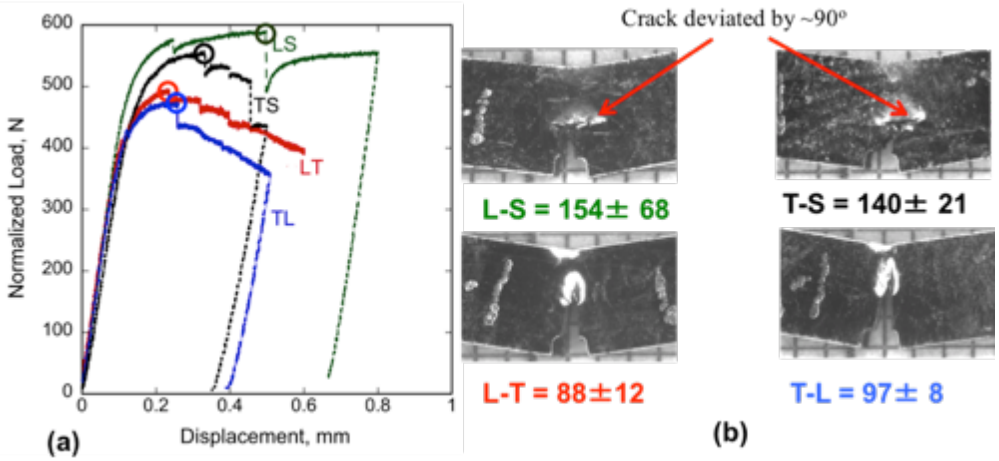

Fig. 1.8 Representative NFA-1: (a) Load-displacement curves for 3PB tests at 23°C in the 4 orientations; and, (b) corresponding macroscopic specimen side views of the propagated crack in the 4 orientations along with the corresponding K_{Jc} (MPa√m). Note: the red, blue, green and black colors represent L-T, T-L, L-S, and T-S specimens, respectively.

Representative fracture surfaces for the L-T and T-L orientations are presented in Fig. 1.9. Fig. 1.9a shows the different crack zones: notch 1; fatigue-precrack 2; stable crack growth 3; and post-test LN_2 cleavage fracture 4. Low magnification images (Figs. 1.9b and e) of zone 3 show the out-of-plane delaminations that develop along with crack tearing. The delaminations in the L-T and T-L orientation are very similar. Higher magnification images (Figs. 1.9c and f) reveal that the ductile tearing fracture surfaces are dominated by shear lips, or knife-edge ruptures, between minor out-of-plane delamination cracks. Ductile dimples are also observed, especially on the T-L fracture surface. The microvoids likely initiate at the Ti-N-O rich and Y-O rich inclusions (Fig. 1.3). No significant brittle cleavage is observed.

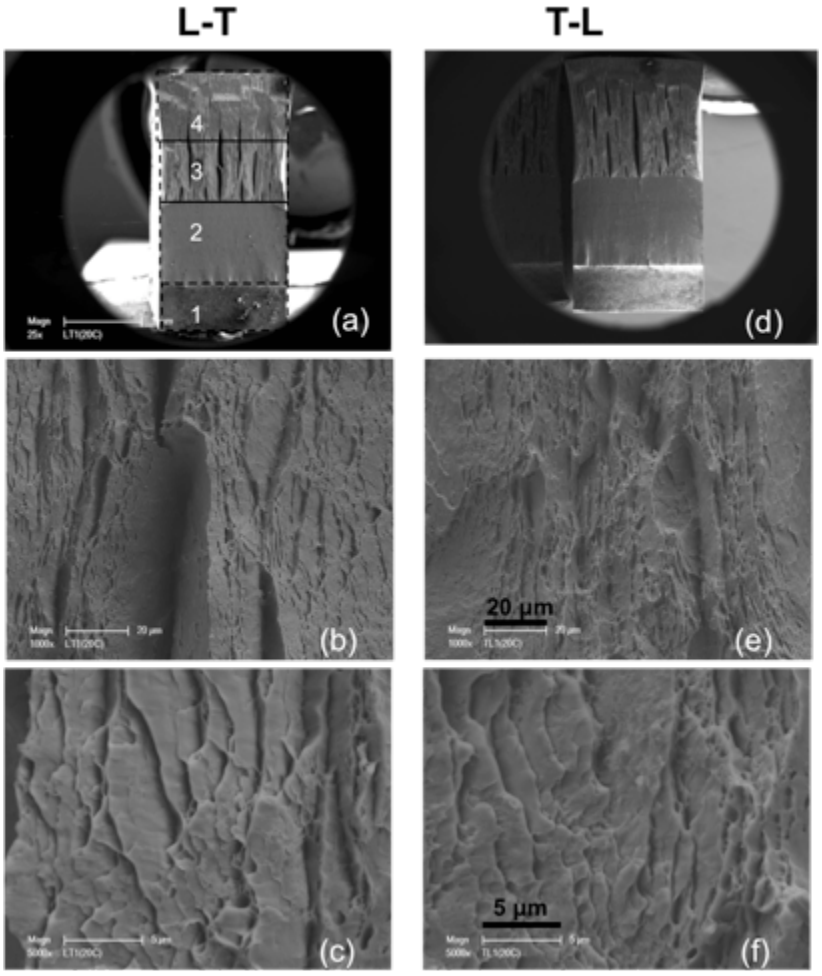

Fig. 1.9 Representative NFA-1 SEM micorgraphs at different magnification for tests at 23°C for L-T (left column a, b, c) and T-L (right column d, e ,f) orientations, showing nearly identical fracture surfaces. Fig. 1.9(a) also shows the different specimen zones: 1-notch; 2-pre-cracked; 3–crack tearing; and 4-final fracture in liquid nitrogen.

Thus the maximum load K_{Jc} is controlled by the combination of the alloy strength and the crack tip opening displacement ductility. The strength relation derives from the fact that ductile tearing occurs

beyond general yielding of the pre-cracked 3PB specimens. The maximum load often occurs at small pop-ins, but this is not always observed. The initiation of crack tearing at maximum load is clearly seen on the ductile fracture surface and occurs at relatively low D_{pmax}, thus the K_{Jc} is modest. If the alloy was stronger, P_{max} would increase, while if it was more locally ductile D_p would increase. In both cases this would lead to larger K_{Jc}. However, from a practical point of view, stable crack tearing beyond general yield is propabably not a significant failure path in most structures. Any failure would be graceful.

Representative fracture surfaces for the L-S/T-S orientations are shown in Fig. 1.10. Fig. 1.10a shows the P-Δ curve of L-S specimen and corresponding side-section L-S *in-situ* optical images at points 1 to 6 that show the 90º deflection from an in-plane Mode I to an out of plane Mode II crack. The load increases up to point-4. The micrograph corresponding to point-4 shows multiple crack-tip plastic zones (dark circles indicated by red arrows) due to the delaminations. Note, these dark regions are due to out-of-plane lateral contraction dimples in the plastic zones. Numerous striation marks/delaminations normal to the loading direction (and parallel to the deviated crack front directions) are seen near the crack-tip (images 4-6 of Fig. 1.10a and Fig. 1.10b). The delmaninations reflect the favourable orientation for microcrack propagation on the {100} cleavage planes along the pancake-shaped grains deformation <110> direction (Figs. 1.1 and 1.2). A relatively large pop-in occurs between points 4 and 5, along with a large increase in crack opening, marked by green arrow in the micrograph for point-5. The micrograph for point-7 is a post-test low-magnification optical image of the fracture surface.

The combination of multiple delaminations and deflected cracks increases the remote loading K_{Jc}. Figure 1.10c shows a low magnification SEM image of the fractured T-S section that includes notch (1), pre-crack (2), and out-of-plane crack propagation (3) zones. Unlike L-T/T-L orientions (zone-3 of 1.7a-b), the L-S/T-S orientations shows virtually no, or very minimal, in-plane cracking near the initiation point (zone 3 of Fig. 1.10c). The higher magnification image in Figure 1.10d, near the crack tip (highlighted by the black box of Fig. 1.10b) shows the elongated grains which have a strong α-fiber texture. Additional T-S/L-S orientation 3PB tests have not been carried out, since in-plane fatigue precracking is nearly impossible. Note most toughness data in the literature on NFAs is for L-T and/or T-L orientations.

1.5.4 Fracture toughness at lower temperatures

The L-T and T-L K_{Jc} at ambient and lower temperatures tests are summarized in Table 1.5 and Fig. 1.11. Representaive P-Δ curves and the macroscopic images of the fracture surfaces are shown in Fig. 1.12. The L-T and T-L K_{Jc}(T) are similar, hovering around 100 MPa$\sqrt{m}$ down to -125°C. Stable ductile tearing is observed down to -150^{o}C with one exception; one of the 3 L-T tests at -150ºC experienced a large cleavage fracture pop-in load drop near general yielding, with a lower K_{Jc} = 52 MPa$\sqrt{m}$. Note this specimen has a sharp notch in its uneven pre-crack front, that may have created a secondary stress concentration leading to the pop-in. The fracture transition region behavior at -175°C is discussed in more detail below.

Stable ductile tearing in the L-T and T-L oreintations is attributed to the delaminations. In contrast to the triaxal, plane-strain crack tip stress state absent delamination, the thin ligament sections transition to a more biaxial plane-stress state. As a result the stresses ahead of the crack tip decrease by a factor of ≈ 3, and their amplitiude falls below the critical local fracture conditions required to initiate cleavage [20].

The delaminations are very straight and almost equally spaced. They generally increase number with decreasing temperature (Figs. 1.12c and d). Figure 1.13 shows higher magnification (x5000) micrographs for L-T and T-L tests from -50^{o}C to -150^{o}C, that have almost identical fracture morphologies. Flake-like

shear lips, along with knife edge features, are observed throughout the fracture surface. Fibrous features are also observed between the knife-edges (see insert image of Fig. 1.13).

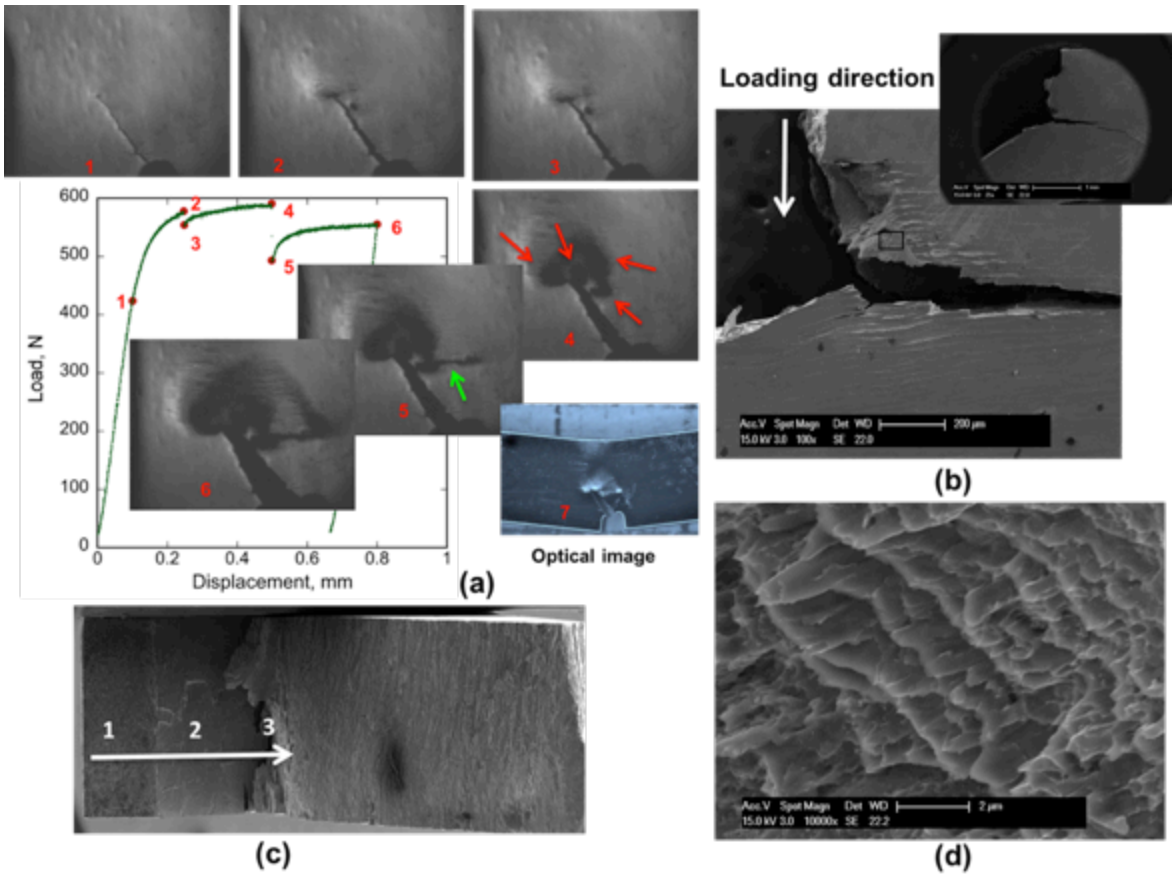

Fig. 1.10 (a) A 23°C P-Δ curve and its corresponding in-situ images at points 1 to 6 for a L-S orientation. The red arrows at point-4 show multiple plastic zones and the green arrow at point-5 shows crack propagation. Point-7 shows a post test macroscopic view of the specimen; (b) SEM images show the 90° crack deflection of loading directions along with lots of micro-delamination parallel to the crack; (c) macroscopic view of fractured face that includes notch (1), pre-crack (2) and out-of-plane crack propagation (3) zones, and (d) magnified view of (b).

Compared to higher temperature tests (see example in Fig. 1.12a), the load-displacement (P-Δ) curves for L-T tests at -175ºC show only a small amount of plastic post yield, D_p, prior to a large cleavage load drop. This brittle behavior is reflected in the fracture surfaces in Fig. 1.14. Fig. 1.14a shows three fracture zones.

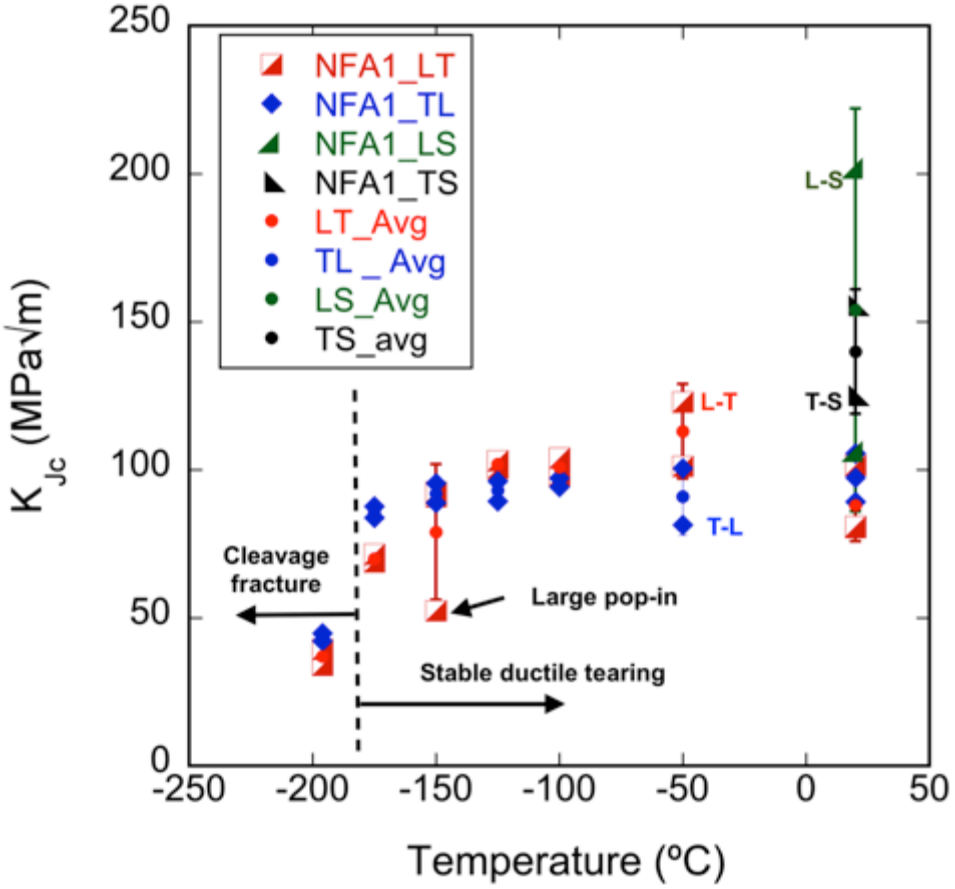

Fig. 11.1 The K_{Jc} (MPa√m) of NFA-1 as a function of temperature for the 4 orientations. Note: the red, blue, green and black colors represent L-T, T-L, L-S, and T-S specimens, respectively. Color-coded small circles represent respective average K_{Jc} values with error bars.

The higher magnification view of zone 1 shown in Fig. 1.14b, reveals only limited delamination and shear-lips. Extensive cleavage faceting is observed in zone 3 (Fig. 1.14d), which is associated unstable crack propagation. Ductile dimples and crater-like features are observed in zone 2, marking the transition between the stable and unstable crack propagation (Fig. 1.14c). The corresponding L-T K_{Jc} at -175ºC is 70 ± 2 MPa√m, falling between ductile tearing delamination dominated fracture at higher temperature and cleavage initiation at -196°C. In contrast, the T-L tests exhibit ductile tearing and stable crack growth at -175ºC, and a higher K_{Jc} = 86 ± 3 MPa√m (see Table 1.5 and Fig. 1.12). SEM fractographs in Figs. 1.14e and f, show -175°C T-L test delaminations that are similar to those at higher temperatures. In contrast, the L-T fracture surface is associated with a number of shallow out of plane delamination cracks and shear-lips.

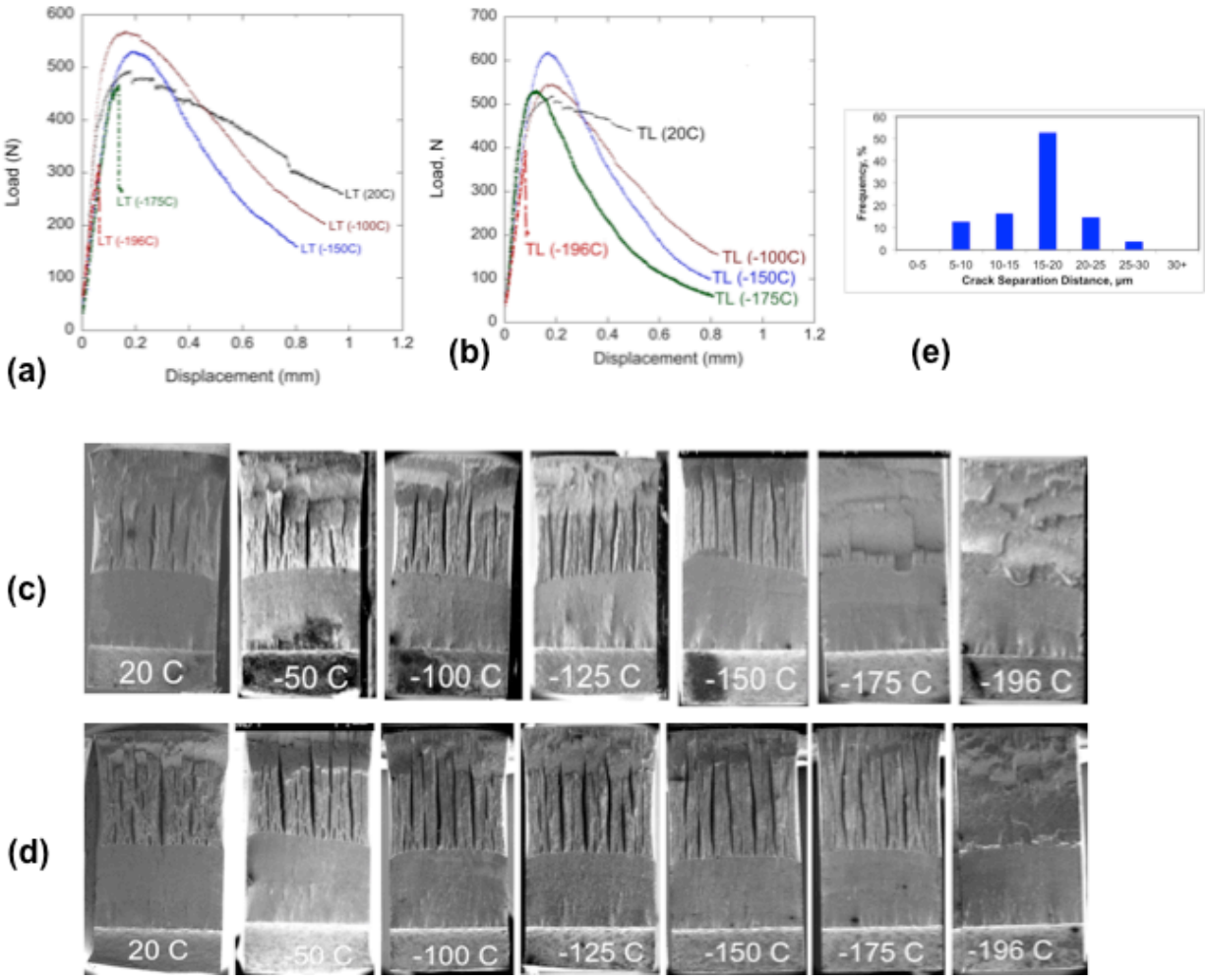

Fig. 1.12 (a and b) Representative NFA-1 L-T and T-L load displacement curves at various temperatures; (c and d) the corresponding macroscopic fracture surfaces showing the delaminations; and, (e) the preexisting crack separation distance distribution in the untested plate.

Both L-T and T-L tests fail by brittle cleavage at liquid nitrogen temperature ≈ -196°C. The P-Δ curves and macroscopic fractures surfaces are shown in Fig. 1.12. The high magnification SEM fractographs in Figure 1.15 show brittle cleavage facet features in both orientations.

In summary, with one exception, fracture of NFA-1 down to -150°C is dominated by ductile tearing and stable crack growth, largely due to delaminations that either shield the crack by deflection or reduction of triaxial stresses. K_{Jc} decreases at lower temperature and fracture is entirely by cleavage at -196°C. Thus a reasonable estimate of the BDTT in NFA-1 is -175°C.

The delaminations derive from propagation of a population of microcracks in the as-extruded and cross-rolled NFA-1 plate. The L-T and T-L toughness are remarkably isotropic compared to other NFA, that typically have tougher transverse versus much more brittle deformation direction orientations. For

example, an as-extruded bar of MA957 was found to be extremely brittle in the axial direction, but much tougher in transverse orientation, where the cracks deflect by 90° [7], similar to the behavior in the L-S and T-S orientations of NFA-1. Thus the multiple underlying fracture mechanisms in NFA-1 are not unique, but due to difference in the processing route, manifest themselves in different ways.

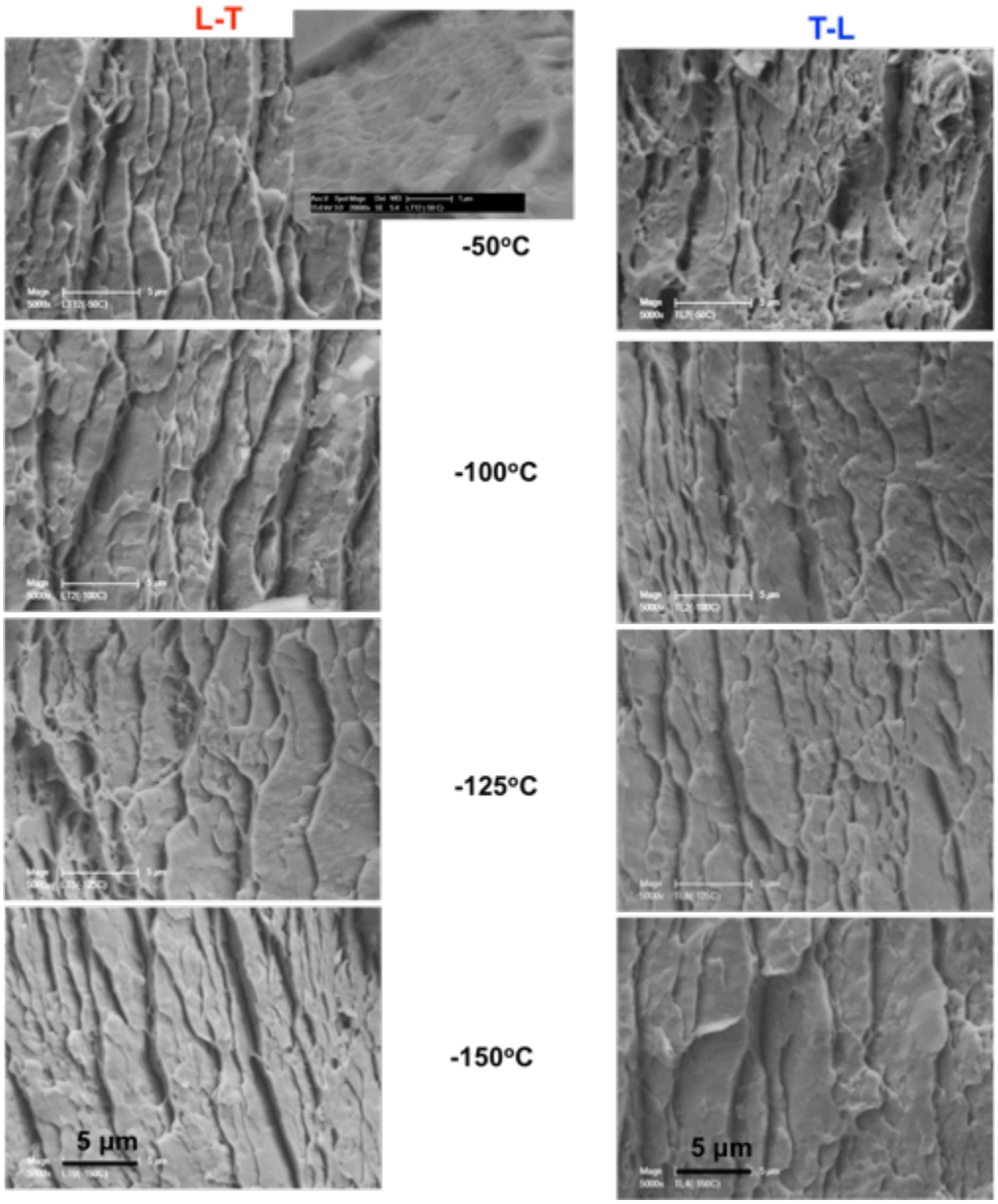

Fig. 1.13 SEM fractographs of 3PB fracture surfaces showing nearly identical, shallow dimples-like features both for L-T (left) and T-L (right) tests from -50°C to -150°C. The high magnification insert taken at the flatter surfaces between the dimple edges shows the fibrous features that are evidence of localized plastic deformation.

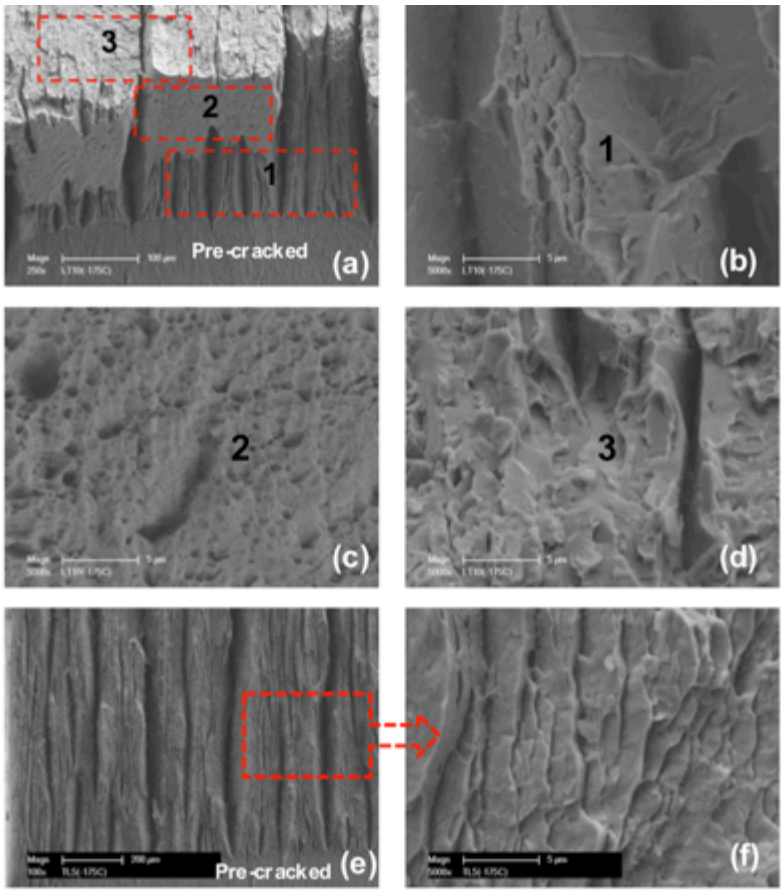

Fig. 1.14 Representative NFA-1 SEM fractographs for a L-T test at -175°C showing the coexistence of: a) delaminations and associated shear-lips; (b), delaminations and dimples; (c) dimples; and, (d) cleavage facets. Fig. 1.14e-f shows shear-lips and delaminations over the entire fracture surface for a corresponding T-L test at -175°C, associated with stable ductile tearing.

In order to provide additional perspective, Figure 1.16 compares the $K_{Jc}(T)$ of NFA-1 to similar nanostructures alloys [8-13]. With one possible exception, NFA-1 has the lowest brittle to ductile transition (BDT) temperature in both orientations. Two 14YWT heats, and a MA957 round bar have [7-10] have higher toughness values than NFA-1 in their tough L-T orientation and for the MA957 L-R orientation, due to crack deflection. However, their fracture properties of these alloys are highly anisotropic, as illustrated by the very low toughness with higher BDTT (-84ºC for L-T vs 18ºC for T-L) of one of the 14YWT heats (SM10) for T-L [9] and MA957 in the C-R and C-L oreintations (equivalent to T-L in the plate). Note, most previous NFA fracture tests were carried out only in the tough orientation.

1.5.5 Delamination and toughening mechanisms

We have already noted that delaminations increase toughness either by crack deflection or the reduction in triaxial stresses as illustrated in Figure (what is now Figures 1.17 b and c) . The underlaying mechanism is propagation of a population of pre-existing microcracks that form during processing. The

mechanism of microcrack formation is briefly summarized here, but a more detailed evaluation of the dislocation level mechanisms is described elsewher [18].

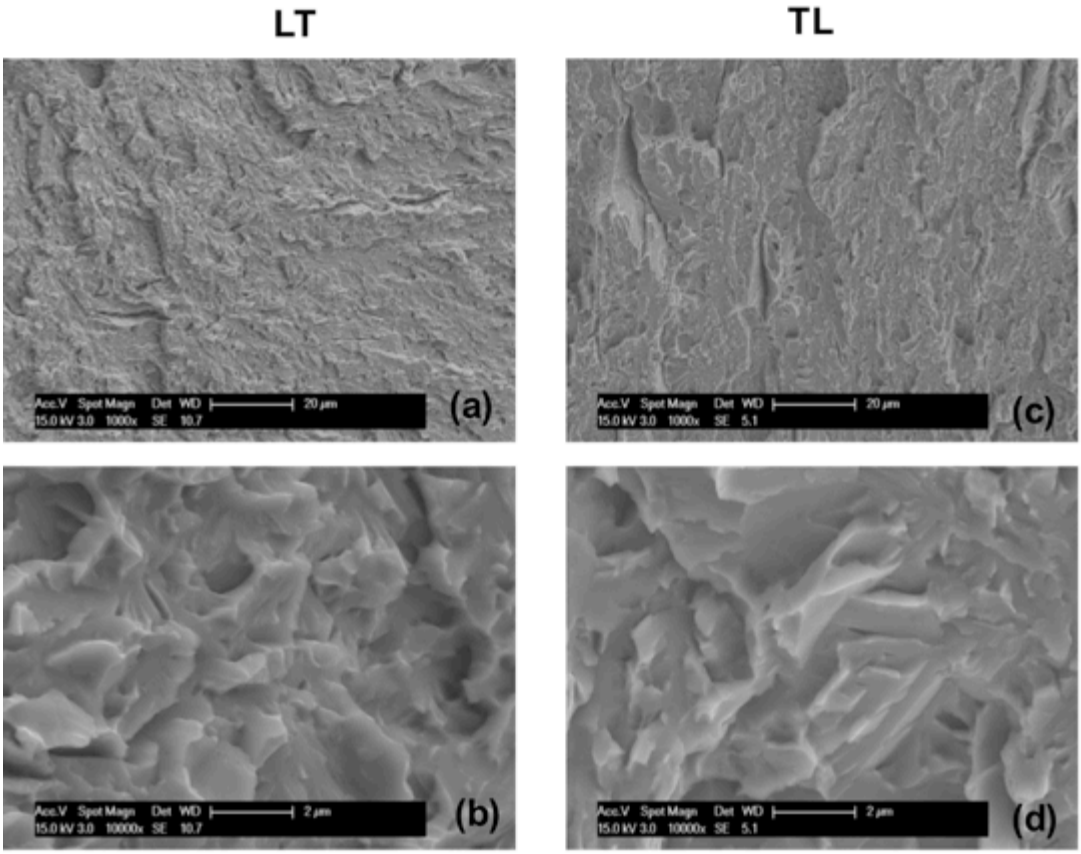

Fig. 1.15 Representative NFA-1 SEM fractographs of cleavage facets at -196°C for: (a and b) L-T tests; and (c-d) T-L tests.

In general, the number and depth of delmaminations increases with decreasing temperature as illustrated in the low maginification fracture surfaces from at 23ºC to -175ºC shown in Fig. 1.12 c and d. At 23°C the primary, and likely first, delamination is in the middle of the uncracked ligament, spliting the crack front in half at the location of the peak transverse stress. The transverse stress peak then moves to the middle of the two halves producing one major additional split. The delaminations are accompanied by a reduction in the internal crack tip stresses, that cannot reach the critical stress-stressed volume condition required for cleavage [4, 22, 39]. Thus, fracture can only take place by ductile tearing and microvoid coalescence producing shallow dimples on the fracture surface [4].

The finite element method (FEM) was used to simulate the P-D curve with no crack extension for both plane strain and stress state conditions. Figure 1.17a compares the FEM curves to corresponding T-L test data at -150ºC. The measured P_{max} falls between the plane strain and plane stress. The P gradually falls off after P_{max}, due to crack tearing with increasing D_p. Clearly, NFA-1 also manifests a large amount of effective engineering ductility even for fracture by tearing of an initially sharp precrack.

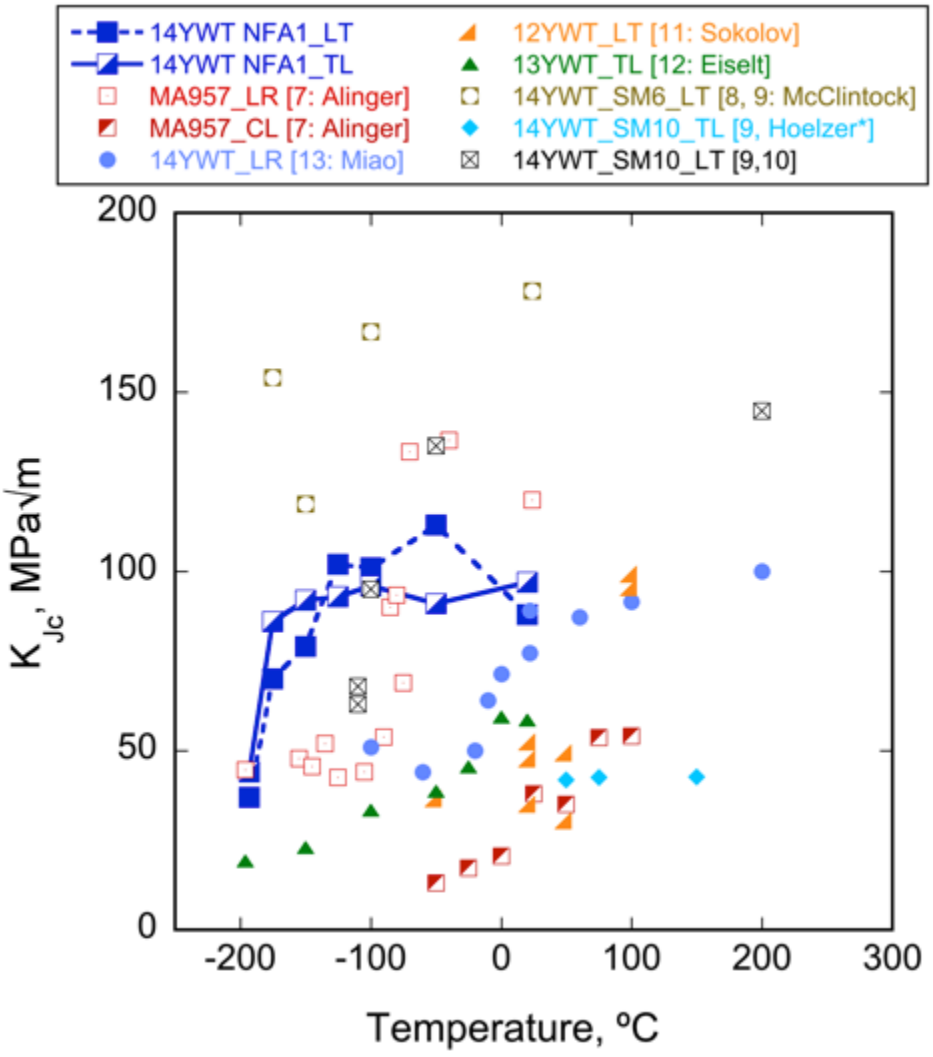

Fig. 1.16 Comparison of the NFA-1 fracture toughness with other ODS/NFA's as a function of temperature [8-13]. Hoelzer* = personal contact.

The L-S and T-S tests experience crack deflection as illustrated in Figs. 1.8 and 1.10. The primary crack travels only a short distance before arresting. Continued increments of Δ result in the propagation of the 90° deflected delaminations and splitting of the specimen. Such delamination cracks are common in some composites, but rare in metals. The loading-crack mode mixity for such kinking delamination cracks has been extensively addressed [40, 41]. However, for the purposes of this study we simply define a higher initiation T-S and L-S K_{Jc} at P_{max}.

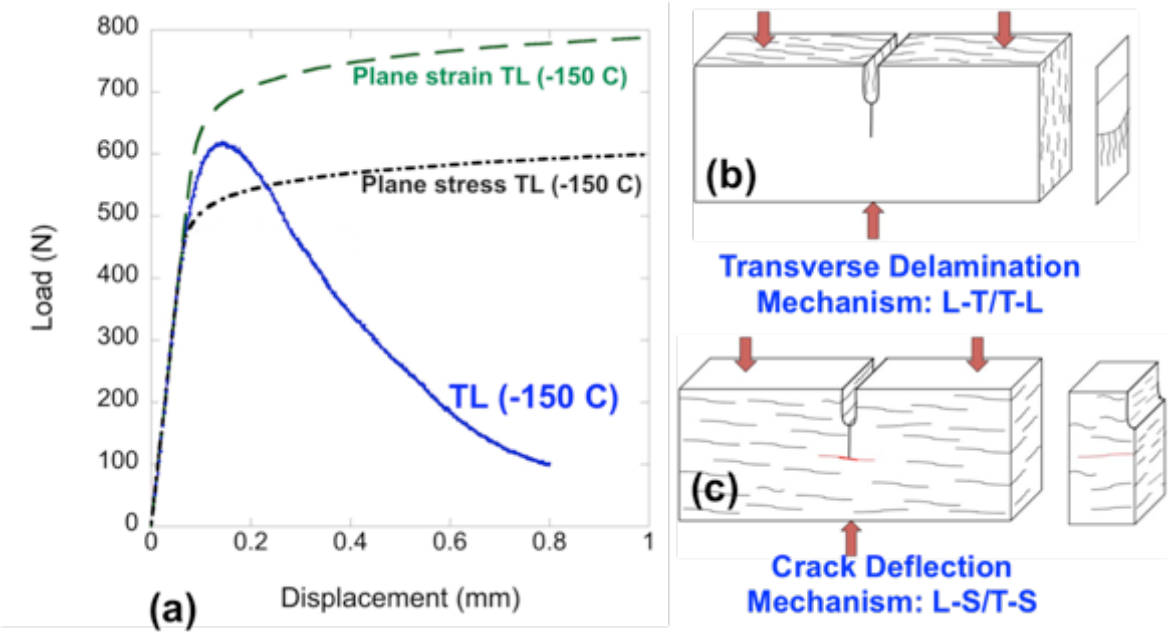

Fig. 1.17 (a) Finite element (FE) method simulations of load-displacement (P-Δ) curves for plane stress and plane strain states, assuming no-crack extension, along with the observed P-Δ curve for a T-L test at -150ºC showing the effect of stable crack tearing; b) a schematic illustration of the transvers delamination mechanism (L-T and T-L); and, c) a schematic illustration of the crack deflection mechanism (L-S and T-S).

1.6 SUMMARY AND CONCLUSIONS

The fracture toughness of 14YWT NFA-1 was characterized over a wide range of temperatures in all relevant loading orientations. The results and conclusions can be summarized as follows:

- The FCRD NFA-1 extruded and cross-rolled plate contains a bimodal size distribution of predominantly sub μm pancake-shaped grains, along with a large population of microcracks lying on planes parallel to plate faces. The microcracks are associated with a strong {001}<110> texture, which is the most brittle cleavage system in bcc-Fe, along with residual stresses developed during the thermomechanical processing.

- The key micromechanism leading to the formation of the {001}<110> cleavage system is reactions between glissile a/2<111> dislocations to form sessile a<100> dislocation stack-ups that constitute a {100} subgrain boundary.

- The microcracks nucleate from a dislocation pile-ups at the subgrain boundary and the leading dislocations for form a nanocrack opening displacement The following the theory of Cottrell [35].

- Both local pile-up and residual stresses lead to formation of μm-scale cracks at temperatures below the Fe-Cr ferrite BDT temperature.

- Room temperature toughness tests show ductile tearing with a peak load K_{Jc} from ≈ 88 to 154 MPa√m.

- Extensive stable ductile tearing is observed both at L-T and T-L orientations from room temperature to -150ºC, and in the T-L orientation down to -175°C, marking an effective BDTT.

- The ductile tearing occurs down to such low temperatures due to extensive delaminations that form by the propagation of the pre-existing microcracks.

- The delaminations in the L-T and T-L orientations split the crack front into thinner sections, leading to a reduction in both stress triaxiality and local tip stresses, thereby suppressing cleavage.

- The delaminations in the L-S and T-S orientations result in 90° crack deflection and higher effective toughness mixed-mode fracture.

ACKNOWLEDGMENTS

The Materials Performance and Reliability Group (MR&PG) at the University of California Santa Barbara (UCSB) carried out the research reported here. The UCSB authors gratefully acknowledge the support provided by U.S. Department of Energy through the Office of Fusion Energy Sciences (DE-FG03-94ER54275), the Office of Nuclear Energy though the Idaho National Laboratory Nuclear Energy University Research Program (IDNL Award #00119430 8-442520-59048) and the Fuel Cycle Research and Development Program through a subcontract from Los Alamos National Laboratory (LANL8-442550-59434). The U.S. National Science Foundation supported California Nanoscience Institute provided facilities critical the success of this research. The. Authors also like to gratefully recognize Dr. D. T. Hoelzer (ORNL, USA) for his key role in fabricating NFA-1 and MR&PG members Takuya Yamamoto, Yuan Wu, David Gragg and Kirk Fields for their important contributions.

REFERENCES

[1] S.J. Zinkle and G.S. Was, “Materials challenges in nuclear energy”, Acta Materrialia 61 (2013) 735-758.

[2] Y. Dai, G.R. Odette and T. Yamamoto, “The effects of helium in irradiated structural alloys” R. Konings: Comprehensive nuclear materials”, 1st Edition, Atlanta, GA: Elsevier (2012).

[3] G. R. Odette, M. J. Alinger and B. D. Wirth, “Recent developments in irradiation-resistant steels”, The Annual Review of Materials Research, 38 (2008) 471-503.

[4] G. R. Odette, “Recent progress in developing and qualifying nanostructured ferritic alloys for advanced fission and fusion applications”, JOM, 66 (2014) 2427-2441.

[5] S. Ukai, “Oxide dispersion strengthened steels”, R. Konings: Comprehensive nuclear

materials", 1st Edition, Atlanta, GA: Elsevier (2012) 241-271.

[6] N. J. Cunningham, Y. Wu, G.R. Odette, D. T. Hoelzer, S. A. Maloy, " Characterization of a larger best practice heat of 14YWT in annealed powder, HIP consolidated and extruded forms," DOE/ER-0313/54 (2013), DOE Fusion Reactor Materials Program Semiannual Progress Report (2013).

[7] M. J. Alinger, G. R. Odette and G. E. Lucas, "Tensile and fracture toughness properties of MA957: implications to the development of nanocomposited ferritic alloys", Journal of Nuclear Materials, 307-311 (2002) 484-489.

[8] D. A. McClintock, D. T. Hoelzer, M. A. Sokolov, and R. K. Nanstad, "Mechanical properties of neutron irradiated nanostructured ferritic alloy 14YWT", Journal of Nuclear Materials, 386-388 (2009) 307-311.

[9] D.T. Hoelzer, J. Bentley, M.K. Miller, M.K. Sokolov, T.S. Byun, Development of high-strength ODS steels for nuclear energy applications, in: Proceedings of the ODS 2010 Materials Workshop, Qualcomm Conference Center, 17–18 November, 2010.

[10] T.S. Byun, J. H. Kim, J.H. Yoon, D.T. Hoelzer, "High temperature fracture characteristics of a nanostructured ferritic alloy (NFA)", Journal of Nuclear Materials, 407 (2010) 78-82.

[11] M. A. Sokolov, D. T. Hoelzer, R. E. Stoller and D. A. McClintock, "Fracture toughness and tensile properties of nanostructured ferritic steel 12YWT", Journal of Nuclear Materials, 367-370 (2007) 213-216.

[12] Ch.Ch. Eiselt, M. Klimenkov, R. Lindau, A. Möslang, G.R. Odette, T. Yamamoto, D. Gragg, "Tensile and fracture toughness properties of the nanostructured oxide dispersion strengthened ferritic alloy 13Cr–1W–0.3Ti–0.3Y_2O_3", Journal of Nuclear Materials, 4 17(2011) 193-196.

[13] P. Miao, G. R. Odette, T. Yamamoto, M. Alinger, D. Hoelzer and D. Gragg, "Effects of consolidation temperature, strength and microstructure on fracture toughness of nanostructured ferritic alloys", Journal of Nuclear Materials, 367-370 (2007) 208-212.

[14] R. Kasada, S. G. Lee, J. Isselin, J.H. Lee, T. Omura, A. Kimura, T. Okuda, M. Inoue, S. Ukai, S. Ohnuki, T. Fujisawa, and F. Abe, "Anisotropy in tensile and ductile–brittle transition behavior of ODS ferritic steels", Journal of Nuclear Materials 417 (2011) 180-184.

[15] S. Ukai, W. Izawa, N. Oono, S. Hayashi, Y. Kohno, S. Ohtsuka and T. Kaito, "Charpy impact property related to {100} cleavage fracture in 15Cr ODS steel", Materials Science and Technology, 30 (2014) 1709-1714.

[16] M.E. Alam, S. Pal, K. Fields, S.A. Maloy, D.T. Hoelzer and G.R. Odette, "Tensile deformation and fracture properties of a 14YWT nanostructured ferritic alloy", Materials Science and Engineering A, 675 (2016) 437-448.

[17] M. J. Alinger, G. R. Odette and D. T. Hoelzer, “On the role of alloy composition and processing parameters in nanocluster formation and dispersion strengthening in nanostructured ferritic alloys”, Acta Materialia, 57 (2009) 392-406.

[18] S. Pal, M. E. Alam, G. R. Odette, D. Hoelzer and S. Maloy, “ Microstructure, texturing, microcracking and delamination behavior of NFA-1”, DOE/ER-0313/58 (2015), DOE Fusion Reactor Materials Program Semiannual Progress Report, 58 (2015) 66-82.

[19] ASTM E1921-13a, Standard Test Method for Determination of Reference Temperature, T_o, for Ferritic Steels in the Transition Range, ASTM International, West Conshohocken, PA, 2013.

[20] T. L. Anderson, “Fracture Mechanics: Fundamentals and Applications”, 3rd Ed, Taylor & Francis Group, FL, USA (2005).

[21] H. Ernst, P.C. Paris, M. Rossow, J.W. Hutchinson, “ Analysis of load-displacement relationship to determine J-R curve and tearing instability material properties”, American Society for testing and Materials, (1979) 581-599.

[22] T. Inoue, F. Yin, Y. Kimura, K. Tsuzaki and S. Ichiani, “ Delamination effect on impact properties of ultrafine grained low carbon steel processed by warm caliber rolling”, Metallurgical and Materials Transactions A, 41A (2010) 341-355.

[23] W. R. Tyson, R.A. Ayres, D.F. Stien, “Anisotropy of cleavage in bcc transition metals”, Acta Metallurgica, 21 (1973) 621-627.

[24] M.L. Hribernik, “Cleavage oriented iron single crystal fracture toughness”, PhD Thesis, University of California Santa Barbara, CA, USA (2006).

[25] M.L. Hribernik, G.R. Odette and M.Y. He, “ On the initiation and arrest cleavage fracture toughness of ferrite”, DOE /ER-0313/40 (2006), DOE Fusion Reactor Materials Program Semiannual Progress Report, 40 (2006) 74-79.

[26] Y. Qiao, and A.S. Argon, “Brittle-to-ductile fracture transition in Fe–3wt.%Si single crystals by thermal crack arrest”, Mechanics of Materials 35 (2003) 903–912.

[27] A. G. Junceda, M. H. Mayoral and M. Serrano, “Influence of the microstructure on the tensile and impact properties of a 14Cr ODS steel bar”, Materials Science and Engineering A, 556 (2012) 696-703.

[28] Y. Kimura, T. Inoue, F. Yin and K. Tsuzaki, “Delamination toughening of ultrafine grain structure steels processed through tempforming at elevated temperature”, ISIJ International, 50 (2010) 152-161.

[29] D. L. Bourell, “ Texture induced cleavage delamination of warm-rolled low carbon steel”, Metallurgical Transaction A, 14A (1983) 2487-2496.

[30] B. L. Bramfitt and A. R. Marder, “A study of the delamination behavior of a very low carbon steel”, Metallurgical Transactions A, 8A (1977) 1263-1273.

[31] T. Terazawa, H. Higashiyama and S. Sekino, “Toward Improved Ductility and Toughness”, Kyoto International Confeence, BISI Transaction, 10937 (1971) 101.

[32] G.R. Odette, T. Yamamoto, H. J. Rathbun, M.Y. He, M.L. Hribernik and J.W. Rensman, “Cleavage fracture and irradiation embrittlement of fusion reactor alloys: mechanisms, multiscale models, toughness measurements and implications to structural integrity assessment”, Journal of Nuclear Materials, 323 (2003) 313-340.

[33] G. R. Odette, H. J. Rathbun, M. Hribernik, T. Yamamoto, M. He, P. Spätig, “A multiscale approach to measuring and modeling cleavage fracture toughness in structural steels”, V. Getta et. al. (eds): Materials Issues for Generation IV Systems” (2008) 203-226.

[34] G. T. Hahn, “The influence of microstructure on brittle fracture toughness”, Metallurgical Transactions A, 15A (1984) 947-959.

[35] A. H. Cottrell, “Theory of brittle fracture in steel and similar metals”, Transactions of the metallurgical society of AIME, 212 (1958) 192-203.

[36] A.S. Tetelman, and W.D. Robertson, “Direct observation and analysis of crack propagation in iron-3% silicon single crystals”, Acta Metallurgica, 11 (1963) 415-426.

[37] A.S. Tetelman, “The effect of plastic strain and temperature on microcrack propagation in Fe-3Si”, Acta Metallurgica, 12 (1964) 993-1004.

[38] L.E. Kaechelets and A.S. Tetelman, “Statistical investigation of microcrack formation”, Acta Metallurgica, 17 (1969) 463-475.

[39] W.J. Yang, G.R. Odette, T. Yamamoto, P. Milao, M.J. Alinger, M. Hribernik, and J.H. Lee, “A critical stress–critical area statistical model of the K_{Jc}(T) curve for MA957 in the cleavage transition”, J. Nucl. Mater. 367-370, (2007) 616-620.

[40] J.W. Hutchinson and Z. Suo, “ Mixed mode cracking in layered materials”, Advances in Applied Mechanics, 29 (1991) 63-191.

[41] K. Tohgo, H. Ishii, “Elastic-plastic fracture toughness test under mixed mode I-II loading”, Engineering Fracture Mechanics 41 (1992) 529-540.